Chem Soc Rev

Chemical Society Reviews

rsc.li/chem-soc-rev

ROYAL SOCIETY
OF CHEMISTRY
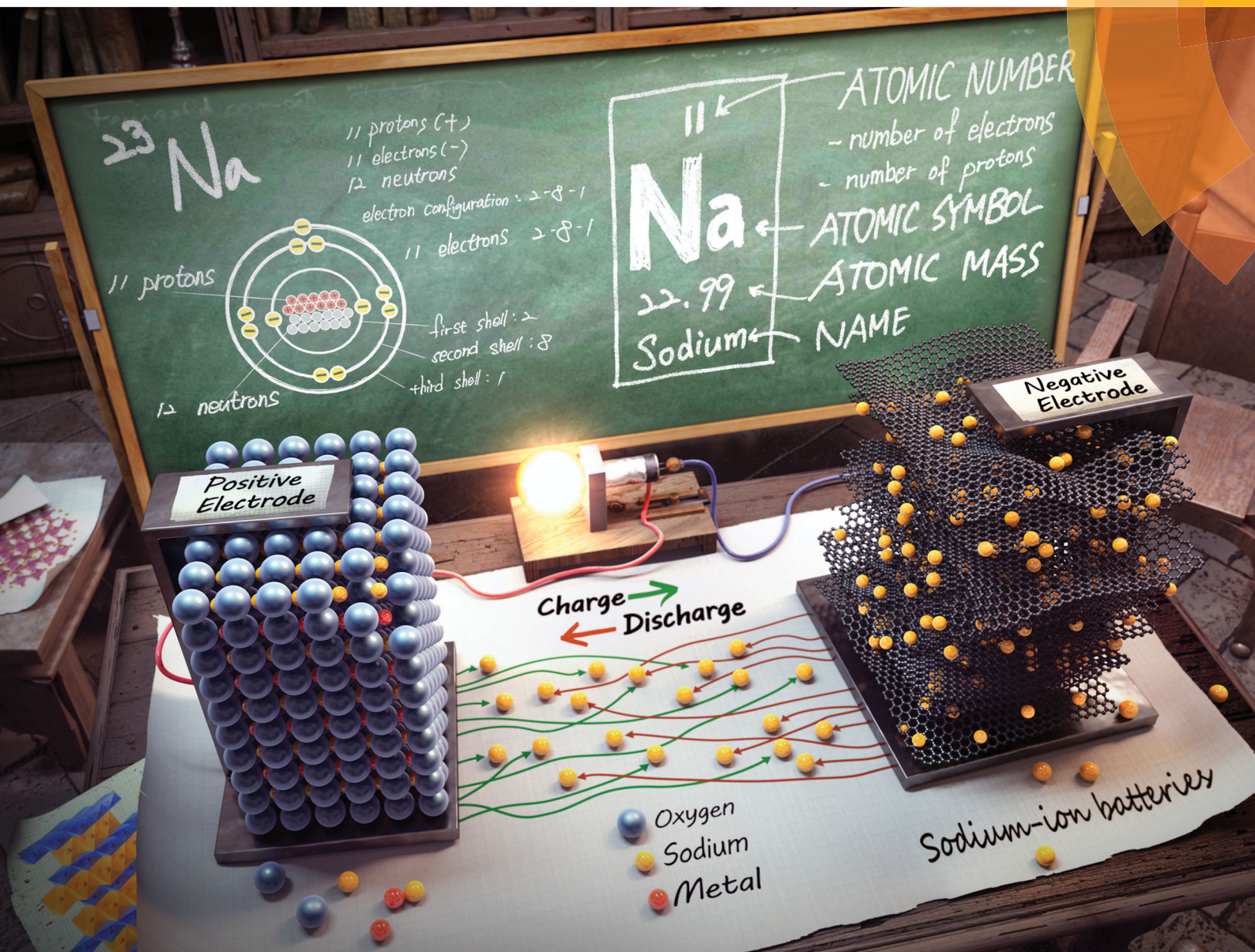
REVIEW ARTICLE
Yang-Kook Sun *et al.*
Sodium-ion batteries: present and future

Sodium-ion batteries: present and future

Jang-Yeon Hwang,†[a] Seung-Taek Myung†[b] and Yang-Kook Sun*[a]

Energy production and storage technologies have attracted a great deal of attention for day-to-day applications. In recent decades, advances in lithium-ion battery (LIB) technology have improved living conditions around the globe. LIBs are used in most mobile electronic devices as well as in zero-emission electronic vehicles. However, there are increasing concerns regarding load leveling of renewable energy sources and the smart grid as well as the sustainability of lithium sources due to their limited availability and consequent expected price increase. Therefore, whether LIBs alone can satisfy the rising demand for small- and/or mid-to-large-format energy storage applications remains unclear. To mitigate these issues, recent research has focused on alternative energy storage systems. Sodium-ion batteries (SIBs) are considered as the best candidate power sources because sodium is widely available and exhibits similar chemistry to that of LIBs; therefore, SIBs are promising next-generation alternatives. Recently, sodiated layer transition metal oxides, phosphates and organic compounds have been introduced as cathode materials for SIBs. Simultaneously, recent developments have been facilitated by the use of select carbonaceous materials, transition metal oxides (or sulfides), and intermetallic and organic compounds as anodes for SIBs. Apart from electrode materials, suitable electrolytes, additives, and binders are equally important for the development of practical SIBs. Despite developments in electrode materials and other components, there remain several challenges, including cell design and electrode balancing, in the application of sodium ion cells. In this article, we summarize and discuss current research on materials and propose future directions for SIBs. This will provide important insights into scientific and practical issues in the development of SIBs.

[a] Department of Energy Engineering, Hanyang University, Seoul, 04763, South Korea. E-mail: yksun@hanyang.ac.kr; Fax: +82 2 2282 7329; Tel: +82 2 2220 0524

[b] Department of Nanotechnology and Advanced Materials Engineering, Sejong University, Seoul 05006, South Korea

† These authors contributed equally to this work.

1. Introduction

Fossil fuels are the most widely used energy resource worldwide. Risks related to resource depletion, environmental pollution, and political unrest with regard to fossil fuel production have led to the rapid emergence of a variety of intermittent renewable and cleaner energy sources such as wind, solar and wave.

Jang-Yeon Hwang received his BS degree from the Department of Chemical Engineering of Hanyang University in 2012. He is presently a PhD candidate in the Department of Energy Engineering at Hanyang University, Korea, under the supervision of Professor Yang-Kook Sun. His research focuses on materials development in the fields of energy conversion and storage, such as cathode, anode and electrolyte materials for sodium-ion batteries.

Jang-Yeon Hwang

Seung-Taek Myung is a Professor of Nano Engineering at Sejong University, South Korea. He received his PhD degree in Chemical Engineering from Iwate University, Japan, in 2003. His research interests embrace development of electro-active materials and corrosion of current collectors of rechargeable lithium and sodium batteries.

Seung-Taek Myung

This journal is © The Royal Society of Chemistry 2017

Chem. Soc. Rev., 2017, 46, 3529–3614 | 3529

In order to integrate these renewable energies into the electrical grid, a large-scale energy storage system (ESS) is vital to peak shift operation.[1] Among various energy storage technologies, using an electrochemical secondary battery is a promising method for large-scale storage of electricity due to its flexibility, high energy conversion efficiency, and simple maintenance.[1,2] LIBs, which have become common power sources in the portable electronic market since their first commercialization by Sony in the early 1990s,[3] are the primary candidates for ESSs. The introduction of LIBs into the automotive market as the battery of choice for powering hybrid electric vehicles (HEVs), plug-in hybrid electric vehicles (PHEVs) and electric vehicles (EVs) could reduce dependence on fossil fuels. Lithium, the primary ingredient in LIBs, is non-uniformly distributed within the Earth's crust. As a result, the Andean states have been dubbed the 'new Middle-East'.[4] However, the increasing demand for lithium associated with these new and large-scale applications is expected to skyrocket the price of lithium, affecting reserves as well, as it is not a naturally abundant element. Based on the calculations, overall global Li consumption in 2008 was nearly 21 280 tons; hence, present mineable resources could be sustained for approximately 65 years at most at an average growth rate of 5% per year,[2,5] making the implementation of the above-mentioned applications difficult and very costly.

Sodium, the fourth most abundant element on earth, has a seemingly unlimited distribution.[6] Supplies of sodium-containing precursors are vast, with 23 billion tons of soda ash located in the United States alone. The abundance of resources and the much lower cost of trona (about $135–165 per ton), from which sodium carbonate is produced, compared to lithium carbonate (about $5000 per ton in 2010), provide a compelling rationale for the development of SIBs to be used as alternatives to LIBs.[7,8] Because an alternative to lithium is needed to realize large-scale applications, SIBs have attracted considerable research attention in recent years. SIBs were initially studied when the development of LIBs began in the 1970s and 1980s, but due to rapid advances in the development and success of commercial applications of LIBs, SIBs were largely abandoned.[9–15] Moreover, during those years, the overall quality of materials, electrolytes and glove boxes was insufficient for handling sodium, making it difficult to observe electrode performance. In the 1980s, prior to the commercialization of LIBS, a few US and Japanese companies developed SIBs in full cell configurations where a sodium-lead alloy composite and a P2-type Na_xCoO_2 were used as the anode and cathode, respectively. Despite the remarkable cyclability over 300 cycles, the average discharge voltages were lower than 3.0 V, which did not attract much attention against carbon// $LiCoO_2$ cells exhibiting an average discharge voltage of 3.7 V.[16–18] The battery components and the electrical storage mechanism of SIBs and LIBs are basically the same except for their ion carriers. In terms of cathode materials, the intercalation chemistry of sodium is very similar to that of lithium, making it possible to use similar compounds for both systems. However, there are some obvious differences between these systems. Na^+ ions (1.02 Å) are larger compared to Li^+ ions (0.76 Å), which affects the phase stability, transport properties, and interphase formation.[9] Sodium is also heavier than lithium (23 g mol^{-1} compared to 6.9 g mol^{-1}) and has a higher standard electrode potential (-2.71 V vs. SHE as compared to -3.02 V vs. SHE for lithium); thus, SIBs will always fall short in terms of energy density. However, the weight of cyclable Li or Na is a small fraction of the mass of the components, and the capacity is determined primarily by the characteristics of the host structures that serve as electrodes. Hence, in principle, there should be no energy density consequences of the transition from LIBs to SIBs.[7] In addition, aluminum undergoes alloy reaction with lithium below 0.1 V vs. Li/Li^+, which indicates that aluminum is available as a current collector for anodes in sodium cells. Therefore, aluminum is a cost-effective alternative to copper as an anode current collector for SIBs.

Various cathode materials for SIBs have been reported; for instance, layer and tunnel type transition metal oxides, transition metal sulfides and fluorides, oxyanionic compounds, Prussian blue analogues and polymers. However, the search for an anode with appropriate Na voltage storage, a large reversible capacity, and high structural stability remains an obstacle to development of SIBs. Graphite, which is a common anode material in LIBs, has a moderate Li storage capacity (~ 350 mA h g^{-1}) at approximately 0.1 V vs. Li/Li^+.[2] Recent studies have demonstrated that graphite does not properly intercalate sodium ions.[19,20] Non-graphitic anodes, which consist largely of various carbonaceous materials such as carbon black[21] and pitch-based carbon-fibers,[22] allow insertion of sodium ions. Hard carbons, which are synthesized at high temperatures from carbon-based precursors, have been comprehensively modeled,[23,24] characterized,[25] and thermally tested[26] in Na cells. These non-graphitic carbonaceous materials are considered to be the "first-generation" anodes of choice for SIB systems. SIBs are not fabricated with sodium metal due to dendrite formation, high reactivity, and an unstable passivation layer in the most organic electrolytes at room temperature. The high reactivity of metallic sodium with organic electrolyte solvents and dendrite formation during Na metal deposition are even more problematic than they are in Li metal anodes. The low melting point of sodium at 97.7 °C also presents a safety hazard for devices using Na metal electrodes at ambient temperature.[27]

Yang-Kook Sun received his PhD degree from Seoul National University, Korea. He was group leader at Samsung Advanced Institute of Technology and contributed to the commercialization of the lithium polymer battery. He has worked at the Hanyang University in Korea as a professor since 2000. His research interests are the synthesis of new electrode materials for lithium-ion batteries, Na ion batteries, Li–S batteries, and Li–air batteries.

Yang-Kook Sun
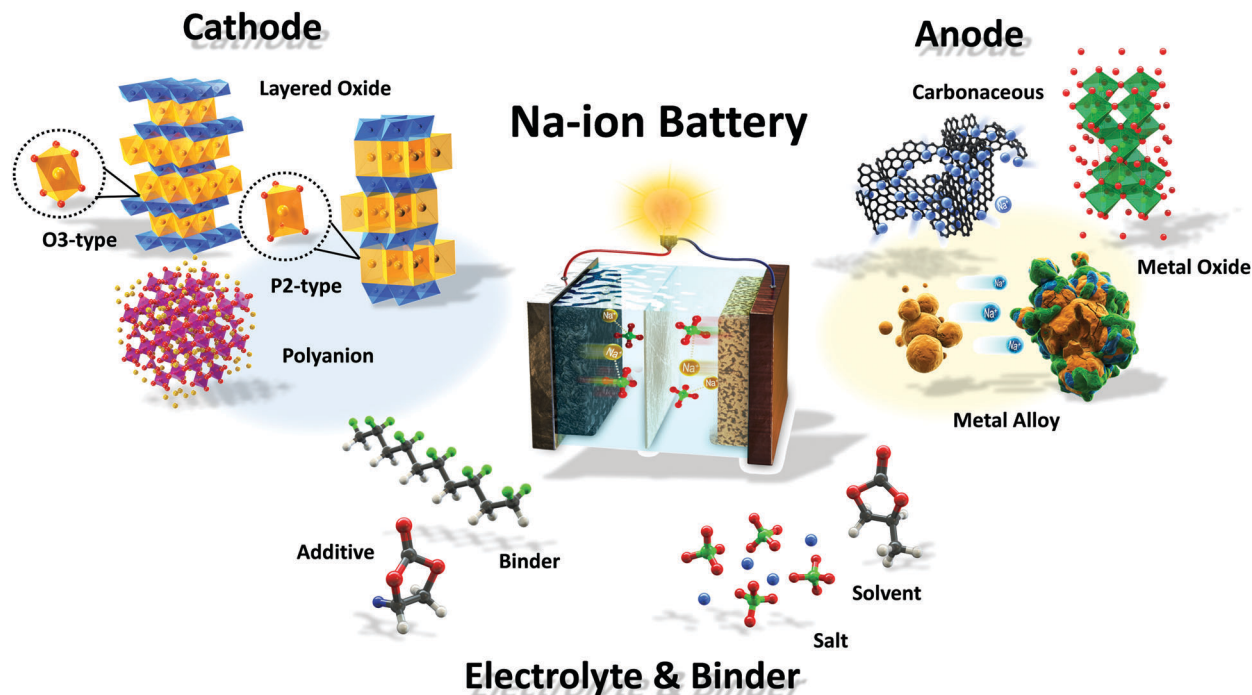
Scheme 1 Illustration of a Na-ion battery system.

Thus, it is important to use a true Na-ion system, where Na ions are exchanged between cathodes and anodes in a 'rocking-chair' format.

A new type of electrolyte for SIBs is needed, as the use of organic liquid electrolytes raises practicality and safety issues. The most common electrolyte formulations for SIBs are $NaClO_4$ or $NaPF_6$ salts in carbonate ester solvents, particularly propylene carbonate (PC). Metallic sodium anodes corrode continuously in the presence of these organic electrolytes, rather than forming a stable solid electrolyte interface (SEI). According to XPS and TOF-SIMS analyses performed by Komaba et al.,[27] when $NaPF_6$ is used as the electrolyte salt, the SEI film on hard carbon is predominantly an inorganic salt that contains precipitated species such as NaF on the surface.[7] Palacin and colleagues[28] found that $NaClO_4$ and $NaPF_6$ in an EC:PC solvent mixture represent the best electrolyte for a hard carbon anode. Developing aqueous electrolytes instead of organic electrolytes could be essential to the success of SIBs. Recently, an aqueous rechargeable battery with $Na_2NiFe(CN)_6$ and $NaTi_2(PO_4)$ as the cathode and anode, respectively, demonstrated a good rate and cycle life with a theoretical energy density of 42.5 W h kg^{-1}.[29] Thus, it is possible to achieve higher energy density by selecting the appropriate electrode material. Nevertheless, an aqueous electrolyte system is more complicated than an organic system because of the (1) elimination of residual O_2 from the electrolyte, (2) maintenance of electrode stability in the aqueous electrolyte, (3) inhibition of H_3O^+ co-intercalation into the electrode and (4) efficiency of the internal consumption of O_2 and H_2 produced from the cathode and anode sides when overcharged, overdischarged or improperly operated in a closed aqueous battery system. All of these issues are important for practical applications of aqueous battery systems.[30,31]

Scheme 1 and Fig. 1 illustrate a schematic SIB image that can adopt several representative candidate materials such as cathode and anode materials, electrolytes, separators, and binders that are discussed in the present paper. Most studies of SIBs explored the electrochemical performance of new electrodes and materials used with Na metal in half-cells, as this field is still in its early stages, and it is thus difficult to create full cells. In that regard, discussion and justification of SIBs are complicated compared to those of LIBs. In addition, experimental conditions such as the purity of Ar gas, electrolyte quality, and the glove box can influence the performance of SIB cells. Hence, comparison of battery performance between studies can be challenging.[18]

2. Cathode materials

Similar to LIBs, highly reversible cathode materials based on the intercalation reaction, which involves interstitial introduction of a guest species (Na^+ in the present context), are needed for high capacity and good cyclability of SIBs. These electrode materials are mainly categorized into oxides, polyanions such as phosphates, pyrophosphates, fluorosulfates, oxychlorides, and NASICON (Na super ionic conductor) types, and organic compounds, which are mentioned in detail in Sections 2 and 3. These cathode materials exhibit a minimal structural change with intercalation, which ensures a reversible intercalation reaction that affects the cycle life. However, continuous structural evolution is inevitable during Na^+ ion intercalation into the host structure interaction because of the large Na^+ ion size (coordination number 6: 1.02 Å) relative to that of Li^+

This journal is © The Royal Society of Chemistry 2017

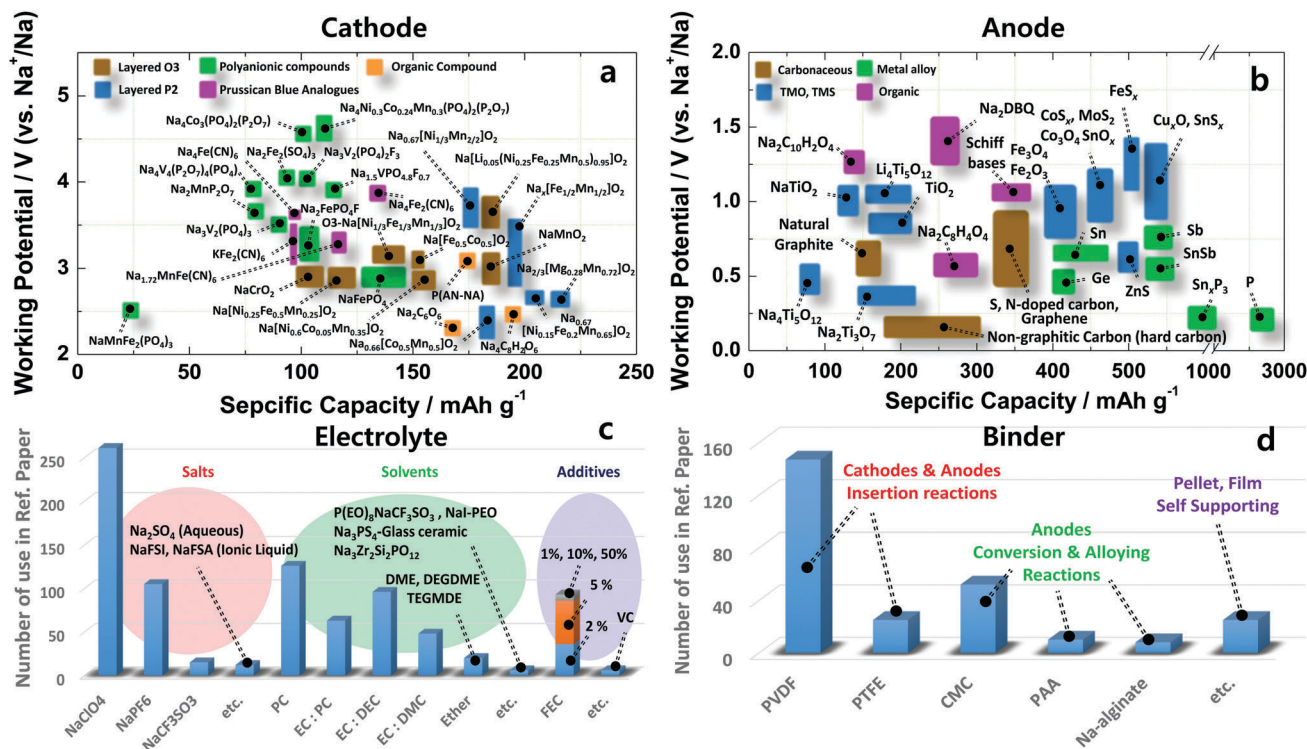Chem. Soc. Rev., 2017, 46, 3529–3614 | 3531

Fig. 1 Recent research progress in sodium ion batteries: (a) cathode, (b) anode, (c) electrolyte and (d) binder.

(coordination number 6: 0.76 Å). Also, sodiated transition metal materials are highly hygroscopic, even with brief exposure to air,[32] and caution is necessary to avoid hydration of the material, particularly the surface, which results in formation of NaOH that degrades electrode performance due to its insulating properties. Thus, the preparation of sodiated cathode materials and batteries requires meticulous handling and moisture-free conditions.

2.1. Two-dimensional layer transition metal oxides

The above-mentioned prototype compounds are composed of two- and three-dimensional crystal structures. Early investigation of two-dimensional layer oxides was performed by Delmas and Hagenmuller in the early 1980s.[13,14,33] They defined the crystal structure of layered compounds depending on the stacking sequence of alkali ions between layers. Sodiated transition metal oxides, $Na_{1-x}MO_2$ (M: transition metal), were representatively classified into two main groups, O3 type and P2 type (Fig. 2), by Delmas et al.[33] Those crystal structures comprise sheets of edge-sharing MO_6 octahedral layers sandwiched between Na ion layers into which ionic species are inserted in an octahedral (O) or a prismatic (P) environment. The number (O2, O3, P2, and P3) indicates the packing number of Na ion octahedral or prismatic layers within each unit cell. In addition, the prime symbol (′) indicates monoclinic distortion, such that O′3 and P′3 represent monoclinic distortion of the O3 and P3 phases, respectively.

The O3 type is stable when the x value is high in $Na_{1-x}MO_2$ (x is close to 0), in which the average oxidation state of M is close to 3+. Electrochemical de-/sodiation of the O3 structure
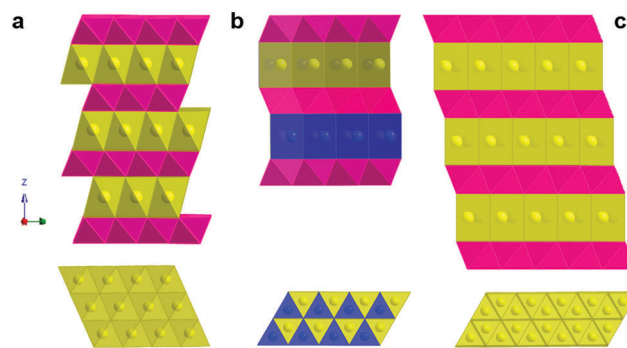

Fig. 2 Crystal structures; (a) perspective view (top) and top view of the (00l) layer of the O3 structure, (b) perspective view (top) and top view of the (00l) layer of the P2 structure in which yellow sphere is face shared Na1 and blue one is edge sharing Na2 atoms, and (c) perspective view (top) and top view of the (00l) layer of the P3 structure.

progresses with reversible structural transformation of O3 ↔ O′3 ↔ P3 ↔ P′3. Na^+ ions energetically favor a prismatic environment when Na^+ ions are partly extracted from the crystal structure, which creates vacancies. At the same time, this extraction induces strong repulsion of oxygen in the Na layers, and the interlayer distance thus expands. Na^+ diffusion occurs faster in the P′3 phase due to the greater interlayer distance compared to O3. These transitions are followed by gliding of the MO_2 slab without breakage of M–O bonds, as proposed by Delmas et al.[33]

The P2 type has a different optimal environment for Na compared to the O3 type. In particular, the structure is stable

when the Na content is in the range of 0.3–0.7 in $Na_{1-x}MO_2$, in which the average oxidation state of M is above 3.3+. The presence of vacancies in the structure causes strong repulsion of oxygen in the Na layers, resulting in expansion of the interlayer distance. This leads to Na^+ ions occupying prismatic (P) sites due to the large Na ionic size. Na^+ ions occupy two different types of trigonal prismatic sites: Na_f (Na1) contacts the two MO_6 octahedra of the adjacent slabs along its face, whereas Na_e (Na2) contacts the six surrounding MO_6 octahedra along its edges. Adjacent Na_f and Na_e sites are too close together (considering the Na^+ ionic radius) to be occupied simultaneously. The P2 phase is maintained in a wide desodiation range up to $Na_{0.46}MO_2$. Further desodiation shifts the phase toward O2 due to gliding ($\pi/3$ rotation) of the MO_6 octahedra and contraction of the crystal structure, reducing the interlayer distance. Based on $O3 \leftrightarrow O'3 \leftrightarrow P'3$ the phase transitions for the O3 type and $P2 \leftrightarrow O2$ for the P2 type, structural variation from the O3/P3 to P2/O2(OP4) type or *vice versa* is not possible in Na cells unless the M–O bond breaks. Apart from phase transition, the P3 type can be produced not only *via* electrochemical desodiation, but also at low temperatures when synthesizing P2 type compounds; P3 and P2 are low and high temperature phases, respectively, indicating that phase transition requires breakage or reformation of M–O bonds *via* heat treatment.

2.1.1. $Na_{1-x}FeO_2$ and derivatives. The O3 type layers, α-, β-, and γ-type $LiFeO_2$, have advantages including non-toxicity and cost effectiveness related to the abundance of Fe. However, de-intercalation does not occur in Li cells.[34–38] This may be because Fe ion distribution is randomized from the 3b ordered state to a 3b–6c disordered state during charge in α-$LiFeO_2$, creating a large irreversible capacity.[39,40] Matsumura *et al.*[41] suggested that $Li_{2/3}[Mn_{1/3}Fe_{2/3}]O_2$, which contains a mixture of O3, O2 and P2 phases, ionic exchange from $Na_{2/3}[Mn_{1/3}Fe_{2/3}]O_2$ showed a reversible charge–discharge capacity of approximately 70 mA h g^{-1} in Li cells. Interestingly, Kikkawa *et al.*[42,43] suggested the possibility of Na^+ deintercalation from α-$NaFeO_2$, creating $Na_{0.9}FeO_2$, using a chemical oxidizing agent (Br_2), while Takeda *et al.*[39] successfully performed electrochemical Na^+ deintercalation to $Na_{0.5}FeO_2$ with an approximate 125 mA h g^{-1} capacity whereas lithium metal was used as the anode (Fig. 3a), which accompanied phase transformation into the monoclinic P3 phase on charge. Further investigation using Mössbauer spectroscopy indicated that the $Fe^{3+/4+}$ redox reaction was responsible for capacity delivery. Approximately 70% of Na^+ ions could be extracted when charging to 4.5 V, but almost no capacity was delivered on discharge, which was possibly disturbed by iron ion migration. When Na^+ ions are extracted from the host structure, vacancies are created at tetrahedral sites contacting FeO_6 octahedral faces. As a result, trivalent iron ions are energetically stabilized at tetrahedral sites and iron ions migrate to the shared face, similar to the phenomena observed in $LiCo_{1-x}Fe_xO_2$.[44] Although the capacity was limited and the material suffered from the irreversible structural change, the electrochemically desodiated $Na_{0.58}FeO_2$ exothermically decomposed above 300 °C with much lower heat generation compared with that
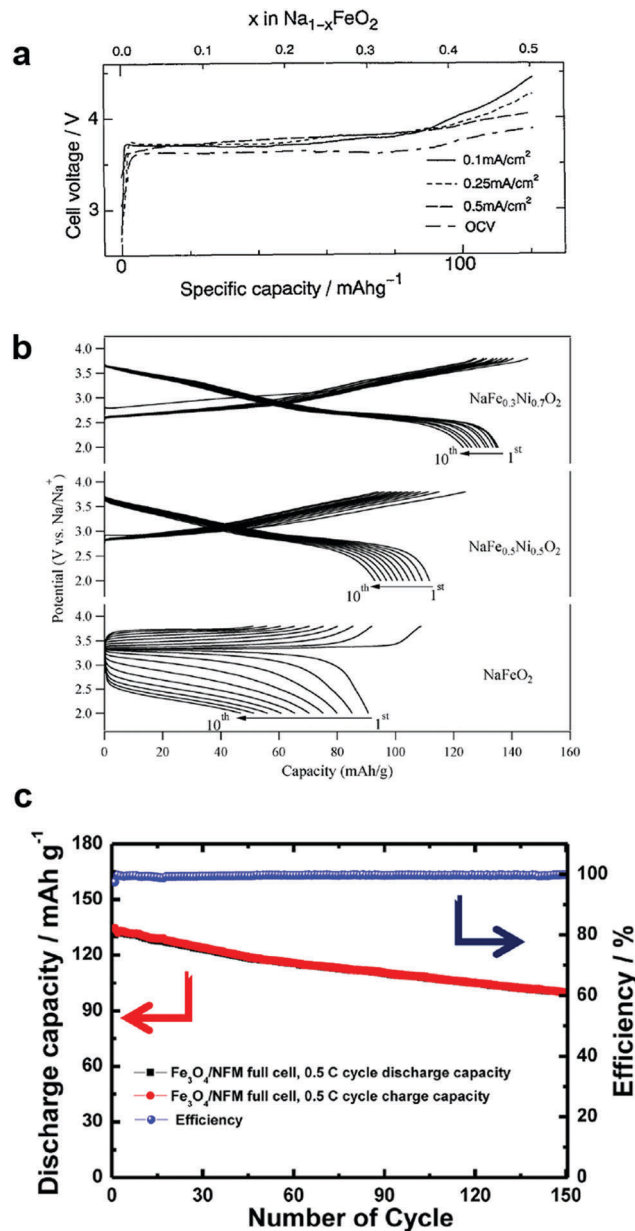

Fig. 3 (a) Charge and discharge curves of O3-$NaFeO_2$. (Reprinted from ref. 39, Copyright 1994, with permission from Elsevier.) (b) Charge and discharge curves of O3-$Na[Fe_{1-x}Ni_x]O_2$. (Reproduced with permission from ref. 48, Copyright 2014 American Chemical Society.) (c) Clce performance for the $Fe_3O_4/Na[Ni_{0.25}Fe_{0.5}Mn_{0.25}]O_2$ full cell. (Reproduced with permission from ref. 51, Copyright 2014 American Chemical Society.)

of $Li_{1-x}CoO_2$.[45] This detrimental effect is suppressed by Mn in $Na[Fe_{0.5}Mn_{0.5}]O_2$, which exhibits a reversible capacity of approximately 100 mA h g^{-1}.[46]

Partial substitution of Fe sites by Co is interesting in terms of capacity retention and rate performance, $NaFe_{0.5}Co_{0.5}O_2$.[47] In particular, the dramatic suppression of the irreversible capacity is attributed to the suppression of iron migration with the help of Co occupation in transition metal sites instead of Fe. Also, the presence of Co enabled an increase in electrical conductivity, such that the electrode was active up to 30 C-rates

(102 mA h g^{-1}). Wang et al.[48] stabilized the crystal structure of NaFeO$_2$ by forming a solid solution with NaNiO$_2$, NaFe$_{1-x}$Ni$_x$O$_2$ (0 ≤ x ≤ 1). The dilution of the Fe concentration, NaFe$_{0.3}$Ni$_{0.7}$O$_2$, effectively increased capacity and retention (135 mA h g^{-1} and 74% retention after 30 cycles) via Fe$^{3+/4+}$ and Ni$^{3+/4+}$ redox couples (Fig. 3b). In addition, they also recorded the ^{57}Fe Mössbauer spectra to determine the valence state and investigate the mechanism of the electrochemical reaction of Fe in O3-NaFe$_{1-y}$Ni$_y$O$_2$ (y = 0, 0.5, and 0.7). Recent report by Nanba et al. also well supported the electrochemical reaction mechanism of NaFe$_{1-x}$Ni$_x$O$_2$ (0 ≤ x ≤ 1) electrodes.[49]

Extension of the layer structure toward a three component system, Na[Ni$_{1/3}$Fe$_{1/3}$Mn$_{1/3}$]O$_2$, was suggested by Kim et al.[50] For synthesis, they used oxalate coprecipitation, [Ni$_{1/3}$Fe$_{1/3}$Mn$_{1/3}$]C$_2$O$_4$, due to the difficulty of forming hydroxides when Fe is involved. Na[Ni$_{1/3}$Fe$_{1/3}$Mn$_{1/3}$]O$_2$ could deliver a discharge capacity of 120 mA h g^{-1} in the voltage range of 2–4 V for a half cell. They also tested the cyclability after adopting a hard carbon anode (100 mA h g^{-1} after 150 cycles). Oh et al. also synthesized spherical Na[Ni$_{0.25}$Fe$_{0.5}$Mn$_{0.25}$]O$_2$ using [Ni$_{0.25}$Fe$_{0.5}$Mn$_{0.25}$](OH)$_2$.[51] They found that the electronic states of Ni, Fe, and Mn were 2+, 3+, and 4+, respectively, of which Ni$^{2+/4+}$ and Fe$^{3+/4+}$ were responsible for electrochemical activity in the range of 2.1–3.9 V via the X-ray absorption nearest edge spectral (XANES) analysis technique. Mn remained electrochemically inactive, but preserved the crystal structure during the electrochemical reaction. A Fe$_3$O$_4$/Na[Ni$_{0.25}$Fe$_{0.5}$Co$_{0.25}$]O$_2$ full cell with a conversion anode and an insertion cathode delivered a capacity of approximately 130 mA h (g-Na[Ni$_{0.25}$Fe$_{0.5}$Mn$_{0.25}$]O$_2$)$^{-1}$ with approximately 76.1% retention at the 150th cycle (Fig. 3c).

Despite the good reversibility of Na[Ni$_{0.25}$Fe$_{0.5}$Mn$_{0.25}$]O$_2$, the discharge capacity limit of 140 mA h g^{-1} in O3 type layer materials needs to be overcome. The voltage limitation to 3.9 V prevents iron migration during charge. Oh et al. suggested another approach to raise the upper voltage cutoff to 4.4 V, in order to offer more capacity in O3 type compounds using the Mn$^{3+/4+}$ redox, but reducing the concentration of Fe^{3+} in Na[Li$_{0.05}$(Ni$_{0.25}$Fe$_{0.25}$Mn$_{0.5}$)$_{0.95}$]O$_2$.[52] As anticipated the compound was active based on the Ni$^{2+/4+}$, Fe$^{3+/4+}$, and Mn$^{3+/4+}$ redox reactions, resulting in a large capacity of approximately 180 mA h g^{-1} at a 0.1C-rate in the voltage range of 1.7–4.4 V. Additionally, the presence of a stronger Li–O bond relative to that of Ni–O and Mn–O in the transition metal layer was responsible for stabilization of the crystal structure, enabling better capacity retention during cycling.

2.1.2. Na$_{1-x}$[Fe$_{1-y}$Mn$_y$]O$_2$ (x ≤ 0.3) and derivatives.

As mentioned in Section 2.1.1, O3 type compounds deliver limited reversible capacities of less than 160 mA h g^{-1}, of which the O3 phase follows a reversible structural transformation (O3 ↔ O′3 ↔ P3 ↔ P′3). Further desodiation results in hexagonal P3″ from P′3 that shows much greater interslab distances of approximately 7 Å compared to the P′3 phase (5.6 Å).[53] This greater distance is not preferred because it induces intercalation of electrolytic molecules formed from oxidative decomposition of electrolytes at high voltage. Hence, delivery of a high capacity of 180 mA h g^{-1} or above is not possible in O3 systems.

Na$_{0.7}$FeO$_2$ is not stable in P2 type layer compounds because of the intrinsic instability of tetravalent Fe in an oxide framework, as described in Section 2.1.1. Yabuuchi and Komaba et al. introduced a P2-Na$_x$[Fe$_{0.5}$Mn$_{0.5}$]O$_2$ layer compound that delivers 190 mA h g^{-1} of reversible capacity (Fig. 4a).[46] Partial substitution of Fe by Mn made it possible to utilize the electrochemical oxidization of Fe^{3+} to Fe^{4+} reversibly, in particular in a voltage range of 3.8–4.2 V. Upon desodiation, the P2 phase was maintained at 3.8 V by the oxidation of Mn$^{3+/4+}$, Na$_{0.42}$[Fe$_{0.5}$Mn$_{0.5}$]O$_2$, after which the oxidation of Fe$^{3+/4+}$ led to phase transformation from P2 to OP4 at 4.2 V (Na$_{0.13}$[Fe$_{0.5}$Mn$_{0.5}$]O$_2$) as shown in Fig. 4b. An in situ XRD study also demonstrated that P2-Na$_{2/3}$[Fe$_{0.5}$Mn$_{0.5}$]O$_2$ undergoes a reversible P2–OP4 phase transition at the end of charge.[54] This achievement is remarkable in terms of capacity in comparison to the O3 type Na[Fe$_{0.5}$Mn$_{0.5}$]O$_2$ that delivers less than 120 mA h g^{-1} in early cycles. Despite a high capacity approximating 190 mA h g^{-1} on the first cycle, capacity fading was inevitable in the P2-Na$_x$[Fe$_{0.5}$Mn$_{0.5}$]O$_2$ compound.

Morternard de Boisse et al. raised another issue regarding the structural change during the first discharge from OCV to 1.5 V.[55] The P2 phase, Na$_{0.62}$[Fe$_{0.5}$Mn$_{0.5}$]O$_2$, was transformed into orthorhombic P′2 (space group: Cmcm), Na$_{0.97}$[Fe$_{0.5}$Mn$_{0.5}$]O$_2$, by cooperative Jahn–Teller distortion at the end of discharge. In a P2 type layer structure, Na$_e$ and Na$_f$ sites are both simultaneously occupied at a ratio close to 2:1. This distribution results from the strong sodium–sodium repulsion interaction, which prevails over sodium–transition metal repulsion. Hence, Na$_e$ and Na$_f$ cannot be occupied simultaneously in the P2 phase. All Na$^+$ ions are located at one site, and the stoichiometry of Na[Fe$_{0.5}$Mn$_{0.5}$]O$_2$ can be stabilized in the orthorhombic structure. Note that the atomic displacement parameter of Na in the P′2 phase (0.7(2) Å^2) is much lower than that of the P2 phase (1.9(3) Å^2), indicating that Na$^+$ ions are less mobile in the orthorhombic P′2 phase. One interesting finding that contrasts with the results of Yabuuchi and Komaba et al. is that when electrochemical sodiation forms the orthorhombic P′2 phase, the resulting desodiation to 4.3 V leads to the formation of not OP4, but also a new and unindexable "Z" phase (Na$_x$[Fe$_{0.5}$Mn$_{0.5}$]O$_2$, x < 0.25) with poor crystallinity (Fig. 4c).[55] Talaie et al. revealed phase "Z", which is a result of migration of Fe^{3+} into tetrahedral sites in the interlayer space, showing a short range order between two adjacent layers.[56] This migration is highly reversible, although it induces polarization of the cell. Addition of Ni instead of Fe was very effective at mitigating migration of Fe^{3+} and thus improved the cycling performance.

Thorne et al. determined the relationship between the Na and Fe content in Na$_{1-x}$[Fe$_{1-x}$Mn$_x$]O$_2$ (0 ≤ x ≤ 0.5).[57] The Na content is a decisive factor establishing the phase (O3, O′3, P2, etc.). As clearly seen in Fig. 4d, the length of the first desodiation plateau increased with x in Na$_{1-x}$[Fe$_{1-x}$Mn$_x$]O$_2$. The length of the first sodiation plateau also increased as x decreased due to more sodium vacancies in Na$_{1-x}$[Fe$_{1-x}$Mn$_x$]O$_2$. The oxidation states in Na$_{1-x}$[Fe$_{1-x}$Mn$_x$]O$_2$ are Fe^{3+} and Mn^{4+}, as suggested by Mössbauer spectroscopy. Therefore, desodiation oxidized Fe^{3+} to Fe^{4+}, while the sodiation of Na$_{1-x}$[Fe$_{1-x}$Mn$_x$]O$_2$ selectively reduced Fe$^{4+/3+}$ at high voltages above 3.5 V and reduced
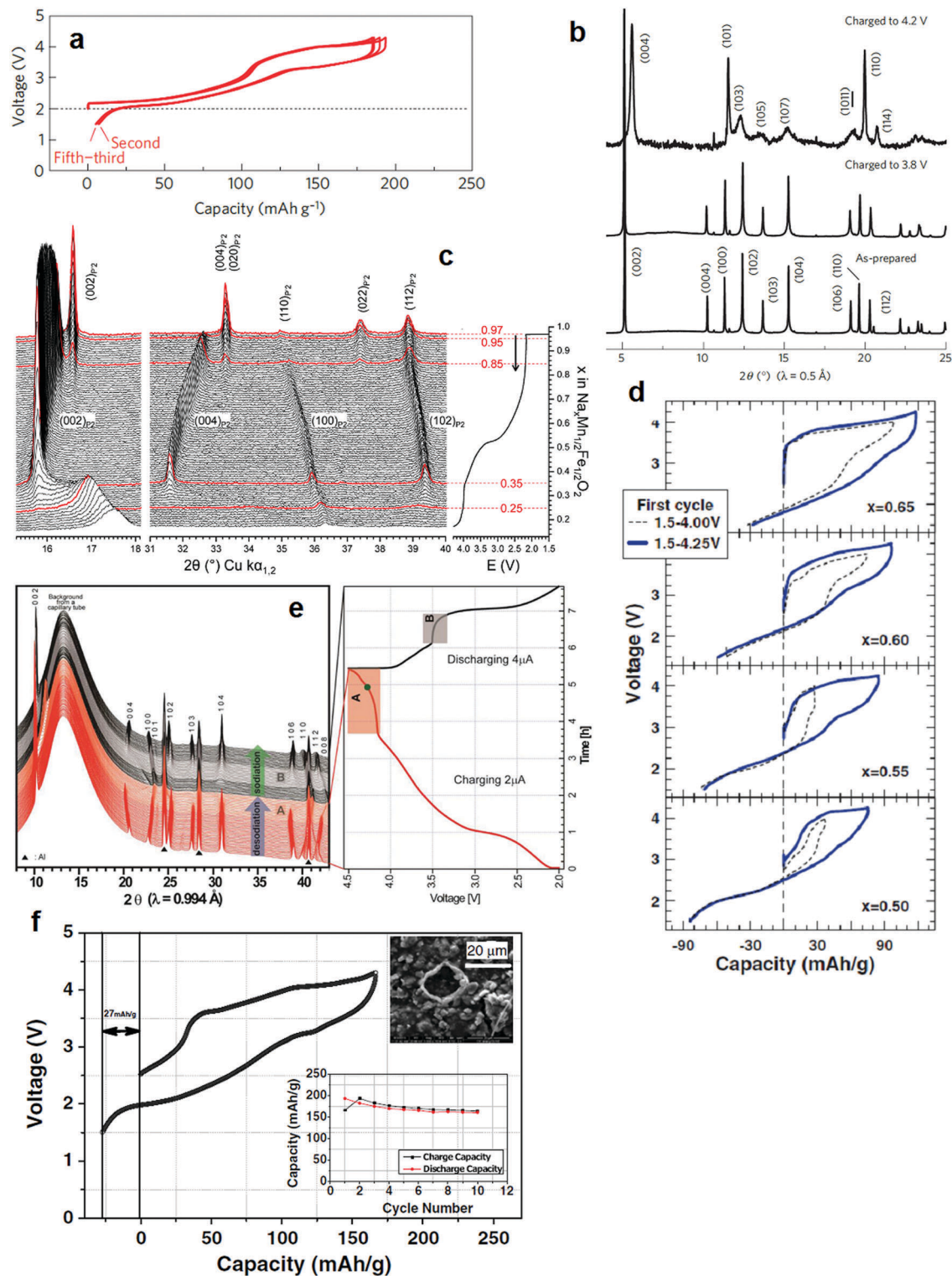
Fig. 4 (a) Charge and discharge curves of P2-Na$_{2/3}$[Fe$_{1/2}$Mn$_{1/2}$]O$_2$ and (b) SXRD patterns of P2-Na$_{2/3}$[Fe$_{1/2}$Mn$_{1/2}$]O$_2$ samples charged to 3.8 and 4.2 V in which the P2 phase was transformed into OP4 one. (Reproduced by permission from ref. 46, Nature Publishing Group, Copyright 2012.) (c) Operando *in situ* XRD patterns of the P2-Na$_x$[Fe$_{1/2}$Mn$_{1/2}$]O$_2$ electrode. The red XRD patterns correspond to the limits of the different structural domains: P′2 phase for $x = 0.85$–0.97 in Na$_x$[Fe$_{1/2}$Mn$_{1/2}$]O$_2$ and Z-phase for $x = 0.25$–0.35 in Na$_x$[Fe$_{1/2}$Mn$_{1/2}$]O$_2$. (Reproduced with permission from ref. 55, Copyright 2011 The Royal Society of Chemistry.) (d) First cycle for 1.5–4.0 V (dashed lines) and 1.5–4.25 (solid lines) for selected cells. (Reproduced with permission from ref. 57, Copyright 2013 The Electrochemical Society.) (e) *In situ* synchrotron XRD patterns of the P2-Na$_{0.7}$[Fe$_{0.4}$Mn$_{0.4}$Co$_{0.2}$]O$_2$. (Reproduced from ref. 58 with permission, Copyright 2015 Wiley-VCH Verlag GmbH & Co. KGaA.) (f) First charge and discharge curves of the Na$_x$[Fe$_{1/2}$Mn$_{1/2}$]O$_2$/NaN$_3$ composite electrode. (Reprinted from ref. 60, Copyright 2013, with permission from Elsevier).

This journal is © The Royal Society of Chemistry 2017

Chem. Soc. Rev., 2017, 46, 3529–3614 | 3535

$Mn^{4+/3+}$ oxidation below 3.5 V. This coincides with the results of Yabuuchi and Komaba. Jung et al.[58] explored the effects of Co on P2-$Na_{0.7}[(Fe_{0.5}Mn_{0.5})_{1-x}Co_x]O_2$ (x = 0–0.2). Note that the partial replacement of Fe by Co in O3-$Na[Fe_{1-x}Co_x]O_2$ dramatically enhanced capacity and performance.[47] Similarly, the addition of Co into the transition metal layers of $Na_{0.7}[(Fe_{0.5}Mn_{0.5})_{1-x}Co_x]O_2$ resulted in higher capacity and contributed to stable cycling behavior during cycling, in particular for $Na_{0.7}[(Fe_{0.5}Mn_{0.5})_{0.8}Co_{0.2}]O_2$. In contrast to P2-$Na_x[Fe_{0.5}Mn_{0.5}]O_2$, P2-$Na_{0.7}[(Fe_{0.5}Mn_{0.5})_{0.8}Co_{0.2}]O_2$ underwent a phase transition toward the O2 phase when desodiated and the O2 phase was transformed into P2 upon sodiation. The P2 to O2 transition was reversibly achieved via the gliding of slabs due to prismatic site instability without Na^+ ions. This simple phase transition is related to the addition of Co in the transition metal layers, as a result of structural stabilization. The phase transition from P2 to OP4 is supposed to occur (Fig. 4e); however, the added Co that stabilizes the crystal structure is likely to suppress phase transition towards the OP4 structure because of the suppression of Fe^{3+} migration to a tetrahedral or octahedral interspace. Therefore, the simple phase transition from P2 to O2 is responsible for the better capacity retention of Co-doped $Na_{0.7}[(Fe_{0.5}Mn_{0.5})_{1-x}Co_x]O_2$. In comparison with the O3 layer structure, the simple phase transition during the de-/sodiation process of P2 layer compounds is obviously advantageous in preserving the original structure during cycling.

However, an important issue regarding the Na-deficient P2 structure is that such high capacities can be obtained only after the first cycle with a Na metal counter electrode. Compensation of Na in the synthetic state causes formation of an O3 and/or O′3 structure with a further increase in the Na content of $Na_x[Fe_{1/2}Mn_{1/2}]O_2$ (x ≥ 0.8).[59] Therefore, the irreversible capacity of the first cycle is an intrinsic issue with P2 type materials. Singh et al. suggested using a NaN_3 additive, sacrificial salt, which acts as follows: $2NaN_3 \rightarrow 3N_2 + 2Na^+ + 2e^-$.[60] This oxidative decomposition was effective in circumventing the irreversible capacity loss in $Na_{2/3}[Fe_{1/2}Mn_{1/2}]O_2$ in the first cycle. NaN_3 was used as a source of extra Na^+ ions added to the cathode. Hence, NaN_3-added P2 $Na_{2/3}[Fe_{1/2}Mn_{1/2}]O_2$ could successfully reduce the irreversible first charge capacity from 58 mA h g^{-1} to 27 mA h g^{-1} (Fig. 4f). Taking into account N_2 release after oxidative decomposition at high potentials, an appropriate amount of NaN_3 is recommended because decomposition can cause swelling of cells. However, degassing is possible in pouch-type cells, such that the addition of sacrificial salts is likely to facilitate full cell configuration of the P2 cathode materials.

Sensitivity in air, in particular uptake of CO_2 in air, is a serious problem because of the formation of electrochemical-inactive Mn^{4+} on the surface of active materials. Ni-doping of the transition metal sites in $Na_x[Fe_{0.5}Mn_{0.5}]O_2$ is less prone to react in air.[61]

2.1.3. $Na_{1-x}CoO_2$ and derivatives. Delmas et al. pioneered Na^+ intercalation properties using O3 type $NaCoO_2$. The structure underwent reversible structural transitions (O3 ↔ O′3 ↔ P′3) in the range of Na_xCoO_2 (x = 0–0.2; Fig. 5a).[33] Apart from the excellent reversibility, the resulting capacity was very small in

comparison with P2 type Na_xCoO_2 (∼140 mA h g^{-1} Delmas et al.).[62] Recent calculations revealed that direct hopping from one octahedral to an adjacent octahedral site requires high activation energy to overcome the barriers. In contrast, the P2 type framework has an open path for Na^+ diffusion that is expected to have a lower diffusion barrier, such that Na^+ diffusion occurs readily in the P2 structure relative to the O3 structure. As mentioned in Section 2.1.1 and Fig. 3a and b, $NaFeO_2$ exhibits poor electrochemical performance. Again, $NaCoO_2$ is active in a very narrow range. However, once a solid solution of $NaCoO_2$–$NaFeO_2$ was formed, a high discharge capacity was obtained at high rates up to a 30C-rate, with $Na[Fe_{0.5}Co_{0.5}]O_2$ in particular.[47]

2.1.4. $Na_{1-x}CoO_2$ (x ≤ 0.3) and derivatives. Although sodium cobaltites can be used in thermoelectric and superconductor applications,[63–68] $Na_{1-x}CoO_2$ is a Na^+ insertion host material according to Delmas et al.[33] Due to the ease of synthesis, this material can be synthesized via a solid state reaction in the temperature range of 500–800 °C under oxygen pressures of 0.4 ≤ x ≤ 0.45 (P′3), 0.26 ≤ x ≤ 0.36 (P2), x = 0.23 (O′3), and x = 0 (O3) in $Na_{1-x}CoO_2$. They suggested that oxygen-deficient Na_xCoO_{2-y} was a stabilized form due to the instability of Co^{4+} when Co^{3+} and Co^{4+} are mixed. Early work found that the P2 structure was maintained over a wide range 0.46 ≤ x ≤ 0.83 in Na_xCoO_2, although two-phase domains were observed in the charge–discharge curves (Fig. 5a).[33] Molenda et al. correlated discharge capacity and the oxygen content using $Na_{0.7}CoO_{2-y}$ (y = 0.004 and 0.073; Fig. 5b).[69] The less-oxygen-deficient phase, $Na_{0.7}CoO_{2-y}$ (y = 0.004), resulted in more Na^+ intercalation than $Na_{0.7}CoO_{2-y}$ (y = 0.073) with a higher operating voltage. The original electron holes arising from oxygen nonstoichiometry lower the electric conductivity via formation of unstable Co^{4+}. Hence, more Na should be added to equalize the Co oxidation state. This was proven experimentally by Chou et al. using the oxygen nonstoichiometric single crystal $Na_{0.7}CoO_{2-y}$ (y ∼ 0.073) in air and $Na_{0.75}Co_{2-y}$ (y ∼ 0.08) in oxygen.[70] For this reason, oxygen deficiency in $Na_{0.7}CoO_2$ induces a lower electrochemical capacity and operating voltage such that an oxygen atmosphere is required to minimize oxygen deficiency and improve electrode performance in terms of capacity and operating voltage.

Delmas suggested the presence of several Na_xCoO_2 structures and Shacklette confirmed that it has four phases.[71] In particular, O3, O′3, and P3 layer structures were formed in a temperature range of 400–600 °C, whereas the P2 structure was stable only when the heating temperature was >700 °C in an oxygen atmosphere via the conversion of the P3 phase, which involved rotation of CoO_6 octahedra and Co–O bond breakage. The voltage profile, operating voltage, and phase transition are very similar for the O3 and P3 phases during de-/sodiation (Fig. 5c). For the P2 phase, although similar behavior was observed in a voltage range of 2.7–3.5 V, phase transition appeared more complicated below 2.7 V compared with O3 and P3 (Fig. 5c). The difference in Na^+ ordering for the P2 and P3 phases could account for the behavior variation below 2.7 V, at which considerable Na^+ is included at trigonal sites. Capacity retention was over 80% for 300 cycles for P2-$Na_{0.7}CoO_2$,
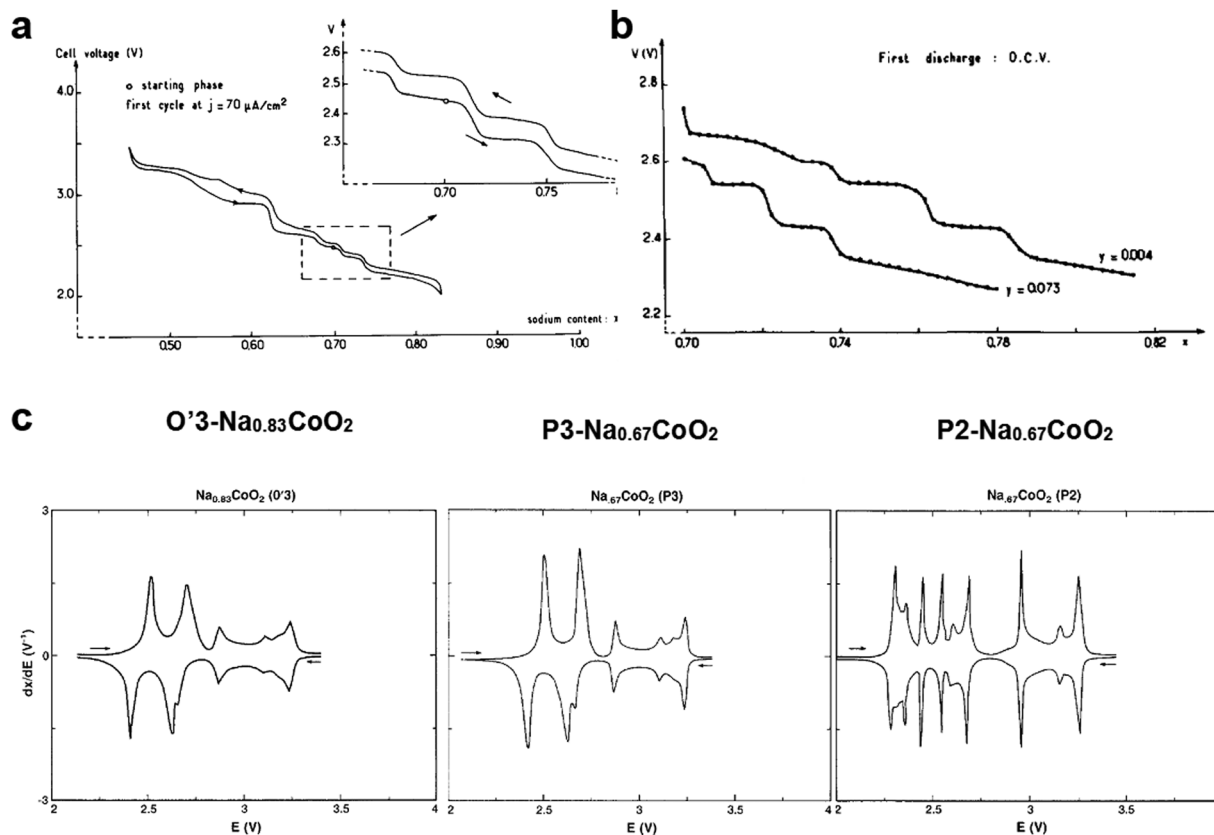
3536 | Chem. Soc. Rev., 2017, **46**, 3529–3614

This journal is © The Royal Society of Chemistry 2017

Fig. 5 (a) First charge and discharge curves of P2-$Na_{0.7}CoO_2$. (Reprinted from ref. 33, Copyright 1981, with permission from Elsevier.) (b) Comparison of open circuit EMF composition curves obtained from P2-$Na_{0.7}CoO_{2-y}$. (Reprinted from ref. 69, Copyright 1989, with permission from Elsevier.) (c) Comparison of dQ/dV curves of O'3-$Na_{0.83}CoO_2$ (left), P3-$Na_{0.67}CoO_2$ (center), and P2-$Na_{0.67}CoO_2$ (right). (Reproduced with permission from ref. 71, Copyright 1988 The Electrochemical Society.)

whereas P3-$Na_{0.7}CoO_2$ exhibited retention of approximately 60% for over 250 cycles. The higher capacity for the P2 phase may be due to its higher crystallinity compared with the P3 material produced at low temperatures. Ma *et al.* confirmed that P2-$Na_{0.7}CoO_2$ can be used for long-term cycling in a $P(EO)_8NaCF_3SO_3$ electrolyte at 90 °C.[72]

Berthelot *et al.* revisited P2-Na_xCoO_2 to investigate the phase diagram in a range of $0.45 \leq x \leq 0.9$, in which nine potential drops were found during the second discharge (Fig. 6a).[62] Weak polarization, which is an intrinsic property of P2-$Na_{0.7}CoO_2$ due to its high conductivity, enabled characterization of each voltage drop *via in situ* XRD. The (008) diffraction peak sometimes splits into two peaks, which is indicative of a two-phase domain when the discharge curve exhibits voltage plateaus, while the voltage drop indicates a strictly fixed peak due to the single phase reaction, demonstrating the presence of ordered phases ($Na_{0.5}CoO_2$, $Na_{0.67}CoO_2$ (No. 3), $Na_{0.72}CoO_2$ (No. 7), $Na_{0.76}CoO_2$ (No. 8), and $Na_{0.79}CoO_2$ (No. 9), although they are present only in very narrow ranges. Between the voltage plateau and the voltage drop, the diffraction peak shifts slightly with solid solution behavior. Na ordering arises from two different repulsive interactions, sodium–sodium and sodium–cobalt. Occupation of Na at the shared edges (Na_e) for P2-$Na_{2/3}CoO_2$ was predicted by first-principles calculations[63,67] and was

experimentally verified.[62,68] At the same time, some of the Na ions are located at the shared faces (Na_f). For P2-$Na_{0.5}CoO_2$, an ordered phase, half of Na occupies Na_e sites while the rest appears at Na_f sites, which probably minimizes the repulsive in-plane interaction between Na_f and Na_e. The distribution of Na^+ ions in these two positions depends on the Na content in the compound, which affects the Na^+/vacancy-ordered structure.

Croguennec *et al.* obtained $T^{\#2}$-$Li_{2/3}[Co_{2/3}Mn_{1/3}]O_2$ *via* ion-exchange from P2-$Na_{2/3}[Co_{2/3}Mn_{1/3}]O_2$, in which the oxidation states of Co and Mn were 3+ and 4+, respectively.[73,74] Cheng *et al.* also confirmed that the oxidation states of Co and Mn for P2-$Na_{2/3}[Co_{2/3}Mn_{1/3}]O_2$ are stabilized at 3+ and 4+, respectively.[75] Carlier *et al.*[76] evaluated P2-$Na_{2/3}[Co_{2/3}Mn_{1/3}]O_2$ in the Na cell and Yang *et al.*[77] extended the stability of P2-$Na_{2/3}[Co_{1-x}Mn_x]O_2$ to $x = 0.5$. The resulting P2-$Na_{2/3}[Co_{2/3}Mn_{1/3}]O_2$ shows suppression of Na^+/vacancy ordering in the structure because the stepwise voltage plateau disappeared in a range of $0.5 \leq x \leq 0.83$ in $Na_x[Co_{2/3}Mn_{2/3}]O_2$ (Fig. 6b). Note that P2-$Na_{0.74}CoO_2$ formed nine distinct phases in a range of $0.5 \leq x \leq 0.9$ in Na_xCoO_2 (Fig. 6a). However, the single phase domain for $x = 0.5$ in Na_xCoO_2 is still found in $Na_{2/3}[Co_{2/3}Mn_{1/3}]O_2$, although the voltage drop at that composition is lower than in Na_xCoO_2. The main difference after Mn substitution for Co is abrupt voltage decay in a range of $0.65 \leq x \leq 0.83$ in $Na_x[Co_{2/3}Mn_{1/3}]O_2$. They further

This journal is © The Royal Society of Chemistry 2017

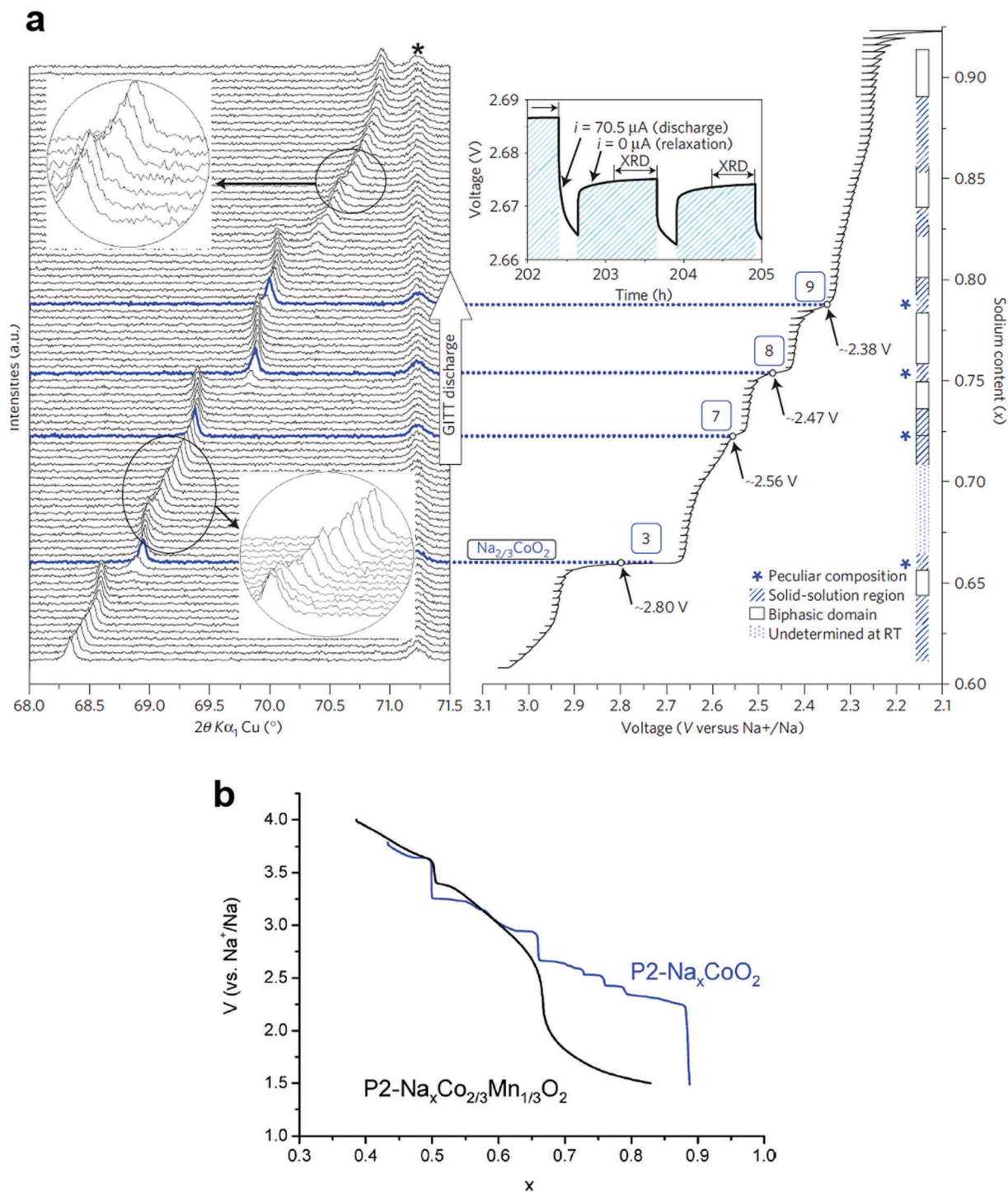*Chem. Soc. Rev.*, 2017, **46**, 3529–3614 | 3537

Fig. 6 (a) *In situ* XRD patterns during sodium ion intercalation in P2-Na$_x$CoO$_2$. (Reproduced by permission from ref. 62, Nature Publishing Group, Copyright 2011.) (b) Comparison between the second discharges obtained for a P2-Na$_x$[Co$_{2/3}$Mn$_{1/3}$]O$_2$ cell (black curve) and a Na$_x$CoO$_2$ cell (blue curve). (Reproduced with permission from ref. 76, Copyright 2011 The Royal Society of Chemistry.)

revealed that Co$^{3+/2+}$ and Mn$^{4+/3+}$ reactions were involved in the low voltage plateau, as similar behavior was found when Li$_{1+x}$[Ni$_{1-x-y}$Co$_x$Mn$_y$]O$_2$ was overlithiated on discharge.

Yang *et al.*[77] successfully stabilized the P2-Na$_{2/3}$[Co$_{1-x}$Mn$_x$]O$_2$ phase to $x = 0.5$, although the resulting capacity was limited to 120 mA h g^{-1}. Meanwhile, Co$^{3+/2+}$ and Mn$^{4+/3+}$ reactions

were more dominant in a voltage range of 1.5–2.1 V. Lowering the synthetic temperature to 700 °C resulted in P2/P3-Na$_{2/3}$-[Co$_{0.5}$Mn$_{0.5}$]O$_2$ compound.[78] This biphasic compound greatly improved the capacity to 180 mA h g^{-1} at a rate of 0.1C in a voltage range of 1.5–4.3 V compared with pure P2-Na$_{2/3}$[Co$_{0.5}$Mn$_{0.5}$]O$_2$.[77] Rate cycling performance at a rate of 5C was also remarkably

high, delivering approximately 125 mA h g^{-1} with retention of 91% for 100 cycles. Even at high rates, half capacity was delivered in the voltage range of 1.5–2.1 V associated with the Co$^{3+/2+}$ and Mn$^{4+/3+}$ reactions. The structural stabilization achieved in the biphasic compound may explain the excellent electrochemical performance. However, the capacity obtained in the low voltage region may decrease the energy density as use these electrode materials for cathodes.

Recently, Matsui et al. explored the possibility of Ca-doping at Na sites to form Na$_{2/3-x}$Ca$_x$CoO$_2$.[79] The similarity in the ionic radius of Ca^{2+} (1.00 Å) versus Na$^+$ (1.02 Å) allows the incorporation of Ca^{2+} into the Na sites. Although the delivered capacity decreased to some extent due to Ca^{2+} in the Na layers, Na$_{2/3-x}$Ca$_x$CoO$_2$ could suppress the multiple phase transition during charge and discharge. For example, Na$_{5/8}$Ca$_{1/24}$CoO$_2$ could be cycled even at 5 mA cm^{-1} with very little capacity decay, while capacity fade was inevitable in Ca-free Na$_{2/3-x}$CoO$_2$. Post-cycled electrodes showed formation of a sodium poor phase of Na$_{2/3}$CoO$_2$, while Na$_{2/3-x}$Ca$_x$CoO$_2$ suppressed this phase separation. This work emphasizes that stability in the Na environment is another topic of investigation that will contribute to development of a long-term cyclable cathode for Na cells.

Xia et al. tested the reactivity of desodiated Na$_{0.35}$CoO$_2$ derived from P2-Na$_{0.65}$CoO$_2$ in the NaPF$_6$-based electrolyte.[80] Na$_{0.35}$CoO$_2$ decomposed to Na$_{0.7}$CoO$_2$ and Co$_3$O$_4$ with oxygen release from the crystal structure. The NaPF$_6$ salt rapidly reacted with Na$_{0.35}$CoO$_2$, and NaCoF$_3$ was produced via the exothermic reaction. This reaction has not been reported in a Li$_x$CoO$_2$ system thus far. Selection of the electrolytic salt is another important issue to utilize the electrode in Na cells.

2.1.5. Na$_{1-x}$NiO$_2$ and derivatives. NaNiO$_2$ is stable as two polymorphs, a low temperature type with an O3 layer structure and a high temperature rhombohedral phase. Similar to α-NaFeO$_2$, the Ni–O layer shares edges between NiO$_6$ octahedra in which the Jahn–Teller Ni^{3+} ions are elongated.[81] Since the starting material, Ni, is divalent, an oxidative environment is needed to synthesize O′3 type NaNiO$_2$ with the space group C2/m. Early work reported by Braconnier et al. suggested that 0.2 mol of Na$^+$, which has approximately 50 mA h g^{-1} of capacity, was deintercalated from NaNiO$_2$ via O′3 ↔ P′3 ↔ P′3 ↔ O′3 multiple phase transition based on the Ni$^{3+/4+}$ redox reaction in the voltage range of 1.7–3.5 V.[33] Later work by Vassilaras reported delivery of a high capacity of approximately 145 mA h g^{-1} in a 2.2–4.5 V voltage range.[81,82] By charging to 4.5 V, however, the capacity retention stabilized when the upper voltage cutoff was lowered to 3.75 V, with 94% of the initial capacity (115 mA h g^{-1}) after 20 cycles. The considerable Coulombic efficiency was due to oxidation of the electrolyte when charged to high voltage (Fig. 7a).

Komaba et al. applied the findings of research on Li[Ni$_{0.5}$Mn$_{0.5}$]O$_2$ to Na[Ni$_{0.5}$Mn$_{0.5}$]O$_2$, in which the average oxidation states of Ni and Mn are 2+ and 4+, respectively.[83] The material was also crystallized into an O3-type layer structure and could be solely activated by the redox reaction of Ni$^{2+/4+}$. In comparison with NaNiO$_2$, the presence of tetravalent Mn induced the formation of Ni^{2+} in Na[Ni$_{0.5}$Mn$_{0.5}$]O$_2$. The two-electron reaction led to a

high discharge capacity of 185 mA h g^{-1} in a voltage range of 2.5–4.5 V (Fig. 7b), whereas optimization of the electrode performance limited the upper voltage cutoff to 3.8 V, resulting in a capacity above 100 mA h g^{-1} over 20 cycles. In contrast to NaNiO$_2$, the O3 ↔ O′3 ↔ P3 ↔ P′3 phase transition was highly reversible in a voltage range of 2.5–3.8 V (Fig. 7c). Fe-substituted Na[Ni$_{0.5}$Mn$_{0.5}$]O$_2$, however, underwent different structural transformation during desodiation compared with Na[Ni$_{0.5}$Mn$_{0.5}$]O$_2$.[84] Phase evolution from P3 to P3″ was predominant in Na[Ni$_{0.5}$Mn$_{0.5}$]O$_2$, whereas Na$^+$ extraction from Fe-substituted Na[Ni$_{0.5}$Mn$_{0.5}$]O$_2$ facilitated a gradual evolution from P3 to OP2 due to the migration of Fe^{3+} ions from the octahedron of the transition metal layers to the interstitial tetrahedron or the octahedron of the Na layers (Fig. 7d). Nonetheless, capacity retention was improved in a voltage range of 2–4.3 V. In particular, a long irreversible reaction due to the formation of P3″ phase transitioned to the OP2 phase in a voltage range of 4–4.3 V on charge, although the length of the plateau did not appear on discharge. This peculiar behavior seems to be related to the effect of Fe. Recently, Hwang et al. investigated the collation of Ni and Fe contents in Na[Ni$_{0.75-x}$Fe$_x$Mn$_{0.25}$]O$_2$ (x = 0.4, 0.45, 0.5, and 0.55).[85] The structural and thermal stabilities, which affect cycle retention and rate capability, were dependent on the Fe content. Although the discharge capacity of higher Fe content materials decreased slightly, the improved cycling performance and rate capability compensate for the slightly reduced capacity. The increase in the Fe content seems to improve conductivity, which is associated with low band gap energy (~2.5 eV for Fe$_2$O$_3$).[86] Therefore, enhanced rate performance with increasing Fe content is attributed to the improvement in electric conductivity derived from Fe in the compound. Also, their DSC study revealed that reactive Ni^{4+} ions in the desodiated host material cause oxygen removal from the crystal structure, and that oxygen evolution can effectively suppress the Fe increase in the crystal structure (Fig. 7e).

They also developed a radially-aligned hierarchical columnar structure in spherical particles with a varied chemical composition from the inner end (Na[Ni$_{0.75}$Co$_{0.02}$Mn$_{0.23}$]O$_2$) to the outer end (Na[Ni$_{0.58}$Co$_{0.06}$Mn$_{0.36}$]O$_2$) of the structure.[87] An electrochemical reaction based on Ni$^{2+/3+/4+}$ had a discharge capacity of 157 mA h (g-oxide)$^{-1}$ with a capacity retention of 80% (125 mA h g^{-1}) over 300 cycles in combination with a hard carbon anode. The cathode also exhibited good temperature performance, even at −20 °C, which enables the Ni redox reaction.

Ti-Substituted O3-Na[Ni$_{0.5}$Ti$_{0.5}$]O$_2$ is also interesting due to its superior cyclability under moderate conditions, with an average operating potential of 3.1 V (vs. Na$^+$/Na) and delivery of a reversible capacity of 121 mA h g^{-1} at 20 mA g^{-1}. Since the average oxidation states of Ni and Ti are 2+ and 4+, respectively, the Ni$^{2+/4+}$ redox reaction is responsible for electrochemical activity.[88] Increasing the Ni content resulted in higher capacity, while a dramatic degradation in capacity and thermal properties was observed. In contrast, increasing the Fe content improved capacity retention and thermal stability in a highly desodiated state. Hence, it is worth noting that Ni redox such as Ni$^{2+/4+}$ or
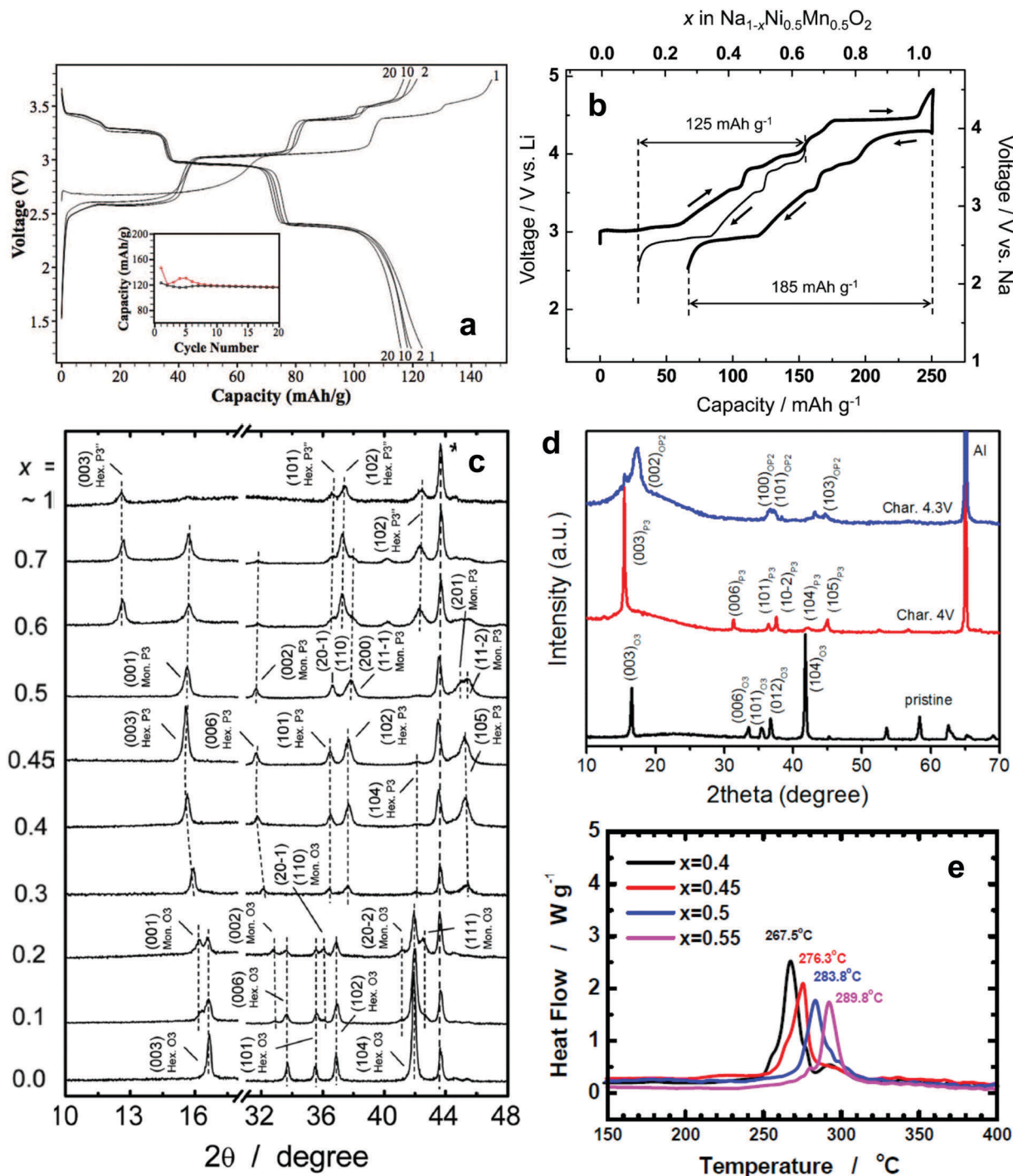
This journal is © The Royal Society of Chemistry 2017

Chem. Soc. Rev., 2017, 46, 3529–3614 | 3539

Fig. 7 (a) Charge and discharge curves of O'3-NaNiO$_2$. (Reproduced with permission from ref. 81, Copyright 2013 The Electrochemical Society.) (b) The first charge and discharge curves of O3-Na[Ni$_{0.5}$Mn$_{0.5}$]O$_2$ and (c) structural evolution of Na$_{1-x}$[Ni$_{0.5}$Mn$_{0.5}$]O$_2$ ($x = 0-1$). (Reproduced with permission from ref. 83, Copyright 2012 American Chemical Society.) (d) *Ex situ* XRD patterns of O3-Na[Fe$_{0.2}$(Ni$_{0.5}$Mn$_{0.5}$)$_{0.8}$]O$_2$ at various charge states. (Reproduced with permission from ref. 84, Copyright 2015 American Chemical Society.) (e) DSC traces of desodiated Na$_{1-d}$[Ni$_{0.75-x}$Fe$_x$Mn$_{0.25}$]O$_2$ obtained after charging to 3.9 V. (Reprinted from ref. 85, Copyright 2016, with permission from Elsevier.)

Ni$^{3+/4+}$ contributes to high capacity delivery, while optimization of the Ni content in the transition metal layer is important in ensuring capacity retention and thermal properties.

2.1.6. Na$_x$MnO$_2$ and derivatives. In comparison to the other compounds, these compounds are in particular interesting because of the cost effectiveness of the Na and Mn elements. Na$_x$MnO$_2$ ($x = 0.44-1$) have been extensively investigated as cathode materials since the first report by Parant *et al.*[89] These structures are three-dimensional at lower x values ($x = 0-0.44$) and two-dimensional at higher x values ($x > 0.5$). With a higher

3540 | *Chem. Soc. Rev.*, 2017, **46**, 3529–3614

This journal is © The Royal Society of Chemistry 2017

sodium content, α-NaMnO$_2$ and β-NaMnO$_2$ are stable, although the phase stability of both compounds is dependent on temperature; for example, α-NaMnO$_2$ (space group: $C2/m$) is the low-temperature form and β-NaMnO$_2$ (space group: $Pmnm$) is the high-temperature form. P2-Na$_{0.7}$MnO$_2$ is no more stable when the Na layer is fully sodiated to NaMnO$_2$ at a low temperature. In a P2 layer structure, Na$_e$ and Na$_f$ sites are simultaneously occupied, due to the strong sodium–sodium repulsion interaction in the Na layers (Fig. 2). Hence, simultaneous distribution of Na$_e$ and Na$_f$ is not possible in the P2 phase, but all Na$^+$ ions are located in one site to form α-NaMnO$_2$ (space group: $C2/m$, O′3 structure, Fig. 8a). The prime symbol is an indication of a monoclinic structure with respect to the hexagonal lattice. Since the average oxidation state of Mn is 3+, the Jahn–Teller distortion prevails in the crystal structure.

Ma and Ceder et al. reported that monoclinic O′3-NaMnO$_2$ could deliver charge and discharge capacities of approximately 210 mA h g^{-1} and 197 mA h g^{-1}, respectively, in a voltage range of 2–3.8 V and at a rate of C/30 (Fig. 8b).[90] This behavior differs from an earlier report by Mendiboure and Hagenmuller.[91] The charge and discharge curves show many plateaus and voltage drops, with eight and five charge and discharge plateaus, respectively. The hysteresis was reversible even after cycling. A long plateau observed at 2.63 V from Na$_{0.93}$MnO$_2$ to Na$_{0.7}$MnO$_2$ is associated with a two-phase reaction. Their ex situ XRD investigation revealed that the second phase was Na$_{0.7}$MnO$_2$, although this was not consistent with orthorhombic Na$_{0.7}$MnO$_2$ (space group: $Cmcm$) or P2-Na$_{0.7}$MnO$_2$ (space group: $P6_3/mmc$). Capacity retention of O′3-NaMnO$_2$ was approximately 74% for 10 cycles without a significant structural change compared to the fresh electrode. In Mn^{3+}-containing cathode materials, capacity fade is usually mentioned with Mn dissolution, which causes disproportionation to Mn^{2+} and Mn^{4+}. Only a small percentage of Mn was dissolved from the active material (less than 32 μg from 2–3 mg of the active material), such that dissolution was not likely to affect electrode performance. Their successive work demonstrated the readiness of the 180° Na–O–Mn^{3+}–O–Na strip formation in contrast to V$_{Na}$–O–Mn^{3+}–O–Na, albeit insufficient Na$^+$ ions in Na$_{5/8}$MnO$_2$, because Na$^+$ ions relax to the highly distorted octahedral sites, where they share the symmetric attraction of two neighboring Jahn–Teller distorted –O–Mn^{3+}–O–Na configurations along the [100] axis.[91] This structural imperfection may be the reason for the gradual capacity fade observed during cycling in this system.

High temperature-type β-NaMnO$_2$ has a zigzag layer structure composed of two edge-sharing stacks of the MnO$_6$ octahedra. Between two neighboring sheets, the sodium ions occupy octahedral sites.[92] In the Li system, orthorhombic LiMnO$_2$ is directly synthesized, indicating that the orthorhombic structure is energetically favored relative to monoclinic LiMnO$_2$, which is usually produced via ion exchange from α-NaMnO$_2$. In the Na system, however, first principles calculations indicate that the monoclinic α-NaMnO$_2$ is energetically more stable than orthorhombic β-NaMnO$_2$.[93,94] β-NaMnO$_2$ is active in a narrow range (0.85 ≤ x ≤ 0.96) in Na$_x$MnO$_2$.[91] In this range, a two-phase domain is attributed to β-NaMnO$_2$ and Na$_x$MnO$_2$.

Phase transformation towards spinel was possible in β-LiMnO$_2$, because Mn can migrate into tetrahedral Li sites to form the spinel phase. This phase transition is unlikely to occur because tetrahedral sites rarely form in spinel with Na due to the large ionic size of Na$^+$ relative to Li$^+$.

Reducing the Na content to 0.7 induces formation of a different crystal structure: P2-, P3, and orthorhombic (P′2) Na$_{0.7}$MnO$_2$ (Fig. 8c).[95] As mentioned in Section 2.1, P3 is the low temperature type and P2 is the high temperature type (Fig. 2). Stoyanova found that orthorhombic Na$_{0.7}$MnO$_2$ (space group: $Cmcm$) is stable at 1000 °C (Na$_{2/3}$[Mn$^{3+}_{3/2}$Mn$^{4+}_{1/3}$]O$_2$).[95,96]

Among these polymorphs, P2-Na$_{0.7}$MnO$_2$ and its derivatives have been intensively studied.[97–99] An early report by Caballero et al. showed reversible capacity delivery of more than 150 mA h g^{-1} in a voltage range of 2–3.8 V in Na cells.[98] They also suggested that intercalation of Na$^+$ ions occurred in several steps, but the resulting capacity fade progressed upon successive cycling tests. Increasing the synthetic temperature to 900 °C, Yabuuchi et al. could improve the capacity up to 190 mA h g^{-1} in a voltage range of 1.5–4.3 V during several early cycles (Fig. 8d).[99,100] The electrode performance is similar to that of O3′-NaMnO$_2$, although the related phase transition is different.

P2-Na$_{2/3}$[Ni$^{2+}_{1/3}$Mn$^{4+}_{2/3}$]O$_2$ was first reported in 2001 by Lu and Dahn et al.[101] This compound is stable in moist air, and hydration via the insertion of water molecules does not occur.[102] Although it has a relatively low theoretical capacity (173 mA h g^{-1}), P2-Na$_{2/3}$[Ni$^{2+}_{1/3}$Mn$^{4+}_{2/3}$]O$_2$ showed an average operating voltage of 3.5 V with a Ni$^{2+/4+}$ redox reaction, delivering approximately 160 mA h g^{-1} in a voltage range of 2–4.5 V (Fig. 8e). Because of the similarity in the ionic size between Ni^{2+} and Mn^{3+}, Ni^{2+} prefers to occupy the Mn^{3+} sites instead of Mn^{4+} in Na$_{2/3}$MnO$_2$. Their in situ XRD study revealed a reversible P2–O2 phase transition stemming from the oxygen shift, in which the O2 phase prevails at a voltage plateau above 4 V on charge and 3.8 V on discharge (Fig. 8f). This is the main difference from P2-Na$_{0.67}$MnO$_2$; the absence of the Jahn–Teller distortion Mn^{3+} is responsible for the occurrence of the P2–O2 phase transition. This transition is associated with a large volume change when the O2 phase appears. Recently, Meng et al. revisited P2-Na$_{2/3}$[Ni$_{1/3}$Mn$_{2/3}$]O$_2$ and observed phase transformation from P2 to O2 at 4.2 V.[103] The long voltage plateau is the evidence of two forms of Na$^+$ ion ordering: one row of Na$_f$ and two rows of Na$_e$ in Na$_{1/2}$[Ni$_{1/3}$Mn$_{2/3}$]O$_2$ and Na orders in rows on either Na$_e$ or Na$_f$ order in Na$_{1/3}$[Ni$_{1/3}$Mn$_{2/3}$]O$_2$, in which the latter corresponds to the region where the O2 phase is dominant. In the P2 phase, the path with the minimum energy passes through a shared face between two neighboring Na prismatic sites. Here, Na$^+$ ions need around 170 meV for diffusion in the P2 phase. In the O2 phase, Na$^+$ ions cross the tetrahedron between two octahedral sites by means of a vacancy mechanism.[104] The required energy for Na$^+$ diffusion in the O2 phase is 290 meV, indicating slow Na$^+$ mobility in the O2 phase, as was confirmed experimentally. It is reasonable because the diffusion path of Na$^+$ ions is more spacious in the P2 phase relative to the O2 phase; this leads to a lower activation barrier (Fig. 8e inset). Hence, a cycling test in the voltage range of 2.3–4.1 V,
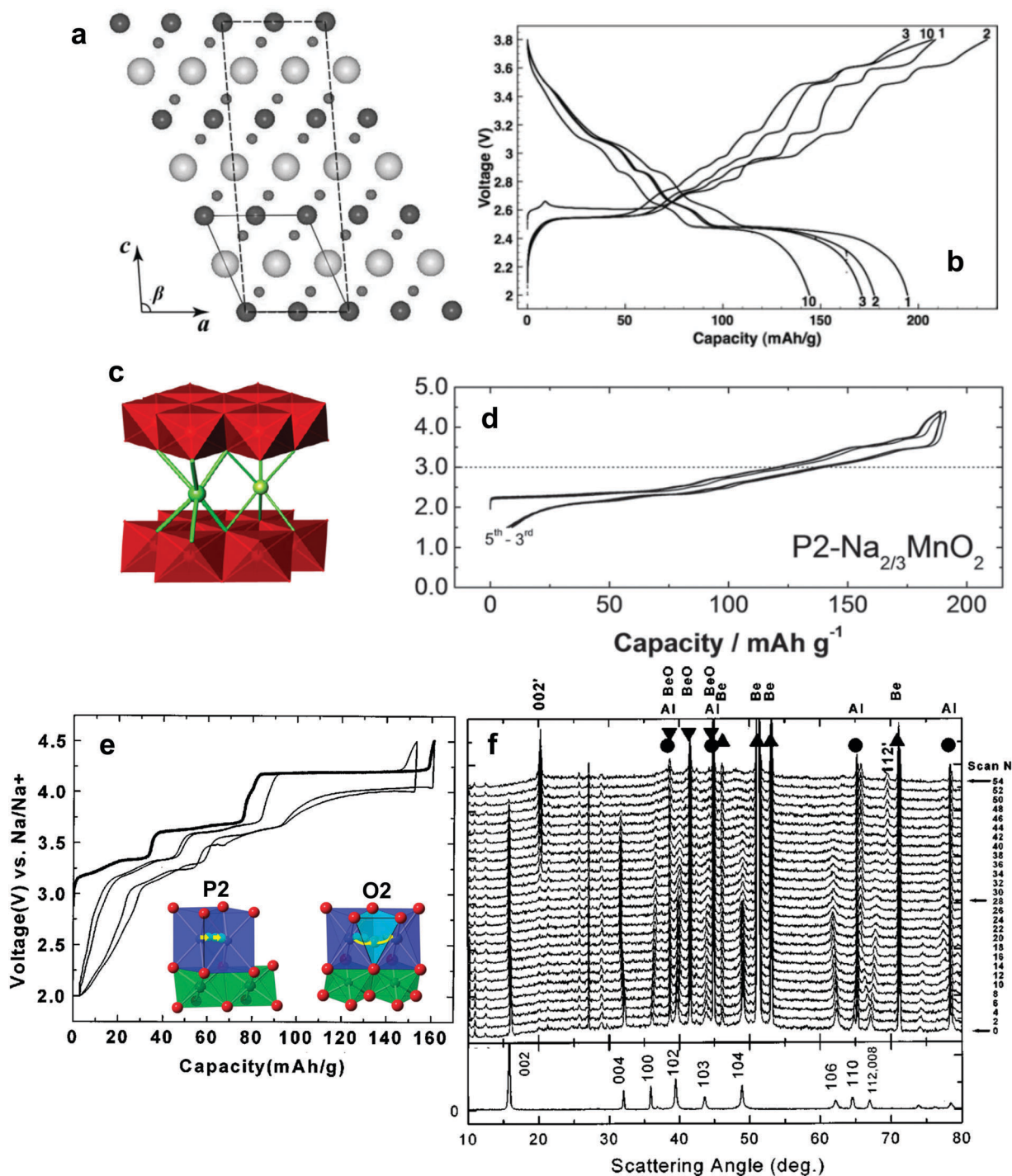
This journal is © The Royal Society of Chemistry 2017

Chem. Soc. Rev., 2017, 46, 3529–3614 | 3541

Fig. 8 (a) Crystal structure of monoclinic O'3-Na$_{0.93}$MnO$_2$ projected in the a–c-plane and (b) charge and discharge curves of monoclinic O'3-Na$_{0.93}$MnO$_2$. (Reproduced with permission from ref. 90, Copyright 2011 The Electrochemical Society.) (c) Schematic illustration of orthorhombic P'2-Na$_{0.7}$MnO$_2$. (Reprinted from ref. 95, Copyright 2010, with permission from Elsevier.) (d) Charge and discharge curves of P2-Na$_{2/3}$MnO$_2$. (Reproduced with permission from ref. 99, Copyright 2014 American Chemical Society.) (e) Charge and discharge curves of P2-Na$_{2/3}$[Ni$_{1/3}$Mn$_{2/3}$]O$_2$ (Reproduced with permission from ref. 101, Copyright 2001 The Electrochemical Society), in which the inset represents the diffusion paths of P2 (left) and O2 (right) that favors diffusion in the P2 phase (Reproduced with permission from ref. 103, Copyright 2013 The Royal Society of Chemistry) and (f) *in situ* powder X-ray diffraction of Na$_{2/3}$[Ni$_{1/3}$Mn$_{2/3}$]O$_2$ showing the reversible evolution of P2–O2 phase transition. (Reproduced with permission from ref. 101, Copyright 2001 The Electrochemical Society.)

which is associated with the P2 phase reaction, resulted in excellent cycling behavior retaining 96% of the initial capacity ($\sim$80 mA h g^{-1}). They further extended their work to inhibit

O2 phase formation in a deeply desodiated state to retain the capacity for a long-term. Surprisingly, Li substitution in the transition metal layer, Na$_{0.80}$[Li$_{0.12}$Ni$_{0.22}$Mn$_{0.66}$]O$_2$, inhibited

P2–O2 transition up to 4.4 V on charge, showing a simple solid solution reaction across the entire range.[105] As a result, there was no characteristic voltage plateau in a voltage range of 4.1–4.4 V. This feature ensured excellent capacity retention as high as 91% for 50 cycles ($\sim$120 mA h g^{-1} at the first discharge).

Substitution of divalent elements such as Mg^{2+} and Zn^{2+} in Ni is effective for diluting the effect of the above-mentioned P2–O2 phase transition.[106–113] A decrease in the initial charge capacity is natural because the electro-active species Ni^{2+} was reduced by substitution, as shown in Fig. 9a, which reflects the origination of the capacity drop from the $Ni^{2+/4+}$ redox reaction. Stepwise voltage plateaus were not dominant throughout the operation range of 2–4.5 V.[106,107] Compared with $Na_{2/3}[Ni_{1/3}Mn_{2/3}]O_2$, the capacity drop in $Na_{0.67}[Ni_{0.2}Mg_{0.1}Mn_{0.7}]O_2$ was only 6 mA h g^{-1} for 50 cycles.[107] Using in situ XRD, instead of the P2 phase, a new phase identified as an OP4 phase was found at voltages above 4.2 V, where a short voltage plateau was observed compared to Mg-free $Na_{2/3}[Mn_{1/3}Mn_{2/3}]O_2$ (Fig. 9b). The presence of electro-inactive Mg^{2+} in transition metal layers facilitates occupation of Na^+ ions in prismatic sites, stabilizing the overall charge balance of the compounds. Since the Na^+ ions are less extracted from the host structure assisted by Mg^{2+} in the transition metal layers, the original P2 phase is retained as the major phase, though transition to OP4 because deep desodiation is observed at high voltage as a minor phase. Hence, the P2–O2 transition and the Na^+/vacancy ordering in $Na_{2/3}[Ni_{1/3-x}Mg_xMn_{0.7}]O_2$ are suppressed during cycling via Mg substitution. This P2–OP4 phase transition is highly reversible; the cycling performance demonstrates its superiority compared to the P2–O2 phase transition.[101] While Zn-substituted $P2-Na_{2/3}[Ni_{1/3-x}Zn_xMn_{2/3}]O_2$ induces reversible phase transition during electrochemical reactions.[111,112] Although the capacity was still limited to approximately 140 mA h g^{-1} by the $Ni^{2+/4+}$ redox reaction due to reductions in electro-active Ni^{2+}, the enhanced structural integrity achieved by Zn^{2+} in the transition metal layer enabled good cyclability due to readiness for transformation and a less variation in unit volume. Further studies explored partial replacement of Ni sites by Al.[113] The substitution displayed sloping charge–discharge curves due to the diminution of the electro-active Ni^{2+} concentration, suggesting that $Ni^{2+/4+}$ redox has superior capacity delivery. The substituent stabilized the host structure and the resulting cyclability was significantly improved, in particular for Al-doped $P2-Na_{2/3}[Ni_{1/3}Mn_{2/3}]O_2$, which had 94.8% (from $\sim$147 mA h g^{-1}) retention over 30 cycles.

Replacement with a trivalent 3d transition metal element such as Co and Fe is also interesting because they are electrochemically active in the same operating range.[114–116] Yoshida et al. investigated the composition of $P2-Na_{0.7}[Mn_{0.6}Ni_{0.3}Co_{0.1}]O_2$, in which the oxidation state of Mn is approximately 3.4+, in a voltage range of 1.5–4.3 V.[114] Note that the oxidation state of Mn is 4+ in $P2-Na_{2/3}[Ni_{1/3}Mn_{2/3}]O_2$. As expected, the material exhibited multiple voltage plateaus. In comparison with $P2-Na_{2/3}[Ni_{1/3}Mn_{2/3}]O_2$, the improvement in capacity during the first cycle (approximately 204 mA h g^{-1}) is due to the additional capacity contributed by $Mn^{3+/4+}$ redox below 4 V (Fig. 9c). The long plateau above 4 V confirmed the validity of the $Ni^{2+/4+}$ redox reaction.

As cycles went by, the length of the upper voltage plateau related to $Ni^{2+/4+}$ and the lower voltage plateaus related to $Mn^{3+/4+}$ 2 V decreased. This can be interpreted in two ways: (1) the progressive formation of the O2 phase at high voltage and the effect of the Jahn–Teller distortion in the crystal lattice. This further limited the cycling region to three parts: 1.5–4.3 V, 1.5–4.0 V, and 1.7–4.0 V. It is evident that, although the Jahn–Teller distortion is present in low voltage regions, severe capacity fade occurs in high voltage regions. This explains that the P2–O2 phase transition is not favored when maintaining the capacity because of the large difference in the c-axis, which causes a drop in the capacity (Fig. 9d). Jahn–Teller distortion seems to be less pronounced in capacity retention. In contrast, instead of Co, Yuan et al. suggested that Ni substitution with Fe ($P2-Na_{0.7}[Mn_{0.65}Ni_{0.15}Fe_{0.2}]O_2$) led to an improvement in capacity and retention: 208 mA h g^{-1} with 71% retention over 50 cycles.[115] The phase transition was P2 to OP4 in this case.[117]

Tetravalent Ti-substituted $P2-Na_{2/3}[Ni_{1/3}Mn_{2/3-x}Ti_x]O_2$ yielded a wide solid solution range of $0 \leq x \leq 2/3$.[118,119] Due to the similarity of both Mn^{4+} and Ti^{4+} in the valence and ionic radius, such a solid solution can be formed readily throughout the range. The reason remains unclear, but an increase in the Ti content resulted in a decrease in capacity. In particular, $Na_{2/3}[Ni_{1/3}Mn_{2/3-x}Ti_x]O_2$ ($x = 1/6$) delivered approximately 127 mA h g^{-1} with an average operating voltage of approximately 3.7 V on discharge, which corresponds to 470 W h kg^{-1}. More importantly, the stepwise voltage profiles of $Na_{2/3}[Ni_{1/3}Mn_{2/3}]O_2$ were obviously diluted by Ti substitution. XRD suggested that the volume change of the fully charged state was reduced from 23.1% in Ti-free compounds to 12–13% for Ti-substituted compounds, confirming the suppression of Na/vacancy ordering and phase transitions during sodium intercalation.

A new mechanism was introduced in $P2-Na_{2/3}[Mg_{0.28}Mn_{0.72}]O_2$ and $P2-Na_{5/6}[Li_{1/4}Mn_{3/4}]O_2$ by Yabuuchi and Komaba et al.[120,121] In this compound, since Mg^{2+} and Li^+ are electrochemically inactive, the only possible reaction should be associated with Mn redox upon de-/sodiation. While the average oxidation states of Mn are 3.84+ for $Na_{2/3}[Mg_{0.28}Mn_{0.72}]O_2$ and 3.88+ for $Na_{5/6}[Li_{1/4}Mn_{3/4}]O_2$. Nonetheless, both materials exhibited large capacities of approximately 220 mA h g^{-1} for $Na_{2/3}[Mg_{0.28}Mn_{0.72}]O_2$ (Fig. 9e) and 180 mA h g^{-1} for $Na_{5/6}[Li_{1/4}Mn_{3/4}]O_2$. Similarly, a recent report by Slater et al. also showed a large capacity of 200 mA h g^{-1} for $P2-Na_{0.85}[Li_{0.17}Ni_{0.21}Mn_{0.64}]O_2$.[7] Taking the $Mn^{3+/4+}$ redox species into account, it is not possible to explain the delivery of high capacity. Indeed, there is almost no delivery of capacity in the voltage cutoff up to 4 V on charge; however, those capacities are delivered above 4 V, which is related to oxidation of oxide ions, resulting in the release of oxygen from the oxide lattice. Oxygen removal causes formation of Mn^{3+}, which simultaneously participates in oxidation on charge and is reduced on discharge. This causes rearrangement of the in-plane cation ordering of the crystal structure, which is similar to a Li-rich Li_2MnO_3 system.[122] P2–O2 transition was also observed in these compounds (Fig. 9f), which is worth mentioning because of the theoretical capacity of 173 mA h g^{-1} based on the $Ni^{2+/4+}$ redox reaction. Ni^{2+} was successfully overcome by the oxygen compensation accompanied by the $Mn^{3+/4+}$ redox reaction.
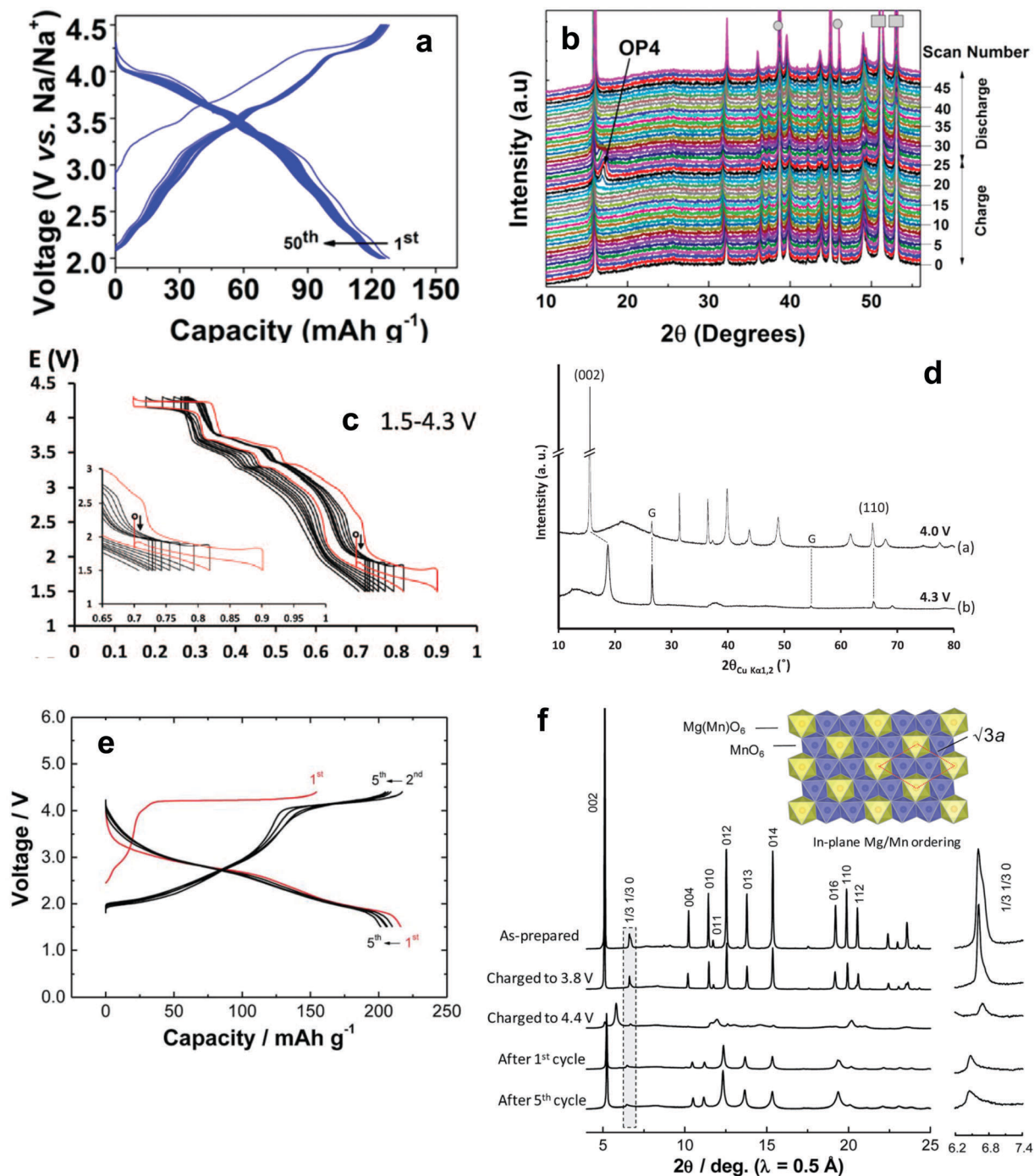
Fig. 9 (a) Continuous charge and discharge curves of P2-Na$_{0.67}$[Mg$_{0.1}$Ni$_{0.2}$Mn$_{0.7}$]O$_2$ and (b) *in situ* powder X-ray diffraction of P2-Na$_{0.67}$[Mg$_{0.1}$Ni$_{0.2}$Mn$_{0.7}$]O$_2$ showing the reversible evolution of P2–OP4 phase transition at the end of the charge and beginning of the discharge. (Reproduced with permission from ref. 107, Copyright 2016 American Chemical Society.) (c) Continuous charge and discharge curves of P2-Na$_{0.70}$[Mn$_{0.60}$Ni$_{0.30}$Co$_{0.10}$]O$_2$ in the voltage range of 1.5−4.3 V and (d) XRD patterns of the material recovered on both sides of the plateau: (a) after charge at 4.0 V and (b) after charge at 4.3 V, where G denotes graphite. (Reproduced with permission from ref. 114, Copyright 2014 The Electrochemical Society.) (e) Initial charge and discharge curves of P2-Na$_{2/3}$[Mg$_{0.28}$Mn$_{0.72}$]O$_2$ and (f) structural changes of P2-Na$_x$[Mg$_{0.28}$Mn$_{0.72}$]O$_2$ in the Na cells examined by synchrotron X-ray diffraction (SXRD). Highlighted SXRD patterns (marked by a dotted square) are also shown in the inset. Mg and Mn superlattice ordering is still visible after electrochemical cycle tests. (Reproduced with permission from ref. 120, Copyright 2014 The Royal Society of Chemistry.)

Surface modification was performed on P2-Na$_{2/3}$[Ni$_{1/3}$Mn$_{2/3}$]O$_2$ *via* wet milling in an Al-containing aqueous solution.[123] Na-containing transition metals react very quickly when moisture is present. Although P2-Na$_{2/3}$[Ni$_{1/3}$Mn$_{2/3}$]O$_2$ is stable in air, ion exchange between Na and H occurs when the reaction progresses in an aqueous medium. Optimized experimental conditions

facilitate the formation of Al_2O_3-coated P2-$Na_{2/3}[Ni_{1/3}Mn_{2/3}]O_2$, although there is some possibility of Al doping in the crystal structure because additional heating after the removal of the aqueous medium was performed at 650 °C for 10 h. Al_2O_3-coated P2-$Na_{2/3}[Ni_{1/3}Mn_{2/3}]O_2$ had good cycling performance for 300 cycles with approximately 72% retention in a voltage range of 2.5–4.3 V. Although the detailed mechanism related to this high capacity retention remains unclear, structural stabilization of the host material by the coating was suspected.

2.1.7. $Na_{1-x}TiO_2$ and derivatives. $NaTiO_2$ was first synthesized by Hagenmuller et al. and Maazaz et al. evaluated its potential as a Na$^+$ insertion/extraction material.[124,125] This material underwent phase transformation from O3 ↔ O′3, in which the chemical composition reaches $Na_{0.7}TiO_2$ (approximately 75 mA h g^{-1}) on desodiation, showing an average operating voltage of 1 V, which is suitable for an anode. In contrast to the other materials, the electrode exhibited a low operating voltage of ~1 V, followed by the Ti$^{3+/4+}$ redox reaction. When a solid solution is formed with $NaNiO_2$ ($Na[Ni_{0.5}Ti_{0.5}]O_2$) as suggested above by Yu et al., the material is sufficiently stable for long-term cycling as a cathode because Ti enables significant structural stability and the Ni$^{2+/4+}$ redox couple contributes to capacity delivery.[88]

2.1.8. $Na_{1-x}CrO_2$ and derivatives. The first study of O3-$NaCrO_2$ showed limited capacity, which was desodiated to $Na_{0.85}CrO_2$.[126] Miyazaki et al. also investigated Na$^+$ desodiation via chemical and electrochemical methods, in which extraction facilitated the formation of $Na_{0.4}CrO_2$.[127] They also confirmed the formation of Cr^{4+} for desodiated $Na_{0.5}CrO_2$, as analyzed based on magnetic susceptibility. Recently, Komaba et al. revisited O3 type layer-structured $NaCrO_2$, in which Na ions could be inserted into/extracted from the host structure.[128] In contrast to $LiCrO_2$ in Li cells, $NaCrO_2$ could deliver a capacity of approximately 110 mA h g^{-1} in the voltage range of 2–3.6 V due to the greater inter-slab distance provided by the presence of large Na$^+$ ions in the Na layers. Despite the high theoretical capacity of about 250 mA h g^{-1}, the practical reversible capacity was approximately 110 mA h g^{-1} ($Na_{1-x}CrO_2$, $0 \leq x \leq 0.5$), with a flattened voltage plateau at 3 V (Fig. 10a). Dahn's group also reported that desodiated $Na_{0.5}CrO_2$ has excellent thermal stability in Na-based non-aqueous electrolytes.[129] However, $NaCrO_2$ electrodes suffer from capacity fading during cycling.[128,129]

In consideration of synthetic conditions, $NaCrO_2$ is usually produced in a reducing atmosphere to retain the oxidation state of Cr at 3+. This condition enables carbon coating, which can dramatically improve electrode performance. Ding et al. found that citric acid-assisted carbon coating slightly improved the cycling stability of $NaCrO_2$ electrodes.[130] Although the cycling performance of carbon-coated $NaCrO_2$ was improved compared to the bare material, operation at high rates was not possible, presumably due to inhomogeneous or excessively thick carbon layers. The XANES study revealed that Cr^{3+} is oxidized to a higher chemical state on charge. The above results are not satisfactory for use in practical applications because of rapid capacity fading (ca. 80% in the 50th cycle) and disappointing rate capability. Yu et al. modified the surfaces of the $NaCrO_2$

particles via carbonization of pitch, which improved the electrical conductivity to approximately 10^{-1} S cm^{-1}.[131] The carbon-coated $NaCrO_2$ electrode exhibited excellent cyclability and an ultrafast rate capability of up to a 150C-rate (Fig. 10b). High electrical conductivity successfully promotes reversible insertion and extraction of sodium ions accompanied by a facile complementary redox reaction of the Cr^{3+}/Cr^{4+} couple as confirmed by XANES (Fig. 10c–e). The $NaCrO_2$ electrode was also sufficiently stable in an intermediate temperature ionic liquid, NaFSA-KFSA, at 363 K.[132] Excellent electrochemical performance of these cathodes was demonstrated in both half and full sodium ion cells. Apart from the electrode performance, the carbon coating layer also delays exothermic decomposition by preventing oxygen evaporation from the crystal lattice; specifically, the lower heat generation from the desodiated $Na_{0.5}CrO_2$ was ascribed to the suppression of oxygen evolution during the exothermic reaction, which results from the presence of carbon coating layers.

A major challenge associated with sodiated cathode materials is immediate water absorption after exposure to air. This leads to the formation of NaOH and Na_2CO_3 on the surface of active materials. The sodium diffuses to the surface, and electrochemically inactive parts are formed within the particles. Even worse, the NaOH and Na_2CO_3 formed are electrical insulators. The carbon coating can prevent moisture uptake due to its hydrophobic characteristics.

2.1.9. $Na_{1-x}VO_2$ and derivatives. Among several $Na_{1-x}VO_2$ compounds, only two compositions, $x = 0$ and $x = 0.3$, have been identified;[133,134] the former represents O3 and the latter, P2. However, O3-$NaVO_2$ reacts in air for a few seconds, leading to desodiated $Na_{1-x}VO_2$ phases.[134] $NaVO_2$ shows highly reversible Na$^+$ insertion and extraction in a voltage range of 1.2–2.4 V (Fig. 11a). The first charge plateau is a typical characteristic of the biphasic domain until the composition reaches $Na_{2/3}VO_2$. Complicated behavior is observed upon further sodiation, showing three voltage plateaus. Approximately 120 mA h g^{-1} was delivered. Upon desodiation, the O3 structure transforms into the O′3 structure via monoclinic distortion. Na$^+$ extraction above $x = 0.5$ in $Na_{1-x}VO_2$ deteriorates electrode performance, resulting from the migration of vanadium ions into interslab vacancies. This phenomenon is similar to $Na_{1-x}CrO_2$.[128,130] Despite considerable voltage variation and oxygen sensitivity, capacity fading was negligible for 15 cycles, as reported by Hamani et al.[135] In P2-$Na_{0.7}VO_2$, the resulting charge and discharge behavior is very reversible in a voltage range of 1.2–2.6 V, delivering approximately 105 mA h g^{-1} (Fig. 11b). In contrast to the Fe- and Mn-based compounds presented in Sections 2.1.2 and 2.1.6, the related phase transition is more or less complicated (Fig. 11c and d). An abrupt voltage drop occurs due to the single phase domain and the plateaus are associated with the solid solution reaction. Hence, four single phase domains and solid solutions are present between the single phase domains, which have been identified in XRD studies.[136] Similarly, these multi-domains are also observed in P2-Na_xCoO_2.[62] Since $NaVO_2$ is stable in a reducing atmosphere, carbon coating of $NaVO_2$ could further minimize oxygen uptake in air. Successful carbon

This journal is © The Royal Society of Chemistry 2017

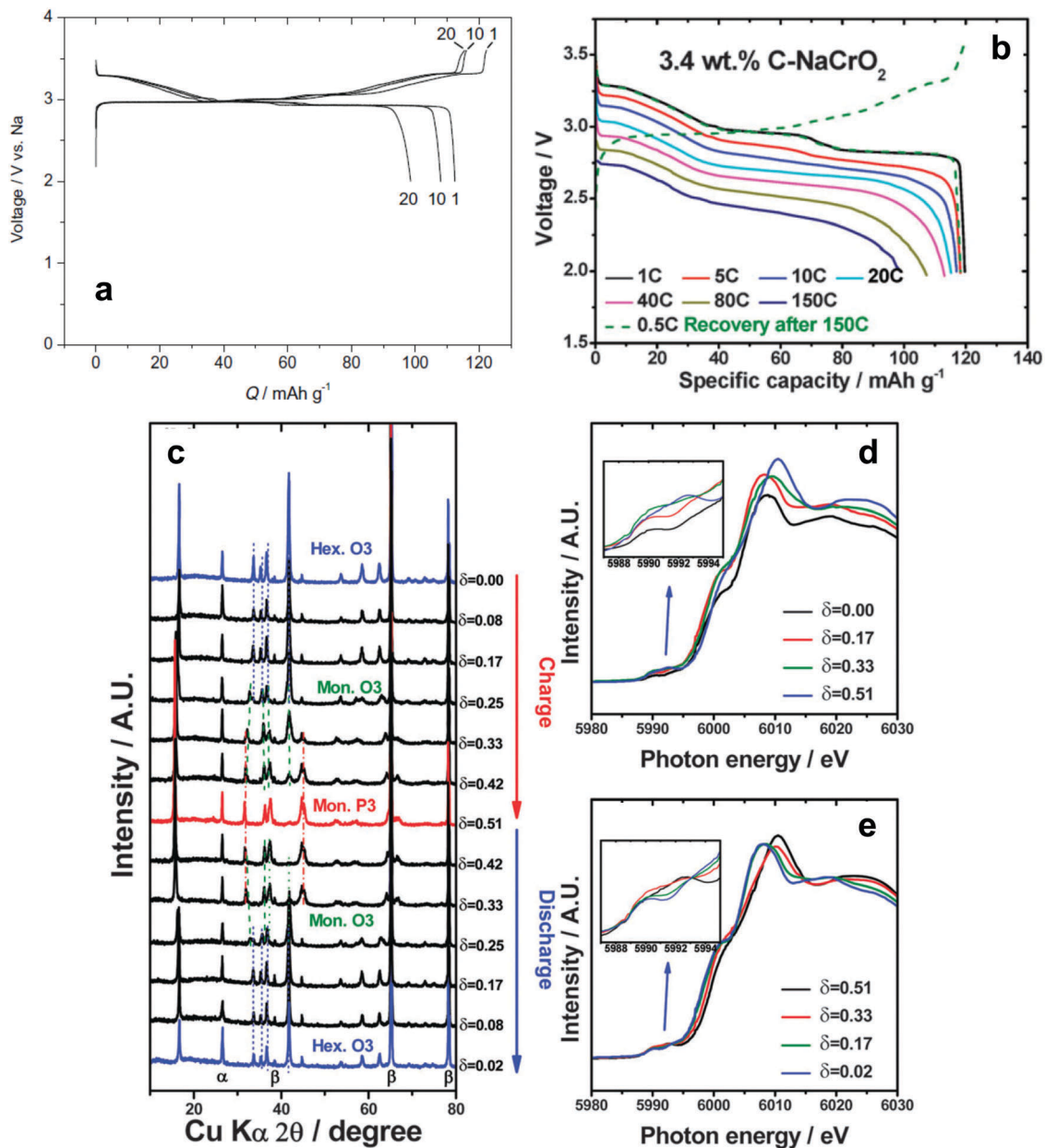Chem. Soc. Rev., 2017, 46, 3529–3614 | 3545

Fig. 10   (a) Charge and discharge curves of O3-NaCrO$_2$. (Reprinted from ref. 128, Copyright 2010, with permission from Elsevier.) (b) Rate performances of 3.4 wt% carbon-coated O3-NaCrO$_2$. (c) *Ex situ* XRD patterns obtained during charging and discharging, Cr K-edge XANES spectra obtained during (d) charging and (e) discharging. (Reproduced with permission from ref. 130, Copyright 2015 The Royal Society of Chemistry.)

coating will provide additional high electric conductivity, which may facilitate improvement in electrode performance even at high rates.

2.1.10.   Na$_2$RuO$_3$. The Na$_2$MO$_3$ (M: metal) layer structure, an analogue of Li$_2$MO$_3$, has alternative layers in a cubic close-packed oxygen array. Na$_2$RuO$_3$ shows metallic conduction and is crystallized in layer structures consisting of Na and Na$_{1/3}$Ru$_{2/3}$ slabs.[137] The crystal structure is indexed as hexagonal $R\bar{3}m$ without ordering of the superstructure, unlike Li$_2$MnO$_3$. The first discharge capacity was approximately 150 mA h g^{-1} at the first cycle and this capacity was maintained throughout the cycling test. For Na$^+$ insertion and extraction, the electrochemical

reaction proceeded *via* a two-phase reaction with hex-I and hex-II phases. Although further studies are needed to elucidate the structural evolution during Na$^+$ insertion and extraction, the use of layered Na$_2$MO$_3$ is an important approach for exploring new transition metal oxides.

2.2.   Two- or three-dimensional layer transition metal oxides and fluorides

Na-deficiency or Na-free transition metal oxides are interesting because of their reversible Na$^+$ insertion and extraction. These compounds usually have an open structure to allow Na$^+$ ions into their crystal structure. Particularly in three-dimensional
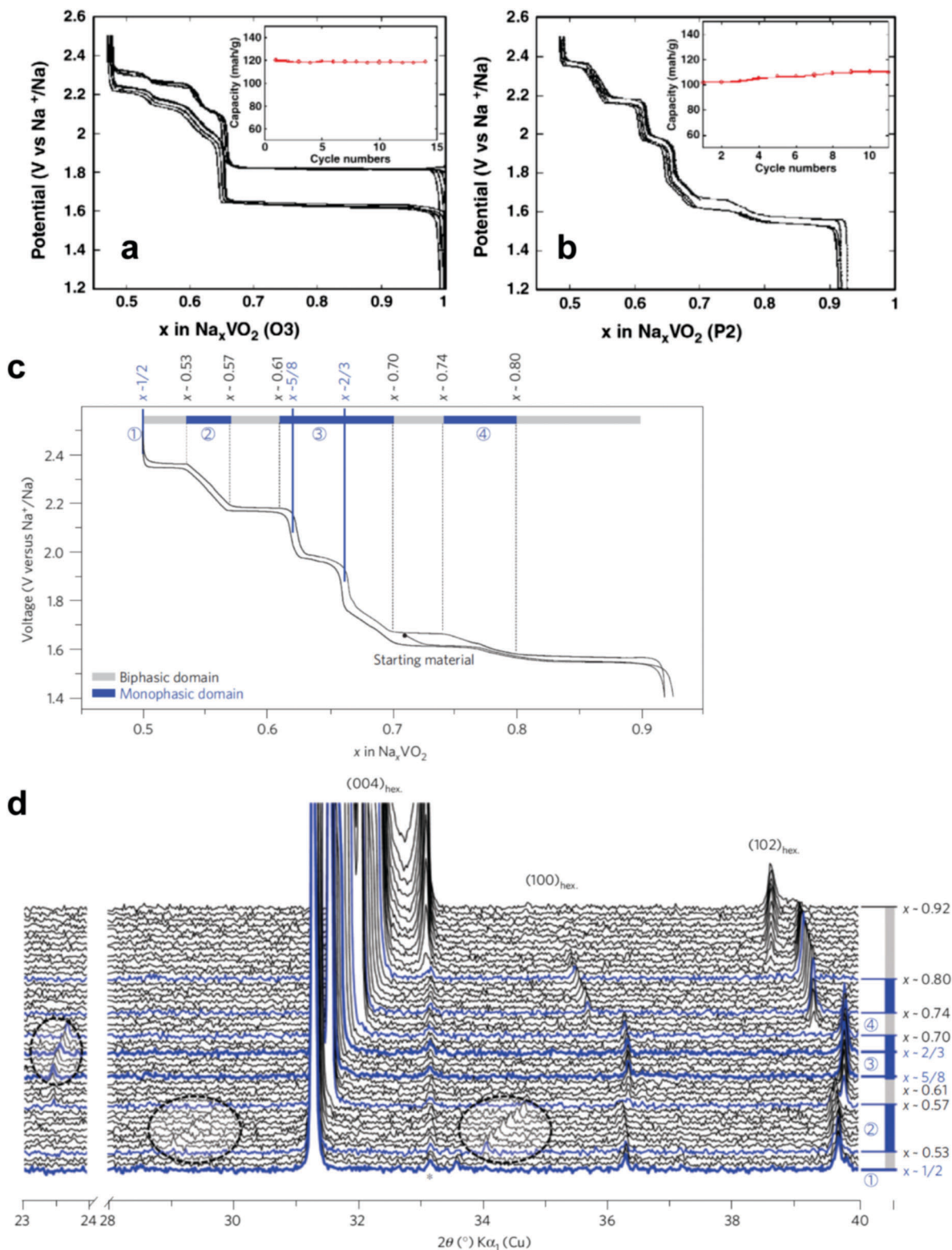
Fig. 11 Voltage–composition curves of (a) O3-NaVO$_2$ and (b) P2-Na$_{0.7}$VO$_2$. (Reprinted from ref. 135, Copyright 2011, with permission from Elsevier.) P2-Na$_x$VO$_2$: (c) the limits of the biphasic domains and the solid solutions (d) *in situ* X-ray diffraction data recorded during the galvanostatic intermittent titration technique experiments. (Reproduced by permission from ref. 136, Nature Publishing Group, Copyright 2013.)

structures, Na$^+$ ions can diffuse in x, y, and z directions; fast Na$^+$ migration is possible relative to two-dimensional structures.

Many of these compounds are synthesized at low temperatures, such that their large surface area with small particles contributes

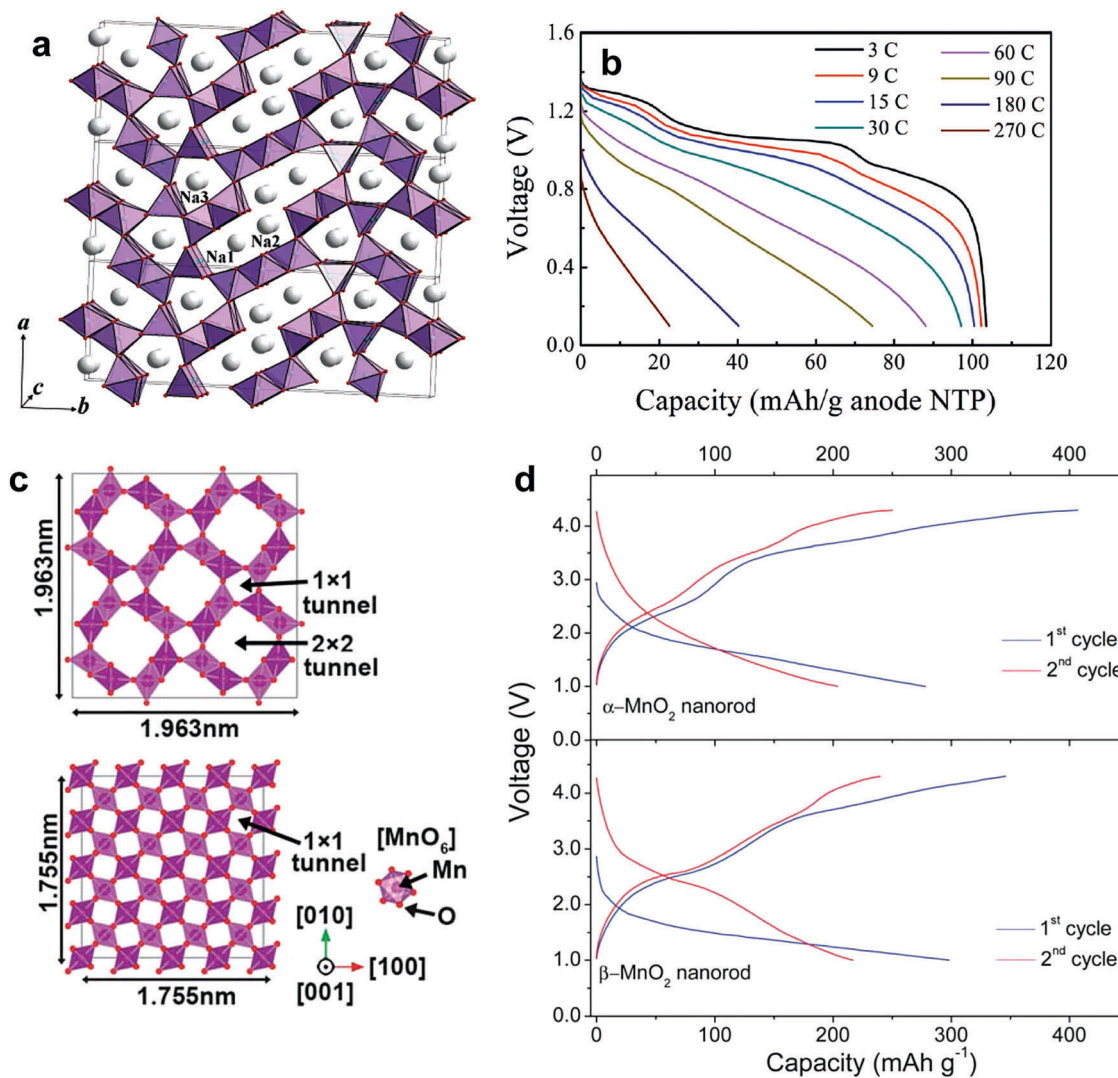Fig. 12 (a) The crystal structure of $Na_{0.44}MnO_2$ perpendicular to the ab–plane. (Reproduced with permission from ref. 141, Copyright 2007 American Chemical Society.) (b) Discharge curves of NTP-C/NMO full cells in two-electrode configuration at different C-rates. (Reproduced from ref. 145 with permission, Copyright 2013 Wiley-VCH Verlag GmbH & Co. KGaA.) (c) The crystal structure of α-MnO_2 along the [001] direction (top) and β-MnO_2 along the [001] direction (bottom) and (d) the resulting initial charge and discharge curves of α-MnO_2 (top) and β-MnO_2 (bottom). (Reproduced with permission from ref. 146, Copyright 2013 The Royal Society of Chemistry.)

to unexpectedly high rate performance. Since the ionic size of Na^+ is larger than that of Li^+, the host structure should be sufficiently rigid or have a large tunnel size to facilitate the entry of large ionic species. Otherwise, the crystal structure could collapse upon repetitive Na^+ insertion and extraction. These electrodes are active compared to Na metal; however, the main difficulty is that a sodiated anode is needed to construct a full cell. Recent research introduced low voltage operating P2-$Na_{0.62}[Ti_{0.37}Cr_{0.63}]O_2$ anode materials.[138] Plenty of possibilities remain regarding the development of full cells utilizing these transition metal oxides and sodiated anode materials.

2.2.1. Manganese oxides. Several types of Na–Mn–O compounds were introduced by Parant *et al.*[89,90] A lower Na/Mn ratio results in adoption of a three-dimensional structure such as $Na_{0.2}MnO_2$,[90] $Na_{0.4}MnO_2$,[89] or $Na_{0.44}MnO_2$ (space group *Pbam*).[89,90,139-145] Among these, $Na_{0.44}MnO_2$, which is isostructural

with $Na_4Mn_4Ti_5O_{18}$, is particularly interesting because of its cycling stability with a reasonable capacity, ~ 120 mA h g^{-1}. Doeff *et al.* first examined the Na^+ insertion properties of $Na_{0.44}MnO_2$ with a solid-state polymer electrolyte at 85 °C.[139,140] The crystal structure consists of four MnO_6 octahedral sites with Mn^{4+} and one MnO_5 square-pyramidal site with a half of Mn^{3+} (Fig. 12a). These are connected by corner sharing to form two types of tunnels. Each unit cell contains a large S-shaped tunnel with four sodium sites, as well as two identical pentagonal tunnels. The Na sites in the small tunnels are nearly fully occupied, while the large tunnel sites are partially occupied: Na1 and 2 sites in the S-shaped tunnels, half-filled; Na3 sites with an inner position in the small tunnels, fully-filled. Both Na^+ ions are highly mobile along the c-axis, contributing to capacity. Sauvage *et al.* performed carbon coating of $Na_{0.44}MnO_2$, which led to a capacity of 140 mA h g^{-1}.[141] They speculated

3548 | *Chem. Soc. Rev.*, 2017, **46**, 3529–3614

This journal is © The Royal Society of Chemistry 2017

that the Na1 and Na2 sites located in the S-shaped tunnels were very accessible in the range of 0.22 to 0.66 in Na_xMnO_2, while the Na^+ ions located in the Na3 site were not generally extracted. An *in situ* XRD study revealed the structural evolution during the electrochemical reaction in Na cells. A biphasic reaction was found upon reduction in the range of $x = 0.2$–0.44 in Na_xMnO_2. In a range of $x = 0.44$–0.612 Na_xMnO_2, not a single solid solution, but several multiphase reactions were associated with the electrochemical oxidation. Unfortunately, the high rate test caused a drastic capacity drop (to $\sim 10^{-16}$ S cm^{-1}) due to some kinetic limitations, as calculated by Cao *et al.*[142] Kim *et al.* suggested that the composition of $Na_{0.44}MnO_2$ and $Na_{0.55}MnO_2$ in a voltage range of 2.6–2.8 V is unfavorable because of electrostatic repulsion, which causes slow Na^+ diffusion.[143] They suggested that Jahn–Teller distortion was another parameter of electrode performance decay. Recent work of Cao *et al.* reported the synthesis of single crystalline $Na_{0.44}MnO_2$ nanowires with a reversible capacity that could be maintained for over 1000 cycles.[142] High crystallinity provided the long-term durability for Na^+ insertion and extraction and the reduced diffusion path also contributed to excellent capacity retention.

The application of $Na_{0.44}MnO_2$ electrodes has also been highlighted in aqueous systems. Whitcare *et al.* documented a full cell with a $Na_{0.44}MnO_2$ cathode and an activated carbon anode in a 1 M $NaSO_4$ aqueous electrolyte.[144] Despite a smaller capacity in the aqueous solution relative to the aprotic ones, the full cell could be tested without apparent capacity loss over 1000 cycles. In the $NaTi_2(PO_4)/Na_{0.44}MnO_2$ system, the cell was capable of operation at over 100C-rates and stable cycling for over 1000 cycles (Fig. 12b).[145]

$Na_{0.4}MnO_2$ consists of a 2 × 3 tunnel structure called romanechite.[89] Ba^+ and water molecules have been introduced to stabilize the large tunnel structure. Although the Na^+ insertion and extraction mechanism remains unclear, 0.3 mol of the Na^+ ion could be inserted into the host structure.

Few studies have explored Na-free MnO_2 for Na^+ insertion. Because of the relatively large tunnel size of α- and β-MnO_2, Na^+ insertion is also possible for both α- and β-MnO_2. α-MnO_2, which is called hollandite, is composed of double chains of edge-sharing MnO_6 octahedra that are linked at the corners to form a 2 × 2 and 1 × 1 tunnel structure (Fig. 12c). Because of the large size of the 2 × 2 tunnel, Na^+ insertion into the empty tunnel is possible, as suggested by Su *et al.*[146] and Islam *et al.*[147] (Fig. 12d). A relatively large capacity of approximately 280 mA h g^{-1} was obtained at the first discharge in α-MnO_2 nanorods, whereas the retained capacity was only 75 mA h g^{-1} after 100 cycles. In contrast, rutile-type β-MnO_2 shows a 1D channel 1 × 1 tunnels along the *c*-axis composed of individual chains of the MnO_6 octahedral units. In general, insertion of ion species, *i.e.*, Li^+, is not easy due to the small size of the 1 × 1 tunnels.[148] Su *et al.* also tested β-MnO_2 in Na cells, which delivers approximately 300 mA h g^{-1} during the first cycle.[146] In comparison with α-MnO_2, the β-MnO_2 nanorods exhibited a higher discharge capacity of approximately 145 mA h g^{-1} after 100 cycles. They attributed the better electrochemical performance of β-MnO_2 to the large number of empty tunnels that

accommodate the Na^+ ions. Since both α- and β-MnO_2 have a different tunnel structure, both materials should exhibit different charge and discharge behavior.[149] Nevertheless, the same voltage profiles showing sloppy discharge curves are more likely to be related to pseudo-capacitance behavior. λ-Type MnO_2, which is produced by electrochemical delithiation of $LiMn_2O_4$, showed discharge of approximately 200 mA h g^{-1} during the first cycle with reasonable capacity retention.[150] The λ-type MnO_2 phase was transformed into $O'3$ $NaMnO_2$ *via* electrochemical cycling and showed stable cycling performance.

2.2.2. Vanadium oxides. Vanadium oxides have been intensively studied as cathode materials for lithium-ion batteries. In Na cells, α-, β-$Na_xV_2O_5$, and $Na_{1+x}V_3O_8$ were investigated for Na^+ ion insertion by West *et al.* in the 1980s. α-V_2O_5 and $Na_{1+x}V_3O_8$ have layered structures, and β-$Na_xV_2O_5$ has a three-dimensional structure with wide channels.[151] In experiments, upon Na^+ ion insertion, α-V_2O_5 underwent a phase transition resulting in a new structure. Meanwhile, sloppy charge and discharge curves were obtained for β-$Na_xV_2O_5$. Na^+ ion insertion in $Na_{1-x}V_3O_8$ proceeded as a multi-phase reaction. Although structural evolution did not occur during Na^+ insertion, the absence of a plateau on Na^+ extraction indicates the slow kinetics of Na extraction. Nevertheless, the capacity retention was above 98% for 100 cycles in a voltage range of 1–3.5 V.

Recently, Tapavcevic *et al.* reintroduced layered α-V_2O_5 using a nanostructured bilayer concept, of which the interslab distance was approximately 13.5 Å, which is significantly larger than that of conventional V_2O_5 showing 4.4 Å.[152] This was possible because they used electrochemical deposition from aqueous vanadyl sulfate on a Ni foil substrate followed by heat treatment at 120 °C for removal of water molecules present in the interslabs (Fig. 13a). The electrode was activated by a $V^{5+/4+}$ redox reaction in a voltage range of 1.5–3.8 V, but showed sloping charge–discharge curves. The electrode delivered a reversible capacity of approximately 250 mA h g^{-1}, which is close to the theoretical capacity, with excellent cyclability of 300 cycles (Fig. 13b).

Surface modification of $VO_2(B)$ using reduced graphene oxide (rGO) substantially improved repetitive Na^+ insertion ability.[153] Although it has an open bronze structure to accommodate ion species into the empty channels, structural collapse or amorphization was observed in Na cells. The charge and discharge curves were sloppy, delivering approximately 150 mA h g^{-1}, in which the $V^{4+/3+}$ reaction was related to the electrochemical reaction. Both Na^+ insertion into $VO_2(B)$ and pseudo-capacitive behavior were confirmed *via* XRD and XAS studies.

2.2.3. Metal fluorides. Fluorine compounds have a high discharge voltage due to their ionic metal–ligand bonds. Perovskite-type metal trifluorides with a corner-sharing matrix ($R\bar{3}c$) have large bottlenecks in diffusion pathways for ion carriers such as Li^+ and Na^+. Although they have a high theoretical capacity (~ 200 mA h g^{-1}), their electrochemical performance is affected by the low electric conductivity of metal fluorides. Success has been achieved through mechanical milling and compositization with nanosized carbons. Okada's group introduced several metal fluorides (metal: Fe, V, Ti, Co, and Mn) including sodiated compounds.[154–157] A reversible
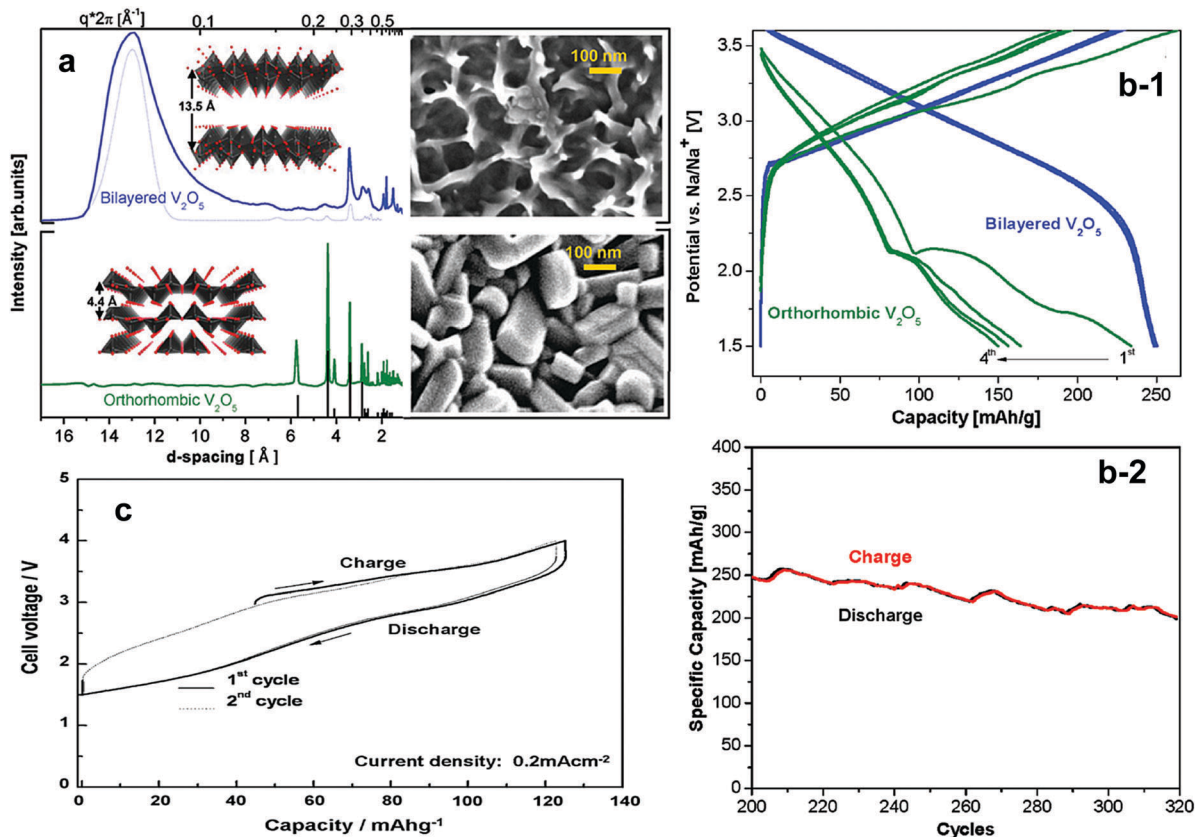
Fig. 13 (a) Synchrotron XRD and SEM images of electrodeposited bilayered V_2O_5 (top) and orthorhombic V_2O_5 (bottom) and (b-1) first four charge–discharge cycles of bilayered V_2O_5 and orthorhombic V_2O_5 and (b-2) the cycle life of bilayered V_2O_5. (Reproduced with permission from ref. 152, Copyright 2012 American Chemical Society.) (c) Initial charge and discharge curves of $NaFeF_3$ (reprinted from ref. 155, Copyright 2009, with permission from Elsevier.)

$Fe^{3+/2+}$ redox reaction achieved Na^+ insertion and extraction, which could deliver 150 mA h g^{-1} during the first cycle. All MF_3 compounds except FeF_3 (M: V, Ti, Co, and Mn) exhibited disappointing Na^+ storage. They further developed sodiated metal fluoride crystallized into the perovskite structure, $NaMF_3$ (M: Fe, Mn, Ni). Among those materials, $NaFeF_3$ had a relatively a large discharge capacity (128 mA h g^{-1}) with an average cell voltage of 2.7 V (Fig. 13c), while $NaNiF_3$ and $NaMnF_3$ suffered from capacities below 40 mA h g^{-1} with sloppy voltage decay. Even when the synthesis method was switched from mechano-milling to a solution-based method, the resulting capacity did not exceed the prior report at the same current density (0.2 mA cm^{-1}), but instead reached 180 mA h g^{-1} at a rate of 0.01C.[157] The strong ionic character of the M–F bond must be overcome to achieve a high capacity even at high rates. Homogeneous dispersion of nanosized metal fluoride materials onto a conducting carbon matrix might facilitate high rate performance.

2.3. Three-dimensional polyanion compounds

In comparison with oxide and fluoride systems, transition metal polyanion materials have shown significant thermal stability, which is supported by the presence of covalent bonds such as P and O, in particular cathodes are in a deeply-charged

(oxidized) state. Oxygen evolution is common in layered compounds at temperatures above 200 °C;[51,85,158–162] however, such behavior is dramatically suppressed by the presence of P–O covalent bonds in the crystal structure. These phenomena prevail in Li cells and also apply to Na systems, since the related material chemistry during electrochemical reactions does not vary significantly from Li systems with the exception of the charge carrier, Na^+, in Na cells. Polyanion-based materials usually exhibit lower electric conductivity relative to oxides, such that surface modifications using electro-conducting carbons, which contribute to a dramatic increase in electrical conductivity, improve electrochemical performance. The basic form begins from $NaFePO_4$; interestingly, some factors such as (i) variation in the charge carrier number of Na in Na sites, (ii) partial or full replacement of Fe by the other transition metals, (iii) a mixed anion system with F, OH, CO_2, and (iv) extension towards mixed phosphate $(PO_4)^{3-}$ and pyrophosphate $(P_2O_7)^{4-}$ ions also stabilize the crystal structure in the Na system. Unfortunately, because moisture absorption occurs easily in these polyanion systems, avoiding hydration and formation of NaOH on the surfaces of particles can be a challenge. Heterogeneous surfaces may lead to misinterpretation of the electrode performance in Na-containing aprotic electrolytes.

2.3.1. Phosphates and fluorophosphates. Maricite $NaFePO_4$ is a thermodynamically favored phase because it can be synthesized at high temperatures. Avdeev *et al.* demonstrated that chemically sodiated triphylite (olivine) $NaFePO_4$ exhibited an irreversible phase transition from olivine to maricite $NaFePO_4$ at around 480 °C, resulting in a significant volume shrinkage.[163] Crystal structures of both polymorphs consist of slightly distorted FeO_6 octahedra and PO_4 tetrahedra. The maricite $NaFePO_4$ has edge-sharing FeO_6 units that share corners with neighboring PO_4. There are no cationic channels for Na^+ movement (Fig. 14a).[164] In contrast, triphylite $NaFePO_4$ has corner-sharing FeO_6, which is linked with the PO_4 edge (Fig. 14b). A one-dimensional Na^+ diffusion channel is clearly seen along the *b*-axis in the crystal structure. The difference between these two polymorphs is the corner sharing and edge sharing FeO_6 chains for triphylite and maricite, respectively. However, direct synthesis of triphylite $NaFePO_4$ is not possible. Thus, chemical and electrochemical sodiation are effective ways to insert Na^+ into heterosite $FePO_4$ (space group, *Pnma*).

Electrode performance is dependent on the crystal structure. Amorphous $NaFePO_4$ exhibited a high discharge capacity of ~ 150 mA h g^{-1}, but operated at a low voltage (2.4 V) with a sloping discharge profile.[165] Maricite $NaFePO_4$ is electrochemically inactive, as the structure blocks Na^+ extraction and insertion.[166] Olivine $NaFePO_4$ shows a relatively high operating voltage (2.8 V) with two distinct voltage plateaus, delivering over 120 mA h g^{-1} capacity (Fig. 14c).[163–173] During the electrochemical reaction, the oxidation state of Fe is systematically altered followed by a redox reaction of $Fe^{3+/2+}$, as confirmed by the XAS studies performed by Ali *et al.*[173] Carbon coating led to excellent long-term cyclability. An interesting feature of triphylite $NaFePO_4$ is the appearance of intermediate $Na_{0.7}FePO_4$, which has the same crystal structure as the triphylite $NaFePO_4$, during electrochemical testing, whereas this phase is not found in $LiFePO_4$. Moreau *et al.* suggested that the advent of $Na_{0.7}FePO_4$ could be related to cationic ordering in the crystal structure.[164] Similar behavior is also observed in Na_xCoO_2[62] in comparison with Li_xCoO_2.[174] Casas-Cabanas *et al.* demonstrated that Na^+ ion insertion into $FePO_4$ occurs *via* the intermediate phases due to large volume mismatches between $FePO_4$ and $NaFePO_4$.[170] Therefore, three phases, $FePO_4$, $Na_{0.7}FePO_4$, and $NaFePO_4$, appear simultaneously on discharge, while they are separated into two first-order phase transitions on charge, which may be related to Na^+/vacancy ordering in the crystal structure. In comparison with $LiFePO_4$, the charge transfer resistance of $NaFePO_4$ is high, and the diffusion coefficient of Na^+ ions is
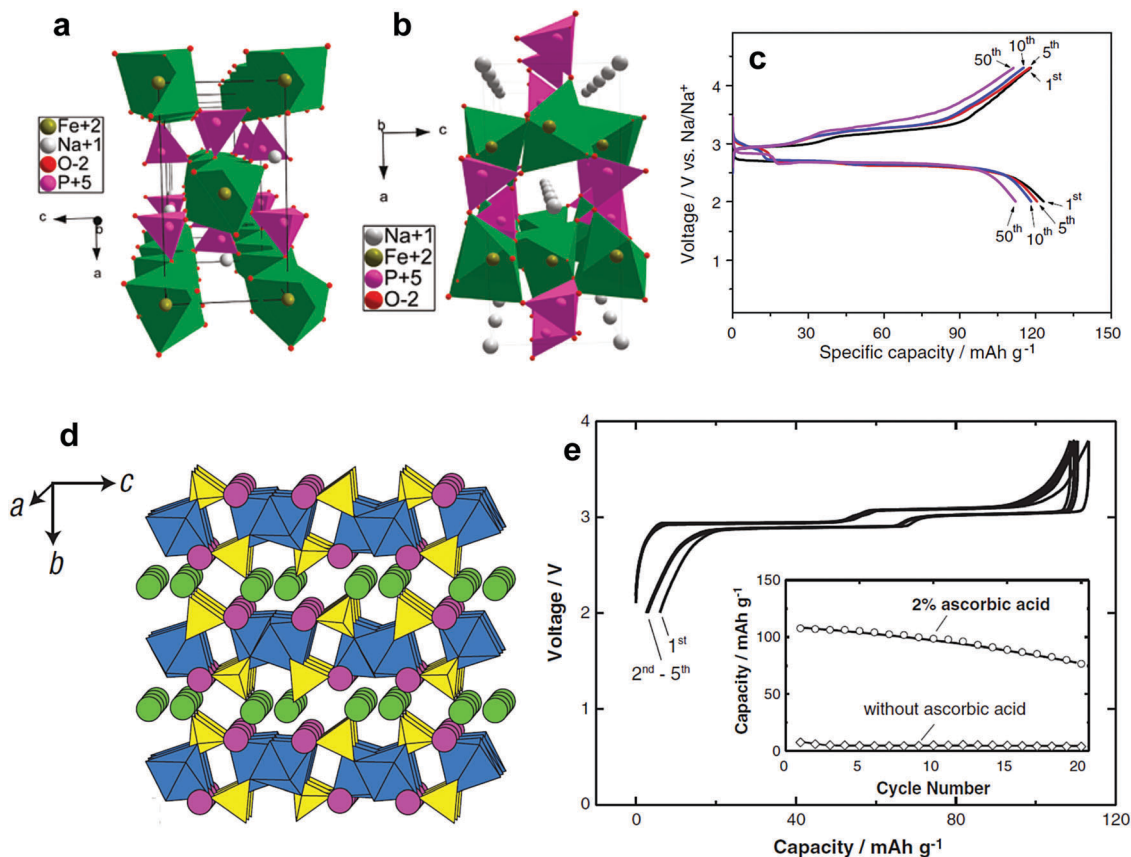
Fig. 14 (a) The crystal structure of maricite $NaFePO_4$ and (b) olivine $NaFePO_4$. (Reproduced with permission from ref. 164, Copyright 2010 American Chemical Society.) (c) Charge–discharge profiles of $NaFePO_4$ for 50 cycles. (Reprinted from ref. 169, Copyright 2012, with permission from Elsevier.) (d) Structure of Na_2FePO_4F along the [100] direction, iron octahedra: blue and the phosphate tetrahedral: yellow, and Na (1) in green and Na (2) in pink. (Reproduced by permission from ref. 176, Nature Publishing Group, Copyright 2007.) (e) Charge/discharge curves of the Na_2FePO_4F cell cycled at a rate of 6.2 mA g^{-1}. (Reprinted from ref. 178, Copyright 2012, with permission from Elsevier.)

approximately 2 orders of magnitude lower.[175] Recent density functional theory calculation revealed that the migration energy of Na$^+$ ions in NaFePO$_4$ is 0.05 eV higher than that of Li$^+$ ions in LiFePO$_4$, which reflects the slow kinetics in NaFePO$_4$.[172] The large ion size of Na$^+$ relative to Li$^+$ is associated with slow diffusion of Na$^+$ ions into the crystal structure. An extension of NaFePO$_4$, Na[Fe$_{0.5}$Mn$_{0.5}$]PO$_4$, could be synthesized;[168] however, the electrode did not show voltage plateaus, but rather a sloping curve due to the high interface strain between the Na-rich and Na-poor phases that was ascribed to the large size of Na$^+$ ions, allowing 0.6 mol Na$^+$ into Na$_x$[Fe$_{0.5}$Mn$_{0.5}$]PO$_4$. Since large Na$^+$ ions are associated with migration, minimization of the interface energy is essential to the utilization of the other transition metals such as Co, Mn, and Ni, among others.

The ionicity of fluorides over oxides and sulfides is ascribed to their higher electronegativity, which thus increases the operating voltage of the electrodes. This concept was successfully applied to the discovery of Na$_2$FePO$_4$F, which is applicable to both Li and Na systems.[176] This material crystallizes in orthorhombic structures with a Pbcn space group (Fig. 14d). Bioctahedral Fe$_2$O$_7$F$_2$ units comprising face-sharing FeO$_4$F$_2$ octahedra are connected via bridging F atoms to form a chain, and are joined by PO$_4$ tetrahedra to form FePO$_4$F layers. The two Na cations located in the interlayer enable facile two-dimensional migration pathways. However, structural evolution from the layer structure to a tunnel one occurred (space group P2$_1$/n) when Fe was substituted for Mn greater than 25%. In the case of the tunnel structure, the Na cations are located within channels.[177] Notwithstanding the advantages of high operating voltage relative to NaFePO$_4$, the strong ionicity lowers the intrinsic electric conductivity. Hence, the bare Na$_2$FePO$_4$F delivered almost no capacity. Surprisingly, the carbon-coated Na$_2$FePO$_4$F could deliver approximately 110 mA h g^{-1}, which corresponds to a 90% theoretical capacity.[178] Two voltage plateaus are evident with small polarization. As anticipated from the crystal structure, Tripathi et al. predicted Na$^+$ ion conduction in Na$_2$FePO$_4$F, which occurs along the two-dimensional interlayer with low activation energy.[179] However, further investigation is needed to improve cycling performance by adding more carbon to provide better electron conduction. Carbon-coated Na$_2$[Fe$_{0.5}$Mn$_{0.5}$]PO$_4$F (6 wt% of carbon) also showed a reversible capacity of 110 mA h g^{-1}, confirming the feasibility of Na$^+$ ion migration into/out of the tunnel structure.[180] Polarization of the Mn redox is clearly greater than that of the Fe$^{2+/3+}$ redox, which is similar to those observed in LiFePO$_4$ and LiMnPO$_4$.

In place of divalent transition metal elements, a trivalent element is also available in the form of NaVPO$_4$F. Barker et al. first introduced the material as an electrode material for hybrid-ion cells in 2003.[181] During the initial charging, Na$^+$ ions are extracted from the host material while Na$^+$ ions are plated on the surface of the Li metal anode in a Li cell. This process releases an atomically equivalent amount of lithium back into the electrolyte. Therefore, Li$^+$ ions are reinserted into the host material during the first discharge because Na is immobilized on the Li metal surface. NaVPO$_4$F has tetragonal

symmetry with a I4/mmm space group, which is an isostructure of α-Na$_3$Fe$_2$(PO$_4$)$_2$F$_3$.[182] This structure demonstrates facile Na$^+$ ion diffusion through an extended three-dimensional framework constructed from VO$_4$F$_2$ octahedra and PO$_4$ tetrahedra (Fig. 15a). Na$^+$ ions are present in the empty channel and diffuse along the c-axis. Coupling with a hard carbon anode, NaVPO$_4$F, led to two-step voltage responses (Fig. 15b), while the delivered discharge declined to less than 50% of the initial capacity (approximately 82 mA h g^{-1}). Zhao et al. found another crystal system in this compound: monoclinic (C2/c) as the low temperature form and tetragonal (I4/mmm) as the high temperature form.[183] Cr-doping into the V site of NaVPO$_4$F crystallized to the monoclinic phase showed a discharge capacity of 80 mA h g^{-1} with 91% retention for 20 cycles.[184,185] Sauvage et al. reinvestigated Na–V–P–O–F materials because the structural parallelism between NaVPO$_4$F and Na$_3$Al$_2$(PO$_4$)$_2$F phases was not straightforward owing to the difficulties encountered in determining the stoichiometry.[186] They found that a 10 wt% excess of NaF could yield a single phase. Reliable refinement results were obtained assuming a crystal structure of Na$_3$V$_2$(PO$_4$)$_2$F, which can be presented as Na$_{1.5}$VOPO$_4$F$_{0.5}$ instead of NaVPO$_4$F. In this structure, Na$^+$ ions are disordered across two sites (8h and 8j) and the oxidation state of V is 4+ (Fig. 15c). The crystal structure is composed of a VO$_5$F octahedral and PO$_4$ tetrahedra sharing O vertices parallel to the ab-plane. Along the c-axis direction, VO$_5$F octahedra are connected via F vertices located in the same ab-plane as the disordered Na atoms. This structure could accommodate 0.56 Na$^+$ (approximately 87 mA h g^{-1}) per formula unit in Na$_{1.5}$VOPO$_4$F$_{0.5}$ with two different voltage plateaus, 3.6 and 4 V (Fig. 15d). In consideration of the theoretical value (156 mA h g^{-1}) assuming a V$^{4+/5+}$ reaction, the delivered capacity can be improved further with electro-conducting coating layers. Due to structural and electrolytic instability, the capacity retention in the upper voltage region is not promising compared to the capacity delivered at the lower voltage plateau. These results, including capacity and retention, agree with an earlier report by Barker et al.[181] The oxidation state of V was lowered to 3.8+ in Na$_{1.5}$VPO$_{4.8}$F$_{0.7}$.[187] In comparison with Na$_{1.5}$VOPO$_4$F$_{0.5}$,[188] the oxygen content was reduced slightly, but the equivalent content of F increased. Although structural refinement was performed based on space group P4$_2$/mnm, the XRD pattern, including the Bragg peak position, is the same for both compositions. Na$_{1.5}$VPO$_{4.8}$F$_{0.7}$ is comprised of tetrahedral PO$_4$ and VO$_5$F/VO$_4$F$_2$ octahedral units that share corners, which yields a three-dimensional open framework with Na$^+$ ions located at interstitial sites (Fig. 15e). Na$_{1.5}$VPO$_{4.8}$F$_{0.7}$ provided a discharge capacity of approximately 137 mA h g^{-1} based on the V$^{3.8+/5+}$ redox reaction (1.2 mol Na$^+$ per formula unit in Na$_{1.5}$VPO$_{4.8}$F$_{0.7}$) with excellent cyclability for 500 cycles (Fig. 15f).

To further lower the average oxidation state of V efforts were made employing Na$_3$V$_2$(PO$_4$)$_3$F$_3$ with space group P4$_2$/mnm.[188–190] Very recently, Bianchini et al. revisited the Na$_3$V$_2$(PO$_4$)$_3$F$_3$ compound to clarify its crystal structure, although the structure was successfully refined by Le Mine et al. in 1988.[191] They claimed that structural discrepancies in the literature originated from the possible existence of F and O mixing in the structure.[182,188–190]

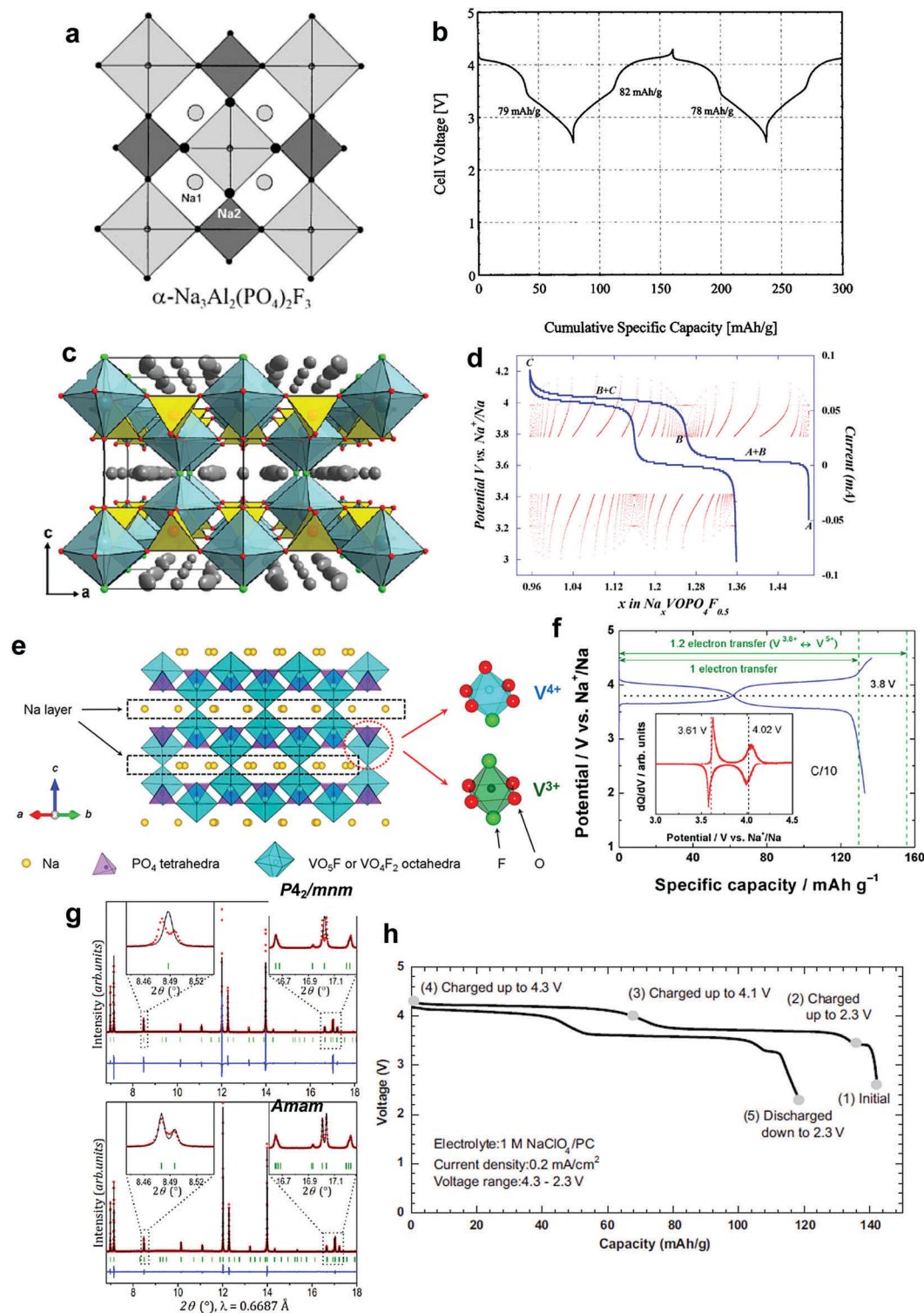3552 | Chem. Soc. Rev., 2017, 46, 3529–3614

This journal is © The Royal Society of Chemistry 2017

Fig. 15 (a) The crystal structure of α-Na$_3$Al$_2$(PO$_4$)$_2$F$_3$ along the a-axis. (Reprinted from ref. 182, Copyright 1999, with permission from Elsevier.) (b) Electrochemical performance data for a typical hard carbon//NaVPO$_4$F cell. (Reproduced with permission from ref. 181, Copyright 2003 The Electrochemical Society.) (c) The crystal structure of Na$_{1.5}$VOPO$_4$F$_{0.5}$ in the (ac) plane and (d) the P.I.T.T. curve of the composite Na$_{1.5}$VOPO$_4$F$_{0.5}$/C recorded at a 1Na/100 h rate. (Reprinted from ref. 186, Copyright 2006, with permission from Elsevier.) (e) The crystal structure of Na$_{1.5}$VPO$_{4.8}$F$_{0.7}$ and two different local environments for V^{4+} and V^{3+} ions (*i.e.*, VO$_5$F and VO$_4$F$_2$ octahedra, respectively): Na (yellow), V cyan), P (purple), O (red), and F (green) atoms and Na layers denoted as dashed boxes and (f) charge–discharge profile at a C/10 rate for the Na$_{1.5}$VPO$_{4.8}$F$_{0.7}$ cathode (voltage window: 2.0–4.5 V *vs.* Na$^+$/Na) appeared with the average voltage (3.8 V *vs.* Na$^+$/Na) as a horizontal dotted line. (Reproduced with permission from ref. 187, Copyright 2013 American Chemical Society.) (g) Synchrotron radiation diffraction data in the $P4_2/mnm$ space group (top) and in the low-symmetry orthorhombic group *Amam* (bottom). (Reproduced with permission from ref. 191, Copyright 2014 American Chemical Society.) and (h) first charge and discharge curves for Na$_3$V$_2$(PO$_4$)$_2$F$_3$ a rate of 0.2 mA cm^{-2}. (Reprinted from ref. 190, Copyright 2013, with permission from Elsevier.)

A high-resolution diffraction study using synchrotron radiation revealed a suitable orthorhombic structure with space group *Amam* rather than a tetragonal structure with space group $P4_2/mnm$ (Fig. 15g). Interestingly, when F was absent, the structure was crystallized to NASICON-type rhombohedral $Na_3V_2(PO_4)_3$ with space group $R\bar{3}c$, which will be addressed in Section 2.3.4. Similar to $Na_{1.5}VOPO_4F_{0.5}$[186] and $Na_{1.5}VPO_{4.8}F_{0.7}$,[187] the presence of fluorine with phosphorus ions raises the operating voltage originating from the strong inductive effects of the anion group, even though the $V^{3+/4+}$ redox couple is available for delivery of high capacity (approximately 120 mA h g^{-1}) in $Na_3V_2(PO_4)_3F_3$ compounds, with two voltage plateaus at 3.7 and 4.2 V (Fig. 15h). Computational calculations revealed that Na$^+$ ions located at the Na2 site are more readily extracted due to the lower diffusion barrier. Compared with two earlier reports by Barker *et al.*[181] and Sauvage *et al.*,[186] this work is notable because variation in the anion configuration and the content of oxygen fluorine dramatically improved electrochemical performance, even at high rates.

2.3.2. Pyrophosphates. Na$^+$ insertion was introduced in $(MoO_2)_2P_2O_7$ in 2003.[192] The crystal structure was stabilized in an orthorhombic system with a *Pnma* space group, which is the same as olivine LiFePO$_4$. The presence of an empty channel enabled Na$^+$ insertion into $(MoO_2)_2P_2O_7$, with a discharge capacity of 190 mA h g^{-1} corresponding to 3.1 mol Na$^+$ per formula unit in $(MoO_2)_2P_2O_7$, although the rate capability was limited due to the large ionic size of the Na$^+$ ion.

In 2008, Adam *et al.*[193] introduced the crystal structure of $Li_2MnP_2O_7$, and it was confirmed using Li$^+$ intercalation cathode materials.[194,195] Recent developments in SIBs have motivated the exploration of facile Na$^+$ intercalation materials towards pyrophosphates. $Na_2FeP_2O_7$ with triclinic $P\bar{1}$ was first studied by Honma *et al.*[196] and Barpanda *et al.*,[197] and the crystal structure was stabilized into the triclinic $P\bar{1}$ phase (Fig. 16a). The structure was comprised of corner-sharing FeO$_6$ octahedra creating Fe$_2$O$_{11}$ dimers, which are interconnected *via* corner-sharing and edge-sharing with P$_2$O$_7$ pyrophosphate groups. FeO$_6$ octahedra and PO$_4$ tetrahedra are connected in a staggered fashion, thus creating large tunnels along the [110] direction, which accommodate Na atoms at four distinct sites. However, these materials are not competitive cathode materials because of the two phosphate groups per transition metal in terms of capacity (theoretical capacity approaching 97 mAh g^{-1}) even though the related material chemistries are interesting. The appearance of stepwise voltage plateaus (roughly at 2.5 and 3 V) may indicate the presence of Na$^+$/vacancy ordering in the structure (Fig. 16b). An *ex situ* study suggested that a two-phase reaction prevails in the upper voltage plateau and a single phase reaction is dominant in the lower voltage region.[198] According to calculation by Clark *et al.*,[199] low activation energy was found for long-range diffusion in all crystallographic directions in $Na_2FeP_2O_7$ (M: Fe and Mn), indicating three-dimensional Na$^+$ ion diffusion. Therefore, electrochemical studies indicated moderate performance at high rates, which is related to the availability of three-dimensionality and low migration energy for Na$^+$ ion diffusion in $Na_2FeP_2O_7$. The good electrode performances of $Na_2FeP_2O_7$ were further evidenced

in an inorganic ionic liquid NaFSA-KFSA (FSA: bis(fluorosulfonyl)amide) at 363 K.[200]

Ha *et al.* extended the composition to $Na_{3.32}Fe_{2.34}(P_2O_7)_2$, which can be represented as $Na_{1.66}Fe_{1.17}P_2O_7$, of which the crystal structure is identical to $Na_2FeP_2O_7$, but the new composition is able to increase the theoretical capacity to approximately 110 mA h g^{-1}.[201] The first irreversible capacity was negligible and the lower voltage was shortened. The electrode performance was superior to that of $Na_2FeP_2O_7$ in terms of capacity retention and rate capability up to a rate of 10C. However, $Na_{3.32}[Fe_{0.5}Mn_{0.5}]_{2.34}(P_2O_7)_2$ and $Na_{3.32}Mn_{2.34}(P_2O_7)_2$ had very low capacities, which was a controversial result of the computational study of Clark *et al.*[199] The poor electrochemical activity seems to be similar to that of LiMnPO$_4$, which requires strategies for nanosizing and doping with the other divalent elements to improve electric conductivity.

Recent work of Barpanda *et al.* identified a new polymorph of β-$Na_2MnP_2O_7$, which was also stabilized into a triclinic structure, $P\bar{1}$.[202] The structure consists of distorted MnO$_6$ octahedral and PO$_4$ tetrahedral blocks creating tunnels accommodating Na atoms along the [001] direction. The structure has corner-sharing MnO$_6$–MnO$_6$ (Mn$_2$O$_{11}$) dimers, which are in turn connected by PO$_4$–PO$_4$ (P$_2$O$_7$) diphosphate units in a mixed-edge and corner-sharing fashion (Fig. 16c). A galvanostatic test of the electrode provides a reversible discharge capacity of 80 mA h g^{-1} associated with an average operating voltage of 3.6 V (Fig. 16d). This coincided with earlier DFT calculations suggesting that this compound can undergo a Mn$^{2+/3+}$ redox reaction at around 3.65 V.[199] The sloppy discharge curve is the signature of β-$Na_2MnP_2O_7$, which is different from $Na_2FeP_2O_7$ operating with two distinct voltage plateaus. Structural investigation is further required to elucidate the reaction mechanism. They also suggest a new pyrophosphate oxyanionic framework compound, tetragonal $Na_2(VO)P_2O_7$ with space group $P4bm$.[202] This material belongs to the fresnoite family consisting of a VO$_5$ or (VO)O$_4$ square pyramid and PO$_4$ tetrahedral units (Fig. 16e). Each VO$_5$ pyramid is connected to four independent PO tetrahedra in a corner-sharing fashion, thus forming [VP$_2$O$_{11}$] units. Also, each PO$_4$ tetrahedron is connected to two VO$_5$ units and one PO$_4$ unit that share corners. The delivered capacity was approximately 80 mA h g^{-1}, which is close to the theoretical capacity (93 mA h g^{-1}) (Fig. 16f). The discharge curve was sloppy with the $V^{5+/4+}$ redox reaction showing an average operating voltage of 3.8 V. Apart from the above-mentioned compounds, the other pyrophosphates with Ni(II), Cu(II), Ti(II), Co(II) and higher transition metal oxidation states have not yet been explored as host materials for Na$^+$ insertion.

2.3.3. Mixed phosphates. Mixed phosphates are composed of phosphate (PO$_4$)$^{3-}$ and pyrophosphate (P$_2$O$_7$)$^{4-}$. This phase was recently discovered in a $Na_4M_3(PO_4)_2P_2O_7$ (M: Mn, Co, Ni) system by Sanz *et al.*[204] These compounds crystallize in the orthorhombic structure with a $Pn2_1a$ space group. The structure is built up from MO$_6$ octahedra and PO$_4$ groups with shared corners. M$_3$P$_2$O$_{13}$ blocks parallel to the bc plane are linked with the P$_2$O$_7$ unit along the *a*-axis (Fig. 17a). Four Na$^+$ sites are located in the three-dimensional channel, which can
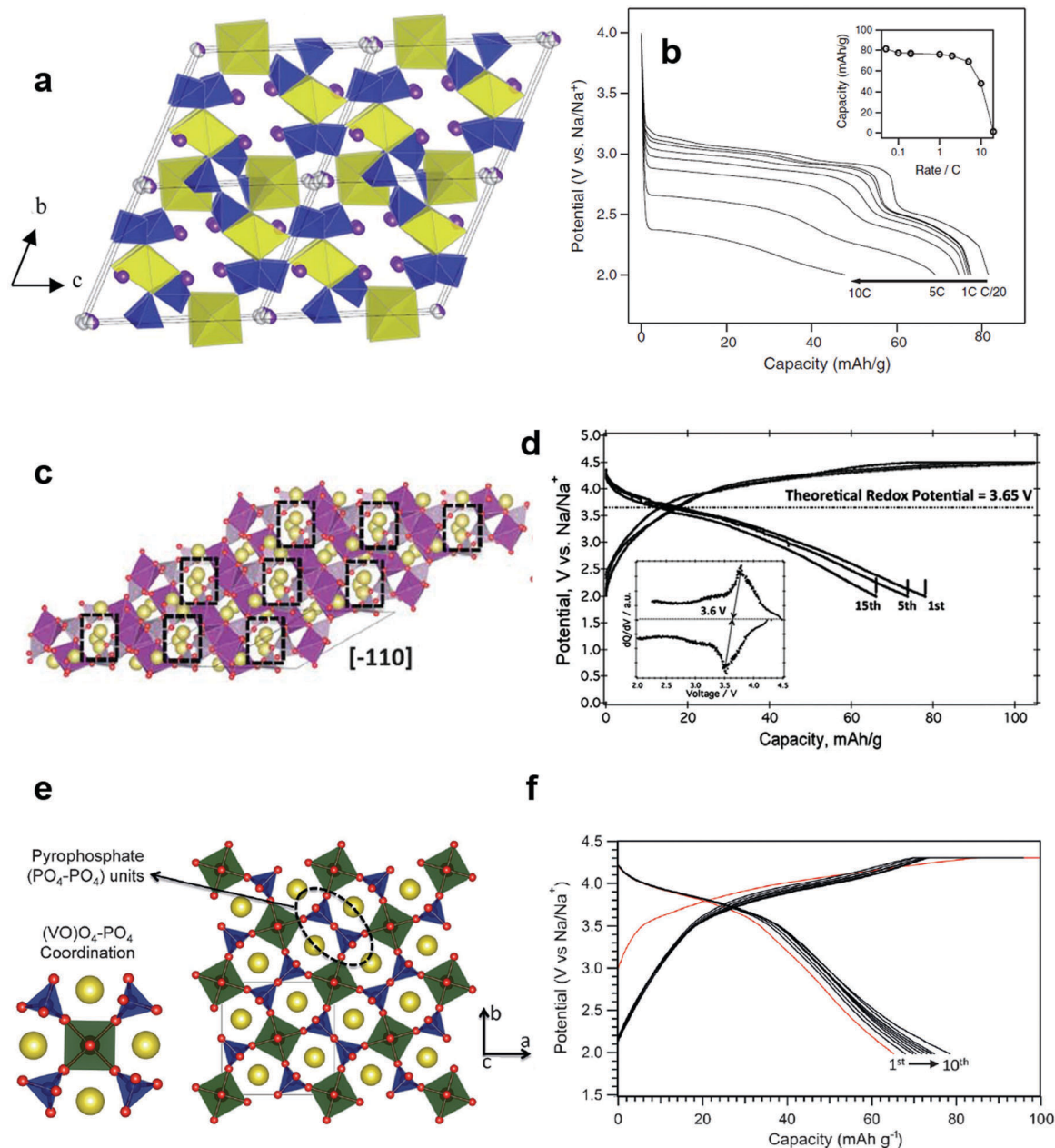
3554 | *Chem. Soc. Rev.*, 2017, **46**, 3529–3614

This journal is © The Royal Society of Chemistry 2017

Fig. 16 (a) The crystal structure of $Na_2MP_2O_7$. (Reproduced with permission from ref. 199, Copyright 2014 The Royal Society of Chemistry.) (b) Discharge capacity of $Na_2FeP_2O_7$ as various current densities. (Reprinted from ref. 197, Copyright 2012, with permission from Elsevier.) (c) The crystal structure of β-$Na_2MnP_2O_7$ polymorph consisting of MnO_6 octahedra (pink), PO_4 tetrahedra (light purple) and Na atoms (yellow) along [−110] projection in which the possible sodium migration tunnels are highlighted by black dotted rectangles and (d) charge and discharge profiles of the β-$Na_2MnP_2O_7$ cathode at a rate of C/20. (Reproduced with permission from ref. 202, Copyright 2013 The Royal Society of Chemistry.) (e) The crystal structure of $Na_2(VO)P_2O_7$: corner-sharing between $(VO)O_4$ and PO_4 units (top) and the side and top view of the $(VO)O_4$ square pyramid (bottom) and (f) the resulting charge and discharge curves of $Na_2(VO)P_2O_7$ at a rate of C/20. (Reproduced from ref. 203 with permission, Copyright 2013 Wiley-VCH Verlag GmbH & Co. KGaA.)

provide better Na^+ diffusion in comparison with a one-dimensional channel. Double chains are formed from simple parallel chains along the [010] direction. Kim *et al.* first utilized the mixed phosphate framework by introducing Fe^{2+} in the M sites to form $Na_4Fe_3(PO_4)_2P_2O_7$.[205] Their first principles calculations demonstrated a low activation barrier for Na^+ diffusion lower than 0.8 eV for all directions. This suggests that rapid Na^+ diffusion is possible, because all Na sites are connected with

reasonably low activation barriers. More specifically, the lowest activation barrier was found in the large tunnel along the *b*-axis. The material could deliver a capacity of 105 mA h g^{-1} with an average operating voltage of 3.2 V (Fig. 17b). Nose *et al.* investigated $Na_4Co_3(PO_4)_2P_2O_7$ instead of the compound with Fe to improve the energy density.[206] Knowledge obtained from experiments with $LiCoPO_4$, which exhibits a high operating voltage from the $Co^{2+/3+}$ redox reaction, was applied to $Na_4Co_3(PO_4)_2P_2O_7$.[207]

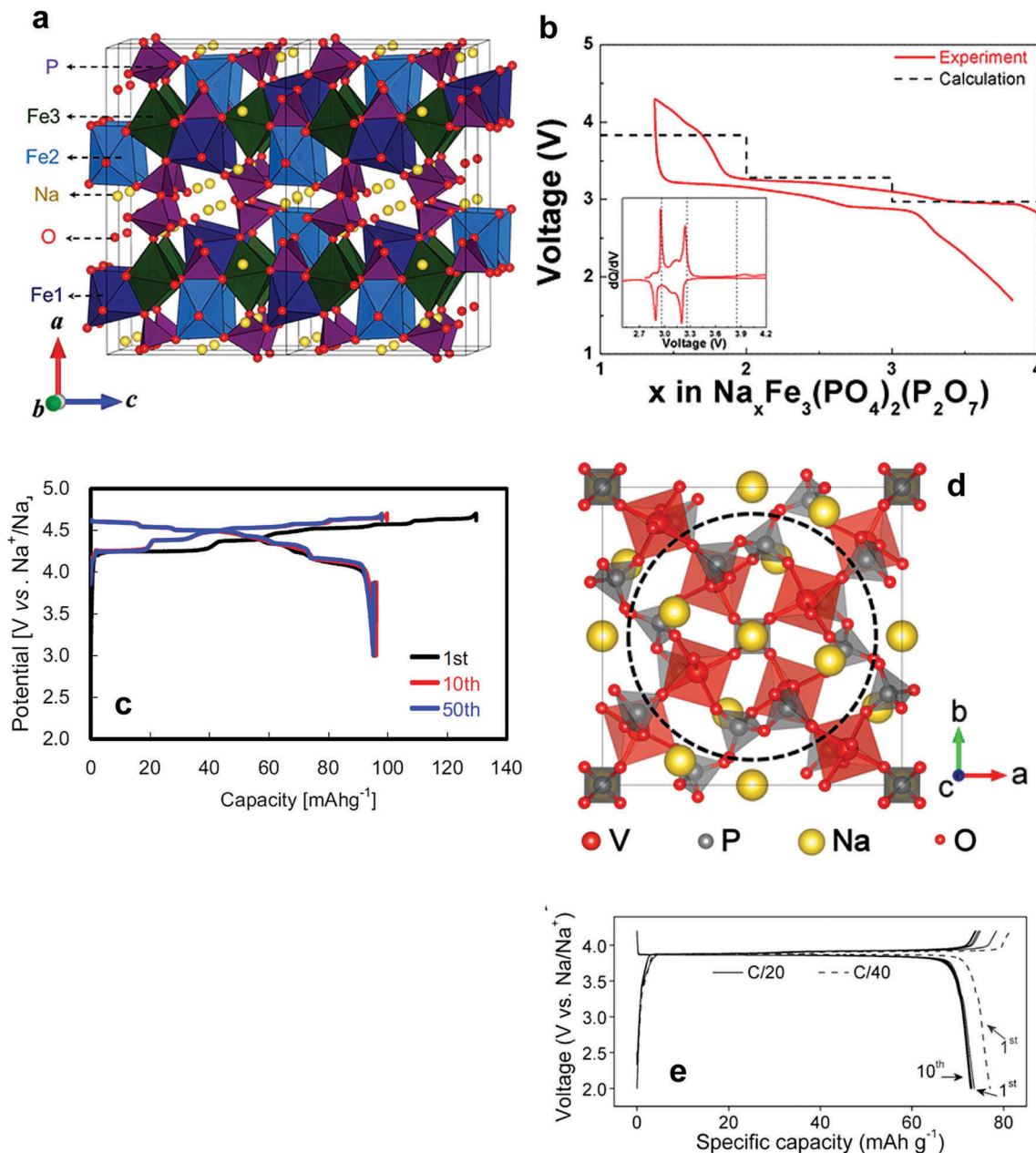This journal is © The Royal Society of Chemistry 2017

Chem. Soc. Rev., 2017, **46**, 3529–3614 | 3555

Fig. 17 (a) Schematic representation of $Na_4Fe_3(PO_4)_2(P_2O_7)$ and (b) galvanostatic charge/discharge profiles of $Na_4Fe_3(PO_4)_2(P_2O_7)$ under a C/40 rate and the calculated average voltage at each region, where the inset shows the dQ/dV curve of initial charge/discharge profiles. (Reproduced with permission from ref. 205, Copyright 2012 American Chemical Society.) (c) Galvanostatic charge/discharge curves at 1st, 10th and 50th cycles of $Na_4Co_3(PO_4)_2P_2O_7$. (Reprinted from ref. 206, Copyright 2012, with permission from Elsevier.) (d) The projected crystal structure along the c-axis: gray tetrahedrons, PO_4; red octahedrons, VO_6; yellow spheres, Na atoms. The $(VP_2O_7)_4PO_4$ unit is denoted as a dashed circle and (e) galvanostatic profiles of $Na_7V_4(P_2O_7)_4PO_4$ measured at C/20 and C/40 in the first cycles. (Reproduced with permission from ref. 208, Copyright 2014 PNAS.)

Although stepwise charge and discharge curves were observed, the average operating voltage was approximately 4.5 V, which is the highest value that has ever been observed in the Na system (Fig. 17c). In contrast to $Na_4Fe_3(PO_4)_2P_2O_7$, the appearance of a stepwise curve would be ascribed to the presence of Na^+/vacancy ordering in the crystal structure. The material could deliver a capacity of approximately 80 mA h g^{-1} even at 25C-rates (4.25 A g^{-1}). This superior electrochemical performance was attributed to the help of the three-dimensional Na^+ diffusion pathways in the crystal structure. In an attempt to mitigate the multistep voltage plateaus, they synthesized $Na_4[Co_{2.4}Mn_{0.3}Ni_{0.3}]$-$(PO_4)_2P_2O_7$. The material also exhibited an average operating voltage of 4.5 V, and a 103 mA h g^{-1} discharge capacity was obtained at a rate of 5C. As expected, partial replacement of Co by Ni and Mn led to sloppy charge and discharge curves. In addition, not only Co, but two substituents, Ni and Mn, participated in the electrochemical reaction in a voltage range of 2–5 V according to an XAS study.

Another interesting compound, $Na_7V_4(P_2O_7)PO_4$, was suggested by Lim et al.[208] This material has a crystallized tetragonal structure with a $P\bar{4}2_1c$ space group. The crystal structure has a basic unit, $(VP_2O_7)_4PO_4$, which is composed of a central tetrahedron $[PO_4]$ that shares corners with four $[VO_6]$ octahedra, and each diphosphate group $[P_2O_7]$ bridges the two adjacent $[VO_6]$ octahedra with shared corners. The interconnected $(VP_2O_7)_4PO_4$ units comprise a three-dimensional channel for Na^+ ion diffusion (Fig. 17d). Based on the $V^{3+/4+}$ redox reaction, $Na_7V_4(P_2O_7)PO_4$ exhibited a flat plateau at 3.88 V associated with a biphasic reaction governed by the first-order transition, delivering approximately 90 mA h g^{-1} (Fig. 17e). Addition of rGO further extended its cycle life to 1000 cycles with 78% capacity retention.

2.3.4. NASICON type phosphates. $Na_3V_2(PO_4)_3$, which crystallizes to a rhombohedral structure with a $R\bar{3}c$ space group, has a NASICON-type framework built up from isolated VO_6 octahedra and PO_4 tetrahedral units interlinked via corners to form a framework anion, $[V_2(PO_4)_3]^{3-}$. Two different Na atoms are located in the empty channels of the framework with two different

oxygen environments (Fig. 18a).[209] Early work by Gopalakrishnan et al. demonstrated the possibility of Na^+ extraction to form $V_2(PO_4)_3$ using chlorine in $CHCl_2$ at room temperature.[210] Electrochemical Na^+ extraction was investigated by Masquelier[211] and Plashnitsa et al.[212] and two voltage plateaus were found at 3.4 and 1.6 V. The latter work also tested a full symmetric cell, adopting $Na_3V_2(PO_4)_3$ for both cathodes, but the performance was unsatisfactory. Jian et al. modified the surface of $Na_3V_2(PO_4)_3$ using electro-conducting carbons derived from sugar.[209] The $Na_3V_2(PO_4)_3$/C electrode exhibited improved capacity in both the upper and lower voltage regions compared with earlier works (Fig. 18b). They further reduced the irreversible capacity, changing the conventional electrolyte to NaFSI/PC from the PC-based compound. The new combination electrolyte increased the initial Coulombic efficiency above 98%.[213] Saravanan et al. employed a solution-based template method using CTAB as a cationic surfactant that left approximately 6 wt% of carbon after synthesis in a reducing environment.[214] They demonstrated stable long-term cyclability for over 30 000 cycles at a
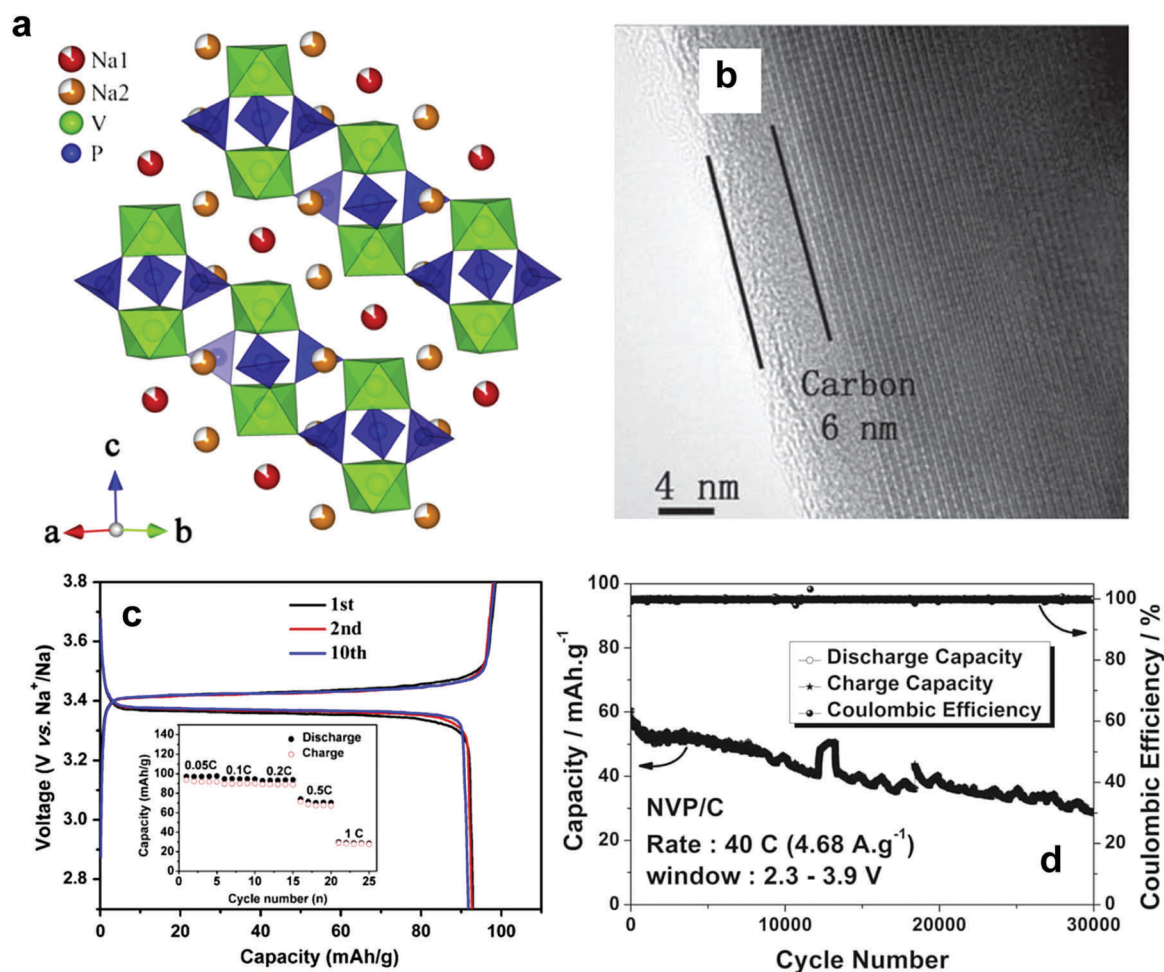
Fig. 18 (a) The crystal structure of $Na_3V_2(PO_4)_3$. (Reprinted from ref. 209, Copyright 2012, with permission from Elsevier.) (b) TEM bright-field image of carbon-coated $Na_3V_2(PO_4)_3$. (Reproduced from ref. 213 with permission, Copyright 2013 Wiley-VCH Verlag GmbH & Co. KGaA.) (c) Charge and discharge curves in a voltage range of 1.0 to 3.8 V for carbon-coated $Na_3V_2(PO_4)_3$. (Reprinted from ref. 209, Copyright 2012, with permission from Elsevier.) (d) Long term cycle life and Coulombic efficiency for 30 000 cycles at a rate of 40C for carbon-coated $Na_3V_2(PO_4)_3$. (Reproduced from ref. 214 with permission, Copyright 2013 Wiley-VCH Verlag GmbH & Co. KGaA.)

This journal is © The Royal Society of Chemistry 2017

Chem. Soc. Rev., 2017, 46, 3529–3614 | 3557

rate of 40C (4.68 A g^{-1}) with superior rate capability (Fig. 18c). Their symmetrical cell also evidenced the cycling stability for over 5000 cycles. Jian *et al.* further analyzed the crystal structure during the electrochemical reaction.[215] As mentioned in Fig. 18a, Na atoms are localized to two different sites (6b, M1 and 18e, M2) in Na$_3$V$_2$(PO$_4$)$_3$. The flat curve during desodiation of Na$_3$V$_2$(PO$_4$)$_3$ indicates a biphasic reaction based on the V$^{3+/4+}$ redox reaction as a result of Na$^+$ extraction at the M2 site, which is related to the formation of NaV$_2$(PO$_4$), in which only one Na (6b, M1) resides in the crystal structure. NMR further revealed that, in Na$_3$V$_2$(PO$_4$)$_3$, the Na atoms were not randomly distributed at M2 sites, but appeared in an ordered arrangement locally; an Na$^+$ ion at the M2 sites in Na$_3$V$_2$(PO$_4$)$_3$ is mobile, whereas an Na$^+$ ion at the M1 site is immobile, corresponding to 2 mol Na$^+$ per formula unit in Na$_3$V$_2$(PO$_4$)$_3$, while 1 mol Na$^+$ per formula unit in Na$_3$V$_2$(PO$_4$)$_3$ can retain the framework during the electrochemical reaction.

2.3.5. Sulfates, fluorosulfates, and carbonophosphates. Substitution of (SO$_4$)$^{2-}$ for the (PO$_4$)$^{3-}$ anion results in a higher operating voltage because of the greater ionicity. When successful, this improves the operating voltage in a tavorite-type material, leading to an OCV increase of 0.6–0.8 V in LiFeSO$_4$F compared to LiFePO$_4$.[216] Similarly, this substitution is also applicable in Na systems, namely, NaMSO$_4$F (M: Fe, Co, and Mn), as suggested by Barpanda *et al.*[217] The compounds are crystallized in a monoclinic structure with a *P*2$_1$/*c* space group (Fig. 19a). Tripathi *et al.* calculated the activation energy for Na$^+$ diffusion. Although NaFeSO$_4$F has a three-dimensional structure in only one direction, [010], it has relatively low activation energy (0.6 eV).[218] The measured ionic conductivity of the compound was sufficiently high at approximately 10^{-7} S cm^{-1}. Notwithstanding, the electrode delivered only 6% of the theoretical capacity (137 mA h g^{-1}) (Fig. 19b). Barpanda *et al.* further developed a sulfate-based sodiated iron compound, which was crystallized to an alluaudite-type sulfate framework, Na$_2$Fe$_2$(SO$_4$)$_3$, with a *P*2$_1$/*c* space group.[219] In this case, the crystal structure was similar to earlier work on NaMSO$_4$F, while the resulting volume of the unit cell was larger by over two-fold. In contrast to A$_x$M$_2$(XO$_4$)$_3$-type compounds, which usually have NASICON-related structures, Na$_2$Fe$_2$(SO$_4$)$_3$ does not contain [M$_2$(XO$_4$)$_3$] units, but has a unique structure with an alluaudite type framework (Fig. 19c). FeO$_6$ octahedra share edges, forming Fe$_2$O$_{10}$ dimer units. These Fe ions could be assigned to two distinct groups, Fe(1) and Fe(2), since local structures of Fe(1) and Fe(2) were found to have two doublets in the Mössbauer spectra. The Fe$_2$O$_{10}$ dimers were linked with SO$_4$ units in a corner-sharing fashion, generating a three-dimensional network framework with large tunnels along the *c*-axis, with Na located in the tunnels. Electrochemical testing of the material revealed that a Fe$^{2+/3+}$ redox reaction led to a high operating voltage of 3.8 V on average, the highest that appeared in the Fe$^{2+/3+}$ reaction, which confirms strong ionicity when (SO$_4$)$^{2-}$ anions occur in the crystal structure instead of (PO$_4$)$^{3-}$. Based on one-electron transfer, the material could deliver approximately 85% of the theoretical capacity (120 mA h g^{-1}) with a moderate rate capability (Fig. 19d). The structure may be able to extend to several family compounds, adopting not only Fe,

but the other transition metal elements such as Ni, Co, V, and Mn, among others.

Sodiated metal carbonophosphates, such as sidorenkite Na$_3$MPO$_4$CO$_3$ (M: Mg, Mn, Fe, Co, Ni, and Cu), were recently introduced as a new intercalation cathode by Chen *et al.*[220,221] Two different series of (PO$_4$)$_3$- and (CO$_2$)^2-ions have bonds with M in Na$_3$MPO$_4$CO$_3$ compounds, which are stable with a sidorenkite structure and a *P*2$_1$/*m* space group (Fig. 19e). In Na$_3$MnPO$_4$CO$_3$, the MnO$_6$ octahedra are connected by a PO$_4$ tetrahedra to form a double layer. The CO$_3$ group shares an oxygen edge with MnO$_6$. The two-dimensional interslab accommodates two Na atoms at two different interstitial sites, where Na1 and Na2 coordinate with seven and six O atoms, respectively. As anticipated, their computations suggested that the sidorenkite structure may have good intercalation properties.[222] Carbophosphate showed high discharge (125 mA h g^{-1}) (Fig. 19f), which represented 66% of the theoretical capacity (191 mA h g^{-1}). It is interesting that Na$_3$MPO$_4$CO$_3$ underwent a topotactic solid solution reaction during cycling, activated by a two-electron electrochemical reaction of Mn$^{2+/3+}$ and Mn$^{3+/4+}$ redox couples.

2.3.6. Cyanides and organic compounds. Prussian blue and its analogues were investigated as hosts for alkali ions, but those works received less attention due to low energy density compared with the above-mentioned materials.[223,224] Recently, Cui and coworkers reported potassium copper hexacyanoferrate to intercalate Na$^+$ ions in aqueous solution at less than 2 V.[225–227] In an attempt to increase the operation voltage, Wang *et al.* utilized KMFe[CN]$_6$ (M: Fe and Mn, which are divalent with high spin), which exhibited high operation voltage plateaus at 3.8 V for charge and 3.5 V for discharge.[228] Their extended work varied the concentration of Na in the MFe[CN]$_6$ perovskite framework: Na$_{1.4}$MFe[CN]$_6$ (*Fm3m*) and Na$_{1.72}$MFe[CN]$_6$ (*R3̄m*).[229] The double-perovskite ordering of both the anion orientations and the cations introduces a rhombohedral site symmetry along each of the four [111] axes that would stabilize alkali-ion displacement along a cubic [111] axis toward the more octahedral-site complex. The four-fold degeneracy of these displacements keeps the cubic phase at higher temperature and lower Na concentration, but a cooperative Na displacement at higher Na concentration reduces the crystal symmetry to rhombohedral, stabilizing the rhombohedral phase (Fig. 20a). Note that the larger is the concentration of Na$^+$ ions in the compound, the higher is the temperature of transition from rhombohedral to cubic symmetry. Electrochemical reactions occurring at low and high voltage are the redox reactions of low-spin Fe$^{3+/2+}$ and high-spin Mn$^{3+/2+}$, respectively. The post-cycled electrode did not show a notable structural change after 50 cycles. Na$_{1.72}$MFe[CN]$_6$ reacted at a rate of 40C (Fig. 20b). Replacement of Mn with Fe, FeFe[CN]$_6$, lowered the operation voltage of the lower voltage plateau to 3.1 V on charge and 2.8 V on discharge, delivering a discharge capacity of approximately 120 mA h g^{-1}.[230] The electrode was substantially stable over 600 cycles with excellent capacity retention. Na$_4$Fe[CN]$_6$ was electrochemically active in Na cells, showing approximately 90 mA h g^{-1} on discharge with a flat voltage plateau at 3.4 V.[231] The lower capacity is due to the one-electron reaction by the low-spin Fe$^{3+/2+}$ redox.

3558 | *Chem. Soc. Rev.*, 2017, **46**, 3529–3614

This journal is © The Royal Society of Chemistry 2017
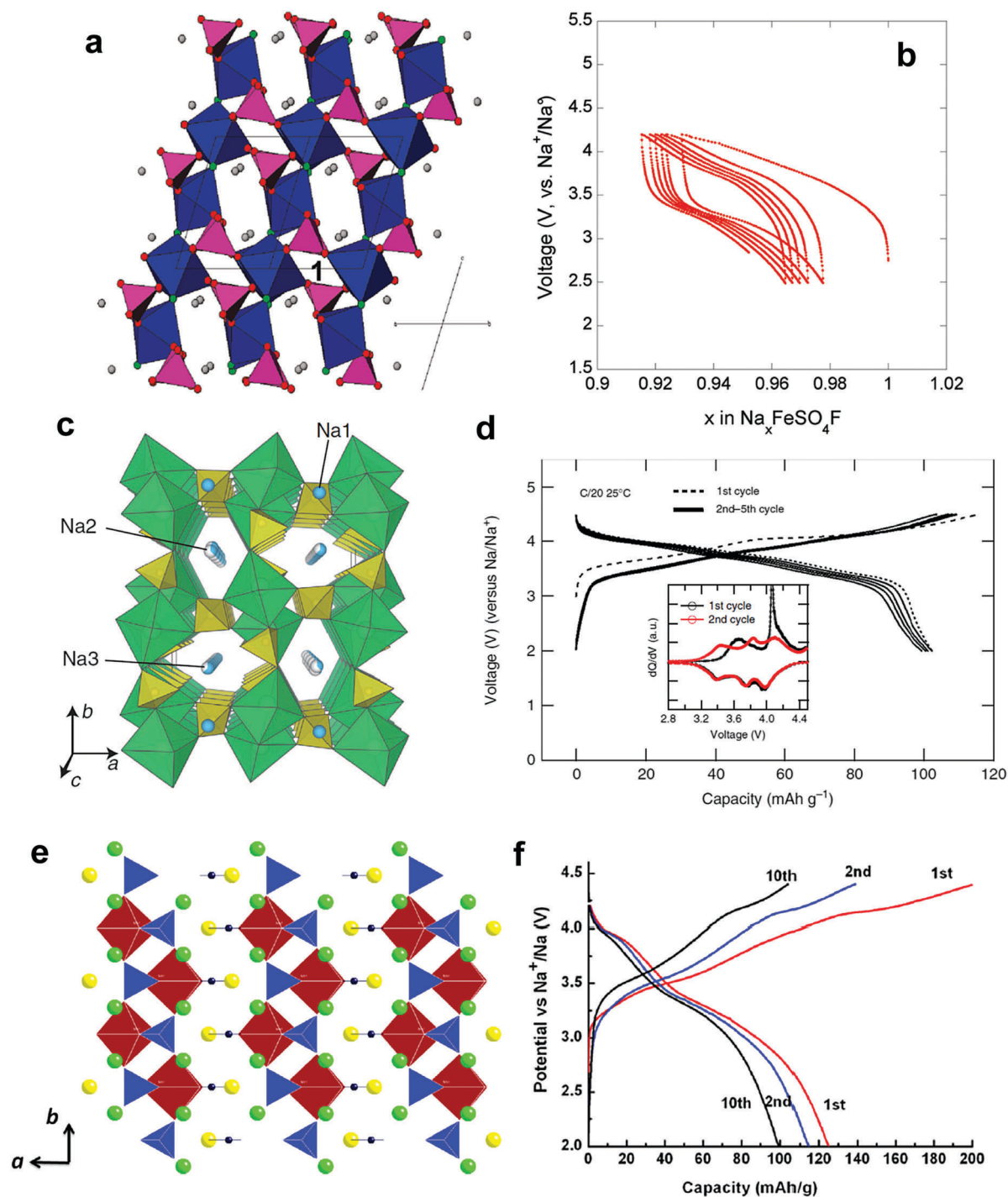
Fig. 19 (a) Crystal structure of Monoclinic sodium-based metal fluorosulphates and (b) the electrochemical voltage profile of NaFeSO$_4$F cycled in a sodium cell with a metallic Na anode and a 1 M Na-TFSI : PC electrolyte at a rate of C/20. (Reproduced with permission from ref. 217, Copyright 2010 American Chemical Society.) (c) Crystal structure of Na$_2$Fe$_2$(SO$_4$)$_3$ projected along the c-axis and (d) galvanostatic charging and discharging profiles of the Na$_{2-x}$Fe$_2$(SO$_4$)$_3$ cathode cycled between 2.0 and 4.5 V at a rate of C/20 (2 Na in 20 h) at 25 °C. First (1st) cycle is shown in dashed black line, and 2nd–5th cycle in solid black lines. (inset) The differential galvanostatic profiles (dQ/dV) of the Na$_2$Fe$_2$(SO$_4$)$_3$ cathode. (Reproduced by permission from ref. 219, Nature Publishing Group, Copyright 2014.) (e) The structure of Na$_3$MnPO$_4$CO$_3$ viewed along [001]: Mn octahedra, brown; PO$_4$ tetrahedra, blue; CO$_3$ triangular planar, black; sodium, green (Na1 site) and yellow (Na2site) spheres and (f) the resulting voltage curves of Na$_3$MnPO$_4$CO$_3$ at the first, second, and 10th cycles with a C/100 rate. (Reproduced with permission from ref. 221, Copyright 2013 American Chemical Society.)

Organic molecules can undergo a reversible electrochemical redox reaction. The advantages of such a reaction are structural diversity, flexibility, molecular level controllability, and resource renewability.[232–235] Recently, Wang *et al.* reported the electrochemical performance of 2,5-dihydroxyterephthalic acid (Na$_4$DHTPA), Na$_2$C$_8$H$_2$O$_6$, with enolate and carboxylate groups

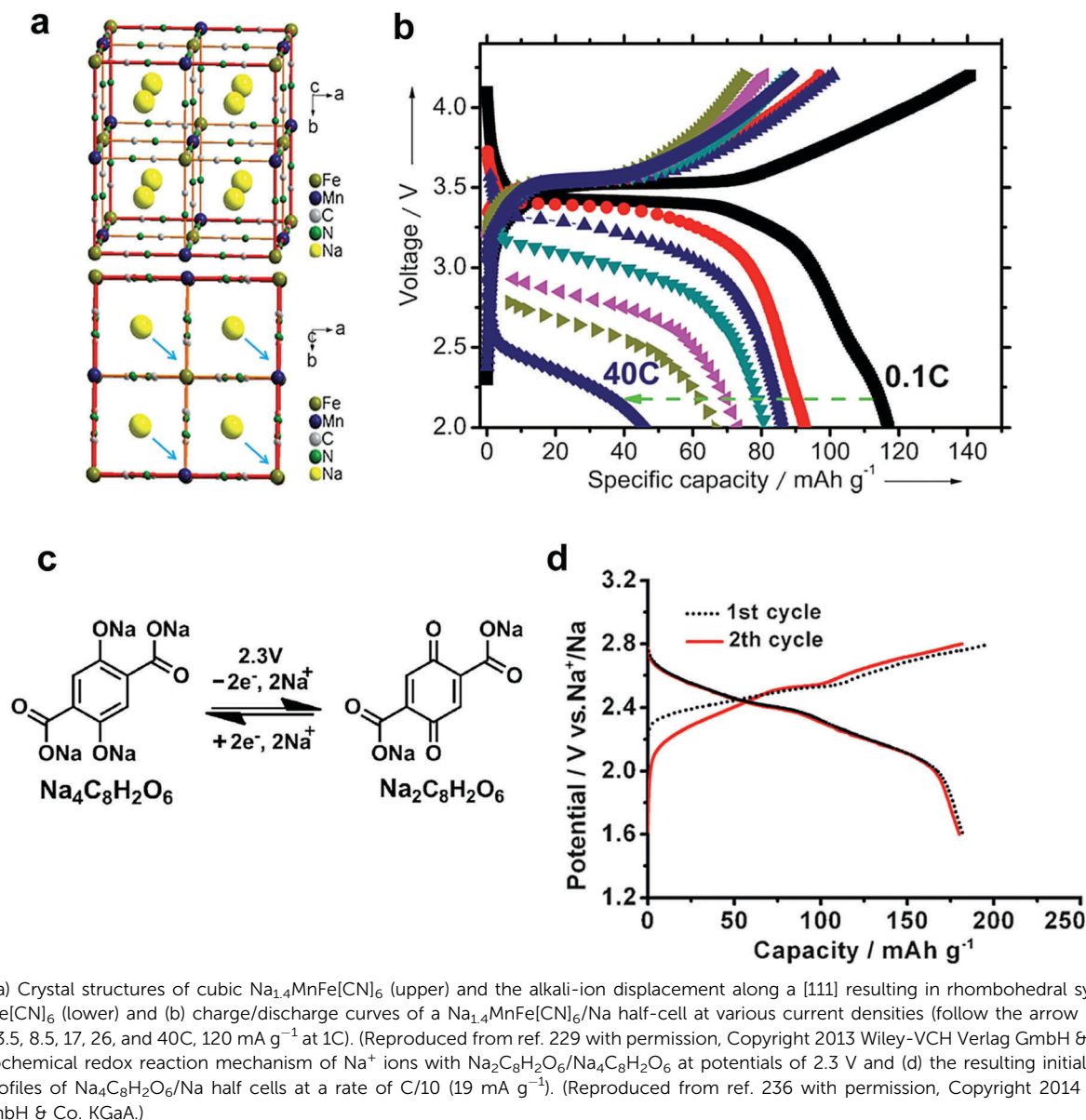**Fig. 20** (a) Crystal structures of cubic $Na_{1.4}MnFe[CN]_6$ (upper) and the alkali-ion displacement along a [111] resulting in rhombohedral symmetry of $Na_{1.72}MnFe[CN]_6$ (lower) and (b) charge/discharge curves of a $Na_{1.4}MnFe[CN]_6$/Na half-cell at various current densities (follow the arrow by order of 0.1, 0.85, 3.5, 8.5, 17, 26, and 40C, 120 mA g^{-1} at 1C). (Reproduced from ref. 229 with permission, Copyright 2013 Wiley-VCH Verlag GmbH & Co. KGaA.) (c) Electrochemical redox reaction mechanism of Na^+ ions with $Na_2C_8H_2O_6$/$Na_4C_8H_2O_6$ at potentials of 2.3 V and (d) the resulting initial discharge/ charge profiles of $Na_4C_8H_2O_6$/Na half cells at a rate of C/10 (19 mA g^{-1}). (Reproduced from ref. 236 with permission, Copyright 2014 Wiley-VCH Verlag GmbH & Co. KGaA.)

as the cathode material for room temperature SIBs (Fig. 20c).[236] They demonstrated that two reversible Na^+ ion electrochemical reactions occurred with redox couples of $Na_2C_8H_2O_6$/$Na_4C_8H_2O_6$ as the cathode at 2.3 V, with a capacity of 180 mA h g^{-1} and excellent cyclability (Fig. 20d). $Na_2C_6O_6$[237] and aniline–nitroaniline copolymer[238] also exhibited high rechargeable capacity over 170 mA h g^{-1} with good cyclability.

3. Anode materials

As mentioned in Section 2, several platforms of cathode materials have been introduced for SIBs.[239] Simultaneously, as the cathode counterpart, the recent development of anodes for SIBs has been achieved by the use of selected carbonaceous materials, transition metal oxides (or sulfides) and intermetallic and

organic compounds, as anodes.[240] Research on the above anode materials for SIBs has been developed in three main categories, based on the reaction mechanism during sodiation/ desodiation processes: (1) the insertion reaction, (2) the conversion reaction, and (3) the alloying reaction. Carbonaceous materials and titanium-based oxides have been introduced as insertion anode materials.[241,242] Recent efforts expand the applications towards transition metal oxides (TMOs) or transition metal sulfides (TMSs) that are driven by a conversion reaction.[243] Also, Na–Me (Me = metal) alloying compounds of group 14 or 15 elements motivated by the alloying reaction are recommended as possible candidate materials with the help of an electro-conducting carbon matrix to improve their specific capacity and cyclability.[244,245] Such conversion and alloying reaction materials are known to deliver high capacities but suffer from huge volume expansion of the host materials due to

3560 | Chem. Soc. Rev., 2017, 46, 3529–3614

This journal is © The Royal Society of Chemistry 2017

the continuous self-pulverization of the electrode materials.[240,243] More seriously, to compete with lithium ion batteries, a great challenge to overcome is the sluggish reaction kinetics from the large ionic size of Na$^+$ ions (1.02 Å), which impedes fast Na$^+$ storage.[99,240,246] Therefore, scientists should make more efforts to improve the electrode performances. In this section, we discuss present research progress in anode materials for SIBs.

3.1. Insertion materials

Based on an insertion reaction, carbonaceous and titanium-based oxides have been extensively studied as anodes for SIBs. Several carbon-based materials such as graphitic and non-graphitic carbons have been investigated for Na$^+$ storage.[241] These carbon materials are widely accepted because of their ability to accommodate Na$^+$ ions into their structure. In particular, hard carbon is interesting because of its reasonable capacity of $\sim$300 mA h g^{-1} and low operating potential (almost zero, $\sim$0 V vs. Na$^+$/Na).[22,23,247] However, the Na$^+$ storage mechanism in a disordered carbon structure is still controversial.[247–251] On the other hand, titanium-based oxide compounds have been widely studied because of their low operation voltage and cost as well.[242] Analogous to LIBs, titanium-based oxide anodes, including various polymorphs titanium dioxide (TiO$_2$), spinel-lithium titanate (Li$_4$Ti$_5$O$_{12}$) and sodium titanate (Na$_x$Ti$_y$O$_z$), were reported as promising anode materials.

3.1.1. Carbon-based anode materials

3.1.1.1. Graphitic carbon (graphite). During the electrochemical reduction, Li$^+$ ions are inserted between graphene layers, and Li-graphite intercalation compounds (Li-GIC) are formed through stage transformations in Li cells.[252,253] Since the 1980s, the electrochemical behavior of graphite with Na$^+$ ions has been studied based on the graphite/polyethylene oxide NaCF$_3$SO$_3$/Na cell[254] (Fig. 21a). However, Na$^+$ insertion into graphite is significantly impeded and degradation of electrolyte and/or electrode materials was observed[255] (Fig. 21b). First-principles calculation results of the formation energy for Na-GIC exhibited that Na hardly intercalates into graphite because of the energetic instability of the Na-GICs. Graphite is stressed when some Na$^+$ intercalates into graphite because of the thermodynamic instability of binary Na-intercalated GICs (b-GIC), which is assumed to be the result of an unfavorable mismatch between the graphite structure and the size of the Na ion.[256] Namely, due to the unfavorable formation of NaC$_6$ and NaC$_8$ that are thermodynamically unstable at the first stage of Na-graphite intercalation compound (Na-GIC) formation in SIBs, the capacity of natural graphite is limited.[256–258] As a recent breakthrough, Jache et al. facilitated Na-ion storage in graphite using solvated-Na-ion intercalation, forming ternary GICs. That is the intercalation of solvated alkali ions "co-intercalation" by reduction of graphite according to the following equation: C$_n$ + e$^-$ + A$^+$ + y sol ν $\leftrightarrow$ A$^+$(sol ν)$_y$C$_n^-$.[258] Zhu et al. also confirmed that solvated Na$^+$ ions intercalate into graphite via a stage-evolution process, forming a set of ternary graphite intercalation compounds.[259] Ether-based electrolytes with a high donor number can form stable Na$^+$ solvated species with non-polar characteristics for co-intercalation into natural graphite.[260–262]

Kim et al. reported a reversible phase transition during intercalation and deintercalation processes of solvated-Na-ions in natural graphite via an operando X-ray diffraction analysis[261] (Fig. 21c). They investigated the unusual Na storage behavior in natural graphite through Na$^+$-solvent co-intercalation using different solvents (EC/DEC, DME, DEGDME and TEGDME) and Na salts (NaPF$_6$, NaClO$_4$, NaCF$_3$SO$_3$). Ether-based electrolytes could suppress electrolyte decomposition, resulting in the formation of a negligible SEI film on the graphite surface, enabling Na$^+$-solvent transport to the graphite lattice. In contrast, carbonate-based electrolytes (EC/DEC) form relatively thick insulating SEI layers on the graphite surface, which block Na$^+$-solvent transport[262] (Fig. 21d). As a result, under the limited conditions using ether-based electrolytes, the natural graphite delivered a capacity of 150 mA h g^{-1} with reasonable retention for 2500 cycles, and produced over 75 mA h g^{-1} at 10 A g^{-1} in the DEGDME electrolyte containing NaPF$_6$ salt. On the other hand, Wen et al. proposed expanded graphite with an enlarged interlayer lattice distance of 4.3 Å. Note that graphite has a typical interlayer space of 3.4 Å.[263] Their in situ TEM study revealed reversible insertion and extraction of Na$^+$ ions during the electrochemical reaction (Fig. 21e). As a result, the expanded graphite could exhibit a moderate capacity of approximately 284 mA h g^{-1} at a current of 20 mA g^{-1} with good capacity retention over 2000 cycles (Fig. 21f). Recently, Kang et al. reported the sodium ion intercalation behavior of expanded graphite oxide (GO) as an anode material. According to their report, the electrochemical properties of GO strongly depend on the amounts and ratios of different functional groups.[264]

3.1.1.2. Non graphitic carbon (hard carbon). In 1993, Doeff and co-workers first reported the Na storage performance of disordered soft carbon prepared by pyrolysis of petroleum coke[251] (Fig. 22a). They demonstrated the extent of the Na$^+$ insertion/extraction reaction into the soft carbon and discussed the possibility of its application for SIBs. Stevens and Dahn reported the insertion mechanism of Na$^+$ ions into disordered hard carbon (Fig. 22b).[22,23,247] The suggested mechanism was the "house of cards" for Na$^+$ ion storage, which is composed of the two domains in a disordered hard carbon structure without staging transition. First, Na$^+$ ions are inserted between parallel graphene sheets (in the sloping voltage region) upon increasing the interlayer space. Second, Na$^+$ ions fill the nanopores (in the plateau region) of the disordered carbon structure.[22,23,249] The hard carbon prepared by carbonization of glucose showed a reversible electrochemical reaction in Na cells and it delivered a high specific capacity of approximately 300 mA h g^{-1} with a low operating potential of about $\sim$0 V. Later, Komaba and co-workers performed a systematic study on electrochemical sodium insertion into hard carbon to understand the related structural change.[27] Upon reduction to 0.2 V (in the sloping region), the resulting XRD peaks shifted to lower angles, indicating that the interlayer spacing between the graphene sheets was expanded due to the sodium insertion (Fig. 22c). They also confirmed the reversible Na$^+$ insertion process into the nanopores via small angle X-ray scattering measurements

This journal is © The Royal Society of Chemistry 2017

Chem. Soc. Rev., 2017, 46, 3529–3614 | 3561
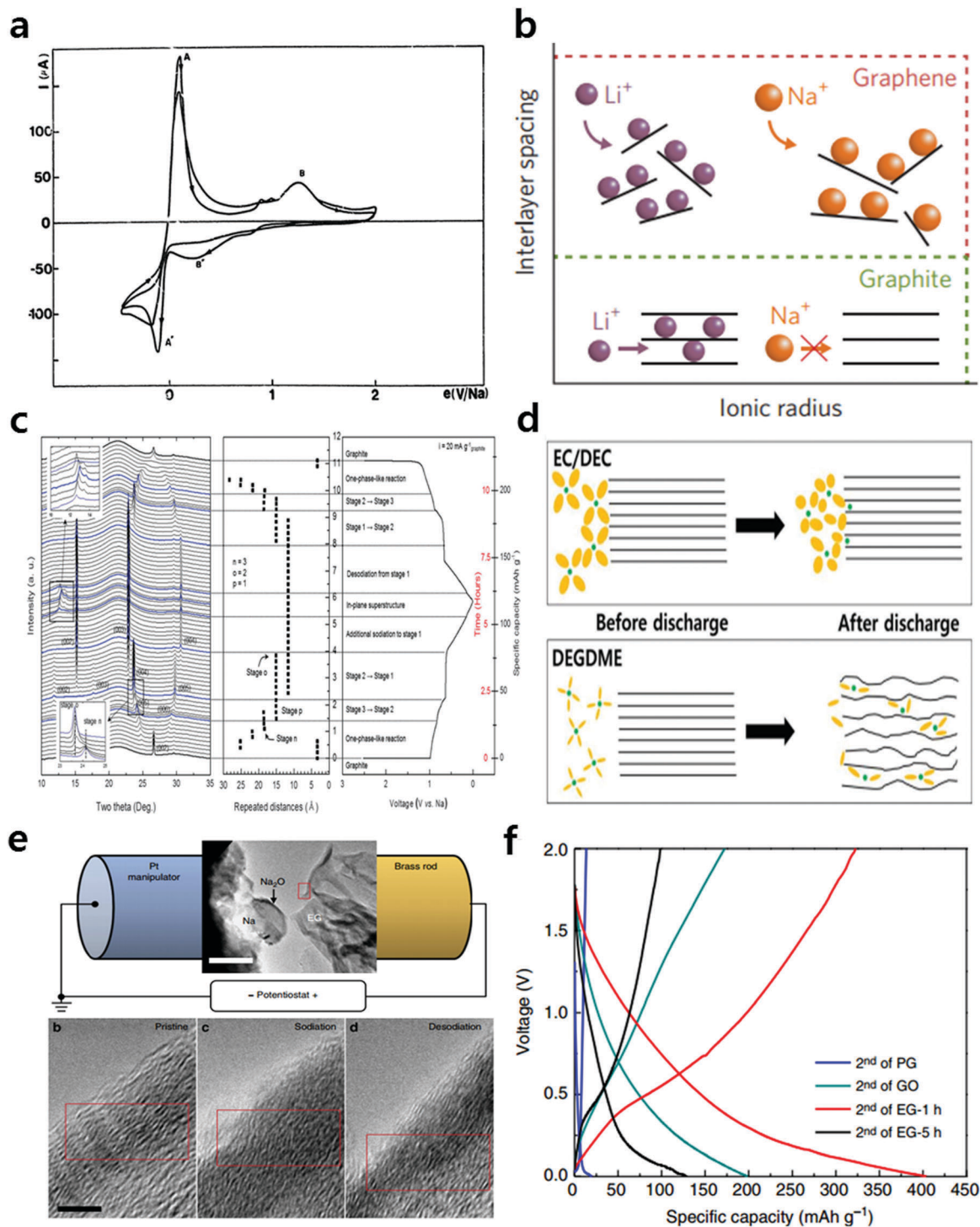
Fig. 21 (a) Graphite current–potential curve in the graphite/PEO-NaCF₃SO₃/Na cell at 82 °C. (Reprinted from ref. 254, Copyright 1988, with permission from Elsevier.) (b) Li⁺ and Na⁺ insertion mechanisms in graphene and graphite. (Reproduced by permission from ref. 255, Nature Publishing Group, Copyright 2015.) (c) In operando synchrotron X-ray diffraction analysis of the structural evolution of the ternary Na–ether–graphite system. (Reproduced with permission from ref. 261, Copyright 2015 The Royal Society of Chemistry.) (d) Different Na storage mechanisms in natural graphite between in NaPF₆ in EC/DEC (top) and NaPF₆ in DEGDME (bottom). (Reproduced from ref. 262 with permission, Copyright 2015 Wiley-VCH Verlag GmbH & Co. KGaA.) (e) In situ TEM investigation of the sodium storage mechanism in the EG-1h sample. (f) Electrochemical performances of PG, GO, EG-1h and EG-5h in organic 1.0 M NaClO₄ in a polycarbonate solvent liquid electrolyte. (Reproduced by permission from ref. 263, Nature Publishing Group, Copyright 2014.)

(SAXS) in the voltage range of 0.2 V to 0 V (in the plateau region) upon reduction. From these results, they suggested that the

enlarged interlayer spacing (*d*-spacing = 3.8 Å) or the smaller crystallite size of the parallel graphene within hard-carbon in

Fig. 22 (a) First cycle of the Na/DME, NaClO$_4$/(ground) petroleum coke cell. (Reproduced with permission from ref. 251, Copyright 1993 The Electrochemical Society.) (b) Sodium potential profiles of glucose pyrolyzed to 1000 °C. The insets show details of the low-potential region. (Reproduced with permission from ref. 247, Copyright 2000 T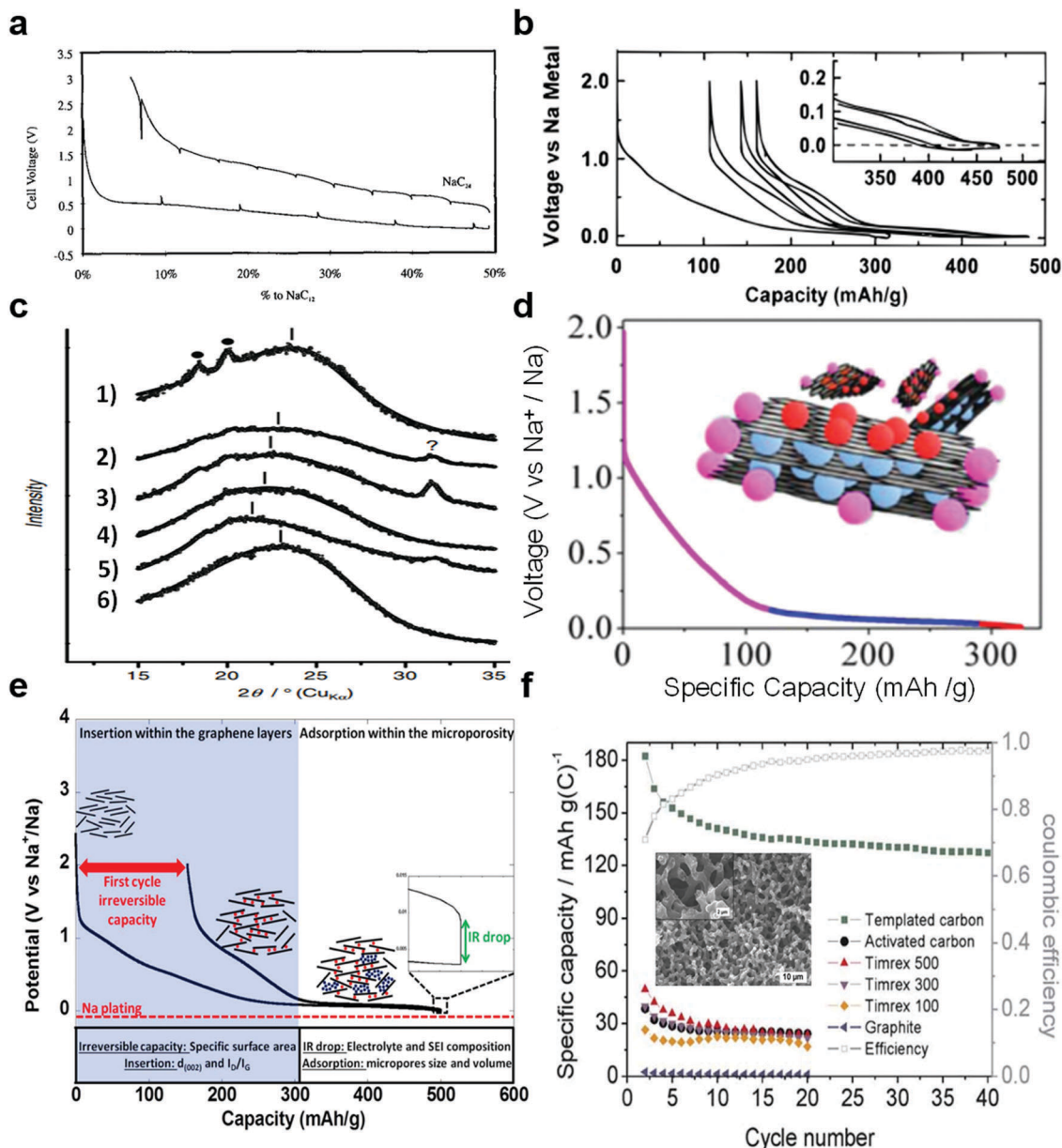he Electrochemical Society.) (c) *Ex situ* XRD patterns of hard-carbon electrodes: (1) pristine electrode, galvanostatically reduced to (2) 0.40 V, (3) 0.20 V (4) 0.10 V, (5) 0.00 V, and (6) oxidized to 2.00 V after reduction to 0.00 V (● PVdF binder, ? unknown). (Reproduced from ref. 27 with permission, Copyright 2011 Wiley-VCH Verlag GmbH & Co. KGaA.) (d) Potentiogram and schematic of the proposed Na-ion three part storage mechanism. (Reproduced with permission from ref. 250, Copyright 2015 American Chemical Society.) (e) Typical potential *vs.* capacity profile of hard carbon when tested against sodium metal counter electrodes. (Reproduced with permission from ref. 249, Copyright 2015 The Electrochemical Society.) (f) Specific capacities (C/5, Na-insertion) upon cycling for different carbons and Coulombic efficiency for the templated carbon at room temperature. (Inset image: the SEM image of templated carbon.) (Reproduced with permission from ref. 266, Copyright 2012 The Royal Society of Chemistry.)

comparison to those of the graphite (*d*-spacing = 3.354 Å) is responsible for the sodium insertion. In addition, the ^{23}Na NMR study demonstrated the reversible electrochemical reaction mechanism of Na$^+$ ions with hard carbon: (i) two resonance peaks at 9.9 ppm and 5.2 ppm were ascribed to reversible sodium present between disordered graphene sheets in hard carbon and (ii) one broader resonance peak between −9 and

−16 ppm was ascribed to the appearance of Na$^+$ ions in heterogeneously distributed closed nanopores in hard carbon.[265] In 2011, Wenzel and co-works demonstrated high capacity carbon anode materials with an excellent rate capability of 100 mA h g^{-1} at C/5 at room temperature for the first time[266] (Fig. 22f). They prepared templated carbon with hierarchical porosity *via* the nanocasting route by using pitch carbon and investigated the

co-relationships between the physico-chemical properties and the electrochemical properties with commercially available porous and non-porous carbon materials (porous carbon: Timrex 100, 300, 500 and activated carbon, non-porous carbon: graphite). The highest surface area (1041 m^2 g^{-1}) of activated carbon and the highest pore volume (1.008 cm^3 g^{-1}) of Timrex 500 show the low reversibility with Na$^+$ ions. Meanwhile, their templated carbon controlled by microstructural approaches minimized the diffusion lengths within the electrode (surface area: 346 m^2 g^{-1}, pore volume: 0.798 cm^3 g^{-1}). As a result, the carbon matrix showed excellent electrochemical activity for Na$^+$ ions. Their results imply that high capacity and rate capabilities cannot be simply achieved by enlarging the surface area or by increasing the porosity. On the other hand, Tsai et al. further confirmed the reaction process through an ab initio study showing that a larger interlayer distance is not the only factor that helps Na intercalation. Additionally, the vacancy defects (MV: mono-vacancy and DV: di-vacancy) in hard carbon can greatly enhance the Na$^+$ ion intercalation because of the strong ionic binding energy between the Na$^+$ ions and the defects, which effectively overcomes the van der Waals interaction.[248] Further, Bommier et al. discussed the new storage mechanism in the sloping region (as a function of the charge–discharge curve), which can be explained through Na$^+$ ion storage at defect sites.[250] They also confirmed that Na$^+$ ions can be intercalated into the hard carbon lattice particularly in the low voltage plateau region. These findings suggest that the Na$^+$ storage is related to a three-step process (Fig. 22d) rather than the two-step storage mechanism proposed in the card-house model (Fig. 22e); (i) Na$^+$ ions are adsorbed at defective sites in the slope-voltage region, (ii) Na$^+$ ions are intercalated in the hard carbon lattice, and (iii) Na$^+$ ions are adsorbed at the pore surface in the plateau region. Such research results show that the Na$^+$ insertion mechanism into a disordered structure is still controversial. Therefore, further theoretical and experimental investigation should be conducted to clarify the related reaction mechanism for development of hard carbon materials.

To date, hard carbons have been the most widely used carbon source of SIB anodes and have been proved to significantly improve the electrochemical performance of SIBs. However, there are a lot of challenges facing the development of hard carbon anodes for practical applications. The reversibility of the hard carbon was found to depend on the carbon precursor, particle sizes and manufacturing processes. And, the appropriate low pore volumes and surface areas can achieve the higher reversible capacities. The suitable additives and electrolytes are highly desirable for reversibility of Na$^+$ storage. Therefore, based on a number of previous studies, we should consider some factors, including particle sizes, additives, electrolytes, vacancy defects and porosity measurements, to develop the high irreversible capacity and high rate capability in hard carbons. Furthermore, we should investigate the relationship between the electrochemical characteristics of hard carbon and solid electrolyte interphase (SEI) layer formation. At the same time, the computational works such as DFT calculation and ab initio calculation should be conducted to predict and support the experimental results.

3.1.1.3. Non graphitic carbon (graphene). Graphene, unique two-dimensional carbon materials, has great physical and chemical advantages such as a large surface area, superior electronic conductivity, and chemical stability.[267] Such advantages of graphene can bring shorter paths for fast ion diffusion and produce a large exposed surface offering more ion insertion channels.[268] Therefore, for LIBs and SIBs, graphene can be considered as an anode material for energy-storage systems[255,269–274] (Fig. 21b). Moreover, graphene or reduced graphene oxide (RGO) help to improving the Li and Na storage capability in its composite anodes. Recently, Wang et al. demonstrated the reversible sodium ion storage performances in reduced graphene oxide (RGO).[274] RGO possesses higher electrical conductivity and active sites with large interlayer distances and provides a disordered structure enabling it to store a larger amount of Na$^+$ ions. In their study, RGO anodes exhibited a moderate specific capacity of 141 mA h g^{-1} at 40 mA g^{-1} with stable cycle retentions for over 1000 cycles. Ding et al. synthesised different kinds of few-layer graphene at different carbonization temperatures (600–1400 °C) and investigated the Na$^+$ ion storage mechanism in their graphene structure.[275] At a higher carbonization temperature of 1100 °C, they obtained an optimized highly ordered pseudo-graphic structure having a large interlayer spacing of 0.388 nm, which exhibited promising Na$^+$ insertion performances. On the other hand, Datta et al. reported that the presence of defects enhances the adsorption of Na atoms in graphene sheets.[276] However, such defects of graphene represent a serious drawback such as low Coulombic efficiency that may cause Na metal plating on the rGO surfaces.[255]

3.1.1.4. Heteroatom doping. As an effective strategy to enhance the electrochemical properties of carbonaceous materials as anodes, heteroatom (such as N, B, S and P) doped hard carbon and graphene (or graphene liked materials) are introduced.[277–291] Hetero atom doping into a carbon structure tends to create a defect site to absorb Na$^+$ ions and improves the electrode–electrolyte interaction by functionalizing the carbon surface. Commonly, nitrogen doping into a carbon structure significantly improves ion transport and charge-transfer processes.[279,280] Wang et al. proposed a 3D interconnected structure of free-standing flexible films composed of nitrogen-doped porous nanofibers that exhibited 212 mA h g^{-1} at 5 A g^{-1} with stable capacity retentions of 99% after 7000 cycles[282] (Fig. 23a). In a recent work, sulfur-doped disordered carbon was proposed as an anode material for SIBs. Sulfur doping into the carbon structure provided additional reaction sites for accommodation of Na$^+$ and/or contributing to facile ion diffusion by enlarging the interlayer distance. Li et al. synthesized a sulfur-doped disordered carbon that has a high sulfur doping level (∼26.9%) and a unique 3D coral-like structure. The as-prepared sulfur-doped carbon exhibited a high reversible capacity of 516 mA h g^{-1} with excellent rate capability as well as superior cyclability for 1000 cycles[288] (Fig. 23b).

3.1.1.5. Biomass derivatives. As mentioned above, disordered carbon appears to be the most suitable anode material for SIBs.
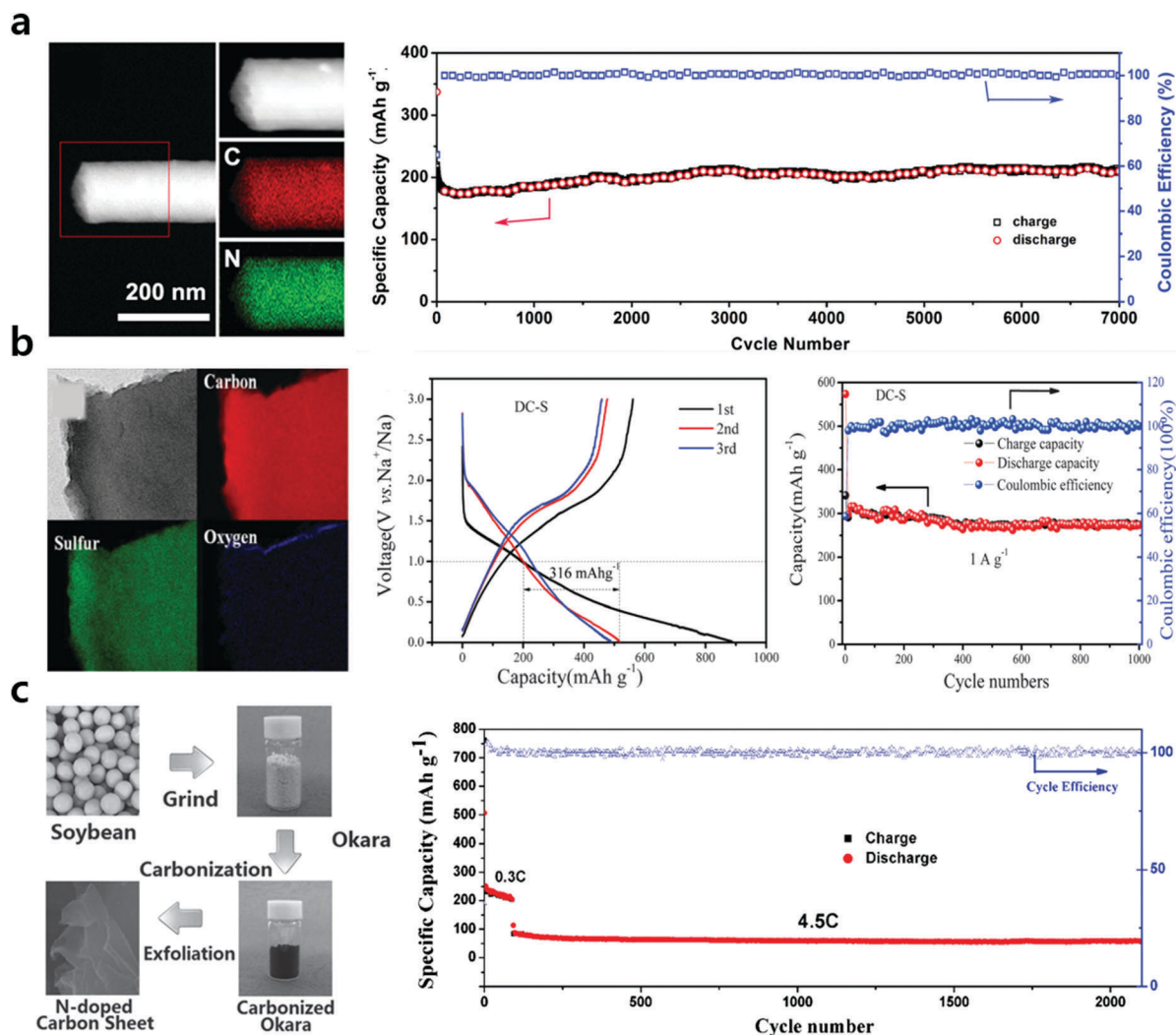
3564 | Chem. Soc. Rev., 2017, 46, 3529–3614

This journal is © The Royal Society of Chemistry 2017

Fig. 23 (a) HAADF image and the elemental mapping of N–CNF (left). Long term cycling performance of N–CNF at a current density of 5 A g^{-1} (right). (Reproduced from ref. 282 with permission, Copyright 2015 Wiley-VCH Verlag GmbH & Co. KGaA.) (b) HR-TEM image and EDS elemental mapping of DC-S (left). Electrochemical performances of DC-S (right). (Reproduced with permission from ref. 288, Copyright 2015 The Royal Society of Chemistry.) (c) The preparation process of NDCS derived from okara (left). High rate capability and long cycling stability of the NDCS at 4.5C for 2000 cycles (right). (Reproduced from ref. 296 with permission, Copyright 2015 Wiley-VCH Verlag GmbH & Co. KGaA.)

Biomass-derived disordered carbon materials have been widely investigated due to their low production cost and low energy consumption during the synthesis procedures.[275,292–297] Wood carbon anodes were derived from natural woods *via* a simple carbonization process, which functions as a binder-free and current collector-free anode material.[292] This material exhibited a high areal capacity of 13.6 mA h cm^{-2} with a high mass loading of 55 mg cm^{-2}. A recent work, reported by Yang *et al.*, showed a sustainable route using a biomass byproduct, okara, as a natural nitrogen fertilizer possessing high content N-doped carbon sheets.[296] Okara was carbonized and exfoliated to expand between carbon sheets that led to a high specific surface area. This benefits facile intercalation and deintercalation of Na$^+$ ions into the carbon structure upon cycling. This unique structure and large surface area were responsible for the high capacity of approximately 292.2 mA h g^{-1} with stable cycling performances for over 2000 cycles (Fig. 23c). From the green and recycle points

of view, using biomass (bio-waste) is of great significance for the future direction of material development.

Such works present that carbonaceous materials exhibit promising Na$^+$ ion storage performances as anodes for SIBs. Notwithstanding, the initial irreversible capacity, limited capacity, poor rate capability, and low mass loading should be resolved for cell balancing for practical battery applications. Herein, we have mentioned few relevant ones and suggest the possible propositions as follows. The irreversible capacity upon the initial cycle is the most critical issue as it severely hindered the practical cell energy density achievable. Attaining an attractive rate capability is another important factor for a practical energy storage system. In addition, tap density is also a crucial parameter determining the volumetric energy density of the cells. The appropriate low pore volumes and surface areas were required for higher reversible capacities. Using suitable electrolytes, additives, and binders is also an effective approach

This journal is © The Royal Society of Chemistry 2017

Chem. Soc. Rev., 2017, **46**, 3529–3614 | 3565

for decreasing the initial irreversible capacity. And morphology and size control is a substantial strategy to facilitate mass transport and storage, which can significantly improve the rate capability. Most of all, for developing practical SIBs using high mass loading electrodes, a comprehensive study of the impact of the electrode thickness on the rate capability, energy and power density and long-term cycling behavior is required.[298]

3.1.2 Titanium based oxides. In general, the low operational potential can cause safety issues for practical applications; such as, metallic sodium plating and sodium dendrite formation on the surfaces of anodes.[241,247,249,250,347] Analogous to LIBs, metal oxide compounds have been studied as Na^+ ion insertion host materials. Titanium-based oxides are particularly interesting as anodes due to their reasonable operation voltage, cost, and nontoxicity;[299,300] representatively, titanium dioxides,[301–333] spinel-lithium titanate,[334–346] and sodium-titanate compounds.[347–364] Note that these compounds are driven by a $Ti^{4+/3+}$ redox couple in Na cells. Recently, most related works have focused on finding the sodiation/desodiation mechanism and improving the electrochemical performance of such materials.

3.1.2.1. Titanium dioxides. The several TiO_2 polymorphs, including anatase-TiO_2,[301–314,316–323] rutile-TiO_2,[324–328] brookite-TiO_2,[329,330,332] and bronze-TiO_2[333] have been investigated as anode materials for SIBs[294–296] (Fig. 24a–d). Among them, most research results were reported using anatase TiO_2 because the activation barrier for Na^+ insertion into the anatase lattice is comparable to that of lithium, which is rather remarkable considering its significantly larger ionic radius.[301–303] Xiong et al. reported the feasibility of electrochemically-grown amorphous titanium dioxide nanotube electrodes in Na cells for the first

time[304] (Fig. 25a). On the other hand, Mattsson et al. claimed that high crystalline and/or micronized TiO_2 cannot easily support Na^+ insertion because of the ionic size of Na^+ and a much higher sodium diffusion barrier compared with Li.[305] Recently, high electrochemical activity of TiO_2 with Na^+ ions was achieved by reducing the particles to the nanometer size for shortening of the migration length for Na^+ insertion. Xu et al. used anatase nanocrystalline TiO_2 for Na^+ storage.[306] Wu et al. interpreted the reaction process during Na^+ insertion and extraction, highlighting the substantial influence of the electrolyte composition (salt and solvent) and cut-off potential[307] (Fig. 25b). Through NMR and electrochemical studies, Gonzalez et al. explained the irreversible process (electrolyte decomposition) up to 0.3 V observed at the first Na^+ insertion process in the TiO_2 electrode.[308] Kim et al. observed that anatase TiO_2 nanorods can be stored in the host structure through the Na^+ insertion and extraction reaction coupled with the Ti^{4+}/Ti^{3+} redox reaction *via ex situ* XRD and XAS studies[309] (Fig. 25c and d). Their carbon coating on the anatase TiO_2 nanorod surface played an important role in improving the capacity and rate capability. Furthermore, they also suggested that the presodiation technique was an effective way to minimize the initial irreversible reaction of the TiO_2 anode. Recently, Passerini's group found that only the (de-)insertion of Na^+ ions in the newly formed amorphous sodium titanate phase appears to be reversible (uptake/release 0.41 Na per TiO_2), while all the other processes (metallic titanium, sodium superoxide, and oxygen evolution) appear to be irreversible (Fig. 25e and f).[310] Usui et al. investigated rutile-TiO_2 that showed the reversible reaction of Na^+ insertion and extraction into and from the crystal lattice of rutile TiO_2[326] (Fig. 26a). In addition, the appropriate amount of Nb doping (0.06 mol%) on rutile TiO_2 materials could substantially improve the electronic conductivity.
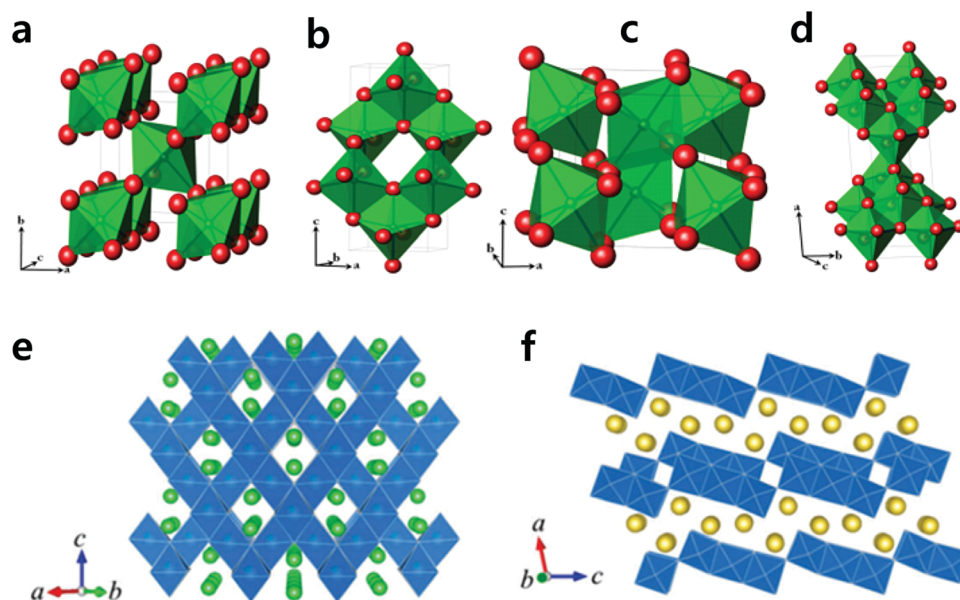
Fig. 24 Crystal structures of TiO_2. (a) Rutile, (b) anatase, (c) bronze, (d) brookite. (Reprinted from ref. 299, Copyright 2015, with permission from Elsevier.) Crystal structures of (e) spinel-type $Li_4Ti_5O_{12}$ and (f) $Na_2Ti_3O_7$. Li and Na atoms are represented by green and yellow spheres, respectively. (Reproduced with permission from ref. 300, Copyright 2016 The Royal Society of Chemistry.)

3566 | Chem. Soc. Rev., 2017, 46, 3529–3614

This journal is © The Royal Society of Chemistry 2017
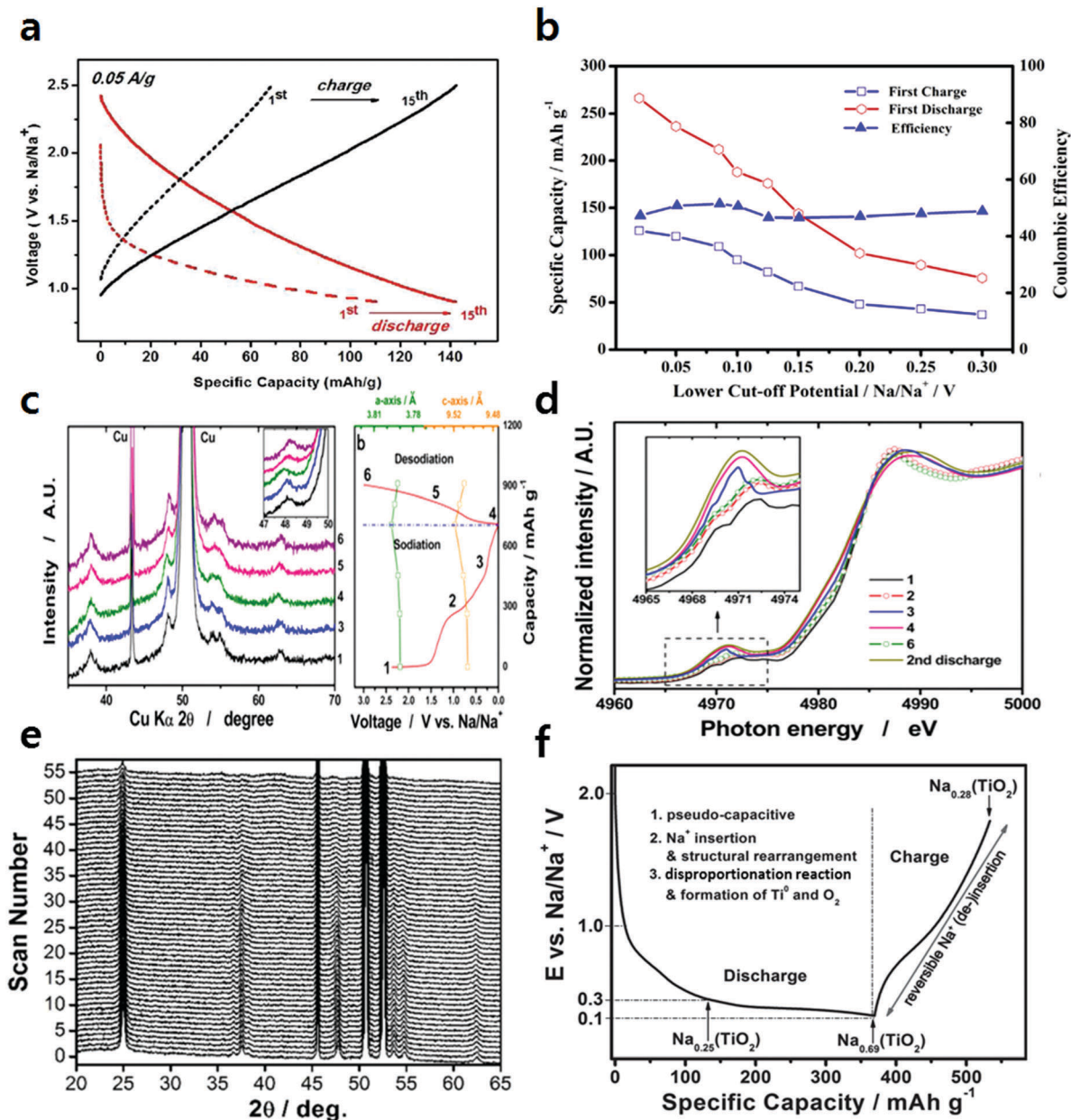
Fig. 25 (a) Charge/discharge galvanostatic curves of amorphous 80 nm I.D. TiO_2NT in Na half cell (red for discharge and black for charge). (Reproduced with permission from ref. 304, Copyright 2011 American Chemical Society.) (b) Galvanostatic investigation of the influence of the lower cut-off potential based on Coulombic efficiency (dis-)charge capacities. (Reprinted from ref. 307, Copyright 2014, with permission from Elsevier.) (c) Ex situ XRD patterns and (d) XANES K-edge spectra of 2.9 wt% carbon-coated anatase nanorod TiO_2. (Reproduced with permission from ref. 309, Copyright 2014 American Chemical Society.) (e) In situ XRD analysis of the (de-)sodiation mechanism of anatase TiO_2 nanoparticles, (f) scheme of the reaction mechanism. (Reproduced from ref. 310 with permission, Copyright 2015 Wiley-VCH Verlag GmbH & Co. KGaA.)

As a result, the $Ti_{0.94}Nb_{0.06}O_2$ electrode exhibited excellent cycling performance with a reversible capacity of 160 mA h g^{-1} at the 50th cycle. Later, Zhang et al. proposed rutile TiO_2 microspheres anchored by nanoneedle clusters, which exhibited a capacity retention of 83.1% after 200 cycles at a current density of 0.1C-rate.[327] Huang et al. found that one of the polymorphs, the low crystalline brookite-TiO_2 was available for Na$^+$ ion storage.[329] Pioneer works of unusual TiO_2 polymorphs, including the brookite-phase, the bronze-phase and their mixture phase, are recently investigated.[330–333]

However, sodium storage of TiO_2 suffers from the sluggish sodium kinetics due to the larger ionic size of Na$^+$ ions. To overcome this drawback, strategies such as the nanoarchitecture modified by metallic Ti and high conductivity carbon additives were introduced.[309,311,328,331] Kim et al. fabricated pitch carbon-coated anatase TiO_2 nanorods, which exhibited a high capacity of 193 mA h g^{-1} and superior rate capability.[309] Recently, Zhang et al. proposed graphene-rich wrapped petal-like rutile TiO_2 tuned by carbon dots, which exhibited the outstanding sodium-storage performances.[328]
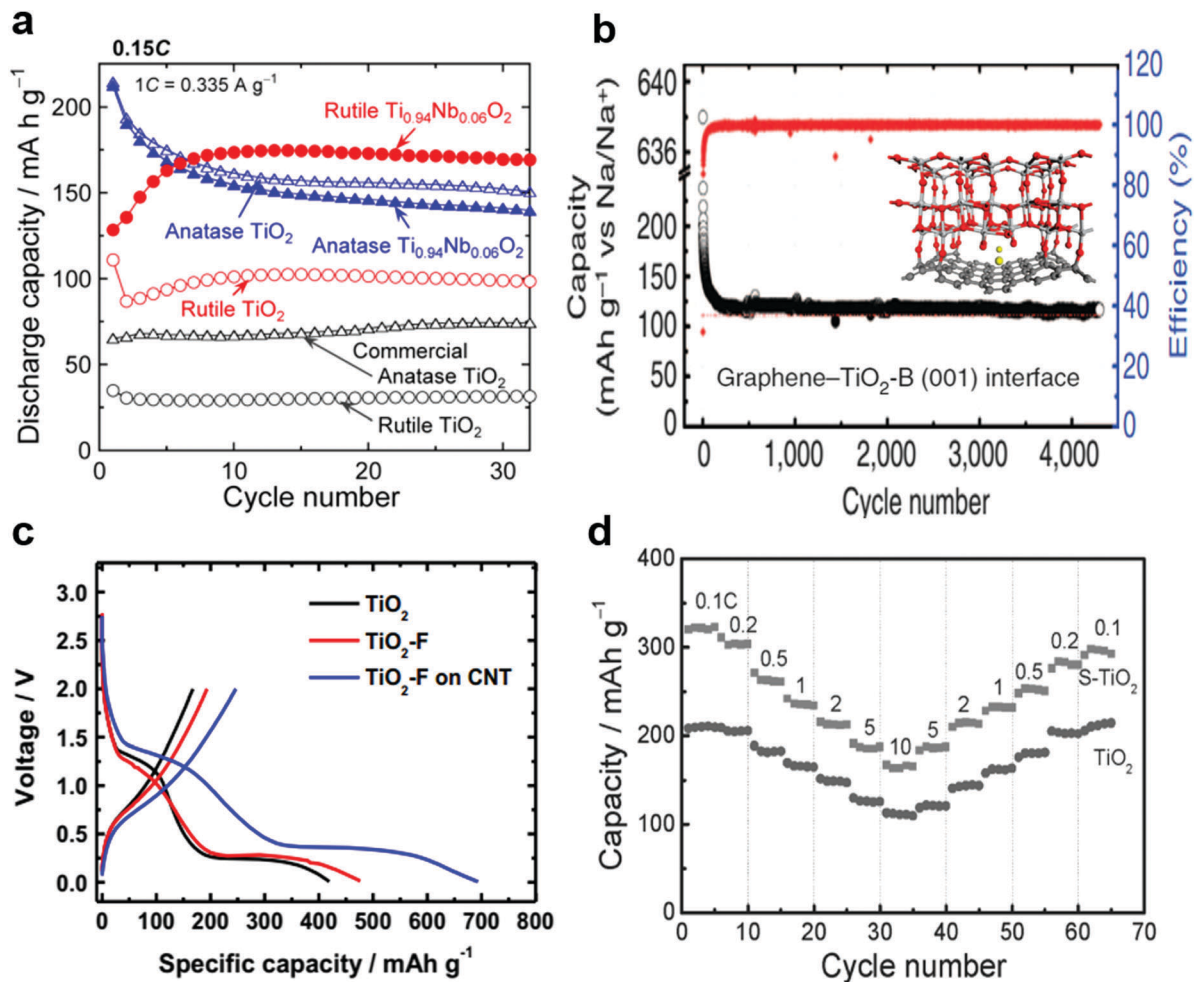
This journal is © The Royal Society of Chemistry 2017

Chem. Soc. Rev., 2017, 46, 3529–3614 | 3567

Fig. 26 (a) Cycling performances of thick-film electrodes consisting of $Ti_{1-x}Nb_xO_2$ with rutile and anatase structure in Na cell. (Reproduced with permission from ref. 326, Copyright 2015 American Chemical Society.) (b) Long-term cycling performance of G–TiO$_2$(B) electrode at a current density of 500 mA g^{-1}. Inset image represent the illustration of partially bonded graphene–TiO$_2$-B (001) interface. (Reproduced by permission from ref. 331, Nature Publishing Group, Copyright 2015.) (c) Charge–discharge voltage curves of TiO$_2$, TiO$_2$-F, and TiO$_2$-F on CNT at 0.1C-rate. (Reprinted from ref. 312, Copyright 2015, with permission from Elsevier.) (d) Rate capability of TiO$_2$ and S-TiO$_2$ at various C-rate. (Reproduced from ref. 323 with permission, Copyright 2016 Wiley-VCH Verlag GmbH & Co. KGaA.)

Chen et al. proposed a chemically bonded graphene (G)–TiO$_2$(B) composite as a long-cycle life material. Kinetics analysis reveals Na$^+$ intercalation pseudo-capacitive behaviour in the G–TiO$_2$ sodium cell, which is highly beneficial to fast charge storage and long-term cyclability[331] (Fig. 26b).

Doping to reduce the average oxidation state of Ti is another interesting strategy to enhance the reversible Na storage performances of TiO$_2$.[312,313,315,323] Hwang et al. reported ultrafast sodium storage performance in fluorine-doped anatase TiO$_2$ nanoparticles embedded on carbon nanotubes[312] (Fig. 26c). Nanosized anatase TiO$_2$ partially doped with fluorine (TiO$_{2-\delta}$F$_\delta$) to form electro-conducting trivalent Ti^{3+} led to facile Na$^+$ insertion into an anatase TiO$_2$ structure. In addition, TiO$_{2-\delta}$F$_\delta$ was modified by electro-conducting carbon nanotubes (CNTs) to further enhance the electric conductivity. Boron doping can also enhance the photocatalytic activity of TiO$_2$ due to or partly due to the formation of Ti^{3+} ions induced by oxygen vacancies which can increase the conductivity of TiO$_2$.[315] Recently, Wang et al. prepared B-doped TiO$_2$ via the facile hydrothermal method and

demonstrated a high reversible capacity of 150 mA h g^{-1} at a high current rate of 2C with stable cycling performance for over 400 cycles.[313] Ni et al. introduced self-supported S-doped TiO$_2$ nanotubes with high electronic conductivity[323] (Fig. 26d). When S is incorporated into TiO$_2$, the S 3p states will be partially delocalized. The S 3p states can contribute to the formation of the valence band, and thus increases the width of the valence band, resulting in a decreased band gap energy (S-TiO$_2$: 2.6 eV, TiO$_2$: 3.0 eV).[334] The high conductivity assisted in decreasing the band gap energy, which enabled delivery of a high capacity of 320 mA h g^{-1} at 33.5 mA g^{-1} with a stable capacity retention of 91% for over 4400 cycles at a high current density of 3.35 A g^{-1}.

3.1.2.2. Lithium titanate.
A spinel Li$_4$Ti$_5$O$_{12}$ has been extensively studied as one of the most promising anode materials for long-life stationary LIBs because it has a flat and high potential around 1.5 V (vs. Li/Li$^+$) during charge and discharge and an excellent cycle life due to the negligible volume change.[335] Recently, Zhao et al. revisited spinel Li$_4$Ti$_5$O$_{12}$ as a Na$^+$ insertion host material for SIBs[300,336]
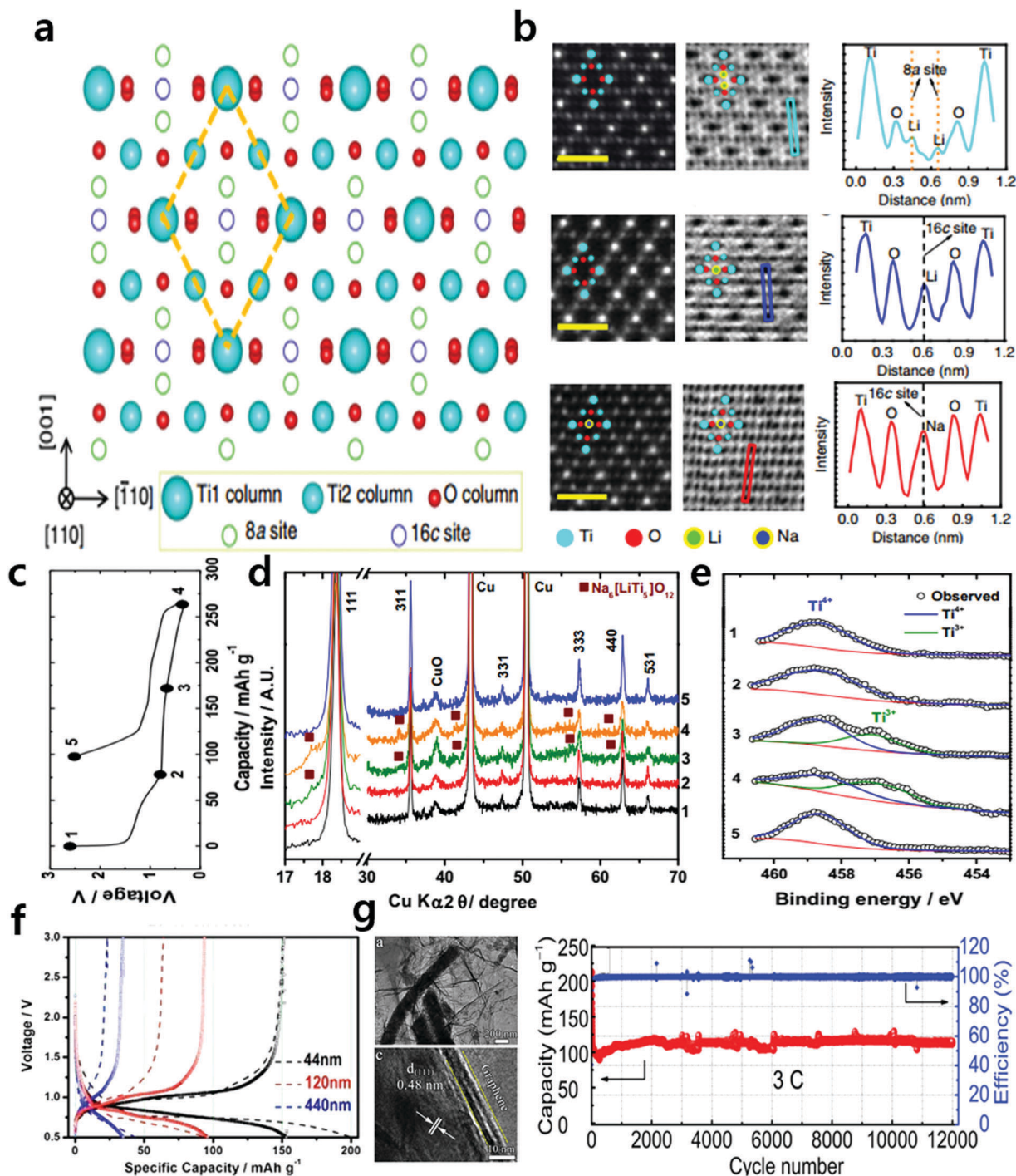
Fig. 27 (a) Crystal structure of spinel $Li_4Ti_5O_{12}$ viewed from the [110] crystallographic direction showing separated Ti and O columns. (b) STEM imaging of a three-phase coexistence region. HAADF, ABF images and ABF line profile of $Li_4Ti_5O_{12}$ (Li4), $Li_7Ti_5O_{12}$ (Li7) and $Na_6LiTi_5O_{12}$ (Na6Li) phase. (Reproduced by permission from ref. 337, Nature Publishing Group, Copyright 2013.) (c) First discharge–charge curve of carbon-coated $Li_4Ti_5O_{12}$ and it indicating the places where *ex situ* XRD and XPS measurements were carried out; (d) *ex situ* XRD patterns (left) and (e) XPS profiles of carbon-coated $Li_4Ti_5O_{12}$ (right). (Reprinted from ref. 339, Copyright 2015, with permission from Elsevier.) (f) The charge–discharge curve of Na storage into the crystallite size distribution of nanosized ($r = 44$ nm, $r = 120$ nm) and submicrosized ($r = 440$ nm) $Li_4Ti_5O_{12}$. (Reproduced with permission from ref. 340, Copyright 2013 American Chemical Society.) (g) TEM, HR-TEM images of G-PLTO (grapheme-wrapped porous $Li_4Ti_5O_{12}$) and long-term cycling performance of G-PLTO at 3C-rate for 12 000 cycles. (Reproduced from ref. 343 with permission, Copyright 2016 Wiley-VCH Verlag GmbH & Co. KGaA.)

(Fig. 24e). A reversible capacity of 145 mA h g^{-1} was delivered with a relatively low insertion/extraction potential of 1.0 V. Also, they suggested an unexpected mechanism with a mixture of $LiNa_6Ti_5O_{12}$ and $Li_7Ti_5O_{12}$ as the final product after Na$^+$ insertion. Later, Sun *et al.* precisely interpreted the Na$^+$ insertion behavior *via* DFT calculations and advanced electron microscopy[337] (Fig. 27a and b).

This journal is © The Royal Society of Chemistry 2017

Chem. Soc. Rev., 2017, **46**, 3529–3614 | **3569**

They also improved the electrochemical properties of $Li_4Ti_5O_{12}$ by varying the electrolyte and binders. Usually, for LIBs, Li^+ insertion into the $Li_4Ti_5O_{12}$ anode occurs through a two-phase reaction between spinel $Li_4Ti_5O_{12}$ and rock-salt $Li_7Ti_5O_{12}$. In Na cells, Na^+ insertion into $Li_4Ti_5O_{12}$ results in a three-phase reaction. Due to the different ionic sizes of Li^+ and Na^+, the Na^+ ions are favorably occupied in the 16c site of the $Li_4Ti_5O_{12}$ lattice, and they simultaneously induce phase separation into two rock-salt phases of $LiNa_6Ti_5O_{12}$ and $Li_7Ti_5O_{12}$ as follows: $2Li_4Ti_5O_{12} + 6Na^+ + 6e^- \leftrightarrow Li_7Ti_5O_{12} + Na_6LiTi_5O_{12}$. Later, Kim *et al.* observed the structural evolution and the chemical state of Ti at the initial cycle based on *ex situ* XRD and XPS measurements[339] (Fig. 27c–e). Yu *et al.* observed three phase transition behavior of $Li_4Ti_5O_{12}$ during Na^+ insertion through *in situ* X-ray diffraction. They also investigated a size-dependent sodium storage mechanism in $Li_4Ti_5O_{12}$.[340] For 440 nm size $Li_4Ti_5O_{12}$, only a small amount of Na can be inserted ($0.27Na^+$ per formula unit of $Li_4Ti_5O_{12}$), which corresponds to a specific capacity of 16 mA h g^{-1}. While the degree of the reversible Na^+ insertion into 44 nm size $Li_4Ti_5O_{12}$ was greatly increased ($3Na^+$ ion per formula unit of $Li_4Ti_5O_{12}$) and nearly reached its theoretical capacity of 175 mA h g^{-1} (Fig. 27f). They claimed that downsizing the Na^+ host structure of $Li_4Ti_5O_{12}$ is a crucial factor to improve the sluggish Na^+ ion diffusion kinetics. Analogous to this scenario, Hasegawa *et al.* reported nanosized $Li_4Ti_5O_{12}$ materials with hierarchically porous structures and flower-like morphologies.[341] According to their reports, Na^+ insertion/extraction capability is strongly dependent on their nanoarchitectural design and calcination temperature. These nanostructured $Li_4Ti_5O_{12}$ electrodes calcined at 700 °C displayed a flower-like porous structure and exhibited a remarkably high rate performance of 146 mA h g^{-1} and 105 mA h g^{-1} at 10C and 30C-rates, respectively, even without carbon-coating. On the other hand, Yu *et al.* reported Na^+ ion transport kinetics and coupled pseudocapacitive charge in thin film $Li_4Ti_5O_{12}$ electrodes.[342] The synergistic effect of typical Na^+ insertion and the extra pseudocapacitive charge storage produced an unexpected high capacity of 225 mA h g^{-1} in thin film $Li_4Ti_5O_{12}$ electrodes. They claimed that the pseudocapacitance effect on a typical insertion electrode is a potential solution to overcome the capacity limit for Na^+ insertion anodes.

Another approach to improve the electrochemical performances is combining carbon additives with $Li_4Ti_5O_{12}$ materials. Kim *et al.* proposed pitch carbon-coated $Li_4Ti_5O_{12}$ nanowires, which significantly increased the electronic conductivity and delivered a high capacity of 168 mA h g^{-1} at 0.2C-rate.[339] Chen *et al.* fabricated porous $Li_4Ti_5O_{12}$ nanofibers confined in a highly conductive 3D-interconnected graphene framework for SIB anodes[343] (Fig. 27g). This unique structure of porous $Li_4Ti_5O_{12}$ nanofibers wrapped with 3D graphene offers not only short pathways for Na^+ diffusion and highly conductive networks for electron transport but also abundant $Li_4Ti_5O_{12}$–electrolyte (solid–liquid) and $Li_4Ti_5O_{12}$–graphene (solid–solid) interfacial sites for Na^+ adsorption, giving rise to additional interfacial Na^+ storage, a high reversible capacity of 195 mA h g^{-1} at a 0.2C-rate (exceeding the theoretical capacity based on the Na^+ insertion reaction) and a long cycle life of 12 000 cycles.

3.1.2.3. Sodium titanate. The $Na_2Ti_3O_7$ structure has been most investigated as a promising anode with the lowest operating potential for SIBs[347–353] (Fig. 24f). Senguttuvan *et al.* firstly reported that sodium titanate, $Na_2Ti_3O_7$, can reversibly uptake 2 mol of Na^+ ions per formula unit with a low operating potential plateau at 0.3 V *vs.* Na/Na^+[347] (Fig. 28a). A plateau with this voltage can be quite advantageous in a full cell with a suitable cathode in terms of energy density compared to the other oxide type anodes. Typical voltage profiles of carbon black and a composite of $Na_2Ti_3O_7$ with carbon black indicated an irreversible electrochemical process at *ca.* 0.7 V *vs.* Na/Na^+, which corresponds to the reaction of carbon black and a reversible plateau around 0.3 V *vs.* Na/Na^+ with concomitant intercalation of additional $2Na^+$ ions in the structure. Xu *et al.* reported the computational and experimental results for an in-depth understanding of the sodium storage mechanism of the $Na_2Ti_3O_7$ structure.[348] Based on the calculations of the electrostatic interaction in the crystal structure, 2 mol of Na^+ ions are intercalated into the $Na_2Ti_3O_7$ structure to form $Na_4Ti_3O_7$ producing strong electrostatic repulsion, leading to structural instability and low operating voltage. Also, this strong electrostatic repulsion in the fully sodiated state induces the self-relaxation phenomena. In addition, they observed the Ti^{4+}/Ti^{3+} redox couple upon cycling *via* the XAS technique (Fig. 28b). Furthermore, their carbon-coated $Na_2Ti_3O_7$ electrodes delivered a theoretical capacity of 177 mA h g^{-1} (corresponding to uptake of 2 Na^+ ions per $Na_4Ti_3O_7$).

Rudola *et al.* investigated the physicochemical and electrochemical properties of $Na_2Ti_3O_7$ and calculated the diffusion coefficient of Na^+ ions in the $Na_2Ti_3O_7$/CB electrode.[349] Later, Rudola *et al.* observed the intermediate phase of $Na_{3-x}Ti_3O_7$ during the sodiation/desodiation process[350] (Fig. 28c). During the sodiation process, based on the *ex situ* XRD results, two discharge plateaus revealed the following two phase reactions: $Na_2Ti_3O_7 \rightarrow Na_{3-x}Ti_3O_7$ (black curve in Fig. 28c) and $Na_{3-x}Ti_3O_7 \rightarrow Na_4Ti_3O_7$ (red curve in Fig. 28c). The lower discharge plateau causes an irreversible transformation that leads to the loss of the sodium storage pathway in subsequent cycles. By controlling the cut-off potential from 0.01–2.5 V (with low plateaus) to 0.155–2.5 V (without low plateaus), the $Na_2Ti_3O_7 \leftrightarrows Na_{3-x}Ti_3O_7$ pathway has the lowest redox voltage of 0.2 V *vs.* Na/Na^+ with a moderate capacity of 89 mA h g^{-1}. In addition, it showed excellent rate performance up to 80C-rate and a good cycle life for over 1500 cycles. On the other hand, Pan *et al.* observed that nanosized $Na_2Ti_3O_7$ intermediate phase is avoided and $Na_4Ti_3O_7$ directly translates to $Na_2Ti_3O_7$ during the Na^+ extraction process.[351] They also discussed two main reasons for the low Coulombic efficiency and continuous capacity fading of the $Na_2Ti_3O_7$ electrode: (i) partial decomposition on the $Na_2Ti_3O_7$ particle surface (instability of the SEI layer) and (ii) structural distortion upon Na^+ insertion/extraction. Later, Muñoz-Márquez *et al.* observed the instability of SEI formation during the charge process and precisely investigated the composition and evolution of the solid–electrolyte interphase in $Na_2Ti_3O_7$ electrodes.[352] Although $Na_2Ti_3O_7$ is considered as a promising anode with the lowest operating potential for

3570 | *Chem. Soc. Rev.*, 2017, **46**, 3529–3614

This journal is © The Royal Society of Chemistry 2017
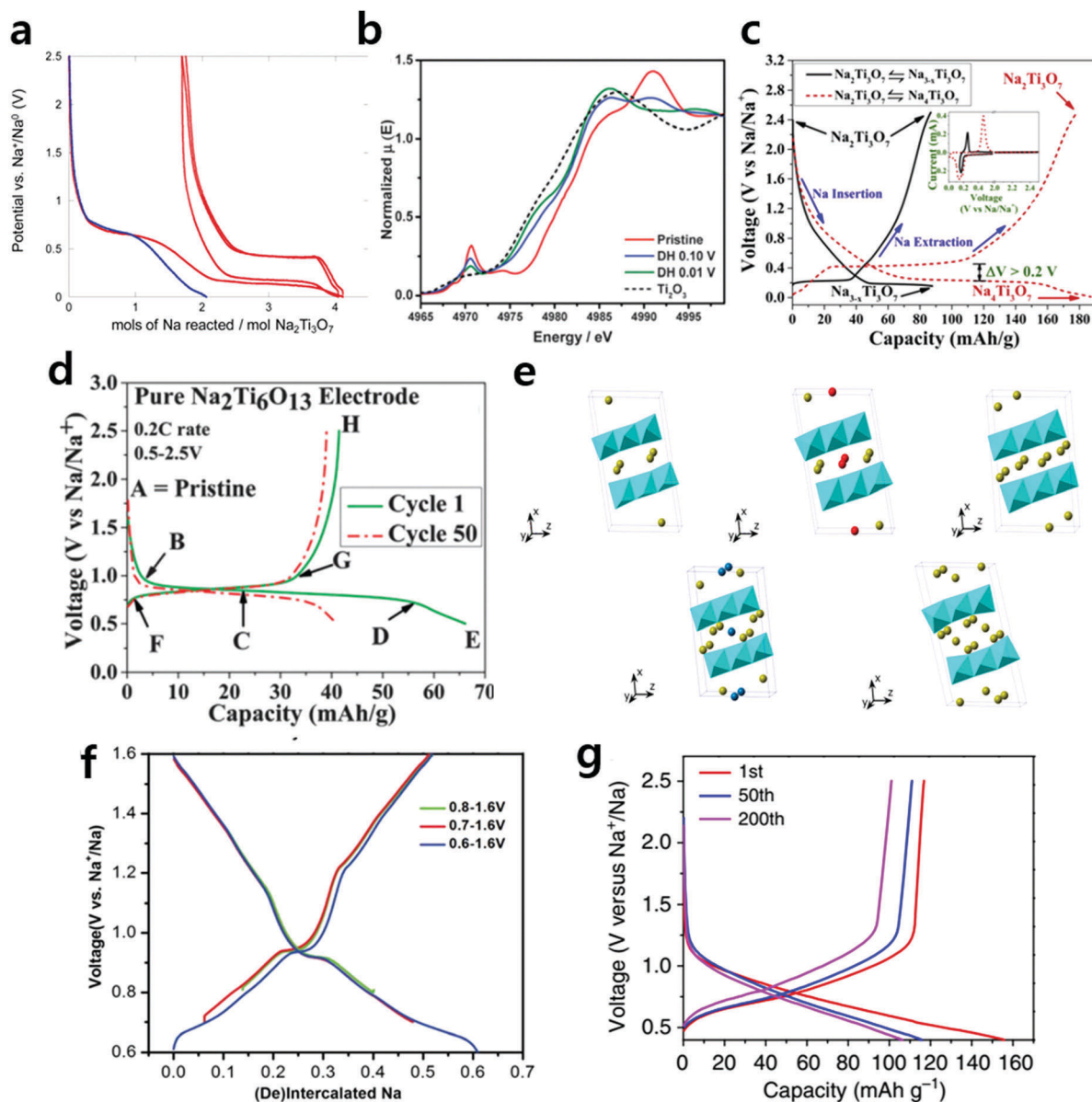
Fig. 28 (a) Voltage *versus* composition profile for the electrochemical reduction of carbon black (blue curve) and composite electrodes containing $Na_2Ti_3O_7$ and 30% carbon black (red curve). (Reproduced with permission from ref. 347, Copyright 2011 American Chemical Society.) (b) Normalized Ti K-edge XANES for $Na_2Ti_3O_7$ at pristine state (red), after discharged to 0.10 V (blue), and after discharged to 0.01 V (green). (Reproduced with permission from ref. 348, Copyright 2014 The Royal Society of Chemistry.) (c) Representative C/5 cycling of $Na_2Ti_3O_7 \leftrightarrows Na_{3-x}Ti_3O_7$ and $Na_2Ti_3O_7 \leftrightarrows Na_4Ti_3O_7$ pathways. (Reprinted from ref. 350, Copyright 2015, with permission from Elsevier.) (d) Charge–discharge curves of $Na_2Ti_6O_{13}$ at 0.2C-rate in the voltage range of 0.5–2.5 V *vs.* Na/ Na^+. (Reproduced with permission from ref. 355, Copyright 2013 The Royal Society of Chemistry.) (e) Crystal structure change at different Na^+ insertion into the $Na_{2+4}Ti_6O_{13}$ structure based on the DFT calculations. (Reproduced with permission from ref. 356, Copyright 2015 American Chemical Society.) (f) Comparison of the amount of cycled Na in voltage windows with lower cut-off voltages from 0.6–0.8 V. (Reproduced with permission from ref. 361, Copyright 2015 The Royal Society of Chemistry.) (g) The 1st, 50th and 200th discharge/charge curves at a current rate of C/10 (10.6 mA g^{-1}) in the voltage range of 0.4 and 2.5 V *versus* Na^+/Na. (Reproduced by permission from ref. 362, Nature Publishing Group, Copyright 2013.)

Na-ion batteries, poor capacity retention remains the serious drawback. Therefore, further investigation including reducing the catalytic activity of Na^+ ions with titanium and application of protective coating of active materials should be conducted to improve the electrochemical performances of $Na_2Ti_3O_7$ electrodes.

Other types of sodium titanates were also widely studied as potential anodes for SIBs.[354–364] Trinh *et al.* reported reversible electrochemical activity of $Na_2Ti_6O_{13}$ in sodium cells with less

than half a mole of sodium per formula unit.[354] Based on the *ex situ* XRD measurements in the voltage range of 0.5–2.5 V, Rudola *et al.* reported the sodium insertion/extraction mechanism of $Na_2Ti_6O_{13}$ as follows: $Na_2Ti_6O_{13} + xNa^+ + xe^- \leftrightarrow Na_{2+x}Ti_6O_{13}$ with x = 0.85.[355] Later, Shen *et al.* show that the capacity of the $Na_2Ti_6O_{13}$ anode material can be enhanced from 49.5 mA h g^{-1} ($Na_{2+1}Ti_6O_{13}$) to 196 mA h g^{-1} ($Na_{2+4}Ti_6O_{13}$) by lowering the cutoff voltage from 0.3 to 0 V.[356] Simultaneously with experimental works,

Shen et al. predicted the structure and average voltage change of reduced phases at various compositions of $Na_{2+x}Ti_6O_{13}$ ($x = 0$–4) by using density functional theory (DFT) calculations (Fig. 28e). Shirpour et al. suggested layered sodium titanate, structurally identical to sodium nonatitanate, which was capable of reversibly intercalating Na^+ ions at a low potential of about 0.3 V vs. Na/Na^+.[357] During the discharge process, typical voltage curves of a dehydrated nonatitanate electrode had a reversible capacity of 125 mA h g^{-1} at 30 mA g^{-1} accompanied by irreversible decomposition of the electrolyte which includes formation of a SEI layer in the voltage range of 0.3–0.9 V similar to the other titanium-based oxides.

The sodium titanate form of $Na_4Ti_5O_{12}$ has been investigated as the two crystal structures of trigonal $Na_4Ti_5O_{12}$ (T-$Na_4Ti_5O_{12}$) and monoclinic $Na_4Ti_5O_{12}$ (M-$Na_4Ti_5O_{12}$) by Woo et al. and Naeyaert et al., respectively.[358,359] T-$Na_4Ti_5O_{12}$ has a tunnel-structured three-dimensional framework, whereas M-$Na_4Ti_5O_{12}$ has a quasi-2D layered structure. Both electrodes can incorporate intercalated Na^+ ions into their structures, however, 2D channels with partially occupied Na sites, providing broader pathways, can deliver higher reversible capacity than T-$Na_4Ti_5O_{12}$. The tunnel structured sodium titanate form of $Na_2Ti_7O_{15}$ was also investigated as a possible Na^+ insertion host material for SIBs anodes. Li et al. proposed $Na_2Ti_7O_{15}$ nanotubes on the Ti net substrate, which exhibited a high reversible capacity of 258 mA h g^{-1} at 50 mA g^{-1} and an excellent capacity retention of 96% after 200 cycles at 1.0 A g^{-1}.[364]

Recently, as promising anode materials, layered structured sodium titanate compounds of O3-NaTiO$_2$ and P2-$Na_{0.66}[Li_{0.22}Ti_{0.78}]O_2$ were introduced.[360–362] Through the in situ X-ray diffraction studies, Wu et al. demonstrated the reversible O3–O$'$3 phase transition of O3-NaTiO$_2$ and proposed the Na^+ insertion/extraction mechanism (Fig. 28f). In an optimal voltage window of 0–1.6 V, approximately 0.5 mol of Na^+ can be reversibly intercalated in NaTiO$_2$, showing a reversible capacity of 152 mA h g^{-1} and stable cycle retention after 60 cycles.[361] For P2-$Na_{0.66}[Li_{0.22}Ti_{0.78}]O_2$, a reversible capacity of 116 mA h g^{-1} was delivered at an average storage voltage of 0.75 V[362] (Fig. 28g). In addition, it exhibited zero strain characteristics of only $\sim$0.77% volume change during sodium insertion–extraction, ensuring a potentially long cycle life for over 1200 cycles.

3.2 Conversion materials

Some kinds of transition metal oxide (TMO),[365–399] transition metal sulfide (TMS)[400–454] and transition metal phosphide (TMP)[455–466] compounds can adopt Na^+ ions through conversion reactions. Unlike intercalation and alloying reactions, where metal atoms are reversibly shuttled in and out of a host lattice, conversion reactions involve the chemical transformation of one or more of the atomic species into a host lattice to form a new compound.[426] Depending on the transition metal, insertion–extraction or alloying–dealloying was combined with conversion reactions. Analogous to the reaction in LIBs, conversion materials have been considered as potential anode materials for SIBs due to their high theoretical specific capacities.

However, large volume expansion/contraction upon the sodiation–desodiation process accelerated tremendous damage of electrodes, which led to the loss of electrical contact and subsequently rapid capacity fading. Moreover, sluggish mobility of Na^+ ions due to the large ionic size (1.02 Å) is still a challenge to fully utilize their theoretical capacity. In recent years, to deal with such problems, strategies such as advances in the nanotechnology and/or carbon-conducting technique have been introduced, facilitating the development of high performance conversion materials as anodes for SIBs. In this section, the recent research achievements for transition metal oxides, transition metal sulfides and transition metal phosphide as Na conversion hosts are summarized and discussed.

3.2.1 Transition metal oxide (TMO) based anode materials. Alcantara et al. first introduced the conversion material concept by using NiCo$_2$O$_4$ spinel oxide as an anode material for SIBs[365] (Fig. 29a). Alcantara et al. described a reversible conversion reaction of sodium with a metal oxide in which Na$_2$O and metals are formed: NiCo$_2$O$_4$ + 8Na → Ni + 2Co + 4Na$_2$O. Subsequent to this work, many research groups have proposed various transition metal oxides (TMOs) such as iron oxide (Fe$_3$O$_4$, Fe$_2$O$_3$),[366–377] cobalt oxide (Co$_3$O$_4$),[378–382] tin (di)oxide (SnO, SnO$_2$),[383–390] copper oxide (CuO),[391–396] molybdenum oxide (MoO$_2$),[397] nickel oxide (NiO, NiO/Ni),[398,399] and manganese oxide (Mn$_3$O$_4$).[398]

3.2.1.1. Iron oxides (Fe$_3$O$_4$, Fe$_2$O$_3$). Komaba et al. reported applicability of Fe$_3$O$_4$ in Na batteries through the insertion reaction in the voltage range of 1.2–4.0 V.[366] Recently, Hariharan et al. proposed the possibility of Fe$_3$O$_4$ materials in the conversion reaction mechanism with Na^+ ions at a discharge voltage of 0.04 V: Fe$_3$O$_4$ + 8e$^-$ + 8Na$^+$ ↔ 3Fe + 4Na$_2$O.[367] Through the conversion reaction, a discharge capacity of 643 mA h g^{-1} was delivered during the initial cycles with a high Coulombic efficiency of 57%. Oh et al. suggested pitch carbon as a coating additive for nano-sized Fe$_3$O$_4$ (Fig. 29b). Oh et al. also observed the conversion reaction of the C/Fe$_3$O$_4$ electrode upon the sodiation–desodiation process[51] (Fig. 29c). To further ensure electric conductivity, Park et al. introduced a composite of C/Fe$_3$O$_4$ embedded on carbon nanotubes, which delivered 440 mA h g^{-1} for the first discharge and 321 mA h g^{-1} for the first charge with a high Coulombic efficiency of 73%.[368] More recently, Liu et al. synthesized extremely small Fe$_3$O$_4$ quantum dots on hybrid carbon nanosheets, which demonstrated a high capacity of 416 mA h g^{-1} at 0.1 A g^{-1} and a superior cycle retention of 70% for 1000 cycles at 1.0 A g^{-1}.[369] Fe$_2$O$_3$ has also been considered to be a promising electrode material for SIBs due to its excellent chemical stability, high capacity, easy fabrication, low cost and nontoxicity.[373–377] Similar to Fe$_3$O$_4$ materials, sodium storage in Fe$_2$O$_3$ is mainly achieved via a reversible conversion reaction, by forming Fe nanoparticles dispersed in the Na$_2$O matrix.

3.2.1.2. Cobalt oxides (Co$_3$O$_4$). Rahman et al. proposed the reversible conversion reaction mechanism of Co$_3$O$_4$ with sodium ion via cyclic voltammogram and ex situ XRD analyses: Co$_3$O$_4$ + 8Na$^+$ + 8e$^-$ ↔ 4Na$_2$O + 3Co.[378] Based on the XRD

3572 | Chem. Soc. Rev., 2017, **46**, 3529–3614

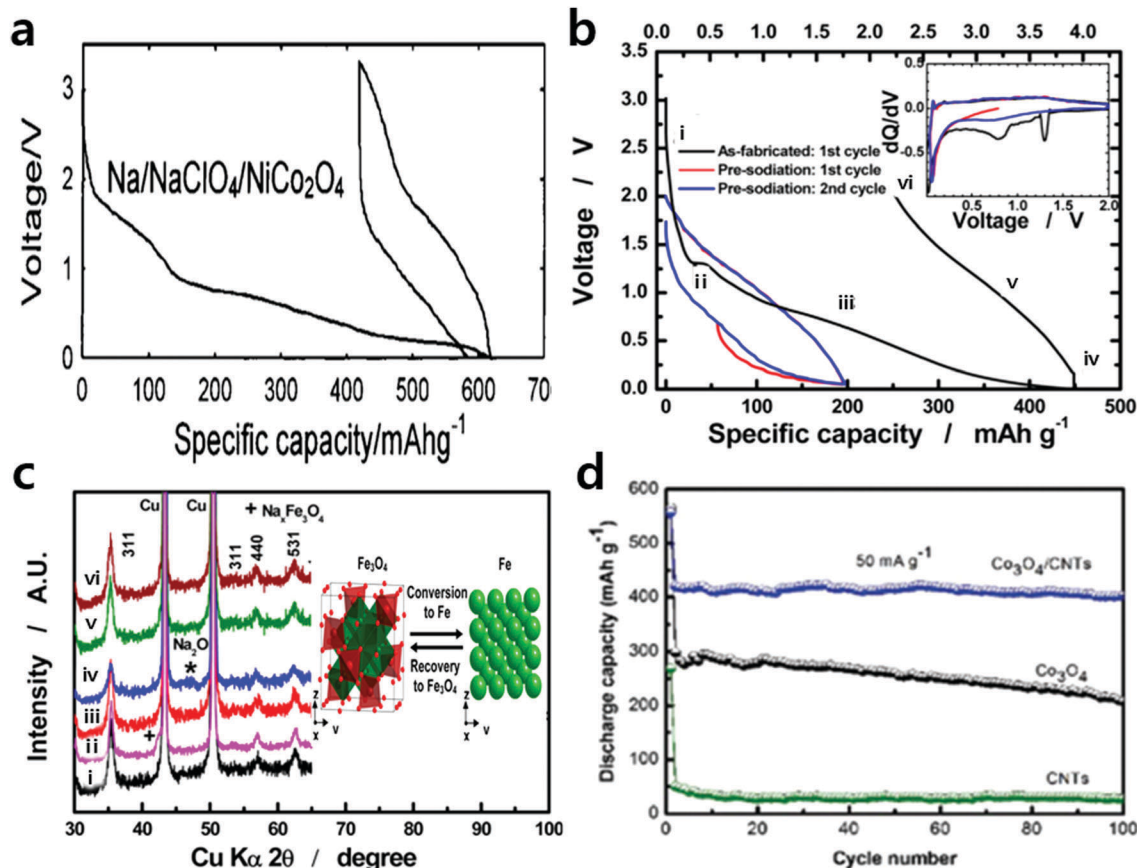This journal is © The Royal Society of Chemistry 2017

Fig. 29 (a) Voltage profile of $Na/NaClO_4(EC:DMC)/NiCo_2O_4$ cell between 3.3 and 0.01 V. (Reproduced with permission from ref. 365, Copyright 2002 American Chemical Society.) (b) The first charge–discharge cycle of a $Na/C–Fe_3O_4$ cell at a constant current density of 20 mA g^{-1} (0.1C-rate, 0–2 V) and related differential capacity curves (inset). (c) *Ex situ* XRD analysis of the $C-Fe_3O_4$ electrode at different discharging and charging state in (b) and scheme of the electrochemical process of the $C-Fe_3O_4$ cell. (Reproduced with permission from ref. 51, Copyright 2014 American Chemical Society.) (d) Cycling performance of CNTs, Co_3O_4 and $Co_3O_4/CNTs$ electrodes. (Reproduced with permission from ref. 379, Copyright 2015 The Royal Society of Chemistry.)

results of the first cycle and after 20 cycles, Rahman *et al.* suggested that the conversion reaction is not completed in the first discharge to 0.01 V, and the conversion reaction tends to continuously occur during further cycling. Following the conversion reaction, a reversible capacity of 447 mA h g^{-1} and ~86% capacity retention were demonstrated after 50 cycles. Later, to improve the electrochemical performances of Co_3O_4, Rahman *et al.* fabricated a carbon composite architecture of $Co_3O_4/CNTs$ by combining a molten salt precipitation process and liquid plasma.[379] CNTs as carbon additives in this composite anode provided several advantages during the sodiation–desodiation process: (1) significantly decreases the absolute stress/strain, (2) accommodates a large volume change and prevents aggregation, (3) its CNT matrix provides electronic conductivity and stability, and (4) reduces the ion or electron transfer time. The results showed a high capacity of 403 mA h g^{-1} at 50 mA g^{-1} and a superior rate capability of 190 mA h g^{-1} at 3.2 A g^{-1} (Fig. 29d).

3.2.1.3. Tin oxides. Recently, various nanostructured tin-based oxide (SnO, SnO_2) materials and their composites have been proposed.[383–390] Gu *et al.* visualized the sodiation–desodiation

process and investigated the failure mechanism of SnO_2 nano-wire anodes *via* an *in situ* TEM technique[383] (Fig. 30a). At the initial stage of the Na insertion process into SnO_2, a displacement reaction occurs, leading to the formation of amorphous Na_xSn nanoparticles dispersed in the Na_2O matrix. Further sodiation led to crystallization to $Na_{15}Sn_4$ ($x = 3.75$) from Na_xSn. At this stage, the nanowire experiences a huge volume expansion from 67 to 145 nm in diameter with the sodiation. Upon desodiation, Na_xSn transforms into Sn nanoparticles. Associated with dealloying, pores are formed, leading to a structure of Sn particles confined in a hollow matrix of Na_2O. These pores greatly increase electric impedance, therefore accounting for the poor cyclability of SnO_2. Later, Lu *et al.* investigated the electrochemical properties and the sodium storage mechanism of SnO and SnO_2 materials[386] (Fig. 30b). Based on *ex situ* XRD analysis and SAED pattern results, they confirmed that SnO and SnO_2 are able to store sodium in their structure through the combined conversion and alloying reactions: (1) SnO → SnO + 2Na^+ + 2e^- ↔ Sn + Na_2O, Sn + Na_2O + xNa^+ + xe^- ↔ Na_xSn + Na_2O, (2) SnO_2 → SnO_2 + 4Na^+ + 4e^- ↔ Sn + 2Na_2O, Sn + 2Na_2O + xNa^+ + xe^- ↔ Na_xSn + 2Na_2O (Fig. 30c). According to their report, low oxygen contents of
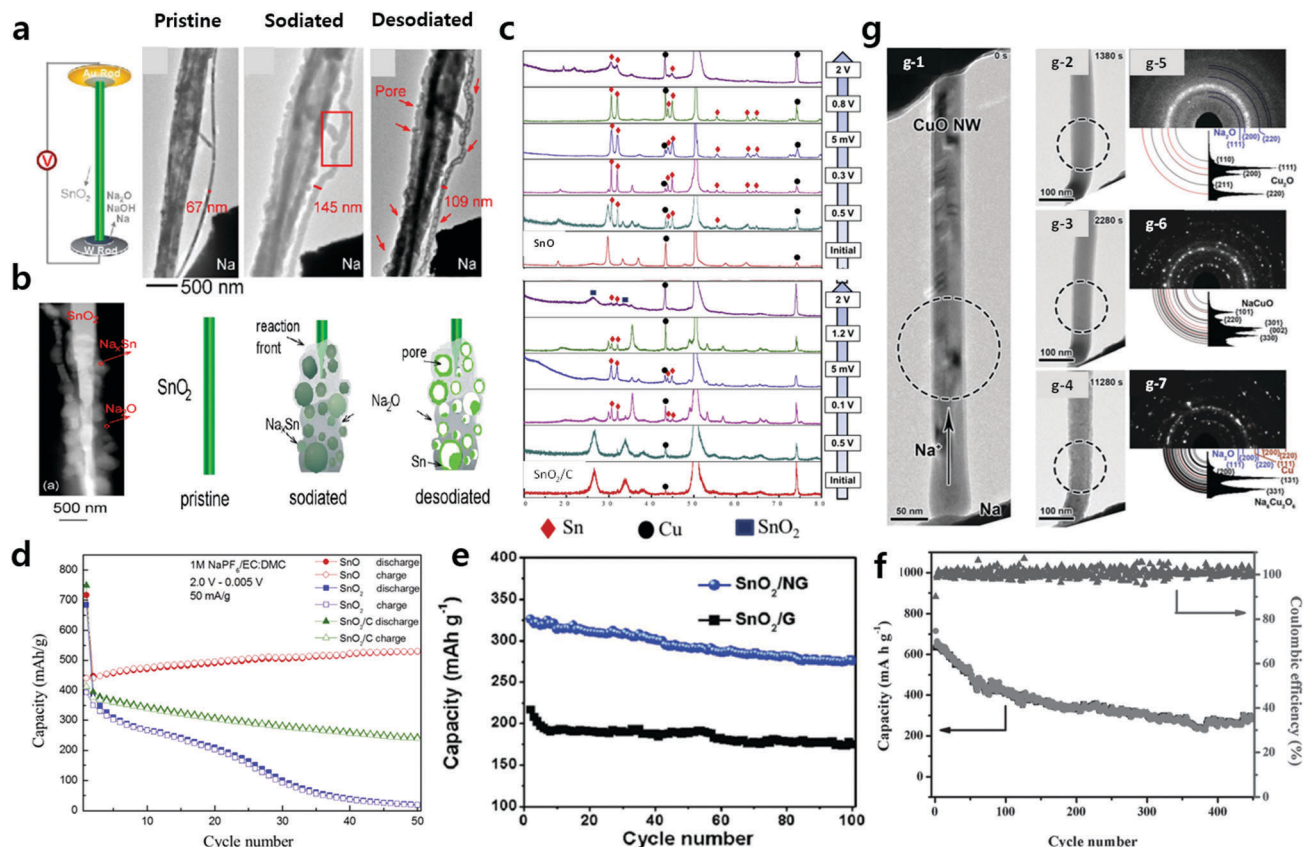
Fig. 30 (a) TEM images of pristine, sodiated, and desodiated states of SnO_2 nanowire. (b) STEM Z-contrast image showing the reaction front of the SnO_2 nanowire (left) and schematic drawing showing the morphology evolution of the SnO_2 nanowire upon Na insertion and extraction (right). (Reproduced with permission from ref. 383, Copyright 2013 American Chemical Society.) (c) *Ex situ* XRD profiles of SnO (top) and SnO_2/C (bottom) electrodes over the first charge/discharge cycle. (d) Cycle life of SnO, SnO_2, and SnO_2/C electrodes. (Reprinted from ref. 386, Copyright 2015, with permission from Elsevier.) (e) Cycling performance of SnO_2/NG and SnO_2/G composites at a current density of 20 mA g^{-1}. (Reproduced with permission from ref. 390, Copyright 2015 The Royal Society of Chemistry.) (f) Cycling performance of the binder-free CuO nanorod array (CAN) electrode at a high current density of 200 mA g^{-1}. (Reproduced from ref. 392 with permission, Copyright 2014 Wiley-VCH Verlag GmbH & Co. KGaA.) (g) *In situ* observation of the sodiation process in CuO nanowires using TEM. (Reproduced with permission from ref. 394, Copyright 2015 The Royal Society of Chemistry.)

SnO showed better electrochemical performances, which implies that the Sn : O ratio and the respective Sn : Na_2O ratio in the converted electrode play important roles in delivering the capacity (Fig. 30d). Recently, a strategy to overcome such failures and maximize the utilization of the high theoretical capacity of SnO_2 ($\sim$782 mA h g^{-1}) has been introduced such as composite anodes with porous carbon, MWCNTs, and graphene.[384–390] Xie *et al.* synthesized SnO_2 with nitrogen-doped graphene nanohybrids *via* an *in situ* hydrothermal method and this composite anode delivered an initial reversible capacity of 339 mA h g^{-1} at 20 mA g^{-1} and excellent capacity retentions even at a high current density of 640 mA g^{-1} [390] (Fig. 30e).

3.2.1.4. Copper oxide. Copper-based oxide materials have also been proposed due to the Earth's abundant distribution, chemical stability, and high theoretical capacity.[391–396] Klein *et al.* reported that Cu_2O can be applicable and thereby exhibited a high capacity of $\sim$600 mA h g^{-1} at 0.1C.[243] Yuan *et al.* proposed flexible and porous CuO nanorod arrays by engraving Cu foils. The arrays delivered a high specific capacity of 640 mA h g^{-1} at 20 mA g^{-1}

and good cycle retentions over 400 cycles[392] (Fig. 30f). Liu *et al.* demonstrated the morphology change and phase transformations in CuO nanowires during the sodiation process. And, based on the *in situ* TEM results, Liu *et al.* suggested detailed conversion mechanisms as follows: $2CuO + 2Na^+ + 2e^- \rightarrow Cu_2O + Na_2O$, $Cu_2O + Na_2O \rightarrow NaCuO$, $7NaCuO + Na^+ + 2e^- \rightarrow Na_6Cu_2O_6 + Na_2O + 5Cu$[394] (Fig. 30g). However, similar to the other metal oxides, Cu-based oxides are still hindered by a large volume change during cycling. Recently, to enhance the electronic conductivity and the accommodation of volume variation upon cycling, Lu *et al.* proposed the micro-nanostructured CuO/C spheres. The as-prepared CuO/C spheres exhibited a high capacity of 402 mA h g^{-1} after 600 cycles at a current density of 200 mA g^{-1} and superior rate capabilities.[395]

3.2.2 Transition metal sulfide (TMS) based anode materials. Transition metal sulfide (TMS) materials have attracted tremendous attention as promising sodium storage materials with high theoretical capacity through electrochemical conversion reactions as well as use of transition metal oxides. In addition, compared to related transition metal oxides, transition metal

3574 | *Chem. Soc. Rev.*, 2017, **46**, 3529–3614

This journal is © The Royal Society of Chemistry 2017

sulfides have great advantages during the sodiation/desodiation process. The M–S bonds in metal sulfide are weaker than the corresponding M–O bonds in metal oxides, which can be kinetically favorable for conversion reactions with Na^+ ions.[410] As a result, transition metal sulfides show improved mechanical stability due to their smaller volume changes and higher initial Coulombic efficiency due to better reversibility of Na_2S than that of Na_2O during the sodiation–desodiation process.[415] Therefore, various metal sulfides have been extensively investigated as high capacity anode materials for LIBs and SIBs such as cobalt sulfides (CoS, CoS_2),[400–410] molybdenum sulfides (Mo_2S, MoS_2),[411–419] iron sulfides (FeS, FeS_2),[423–432] tin sulfides (SnS, SnS_2),[433–445] copper sulfide (CuS),[446] manganese sulfide (MnS),[447] nickel sulfide (NiS),[448,449] titanium sulfide (TiS_2),[450] tungsten sulfide (WS_2),[451,452] and zinc sulfide (ZnS).[453,454] Depending on the transition metal elements, the Na^+ ion storage mechanism of metal sulfide materials can be classified as the conversion reaction and/or combined insertion and the alloying reaction.

3.2.2.1. Cobalt sulfides.
Cobalt sulfide is an interesting metal chalcogenide semiconductor material and has a number of applications.[400–403] Recently, superior Li-storage properties of cobalt sulfide were achieved by designing a novel nanoarchitecture and fabricating hybrid nanocomposites with various carbon additives.[404–406] Shadike et al. fabricated CoS_2 and CoS_2–MWNCT materials and investigated their electrochemical performances with a Na storage mechanism in ether-based electrolytes and commonly used carbonate-based electrolytes. They also investigated the evolution processes of CoS_2 and CoS_2–MWCNT during cycling via ex situ TEM[407] (Fig. 31a). During the sodiation/desodiation process, CoS_2 can accommodate Na^+ ions as follows: $CoS_2 + 4Na^+ + 4e^- \leftrightarrow Co + 2Na_2S$. Both CoS_2 and CoS_2–MWCNT electrodes have a similar sodium storage mechanism, but their electrochemical performances are quite different. Using MWCNTs as carbon additives provides several advantages such as 3D electron conductive networks with a high surface area, which facilitate the fast penetration of sodium ions and diffusion of electrolytes. As a result, the CoS_2–MWCNT electrode exhibited a high initial discharge capacity of 826 mA h g^{-1} with a high Coulombic efficiency of 93%, and a stable cycle life for 100 cycles in an ether-based electrolyte (1 M $NaCF_3SO_3$–DGM) (Fig. 31b).

Later, Peng et al. proposed the unique hybrid nanocomposite of cobalt sulfide (CoS) nanoplates anchored onto reduced graphene oxide (rGO) sheets and demonstrated the impressive high specific capacity of 540 mA h g^{-1} at 1 A g^{-1}, excellent rate capability, and superior cycle retention of 88% after 1000 cycles in Na cells.[409] More recently, Zhou et al. fabricated Co_3S_4@PANI (polyaniline) nanotubes, in which polyaniline is uniformly coated on both the exterior and inner surfaces of Co_3S_4 nanotubes (Fig. 31c).[410] Based on the CV results in the potential window of 0.05–2.0 V (vs. Na^+/Na), they claimed that Co_3S_4 electrodes can store Na^+ ions through the combined insertion and conversion reaction. In the first scan, a cathodic peak at 0.98 V is commonly assigned to an initial process of the Na^+ insertion reaction: $Co_3S_4 + xNa^+ + xe^- \rightarrow Na_xCo_3S_4$. The peak at

0.72 V is related to the conversion reaction of Co_3S_4 with Na and the formation of a solid electrolyte interphase: $Na_xCo_3S_4 + (8 - x)Na^+ + (8 - x)e^- \rightarrow 4Na_2S + 3Co$. The flexible PANI layers coated on both outer and inner surfaces of Co_3S_4 nanotubes would form "protective layers", thus preventing structure collapse and pulverization of the Co_3S_4 nanotubes during cycling.

3.2.2.2. Molybdenum sulfides.
In the case of molybdenum disulfide (MoS_2), Mo and S atoms are covalently bonded to form 2D S–Mo–S trilayers and the adjacent planes are stacked by van der Waals interactions, which facilitate intercalation of the large Na^+ ion.[411,414] According to previous reports, MoS_2 can store the Na^+ ions through the intercalation and/or conversion reactions depending on the operation voltage window.[413,415–417,419] The electrochemical reaction of MoS_2 is interpreted as the following two step reactions: $MoS_2 + xNa^+ + xe^- \rightarrow Na_xMoS_2$ (above 0.4 V), $Na_xMoS_2 + (4 - x)Na^+ + (4 - x)e^- \rightarrow 2Na_2S + Mo$ (below 0.4 V).[413] Hu et al. prepared MoS_2 nanoflowers with expanded interlayer spacing of the (002) plane, which exhibited stable electrochemical performances that followed an intercalation reaction by controlling the cut-off voltage to 0.4–3.0 V[413] (Fig. 31d). As a result, this material delivered a high discharge capacity of 350 mA h g^{-1} at 50 mA g^{-1} and stable cycle retention for over 1500 cycles. On the other hand, the intercalation reaction of MoS_2 at a limited voltage above 0.4 V delivered a lower specific capacity in consideration of their theoretical capacity of 668 mA h g^{-1} when $4Na^+$ ions reacted with MoS_2 through the conversion reaction.[417,419] However, a conversion type chemical reaction usually brings about a serious volume change to the electrode materials and sluggish kinetics for reconstruction of the original active materials. Recently, to overcome such problems through the electrochemical conversion reactions of MoS_2 (below 0.4 V), high conductivity carbon additives and novel nanoarchitecture design were proposed.[414–422] Su et al. prepared few-layer MoS_2 nanosheets and conducted the electrochemical test in the voltage range of 0.01–3.0 V.[418] The results show that few-layer MoS_2 nanosheets exhibited a high capacity of 530 mA h g^{-1} and a high rate capability. Xie et al. prepared a series of sheet-on-sheet structured MoS_2/RGO nanocomposites and investigated the effect of heterointerfacial areas on sodium storage performances.[419] Computational calculation and experimental results show that the 2D MoS_2/rGO heterointerface can increase the conductivity of MoS_2 and capture more Na atoms due to maintaining the high diffusion mobility of Na^+ ions on the MoS_2 surface and high electron transfer efficiency from Na to MoS_2, respectively. As a result, this material delivered a high capacity of 352 mA h g^{-1} even at a high current density of 640 mA g^{-1} in the voltage range of 0.01–3.0 V (Fig. 31e).

3.2.2.3. Iron sulfides.
Natural and/or synthetic FeS_2 materials have been demonstrated to be potential electrode materials among metal sulfides due to their high theoretical capacity of 894 mA h g^{-1} and environmental friendliness. Ahn and co-works reported a Na/synthetic FeS_2 battery for the first time[423,424] (Fig. 32a). Later, Hu et al. demonstrated room temperature sodium storage performances of the FeS_2 microspheres with

This journal is © The Royal Society of Chemistry 2017

Chem. Soc. Rev., 2017, 46, 3529–3614 | 3575
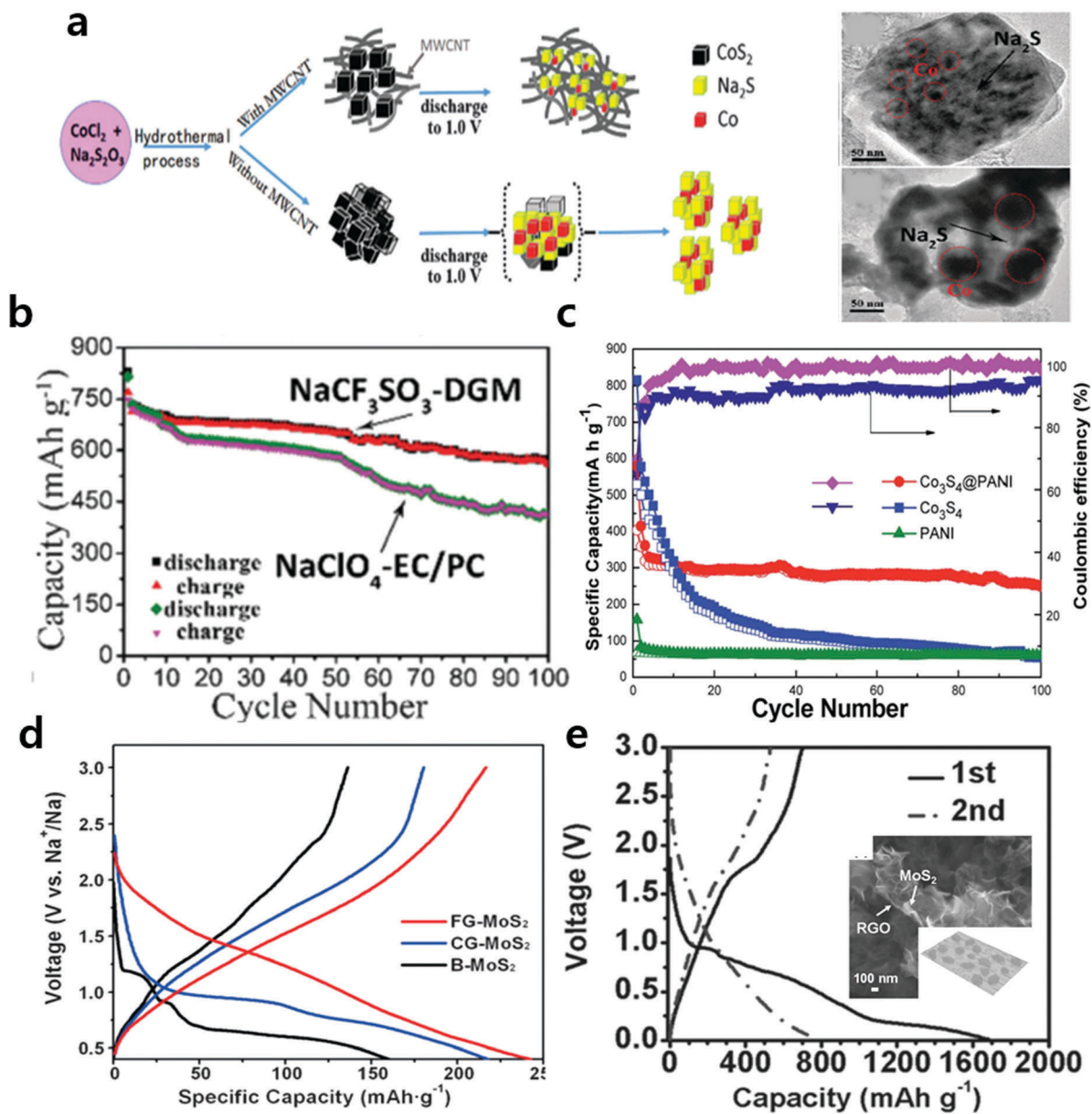
Fig. 31 (a) Schematic diagram of the evolution process of the as-prepared CoS_2–MWCNT and bare CoS_2 electrodes before and after the first discharge to 1.0 V (left). And, *ex situ* TEM images of sodiated CoS_2–MWCNT and bare CoS_2 particles (right). (b) CoS_2–MWCNT electrodes at a current density of 100 mA g^{-1} in 1.0 M $NaCF_3SO_3$–DGM and 1.0 M $NaClO_4$–EC/PC. (Reproduced with permission from ref. 407, Copyright 2015 The Royal Society of Chemistry.) (c) Cycling performance of Co_3S_4, PANI, Co_3S_4@PANI electrodes. (Reproduced with permission from ref. 410, Copyright 2016 The Royal Society of Chemistry.) (d) Charge and discharge curves of the as-prepared FG-MoS_2, CG-MoS_2, and B-MoS_2 at the first cycle. (Reproduced from ref. 413 with permission, Copyright 2014 Wiley-VCH Verlag GmbH & Co. KGaA.) (e) Galvanostatic charge–discharge profiles of MG-3 and SEM and TEM images of MG-3 (inset image). (Reproduced from ref. 419 with permission, Copyright 2015 Wiley-VCH Verlag GmbH & Co. KGaA.)

only the intercalation reaction by simultaneously selecting a compatible ether-based electrolyte and tuning the cut-off voltage to 0.8 V. The intercalation reaction mechanism between Na^+ ions and FeS_2 within the operation voltage range of 0.8–3.0 V is as follows: $FeS_2 + xNa^+ + xe \rightarrow Na_xFeS_2 \ (x < 2)$,[429] The resulting exhibited high capacity of 170 mA h g^{-1} at a high current density of 20 A g^{-1} and superior long term cyclability over 20 000 cycles (capacity retention of ~90%) (Fig. 32b). Based on the *ex situ* XRD and TEM measurements, they also observed the structural evolution of FeS_2 during the electrochemical reaction with

Na^+ ions (Fig. 32c). The XRD patterns collected at the charge-end state after the 50th cycle (VIII) indicates the formation of a layered compound of trigonal Na_xFeS_2 with x around 1.6. Also, the layered structures of FeS_2 could be maintained within the selected potential window of 0.8–3.0 V, enabling the highly reversible intercalation reaction. On the other hand, Walter *et al.* applied nanocrystalline FeS_2 materials within the operation voltage range of 0.02–2.5 V. The conversion reaction mechanism between Na^+ ions and FeS_2 is as follows: $FeS_2 + 2Na^+ + 2e^- \rightarrow Na_2FeS_2$, $Na_2FeS_2 + 2Na^+ + 2e^- \rightarrow 2Na_2S + Fe$.[430] Upon sodiation
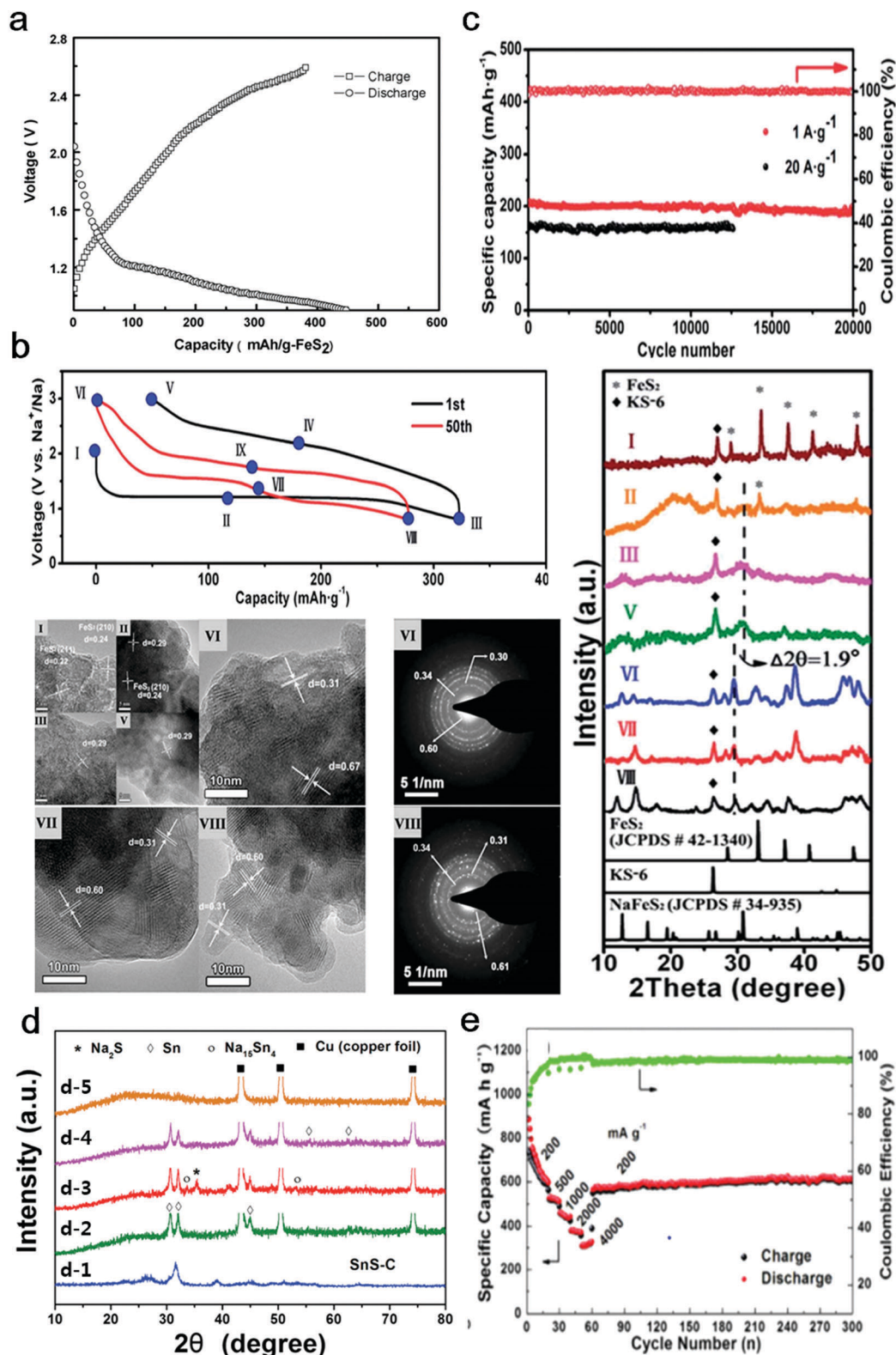
Fig. 32 (a) Charge–discharge voltage profiles of the Na/FeS$_2$ cell at room temperature. (Reprinted from ref. 423, Copyright 2008, with permission from Elsevier.) (b) Structural evolution of FeS$_2$ during the electrochemical reaction with sodium: TEM images (left) and *ex situ* XRD results (right). (c) Cyclic performance of FeS$_2$ microspheres. (Reproduced with permission from ref. 429, Copyright 2015 The Royal Society of Chemistry.) (d) *Ex situ* XRD patterns of the SnS−C electrode at different discharging and charging states. (d-1: fresh electrode; d-2: after 1st discharging to 0.6 V; d-3 after 1st discharging to 0.01 V; d-4 after 1st charging to 0.8 V; d-5 after 1st charging to 2.0 V.) (Reproduced with permission from ref. 433, Copyright 2014 The Royal Society of Chemistry.) (e) Rate capability and long-term cyclability with Coulombic efficiency of the SnS$_2$/G-20 electrode. (Reproduced with permission from ref. 442, Copyright 2015 The Royal Society of Chemistry.)

This journal is © The Royal Society of Chemistry 2017

Chem. Soc. Rev., 2017, 46, 3529–3614 | 3577

below 0.8 V, FeS_2 nanocrystals led to the formation of Na_2S involving most likely only amorphous phases. This amorphous state can effectively reduce mechanical stress upon expansion and contraction during cycling. The FeS_2 nanocrystals delivered a high capacity above 500 mA h g^{-1} for 400 cycles at a current density of 1 A g^{-1}. Compared to pyrite (FeS_2), a few studies on ferrous sulfide (FeS) are reported due to poor cyclability and rate capability.[431,432] Recently, Wei et al. proposed the flexible and self-supported carbon-coated FeS on carbon cloth films, which display high reversible capacity and superior rate capability.[431]

3.2.2.4. Tin sulfides. Tin-based sulfide (SnS, SnS_2) compounds have attracted considerable attention due to their high theoretical capacity with combined conversion and alloying electrochemical reactions.[433–437] Wu et al. proposed tin-sulfide nanocomposite (SnS–C) anode materials based on combined conversion and alloying reactions: $SnS + 2Na^+ + 2e^- \leftrightarrow 5Na_2S + Sn$ (conversion reaction), $Sn + 3.75Na^+ + 3.75e^- \leftrightarrow Na_{3.75}Sn$ (alloying reaction)[433] (Fig. 32d). The prepared SnS–C composite has a small crystalline size of SnS and good carbon coating, which synergistically facilitates electrochemical utilization and maintains the structural integrity. As a result, the prepared SnS–C composite exhibited a high Na storage ability delivering a capacity of 568 mA h g^{-1} at 20 mA g^{-1} and an excellent cycling stability of 97.8% after 80 cycles as well as a high-rate capability. Later, Zhu et al. proposed a 3D porous interconnected metal sulfide/carbon nanocomposite by the ESD technique without adding carbonaceous materials such as carbon nanotubes and graphene.[436] SnS_2 has also been applied as an anode material for SIBs.[438–448] SnS_2 has a sandwich structure that consists of covalently bonded S–Sn–S trilayers separated by a relatively large van der Waals interaction.[438] A large interlayer d-spacing of 5.90 Å can effectively accommodate Na$^+$ ions.[439–441] In addition, intermediate products of amorphous NaS_2 suppress the pulverization and aggregation during Na–Sn alloying reactions.[440] Liu et al. synthesized exfoliated-SnS_2 restacked on graphene that ultrasmall SnS_2 nanoplates (with a typical size of 20–50 nm) composed of 2–5 layers are homogeneously decorated on the surface of graphene.[442] This unique structure facilitates Na$^+$ ion diffusion and delivers a high capacity of 650 mA h g^{-1} at 200 mA g^{-1} with stable cyclability at $\sim$610 mA h g^{-1} without notable capacity fading for 300 cycles (Fig. 32e). SnS_2 can store the Na$^+$ ions through following three step processes: (1) intercalation reaction: $xNa^+ + SnS_2 + xe^- \rightarrow Na_xSnS_2$, (2) conversion reaction: $4Na^+ + SnS_2 + 4e^- \rightarrow 2Na_2S + Sn$, (3) alloying reaction: $Sn + 3.75Na^+ + 3.75e^- \rightarrow Na_{3.75}Sn$. Such improved electrochemical performances of conversion materials are attributed to the electro-conducting carbons. The introduction of carbon additives such as graphene and/or carbon nanotubes into active materials is indispensable to have advantages over conversion materials such as effective stress relief, accommodation of large volume expansion/shrinkage, and facilitation of electron and Na$^+$ ion transport.

3.2.3 Transition metal phosphide (TMP). Phosphorus based transition metal phosphide (TMP) compounds have been investigated as promising anode materials for SIBs. It is well

known that the main reason for the faster capacity fading of the phosphorous anode is the continuous pulverization during the sodiation–desodiation process.[240] One strategy for dealing with this problem is fabricating a binary metal–phosphide form by employing secondary metals (M–P, M = Ni, Fe, Co, Cu and Sn).[455–466] This is because if these elements can form an intermediate compound (Na_xM or Na_xP, $x \geq 0$,) during the charge–discharge process, pulverization can be partially repaired and the accumulation of pulverization can be terminated.[460,462] Therefore, a combined two-step reaction consisting of conversion and alloying is a very effective way to overcome the huge volume expansion issues. An excellent example of this process is tin–phosphorus compounds of Sn_4P_3. Kim et al. prepared an intermetallic compound of Sn_4P_3 by facile high-energy mechanical ball milling and demonstrated its electrochemical performance as an anode material for SIBs.[460] This material delivered a reversible capacity of 718 mA h g^{-1} and very stable cycle performance with negligible capacity fading over 100 cycles with an appropriately low redox potential of about 0.3 V vs. Na/Na$^+$. These properties of the Sn_4P_3 electrode can be ascribed to the fact that the pulverization of Sn and P during the alloy process was partially self-healed by the conversion reaction process[462] (Fig. 33a). Recently, Liu et al. proposed uniform yolk–shell $Sn_4P_3@C$ nanospheres.[463] The rationally designed void space in between the shell and nanoparticles allows for the expansion of Sn_4P_3 without deforming the carbon shell or disrupting the SEI on the outside surface. As a result, yolk–shell $Sn_4P_3@C$ nanospheres exhibited superior excellent cycling performance for over 400 cycles (Fig. 33b). The enhancement in Sn_4P_3 can be attributed to a reversible reaction of $Sn_4P_3 + 9Na \leftrightarrow 4Sn + 3Na_3P$, which repairs the cracks, damage, and aggregation of Sn particles that occurred in the alloy process of $4Sn + 15Na \leftrightarrow Na_{15}Sn_4$ during cycling and, hence, terminates pulverization. It means that the damage can be healed by itself during cycling[465] (Fig. 33c). Similar to Sn_4P_3 materials, the stable cycling performances of SnP_3/C composites were derived by the self-healing effect of the conversion reaction for the alloying process.[462] To date, binary-intermetallic systems such as NiP_3,[455] (CuP_2,[456] Cu_3P[457]), FeP[458] and CoP,[464] FeP_4[466] exhibit impressive results, however, these binary inter-metallic systems still need to improve in terms of material design and electrode formulation for high performance practical SIBs.

3.3 Alloying reaction materials

Na$^+$ insertion materials, such as carbonaceous materials and titanium-based oxide compounds, have been successfully applied as Na storage materials that deliver a reasonable capacity with relatively small volume expansions during the electrochemical insertion/extraction reaction with Na.[241,300] However, these materials still suffer from limited capacity utilization due to their intrinsic constraint ascribed to their structures, which lowers the specific energy density of SIBs. Similar to the conversion materials, alloying materials can be suggested as attractive anodes for SIBs because they can store a large number of sodium ions in the host structure with a relatively low operating potential (below 1.0 V).[244,245] Multiple reactions
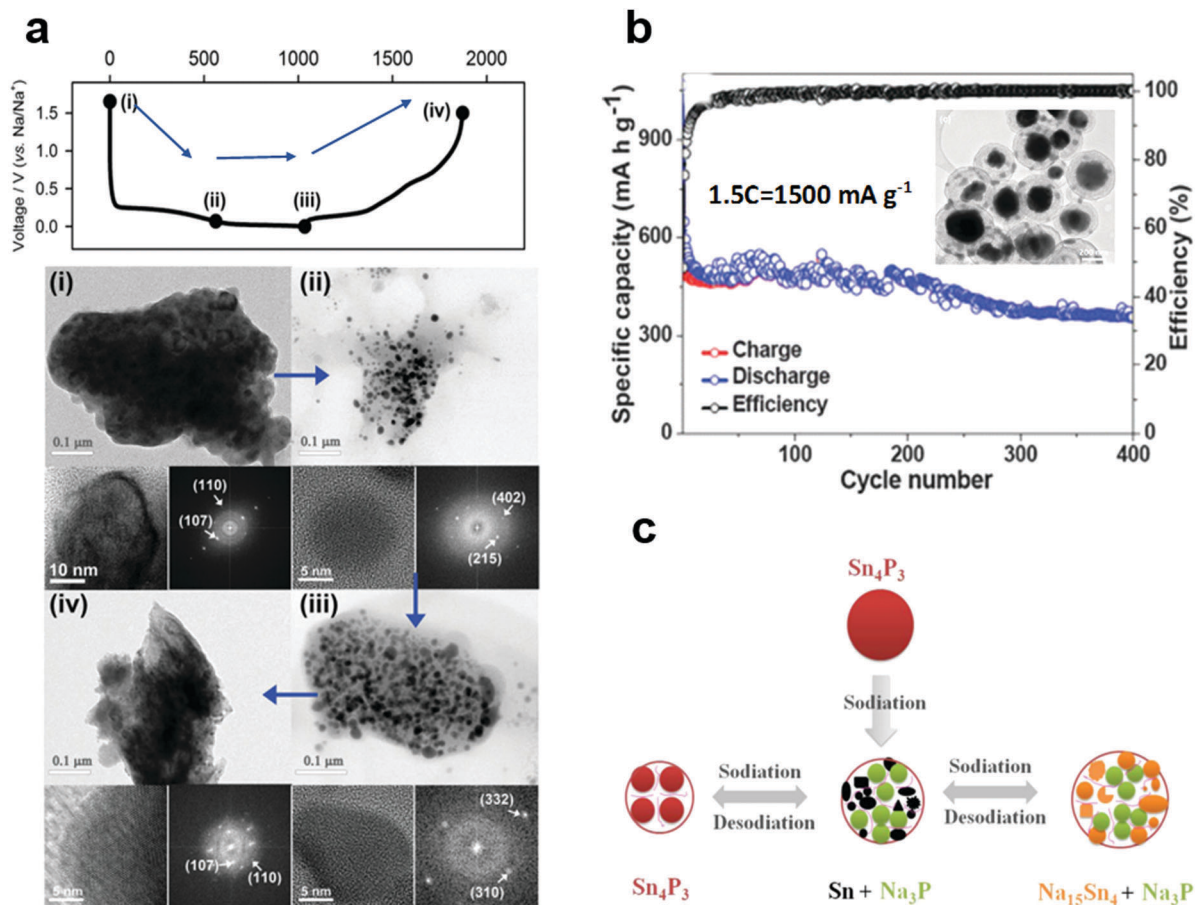
Fig. 33 (a) First galvanostatic charge and discharge profiles of the Sn_4P_3 electrode (top). The *ex situ* HR-TEM bright-field images, enlarged HR-TEM images and corresponding FFT patters at each point. (Reproduced from ref. 460 with permission, Copyright 2014 Wiley-VCH Verlag GmbH & Co. KGaA.) (b) Long cycling performances of yolk–shell Sn_4P_3@C nanospheres at 1.5C. (Reproduced with permission from ref. 463, Copyright 2015 The Royal Society of Chemistry.) (c) Self-healing effect of the conversion reaction for the Sn_4P_3 anode. (Reproduced with permission from ref. 465, Copyright 2016 American Chemical Society.)

with Na per single atom produce a high specific capacity during the alloying–dealloying reactions.[99] Metals (Sn, Bi), metalloids (Si, Ge, As, Sb) and polyatomic nonmetal compounds (P) in group 14 (Fig. 34) or 15 elements (Fig. 37) in the periodic table have been widely studied as potential anode materials for SIBs. However, depending on the host materials and electrochemical sodiation levels, the large Na^+ ion causes huge volume changes during the alloying–dealloying reaction. This repetitive volume changes under the constraints imposed by the battery packaging give rise to complex mechanical stresses in active particles, ultimately leading to their fracture or pulverization.[240] To date, through various experimental works focusing on electrochemical and mechanical responses of these alloys to Na interactions, the desirable architectures and/or enhanced electrode designs have been investigated. In this section, we specifically discussed group 14 and group 15 elements with a focus on their Na alloy reaction mechanisms and summarize various strategies for high performance sodium anode materials.

3.3.1 Alloying compounds in group 14

3.3.1.1. Silicon. In recent years, Si-based anode materials were intensively studied for LIBs due to their abundance in Earth's

crust and their high specific capacity through electrochemical alloying reactions with Li.[467,468] Theoretically, silicon can uptake 4.4 Li^+ ions per Si atom and deliver a high specific capacity of 4000 mA h g^{-1}. Morito *et al.* firstly demonstrated the phase diagram between Na and Si, which indicated the fully sodiated form of Na–Si.[469] However, based on a single-atom diffusion model, Morito *et al.* deduced that bulk Si is not a promising anode material for Na batteries because Si can only uptake 1Na per Si atom and exhibit poor Na diffusion kinetics[469] (Fig. 34a). Through the computational calculation, desirable electrode design to facilitate Na^+ intercalation and migration into Si was suggested such as structural modification and control of the activation barrier.[470–476] Structurally modified Si was predicted to demonstrate better electrochemical performance such as in amorphous Si due to more favorable binding between Na and Si. Reasonable activation barriers for Na^+ diffusion were also predicted, where 0.4 eV was required for Na^+ migration in amorphous Si.[457] Based on theoretical works, Xu *et al.* experimentally proved reversible electrochemical Na^+ ion uptake in Si for the first time[475] (Fig. 35a and b). Xu *et al.* prepared nanoparticles containing both amorphous and

This journal is © The Royal Society of Chemistry 2017

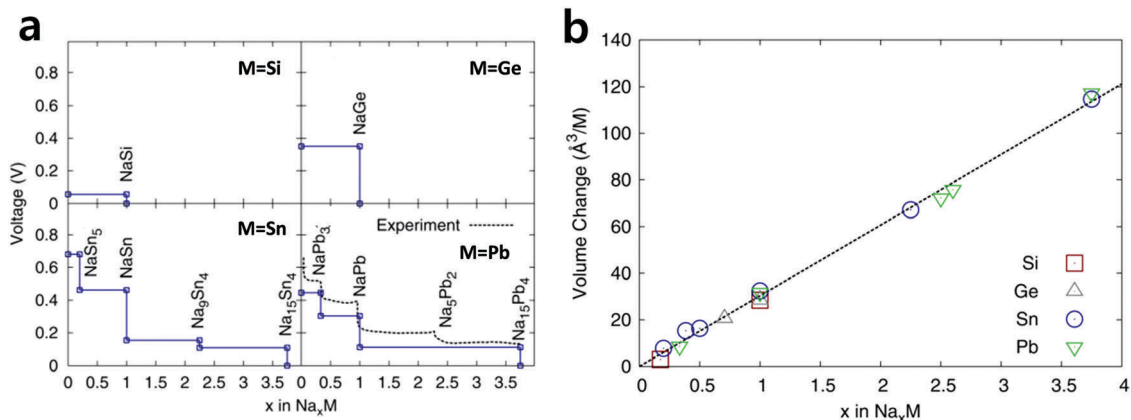*Chem. Soc. Rev.*, 2017, **46**, 3529–3614 | 3579

Fig. 34 (a) Na–M voltage curves calculated using DFT and (b) the volume changes for group 14 elements in periodic table. (M = Si, Ge, Sn, and Pb.) Experimental values are also given if available. (Reproduced with permission from ref. 244, Copyright 2011 The Electrochemical Society.)

crystalline Si, which demonstrated an excellent reversible capacity of 279 mA h g^{-1} at 10 mA g^{-1} and a stable capacity retention of 248 mA g^{-1} after 100 cycles at 20 mA g^{-1}. Also, through the various analysis techniques, they proposed the possible Na storage mechanism as follows: xNa + Si $\leftrightarrow$ xNaSi + $(1 - x)$Si (sodiation), NaSi $\leftrightarrow$ Na$(1 - x)$Si + xNa (desodiation). More recently, Zhang *et al.* precisely investigated the sodiation/desodiation behavior of microsized and nanosized crystalline-Si, hereafter referred to as c-Si, electrodes during the Na$^+$ insertion/extraction processes *via* cyclic voltammogram, operando XRD and Raman analysis.[476] The operando XRD patterns reveal that no structural conversions or reversible reactions could proceed in the microsized c-Si electrode, and the capacity of the microsized c-Si electrode is negligible. On the other hand, the voltage plateau of the nanosized c-Si electrode below 0.5 V in the discharge profile is consistent with the reduction peak at 0.2 V in the CV curve, which is related to the Na ion uptake and the alloying process with c-Si (Fig. 35c). It means that the electrochemical behavior of c-Si strongly depends on the particle size. The operando Raman analysis results demonstrated that an irreversible crystal structure transformation from c-Si to amorphous-Si takes place during the first sodiation process. This newly generated a-Si is beneficial for the reversible Na$^+$ insertion reaction due to its more disordered crystal structure (Fig. 35d). According to their report, the whole process includes four phases along with a growing degree of sodiation. In stage one, Na ions diffuse along the ion channels and accumulate at tetrahedral sites between (111) planes because this position is the most stable site for Na-ion insertion. In stage two, along with the increase of the concentration of Na$^+$, the bonds of Si–Si are broken, and Na atoms make new bonds with Si atoms in stable positions. In stage three, further sodiation leads to the break of the majority of the Si–Si bonds, and crystalline Si is transformed into an amorphous Na–Si alloy. In stage four, after the desodiation process, the amorphous structure is maintained, leading to the a-Si structure (Fig. 35e).[476]

3.3.1.2. Germanium. Germanium has a similar chemistry to silicon, bonding with a maximum of one Na atom.[477,478] The theoretical calculation predicted that sodium could alloy with germanium to form Na–Ge compounds which delivers a theoretical capacity of 369 mA h g^{-1}.[479] However, similar to silicon, germanium is also theoretically predicted not to be capable of storing Na in its crystalline structure because the large ionic size of sodium compared to lithium results in much higher activation energy for hopping between interstitial sites in the lattice (0.51 eV for lithium *vs.* 1.5 eV for sodium).[479] Therefore, to overcome the sluggish kinetics of Na$^+$ in germanium, a novel nanostructure and/or electrode design was introduced such as amorphous germanium in thin film and nanowire form. Baggetto *et al.* prepared a germanium thin film electrode and demonstrated the reversible reaction with a high discharge capacity of 350 mA h g^{-1}, which is close to the theoretical value.[480] The shapes of the sodiation and desodiation voltage profiles are quite flat which indicates that the sodiation reaction proceeds *via* a two-phase reaction mechanism: a reaction front separating the sodium-rich and sodium-poor phases propagates through the material as the reaction progresses. Recently, Kohandehghan *et al.* proposed amorphous germanium nanowires and thin films with a single lithiation–delithiation activation process.[481] Activation with Li induces amorphization in germanium nanowires and thin films, which reduces the barrier for nucleation of the Na$_x$Ge phase. Also, a dense distribution of nanopores provides an additional Na diffusion path during the sodiation–desodiation process. The TEM and EELS mapping results clearly show that activated germanium nanowires (GeNWs-A) uniformly take up more Na$^+$ ions at the sodiated state compared to unactivated germanium nanowires (GeNWs). For the case of GeNWs, the Na$^+$ ion is primarily present on its surface at the sodiated state, being associated with both the SEI layer and the irreversibly formed sodium oxide (Fig. 35f) As a result, GeNWs-A delivered a high reversible capacity of 355 mA h g^{-1} at a 1C-rate and superior rate capabilities (Fig. 35g).

3580 | *Chem. Soc. Rev.*, 2017, **46**, 3529–3614

This journal is © The Royal Society of Chemistry 2017
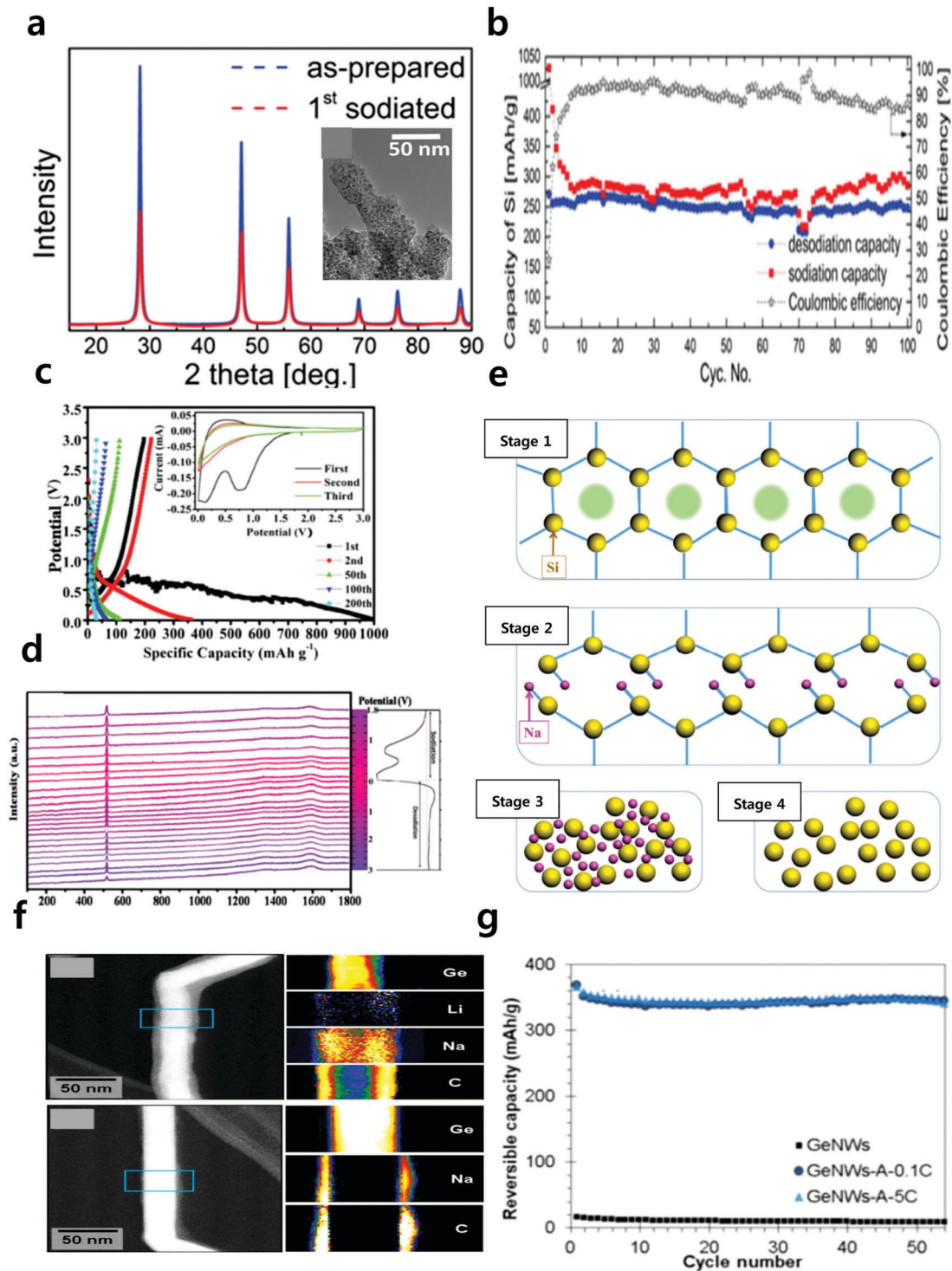
Fig. 35 (a) X-ray diffraction patterns on as-synthesized Si nanoparticles and inset image show the morphology of sodiated Si NP electrode after charge/discharge for 100 cycles at 20 mA g^{-1}. (b) Cycling test of Si NP electrodes in the voltage range of 0.01–2.8 V. (Reproduced from ref. 475 with permission, Copyright 2015 Wiley-VCH Verlag GmbH & Co. KGaA.) (c) Charge–discharge profiles for selected cycles at 500 mA g^{-1} (inset: the first three CV curves for the nanosized c-Si electrode), (d) in operando Raman analysis of the electrochemical behavior towards Na$^+$ for the nanosized c-Si electrode and (e) schematic illustrations explaining the changes in the nanosized c-Si during cycling. (Reproduced from ref. 476 with permission, Copyright 2016 Wiley-VCH Verlag GmbH & Co. KGaA.) (f) TEM analysis of GeNWs-A-0.1C and GeNWs after initial sodiation process and HAADF micrograph and EELS elemental maps of Ge, Na, Li, and C. (g) Reversible capacity as a function of cycle number for GeNWs and GeNWs-A electrodes. (Reproduced with permission from ref. 481, Copyright 2014 American Chemical Society.)

3.3.1.3. Tin. Sn has been regarded as one of the most promising anode materials owing to its high theoretical specific capacity of 847 mA h g^{-1}, based on the full sodiation state of Na$_{15}$Sn$_4$.[482–495] Based on the theoretical calculations,

This journal is © The Royal Society of Chemistry 2017

Chem. Soc. Rev., 2017, **46**, 3529–3614 | **3581**

Chevrier and Ceder *et al.* proposed a voltage profile for sodium insertion into tin compounds[244] (Fig. 34a). The phase diagram of Na–Sn indicated that the sodiation of Sn progressed in a series of steps: $Sn \rightarrow NaSn_5 \rightarrow NaSn \rightarrow Na_9Sn_4 \rightarrow Na_{15}Sn_4$.[482–484] Komaba *et al.* experimentally demonstrated that Sn undergoes a reversible electrochemical redox reaction to reversibly form Sn–Na intermetallic phases.[482] Based on the DFT calculations and *in situ* X-ray diffraction results, Ellis *et al.* suggested that electrochemical sodiation of Na with Sn proceeds through the following reaction steps: plateau 1: $Na + Sn \rightarrow NaSn_3^*$,

plateau 2: $Na + NaSn_3^* \rightarrow a\text{-}NaSn$, plateau 3: $5Na + 4(a\text{-}NaSn) \rightarrow Na_9Sn_4$, plateau 4: $6Na + Na9Sn_4^* \rightarrow Na_{15}Sn_4$ (a-amorphous, *-new crystalline phase)[483] (Fig. 36a). Huang's group investigated the microstructural evolution and phase transformation with volumetric expansions of tin nanoparticles during electrochemical sodiation *via* the *in situ* transmission microscopy technique[484] (Fig. 36b). According to their report, Sn undergoes a two-step sodiation process to form amorphous $NaSn_2$ (56% expansion) in the first step and sequentially to form amorphous Na_9Sn_4, Na_3Sn (336% expansion), and crystalline
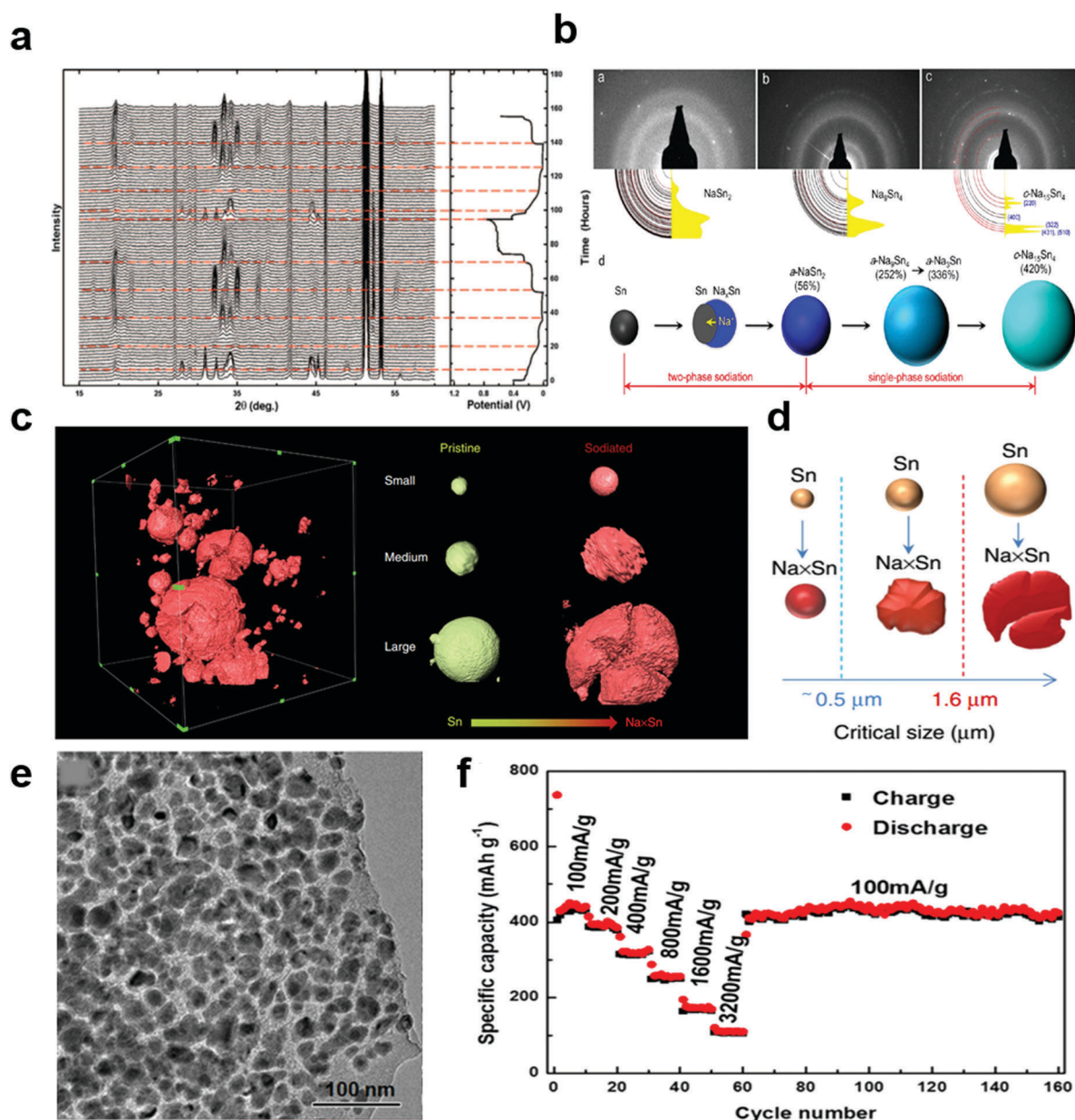
Fig. 36 (a) *In situ* XRD data and the corresponding voltage curve. Dashed lines indicated the separating two-phase regions. (Reproduced with permission from ref. 483, Copyright 2012 The Electrochemical Society.) (b) Three a-Na$_x$Sn phases in the single-phase sodiation and schematic illustration of the structural evolution of Sn NPs during the sodiation. (Reproduced with permission from ref. 484, Copyright 2014 American Chemical Society.) (c) 3D morphologies of the sodiated electrode and selected three particles with different sizes and fracture and (d) schematic illustration of two critical sizes for Sn fracture in NIB. (Reproduced by permission from ref. 485, Nature Publishing Group, Copyright 2015.) (e) TEM images of F-G/Sn@C composites and (f) rate capability and capacity retention of the F-G/Sn@C electrode. (Reprinted from ref. 493, Copyright 2016, with permission from Elsevier.)

$Na_{15}Sn_4$ (420% expansion) phases in the second step. Later, Wang et al. visualized the 3D structural/chemical evolution of the Sn electrode during multi-electrochemical cycles (sodiation–desodiation) via in situ synchrotron hard X-ray nanotomography[485] (Fig. 36c). They also suggest two important critical sizes of 0.5 μm for low complexity and 1.6 μm for high complexity, which provide new insights into the failure mechanism and materials fracture in SIBs (Fig. 36d). Such various strategies have been tested to clarify the electrochemical sodiation mechanism of Sn; however, there remains disparity between computational and experimental works.[486] And the extremely high volumetric expansion–contraction during the uptake–release process of 3.75 Na atoms in Sn is the main obstacle for full use of the tin-based anode. Because it will lead to cumulative pulverization, leading to the loss of electrical contact and accelerating the capacity decay during cycling. Therefore, most works focused on dealing with the serious volume change during alloying–dealloying reactions. Carbon-conducting techniques such as carbon coating and/or formation of composites with a 2D or 3D carbon matrix are very effective for buffering the volume strain and creating the electric conducting pathways.[487–495] Xie et al. suggested a unique free standing electrode configuration with 3D architectures. They prepared a free-standing electrode composed of core–shell structured Sn@CNT nanopillar arrays on a carbon paper (Sn@CNT-CP).[490] This 3D architecture was able to provide buffering capability against mechanical strain during Na_xSn alloy formation and efficient 3D transport pathways for both Na^+ ions and electrons. As a result, the as-prepared Sn@CNT-CP electrode exhibited promising electrochemical performance, including high capacity and good cyclability extending to 100 cycles. The 2D graphene-backboned matrix was also introduced to function as a physical barrier to buffer the drastic volume change and impede the aggregation of Sn nanoparticles during Na–Sn alloying–dealloying reactions. Recently, Sn@C composites with ultrasmall tin nano particles (1–8 nm) are introduced by Liu et al.[491,492] Later, Luo et al. fabricated a hierarchical tin@carbon composite composed of a graphene carbonaceous matrix and well-confined tin nanoparticles with a typical size of ∼15 nm as anodes for Na storage[493] (Fig. 36e). This composite delivered a high specific capacity of 413 mA h g^{-1} and reversible sodium storage properties with negligible capacity fading after100 cycles (Fig. 36f).

3.3.2. Alloy compounds of group 15. The group 15 elements antimony (Sb), phosphorus, (P) bismuth (Bi) and arsenic (As) offer the prospect of serving as functional alloying elements for high-capacity alloy anodes for SIBs (Fig. 37a). A large specific capacity of Na alloys with group-15 elements underpins their potential application as anodes. The expected electrochemical properties of sodium (Na) alloys with group 15 elements were demonstrated using first principles calculations.[245] However, similar to group 14 elements, sodiation in such alloys is generally characterized with substantial volume expansion during charge and equivalent contraction during discharge (Fig. 37b). This causes the serious volumetric and asymmetric expansion/shrinkage upon cycling, which is the main difficulty in utilizing alloy-based anode materials for SIBs.

3.3.2.1. Antimony. Antimony delivers a theoretical capacity of 660 mA h g^{-1} according to formation of Na_3Sb (fully sodiation state).[496–498] Qian et al. suggested two steps of Na alloying/dealloying reactions as follows: first step: $Sb + Na^+ + e^- \leftrightarrow NaSb$, second step: $NaSb + 2Na^+ + 2e^- \leftrightarrow Na_3Sb$[497] (Fig. 38a). Darwiche et al. more precisely investigated the electrochemical reaction mechanism of Sb with Na and observed the unexpected intermediate amorphous Na_xSb phase via an in situ XRD technique[498] (Fig. 38b). The crystalline Sb first transforms upon discharge into an intermediate amorphous phase Na_xSb; when, all of the Sb is almost completely reacted, this Na_xSb amorphous phase starts converting into cubic-hexagonal Na_3Sb mixture phases before being stabilized as hexagonal Na_3Sb. Upon desodiation, crystalline Na_3Sb is transformed into amorphous Sb. (Sodiation: $cSb \rightarrow aNa_xSb$, $aNa_xSb \rightarrow Na_3Sb_{hex}/cNa_3Sb_{cub} \rightarrow cNa_3Sb_{hex}$, desodiation: $cNa_3Sb_{hex} \rightarrow aSb$, c: cubic,
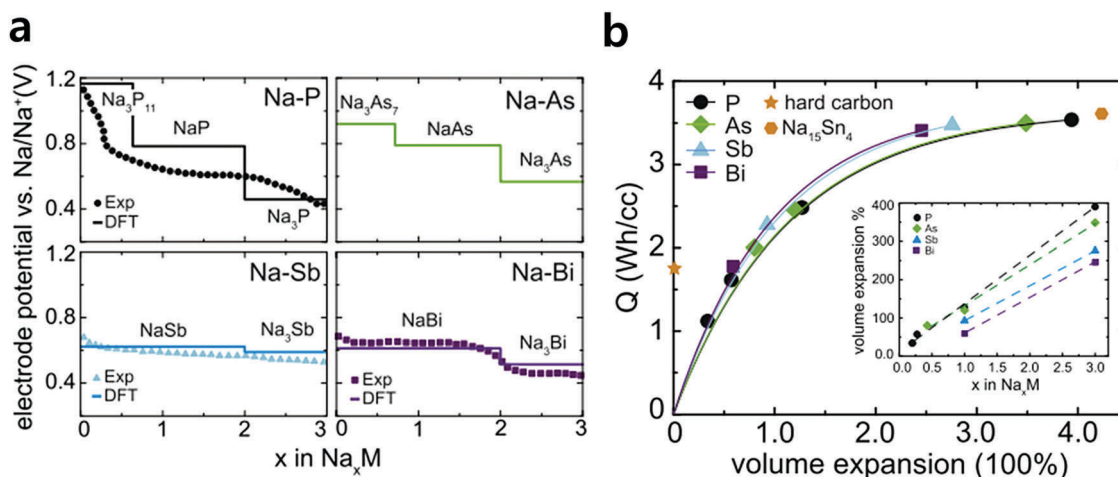

Fig. 37 (a) Na–M voltage curves calculated using DFT and (b) the volume changes for group 14 elements in periodic table. (M = P, As, Sb, and Bi.) Experimental values are also given if available. (Reprinted from ref. 245, Copyright 2015, with permission from Elsevier.)

This journal is © The Royal Society of Chemistry 2017

Chem. Soc. Rev., 2017, 46, 3529–3614 | 3583

a: amorphous, hex: hexagonal.) They demonstrated that the intermediate amorphous phase may act as a buffer to relieve strain, accounting for the improved cycling in Sb–Na alloying reactions. Through the mechanistic studies, antimony can uptake/release nearly three Na atoms per Sb upon sodiation–desodiation process. However, this multiple electrochemical reaction between tin and Na^+ ions leads to drastic volume changes of ∼390% during the Na alloying/dealloying process.[499] Therefore, in order to mitigate volumetric changes and to enhance kinetics of alloying reactions, several research efforts are focused on nanostructuring of the active material and employing of the carbon conducting additives.[497,498,500–509] He et al. proposed monodisperse antimony nanocrystals with a mean size tunable in the 10–20 nm range as anodes for SIBs.[503] Downsizing of the primary Sb to 10–20 nm can result in significantly faster kinetics and more stable operation at higher current densities. In comparison to microcrystalline bulk Sb, nanocrystal Sb exhibited an enhanced rate capability and higher cycling stability in Na cells (Fig. 38c). To provide a conductive pathway and a buffering matrix for effective release of mechanical stress, Wu et al. prepared a uniform nanofiber structure with the Sb nanoparticles embedded homogeneously in the carbon nanofibers.[504] The prepared Sb–C

electrode delivered a large reversible capacity of 631 mA h g^{-1} at C/15, a greatly improved rate capability of 337 mA h g^{-1} at a rate of 5C and a excellent cycling stability for over 400 cycles (Fig. 38d). Recently, Hu et al. proposed an antimony/multilayer graphene hybrid, in which antimony is homogeneously anchored on multilayer graphene.[508] A common drawback of carbon composite materials is their structural instability, which originates from the weak interaction between the active component and the carbon matrix. Therefore, to improve the above limitation of carbon composite materials, they proposed the chemically bonded antimony–multilayer graphene (MLG) hybrid nanostructure anode. The MLG strongly couples the Sb nanoparticles via chemical bonding, which can not only increase the electrical conductivity but also allow MLG to serve as a conductive matrix to maintain electrical contact with Sb during the large volume expansion and to help stabilize the SEI layer. This material delivered a high initial charge capacity of 452 mA h g^{-1} with stable capacity retentions of 90% for 200 cycles and exhibited a superior rate capability of 210 mA h g^{-1} at 5 A g^{-1}.

3.3.2.2. Phosphorus. Phosphorus electrochemically reacts with sodium to form Na_3P at an attractive potential for an
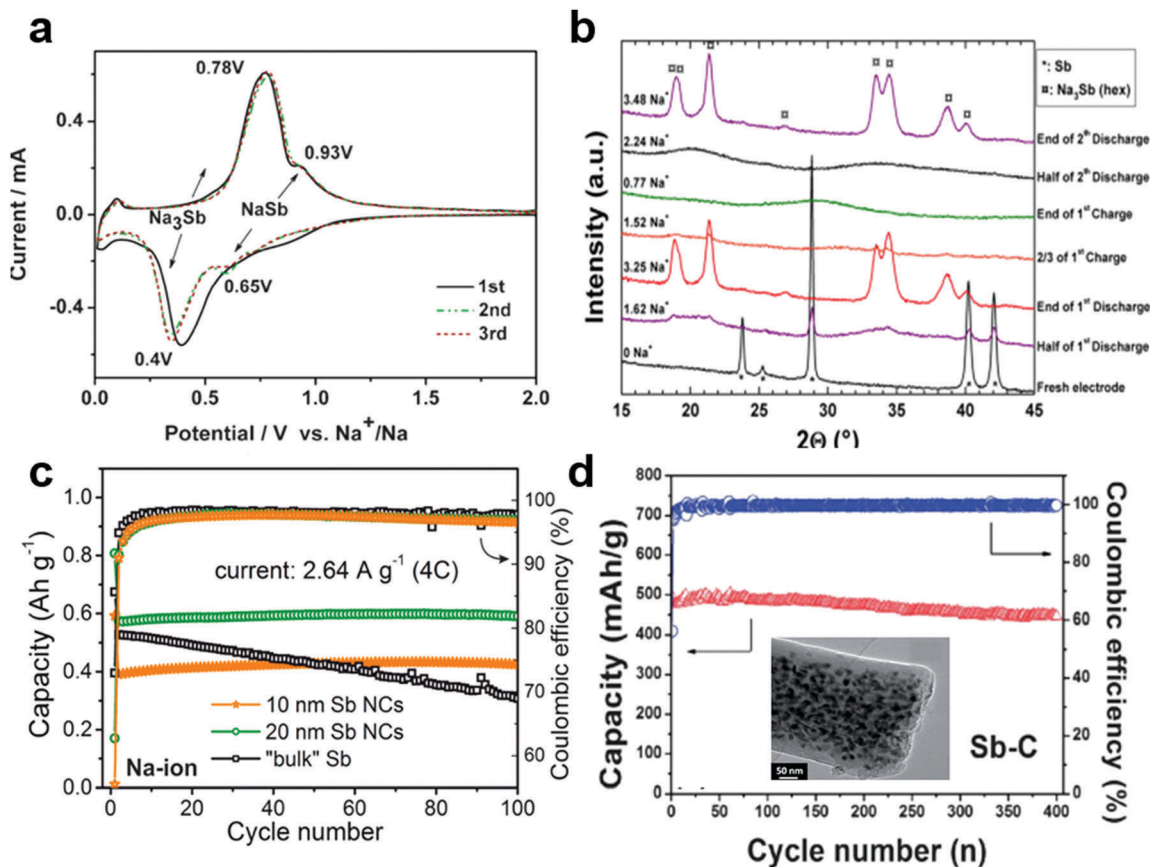
Fig. 38 (a) The CV curve of Sb/C nanocomposites. (Reproduced with permission from ref. 497, Copyright 2012 The Royal Society of Chemistry.) (b) Selected operando XRD patterns at various stages of discharge and charge of a Sb/Na cell. (Reproduced with permission from ref. 498, Copyright 2012 American Chemical Society.) (c) Cycling performance of different size Sb NC electrode. (Reproduced with permission from ref. 503, Copyright 2014 American Chemical Society.) (d) Cycling performance of the Sb–C electrode at a cycling rate at 200 mA g^{-1} and inset image represent that TEM image of the Sb-C nanofibers. (Reproduced with permission from ref. 504, Copyright 2014 The Royal Society of Chemistry.)

anode material, and its light atomic weight can achieve a higher theoretical capacity of 2596 mA h g^{-1} than any other SIB anodes presently available.[510–512] Phosphorous exists in three main allotropes of white phosphorus, red phosphorus, and black phosphorus[512,513,518] (Fig. 39a). White phosphorus (white-P) is volatile and unstable; it bursts into flames when it is exposed to the natural atmosphere. Red phosphorus (red-P) is usually amorphous in nature and is widely commercially available. Black phosphorus (black-P) is a crystalline phase, thermodynamically stable below 550 °C, and transforms into red (amorphous) phosphorus at higher temperature.[512] For this reason, the amorphous red-P and orthorhombic black-P forms are being widely studied as anodes for SIBs. However, the electrochemical properties of both red-P and black-P are hindered by the enormous volume change (490%) occurring during the electrochemical sodiation/desodiation process.[513] Qian et al. reported the improved electrochemical activity of amorphous red-P carbon composites (a-P/C) compared to pure red-P and black-P[514] (Fig. 39b). Upon sodiation/desodiation, the pure red P shows a quite large discharge (sodiation) capacity of 897 mA h g^{-1} but gives only a negligible charge (desodiation) capacity of 15 mA h g^{-1}, indicating the inactivity of this material for a sodium ion insertion reaction because of its insulating electronic nature (electrical conductivity of red-P: below 1×10^{-14} S cm^{-1}). In contrast, a-P/C exhibited greatly enhanced electrochemical performance with initial charge/discharge capacities of 2015 mA h g^{-1} and 1764 mA h g^{-1}, respectively, and a very high initial Coulombic efficiency of 87%, suggesting that the amorphous structure of phosphorus can effectively buffer the strong volumetric expansion during cycling. Over the same period of time, Kim et al. reported on an amorphous red phosphorus/carbon composite anode, which exhibited an appropriate redox potential of ca. 0.4 V vs. Na/Na$^+$ with a reversible capacity of 1890 mA h g^{-1} and good rate capability delivering 1540 mA h g^{-1} at a high current density of 2.86 A g^{-1}[511] (Fig. 39c). They also observed the formation of Na$_3$P at the full sodiated state through ex situ XRD analysis (Fig. 39d). Recently, varieties of amorphous phosphorous with nanoarchitectures and 2D or 3D carbon matrices having high conductivity were applied to achieve a high capacity and a stable cycle life.[511,513–519] Song et al. reported a novel phosphorus/graphene nanosheet hybrid through a facile ball milling process[513] (Fig. 39e). The graphene stacks are mechanically exfoliated to nanosheets that chemically bond with the surfaces of phosphorus particles. This chemical bonding facilitates robust and intimate contact between phosphorus and graphene nanosheets. Furthermore, the graphene at the particle surfaces can assist to maintain electrical contact and stabilize the solid electrolyte interphase upon the large volume change of phosphorus during cycling. As a result, this composite anode delivers a high reversible capacity of 2077 mA h g^{-1} with an excellent cycling stability of 1700 mA h g^{-1} after 60 cycles. On the other hand, black phosphorus is potentially very attractive, as it has a layered structure similar to graphite but a greater interlayer distance.[512,520–523] Namely, black phosphors are composed of the two dimensional single layer of phosphorene, which has a large interlayer channel size (3.08 Å), meaning that sodium (1.04 Å) ions can be stored between the phosphorene layers. In addition, orthorhombic black phosphorous with its layered crystal structure is thermodynamically the most stable allotrope.[513] The higher bulk conductivity of black phosphorus compared with Red-P is additional advantages for electrochemical activity in Na cells.[514,515] Hembram et al. proposed an atomistic mechanism for the sodiation of black phosphorus, based on first principles calculations.[521] The layered structure of black phosphorus is maintained up to the composition of Na$_{0.25}$P, with one-dimensional sodiation (an intercalation process) occurring in the interlayer spaces of the black phosphorus, resulting in sliding of the phosphorene layers because one Na atom tends to bind to four P atoms. At Na levels beyond Na$_{0.25}$P, the intercalation process changes to an alloying process. Although the sodiation mechanism changes from an intercalation process to an alloying process at critical composition of Na$_{0.25}$P, the volume expansion of black phosphorus increases linearly with Na concentration. Ramireddy et al. prepared nanocomposites of black (orthorhombic) phosphorus with graphite carbon via ball milling and applied the electrochemical test at different cut-off voltage windows.[516] Within the voltage window of 0.01–2 V Na/Na$^+$, the composite anode exhibited a high initial capacity of 1300 mA h g^{-1}, however, the capacity gradually decreased. In contrast, attractive stable cyclic performances over 100 cycles were observed in the voltage windows of 0.33–2.0 V vs. Na/Na$^+$. The post-cycling SEM studies showed that the electrodes gradually disintegrated and delaminated from the current collectors when electrochemical testing was performed within a larger potential window of 0.01–2.0 V vs. Na/Na$^+$. However, this effect was absent for the restricted potential windows of 0.33–2.0 V vs. Na/Na$^+$, leading to stable cyclic performances. To achieve both high capacity and stable cyclability, Sun et al. proposed a nanostructured phosphorene–graphene hybrid with a few phosphorene layers sandwiched between graphene layers[512] (Fig. 39f). They also investigated the two-step sodiation mechanism of intercalation and alloying using in situ transmission electron microscopy (TEM) and ex situ X-ray diffraction (XRD) techniques. This nanoarchitecture delivers several advantages: (1) the graphene layers provide an elastic buffer layer to accommodate the anisotropic volumetric expansion during the sodiation process, (2) the phosphorene layers with an increased interlayer distance offer a short diffusion length for sodium ions, and (3) the graphene layers function as an electrical highway. As a result, the phosphorene–graphene hybrid nanostructure exhibited an extremely high specific capacity of 2440 mA h g^{-1} at 0.05 A g^{-1} and 83% capacity retention after 100 cycles in the voltage range of 0–1.5 V vs. Na/Na$^+$. Recently, to provide an in-depth understanding of the reaction mechanism and the solid electrolyte interface (SEI) formation process of black phosphorous anodes in Na cells, Dahbi et al. investigated the structural change upon the sodiation/desodiation process via ex situ XRD analysis and electrode/electrolyte interfaces via powerful surface characterization techniques such as HAXPES and TOF-SIMS analyses.[522] In the as-prepared electrode, black P exists as a crystalline phase with the orthorhombic lattice. In the full reduction state at 0 V in Na cells, orthorhombic black P changes into trisodium phosphide (Na$_3$P) with a hexagonal lattice.

This journal is © The Royal Society of Chemistry 2017

Chem. Soc. Rev., 2017, 46, 3529–3614 | 3585
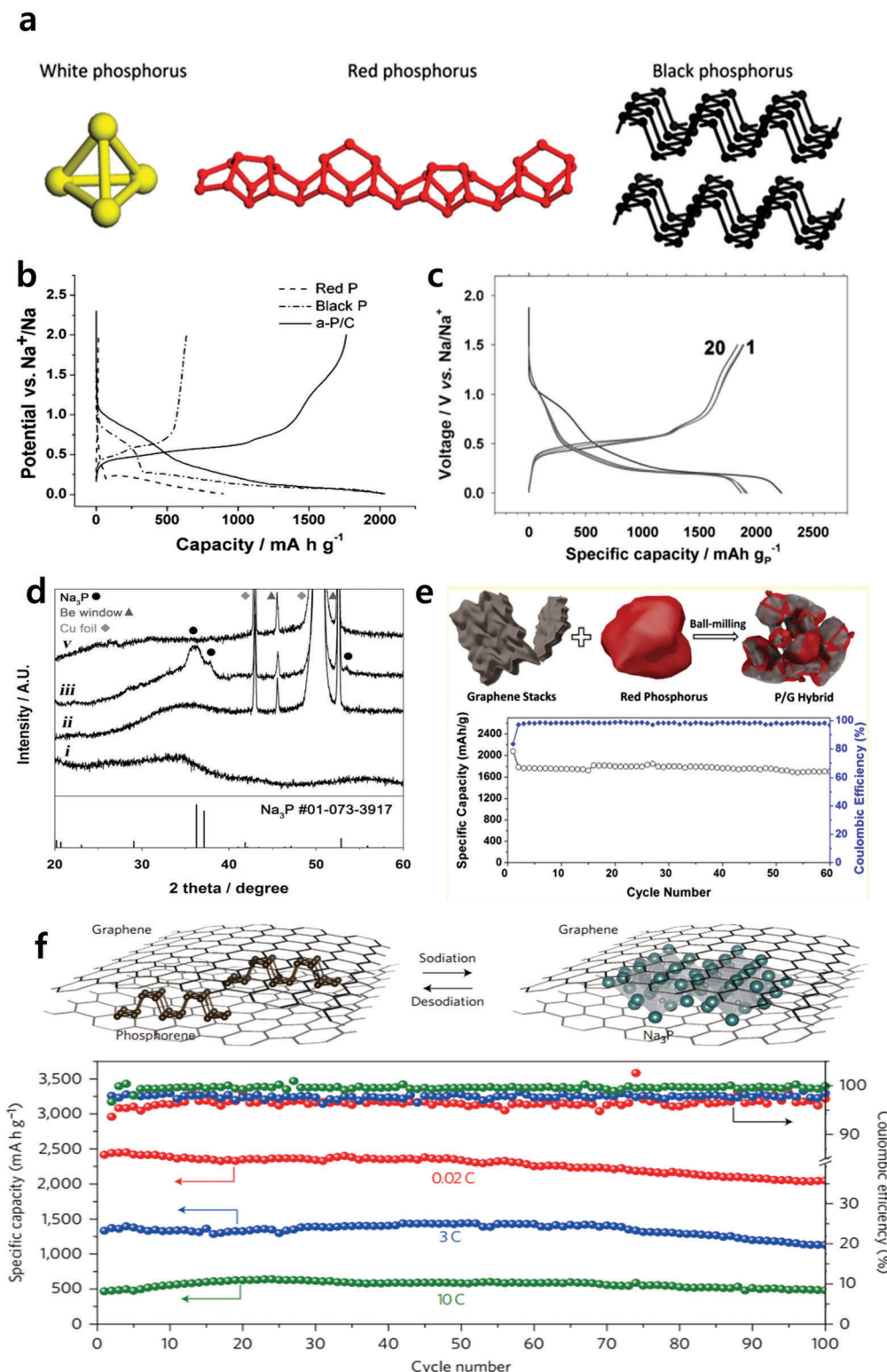
Fig. 39 (a) Schematics of white, red, and black phosphorus. (Reproduced with permission from ref. 518, Copyright 2014 American Chemical Society.) (b) Initial charge/discharge curves of three phases of phosphorus: red phosphorus, black phosphorus, and a-P/C nanocomposites. (Reproduced from ref. 514 with permission, Copyright 2013 Wiley-VCH Verlag GmbH & Co. KGaA.) (c) Charge–discharge voltage profile of the red P/C composite electrode. (d) *Ex situ* XRD patterns of amorphous red P/C composite electrodes. (Reproduced from ref. 511 with permission, Copyright 2013 Wiley-VCH Verlag GmbH & Co. KGaA.) (e) Schematic Illustration of the synthesis of phosphorus/graphene nanosheets (P/G) hybrid and its cycling performance. (Reproduced with permission from ref. 513, Copyright 2014 American Chemical Society.) (f) Structural evolution of the sandwiched phosphorene–graphene structure during sodiation and cycling performance of phosphorene/graphene composites at different current density. (Reproduced by permission from ref. 512, Nature Publishing Group, Copyright 2015.)

The reduction product is found to be the same as red P. After forming Na_3P, the cell is oxidized to 2.0 V, and reformation of the crystalline phase of black P was not found. This observation shows that black P is a metastable polymorph, and amorphous P would be formed as the oxidation product in the Na cell.[522,524] They also observed that the VC-added electrolyte especially improves the reversible capacity and achieves a longer cycle life for black P electrodes with $NaPF_6$ in EC/DEC by forming the stable SEI. On the other hand, Xu *et al.* proposed a black phosphorous–ketjenblack-multiwalled carbon nanotube composite with a high phosphorous loading of 70% as an anode for SIBs.[524]

3.3.2.3. Bismuth. Bismuth (Bi), belonging to the same group in the periodic table as phosphorus and antimony, has been recently regarded as a potential anode material for LIBs[525,526] and SIBs[527–531] due to the unique layered crystal structure with a large interlayer spacing. Ellis *et al.* reported that the sodiation and desodiation mechanisms reversibly follow the Na–Bi equilibrium phase diagram with the formation of NaBi and Na_3Bi.[527] Bi reacts with Na to form Na_3Bi, giving a theoretical capacity of 385 mA h g^{-1}. Later, Sottmann *et al.* showed that alloying of sodium and bismuth proceeds *via* two distinct structural mechanisms depending on the crystallite size in the Bi/C anode.[529] The transformation of NaBi into c-Na_3Bi (c: cubic) requires less disturbance of the crystal structure than NaBi into h-Na_3Bi (h: hexagonal) conversion. According to their report, phase fractions of the Na–Bi phases in the charged (2 V) and discharged state (0 V) in the 100th cycle show that c-Na_3Bi is favored in the nanocrystalline anode as it forms on the crystallite surfaces. On the other hand, through DFT simulations, Su *et al.* calculated that Bi could provide facile sites for Na$^+$ ion diffusion and accommodation, based on the intercalation mechanism instead of the alloying process.[530] Their *ex situ* XRD and TEM results consistently showed that bismuth undergoes the Na$^+$ ion intercalation process in Na cells. They also prepared a bismuth–graphene nanocomposite (Bi@graphene) and demonstrated its sodium storage performances in a bismuth crystal structure. The Bi@graphene nanocomposite demonstrated reasonable rate performance ascribed to the unique layered crystal structure of Bi, which has a large interlayer spacing along the *c*-axis (d(003) = 3.95 Å) to accommodate the Na$^+$ ions.

3.3.3 Binary inter-metallic compounds. Another approach to develop a high-performance anode materials is design of binary intermetallic alloys which is resulting in new physio-chemical properties. Most studies on binary alloys are focused on developing, in particular, Sn–M and Sb–M compounds (M = metal). Among them, secondary element M is classified into two main categories; namely, electrochemical inactive elements[532–537] (Ni, Cu, Fe, Zn and Mo) and electrochemical active elements[538–541] (Sn, Sb, Bi) through an alloying–dealloying reaction with Na. During the sodiation/desodiation process, these compounds can store Na$^+$ ions through two electrochemical reaction mechanisms of conversion and alloying. In this binary compound system, the primary beneficial role of the secondary elements M is to improve the cycling performances. And, the two different intermediate phases can work as a mechanical buffer to accommodate for the volume changes, which can provide a more stable structure and more efficient electronic conduction during cycling.[532,535,542] Liu *et al.* reported highly porous Ni_3Sn_2 microcages composed of tiny nanoparticles[532] (Fig. 40a). According to their report, the Ni–Sn intermetallic anode can act as storage for Na ions *via* the following sodiation–desodiation mechanisms: $Ni_3Sn_2 + 7.5Na^+ \, 7.5e^- \rightarrow 2Na_{3.75}Sn + 3Ni$, $Na_{3.75}Sn \rightarrow Sn + 3.75Na^+ + 3.75e^-$. After the first sodiation process, the Ni_3Sn_2 porous microcages are converted into both *in situ* formed zero-dimensional electroactive Na–Sn particles and three-dimensional conducting Ni in hollow matrix form. The mechanical strain of Sn during charge/discharge processes is effectively suppressed by the hollow core structure and the presence of the Ni matrix in the hollow microcages. Moreover, homogeneously encapsulated Ni converted from the sodiation of Ni_3Sn_2 is beneficial for the necessary electron transport. As a result, it demonstrated a high reversible capacity of 348 mA h g^{-1} and a stable cycle retention of ∼91% after 300 cycles at a 1C-rate. Antimony based binary intermetallic compounds, including copper–antimony (Cu_2Sb) and iron–antimony ($FeSb_2$) compounds, were also investigated.[533,534] During the sodiation process, the reaction starts with the conversion of Cu_2Sb and $FeSb_2$ followed by the formation of nanocrystalline Na_3Sb and the amorphous phase of Na–Cu–Sb and Fe_4Sb, respectively. However, the irreversible formation of intermediate compounds leads to a lower reversible storage capacity than that for a pure Sb electrode. On the other hand, in the case of active alloying elements, Sn–Sb and Sn–P (in Section 3.2.3.1) binary-compounds have received much attention as anode materials for SIBs due to their high reversible capacity and stable capacity retentions. Xiao *et al.* reported a high capacity with the reversible alloy reaction in SnSb/C nanocomposites for SIBs for the first time.[499] Based on the CV results, they demonstrated Na$^+$ storage, which is composed of the alloying–dealloying reaction of Na–Sb and Na–Sn as well as Na insertion into super P carbon (Fig. 40b). Further, initial charge–discharge voltage profiles of SnSb/C nanocomposite electrodes revealed two main plateaus, of which the plateau in the higher potential region (around 0.45 V at discharge and 0.58 V at charge) is mainly related to the Na–SnSb alloying–dealloying reaction that produces Na_3Sb and metallic Sn. The plateau in the lower potential range (0.05 V at discharge and 0.17 V at charge) is mainly attributed to the Na-ion insertion into super P carbon and the Na–Sn alloying–dealloying process. After initial cycles, however, most of reversible capacity is led by the alloy reactions. According to the above results, the detailed sodium storage mechanism of the SnSb/C nanocomposite electrodes can be described as follows: $SnSb + 3Na^+ + 3e^- \leftrightarrow 3Na_3Sb + Sn$, $Na_3Sb + Sn + 3.75Na^+ + 3.75e^- \leftrightarrow 3Na_3Sb + Na_{3.75}Sn$. Later, Ji *et al.* demonstrated the improved electrochemical performance of SnSb binary inter-metallic compounds through employing a porous carbon fiber and controlling the SEI formation using FEC additives.[539] These porous CNF–SnSb nanocomposite electrodes delivered a high reversible capacity of 350 mA h g^{-1} at 0.2C, an excellent capacity retention for more than 200 cycles and an enhanced reversible capacity of more than

This journal is © The Royal Society of Chemistry 2017

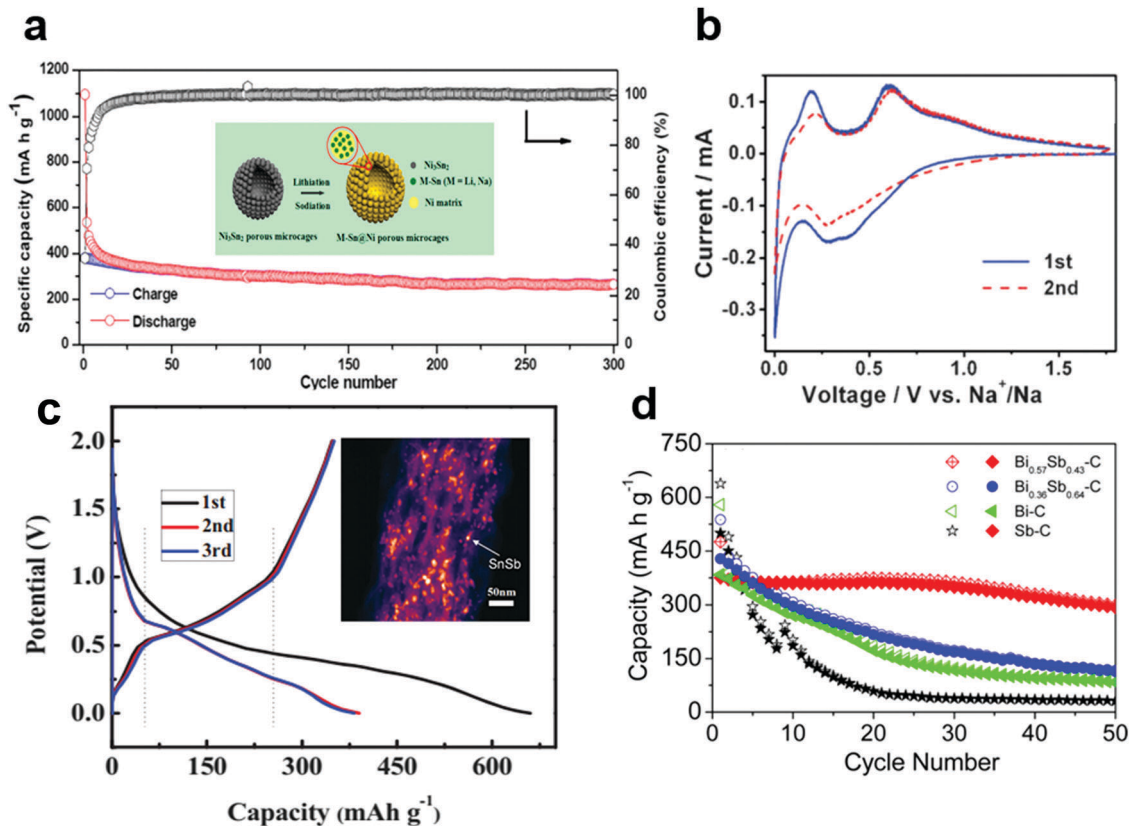*Chem. Soc. Rev.*, 2017, **46**, 3529–3614 | 3587

Fig. 40 (a) Cycling performances of Ni_3Sn_2 at a 1C-rate. Inset image represents the schematic representation of the first lithiation and sodiation of porous Ni_3Sn_2 intermetallic microcages. (Reproduced with permission from ref. 532, Copyright 2014 American Chemical Society.) (b) The initial two CV curves of the SnSb/C nanocomposite electrode from open circuit voltage to 0.0 V *vs.* Na^+/Na at a scan rate of 0.1 mV s^{-1}. (Reproduced with permission from ref. 499, Copyright 2012 The Royal Society of Chemistry.) (c) First galvanostatic charge and discharge profiles of porous CNF−SnSb electrodes. (Reproduced from ref. 539 with permission, Copyright 2014 Wiley-VCH Verlag GmbH & Co. KGaA.) (d) Cycle performance of the Sb−C, Bi−C, $Bi_{0.57}$−$Sb_{0.43}$−C and $Bi_{0.36}$−$Sb_{0.64}$−C electrode in SIB under galvanostatic conditions with a current density of 100 mA g^{-1}. (Reproduced with permission from ref. 541, Copyright 2014 American Chemical Society.)

110 mA h g^{-1} at a high rate of 20C (Fig. 40c). Recently, to design high-performance M–Sb alloy anodes with a long flat voltage profile, high capacity, and stable cycle, Zhao *et al.* proposed bismuth (Bi) for the secondary metal.[541] They fabricated a Bi–Sb–C composite anode *via* facile high-energy mechanical milling with carbon and demonstrated a high initial desodiation capacity of 375 mA h g^{-1} with a capacity retention of 78% at the 50th cycle (Fig. 40d).

As mentioned above, carbon conducting techniques for conversion and alloying materials are very effective for buffering the volume strain and creating the electric conducting pathways. Unfortunately, despite the enormous advancement, the use of such approaches still requires further development for their practical applications. The major drawbacks of carbon conducting techniques such as carbon coating and/or formation of composites for practical applications are as follows. First, a high electrolyte/electrode surface area may lead to more significant side reactions with the electrolyte. For instance, typical disadvantage of carbon coating and/or formation of composites is the irreversible capacity charge loss in the first cycle due to the SEI formation on the carbon surface that needs to be overcome during the battery charge phase. Second, the tap density of carbon coated and/or composite materials is generally decreased

compared with the same materials formed from without carbon contents. As a result, the whole capacity of the active material in the electrode is decreased and limited the total energy of the cell. Therefore, to achieve the high energy density and excellent battery performances at the same time, we should well-balance the carbon additive amount with active materials.

3.4. Organic compounds

Organic compounds have so far received less attention as potential anode materials for Li- and/or Na-ion batteries, mainly because of the success of inorganic materials in both research and commercial applications.[543] However, new requirements in secondary batteries such as flexibility accompanied by low production costs and environmental friendliness, particularly for portable devices, reach the limit of inorganic electrode materials. In this respect, organic compounds have several advantages, including their chemical diversity, tunable redox property, lightweight, mechanical flexibility and cost-effective aspects, thus offering a wide selection of applications for use in batteries.[544,545] Recently, oxocarbon salts with tailored frameworks and metal ions have been introduced as electrodes in rechargeable (Li, Na, K) batteries by Zaho *et al.*[546] Most of all, for SIBs, inorganic

compounds display poor cycling stability, mainly due to the larger ion radius of Na^+.[99,545] In contrast, the redox reaction of organic carbonyl materials is less influenced by the ionic size of alkali ions due to their soft nature.[543] Therefore, the major organic carbonyl compounds, including the conjugated carboxylates-, imides- and quinones- and Schiff base-groups, are widely investigated as promising alternative anode materials for SIBs. Despite these advantages, there still remain three major challenges to compete with high performance carbonaceous and/or inorganic compounds: (1) slow reaction kinetics from the extremely low electronic conductivity, (2) particle pulverization induced by a large volume change during the Na^+ ion insertion/extraction process and (3) chemical instability in the organic solvent upon cycling.[543] Such thresholds can induce the serious capacity fading and loss of active mass upon cycling. In this section, we discuss the Na storage performances of various organic compounds and summarized the present research achievements.

Conjugated carboxylates group compounds reveal reversible redox-reactions at low potential (0.2 to 0.5 V $vs.$ Na^+/Na) and

stable charge/discharge behavior over multiple cycles.[543–555] Carboxylate-based organic materials and terephthalate based materials were widely investigated as potential anode materials for SIBs.[532–538] Zhao $et\ al.$ firstly proposed the $Na_2C_8H_4O_4$/KB (ketjen black) composite electrode for SIBs, which has a reversible capacity of 250 mA h g^{-1}, corresponding to a two electron transfer, with excellent cycling performance[544] (Fig. 41a). In addition, ALD Al_2O_3 coating on the surface of the $Na_2C_8H_4O_4$/KB electrode significantly improves the sodium storage performances. Several disodium terephthalate derivatives such as No_2–Na_2TP, NH_2–Na_2TP, and Br–Na_2TP were introduced by Park $et\ al.$[545] According to their reports, the substituents on a phenyl ring (amino-, bromo-, and nitro-functional groups) and the regio-isomerism form of dicarboxylates ($meta$ and $para$ positions) can affect the thermodynamic and kinetic properties of disodium terephthalate and its derivatives. The results demonstrated that the Na_2TP electrode delivered a reversible capacity of about 295 mA h g^{-1} during the sodium insertion/extraction process. This reversible Na^+ ion (de)insertion of Na_2TP can be ascribed to the stabilized
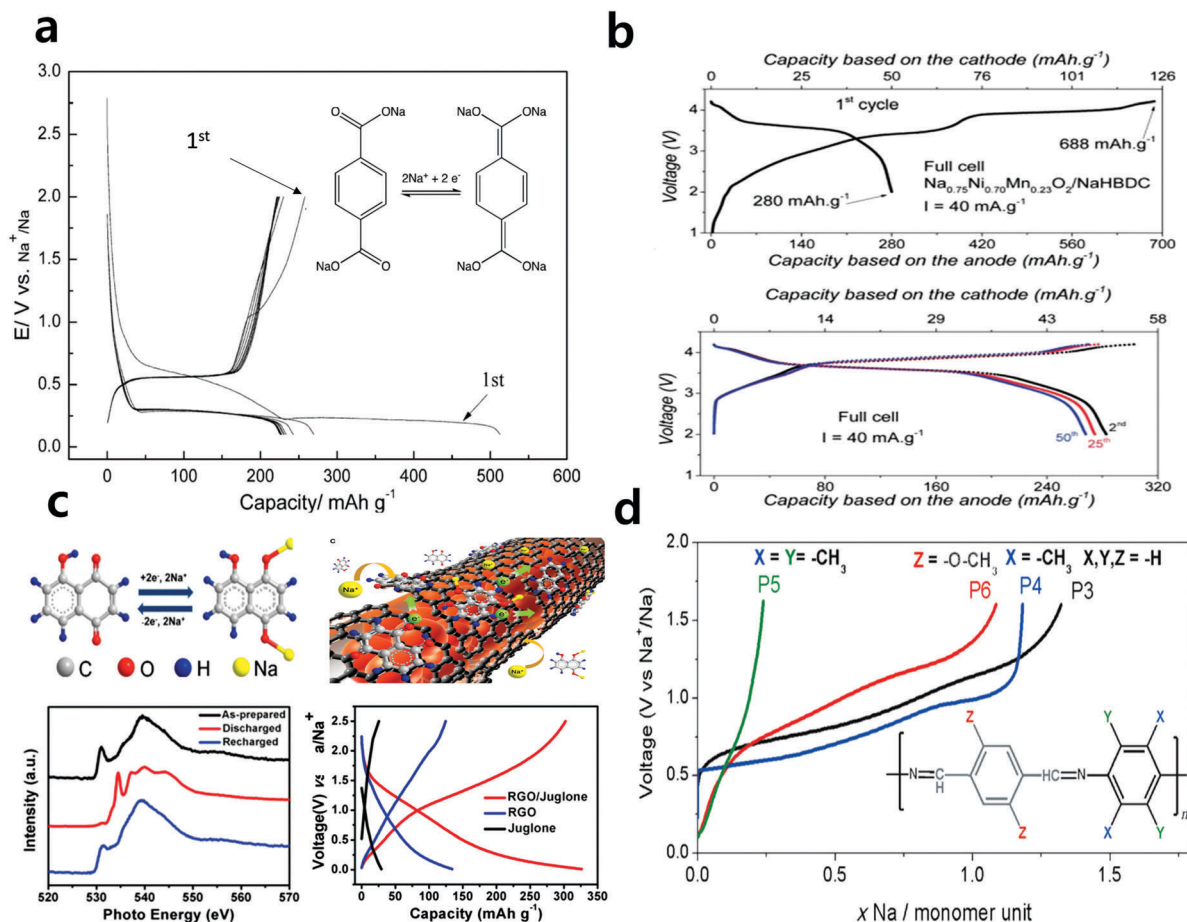
Fig. 41 (a) The discharge−charge cycles of the $Na_2C_8H_4O_4$/KB composite electrode. Inset shows the molecular structure of disodium terephthalate ($Na_2C_8H_4O_4$) and the Na insertion/deinsertion mechanism. (Reproduced from ref. 544 with permission, Copyright 2012 Wiley-VCH Verlag GmbH & Co. KGaA.) (b) First charge−discharge curves and cycling performance of $Na_{0.75}Mn_{0.7}Ni_{0.23}O_2$/NaHBDC full cell. (Reproduced from ref. 547 with permission, Copyright 2012 The Royal Society of Chemistry.) (c) Schematic diagram of juglone molecules with RGO nanosheets and the reversible sodium-ion de-/insertion mechanism (top). XANES spectra of Juglone/RGO electrodes and its capacity−voltage profiles at 0.1 A g^{-1}. (Reproduced from ref. 561 with permission, Copyright 2015 Wiley-VCH Verlag GmbH & Co. KGaA.) (d) Voltage $versus$ specific capacity for the first galvanostatic oxidation for the different polymeric Schiff bases. (Reproduced from ref. 564 with permission, Copyright 2014 Wiley-VCH Verlag GmbH & Co. KGaA.)

This journal is © The Royal Society of Chemistry 2017

Chem. Soc. Rev., 2017, **46**, 3529–3614 | **3589**

conjugated structure between the carbonyl group and the phenyl rings. Br–Na$_2$TP and No$_2$–Na$_2$TP electrodes delivered a high capacity of 300 mA h g^{-1}; however, NH$_2$–Na$_2$TP delivered a relatively low capacity of 200 mA h g^{-1}. Abouimrane et al. first incorporated a disodium terephthalate-based organic anode material into sodium-ion full cells with transition-metal cathode materials[547] (Fig. 41b). The Na$_4$C$_8$H$_2$O$_6$ electrode revealed that two reversible electrochemical reactions occurred with two redox couples of Na$_2$C$_8$H$_2$O$_6$/Na$_4$C$_8$H$_2$O$_6$ as the cathodes at 2.3 V and Na$_4$C$_8$H$_2$O$_6$/Na$_6$C$_8$H$_2$O$_6$ as the anode at 0.3 V.[236] By using symmetric reactions, Wang et al. fabricated an all-organic SIB using Na$_4$C$_8$H$_2$O$_6$, which delivered a reversible capacity of 180 mA h g^{-1} with an average operation voltage of 1.8 V. Later, to enhance the fast insertion/extraction of Na-ions at high current densities, Wang et al. suggested an extension of the π-conjugated system by using sodium 4,4'-stilbene-dicarboxylate (SSDC).[552] Remarkably, the designed electrodes exhibited a much enhanced high rate performance with reversible capacities of 105 mA h g^{-1} at a current density of 2 A g^{-1} and 72 mA h g^{-1} at a current density as high as 10 A g^{-1}. According to their report, excellent sodium storage performances under high rate charge–discharge conditions can be ascribed to the following two main reasons: (1) improvement of the charge transport and stabilization of the charged and discharged states, and (2) enhancement of the intermolecular interactions and the resulting terrace packing structure; both of these can facilitate the insertion/extraction of Na$^+$ ions. On the other hand, one main reason for the capacity fading of organic compounds is the dissolution of the active compound in polar liquid electrolytes.[556] To circumvent unwanted active mass dissolution during cycling, various strategies are introduced such as the application of polymers as active materials or the immobilization of active molecules onto the conductive additives.[543,556–558] Recently, Chen et al. proposed the use of PNTCDA, a kind of polyimide.[557] The intrinsic stability and insolubility of the polyimide ensure that it is not dissolved in the electrolyte, and thus allows for an excellent cycling stability and a high initial coulomb efficiency of 97.6%. Another promising candidate for organic compounds, biomolecule-based electrodes have also been widely studied. A biomolecule-based organic compounds contained the quinone and carbonyl group.[559–563] Recently, Wang et al. proposed renewable-juglone biomolecules with well-defined redox-active quinone carbonyl groups, which exhibit promising electrochemical performance in reversibly transferring sodium ions[561] (Fig. 41c). Also, juglone can be immobilized onto reduced graphene oxide (rGO) nanosheets owing to the strong π–π interaction between the aromatic structure and the carbon scaffold. Optical and photoelectron spectra results demonstrated non-covalent immobilization of the redox molecules via π–π interactions on the rGO carbon scaffold, which suppresses the dissolution puzzle of organic materials and enhances both the conductivity and sodium-ion accessibility of the electrode. As a result, juglone/RGO electrode demonstrated a high capacity of 305 mA h g^{-1} and stable cycle retention after 100 cycles. Armand's group reported polymeric and oligomeric Schiff-based electrodes[564,565] (Fig. 41d). Polymeric Schiff bases have the (N=CH–Ar–HC=N) repeat unit, which can work as a

redox center for sodium storage.[551] The reduction reaction proceeds in two steps in the voltage range from 0.005 to 1.6 V versus Na$^+$/Na corresponding to two different processes. Later, the oligomeric Schiff bases are also investigated. López-Herraiz et al. reported for the first time the electrochemical activity of the 10-π-electron end group (–OOC–ϕ–CQN–) (ϕ: refers to the phenyl group) and the central (–NQC–ϕ–CQN–) Hückel units.[565] They claimed that the maximum capacities are achieved for oligomers in which H$^+$ ions are replaced by Na$^+$ ions due to the fact that the hydrogen bond of the carboxylic end groups acting as crosslinks is removed, thus helping to accommodate more easily for the inserted Na$^+$ ions.

4. Electrolytes, additives, and binders

SIB technology is a very important and promising follow-up to LIB technology. The significance of SIBs is cost effectiveness owing to the geographical distribution of sodium in comparison with lithium. Therefore, in the long term, sodium-ion batteries will replace and/or substitute lithium-ion batteries in mid-large scale battery market.[566] However, SIBs have still faced several challenges in terms of developing optimized electrode materials and electrolytes with a suitable capability for stable sodium storage. To date, while a number of efforts have been directed toward the searching for new electrode materials for SIBs, studies dealing with the electrolyte itself are much scarcer.[28,567] However, looking back through the history of LIBs, it is clear that a suitable choice of electrolyte and binders is equally as important as the choice of electrode material for making operational SIBs; this is because the electrolyte and binders form a protective layer at both the cathode and anode, the surface layer (SL) and the solid electrolyte interfaces (SEI), respectively.[568] Therefore, identifying suitable formulation electrolytes is indispensable to developing high performance SIBs. To accomplish this, we borrow ideas and techniques from those typically used in LIB electrolyte development. In the case of LIBs, various electrolytes, including organic electrolyte solutions, solid- and gel-polymer electrolytes, inorganic solid electrolytes, and ionic liquids have been investigated, and their development is still in progress.[99] Organic electrolyte solution based on carbonate-ester polar solvents, where sodium salts are dissolved with complex containing functional additives, are mainly used in the practical development of SIBs due to their large potential window, high ionic conductivity and good temperature performance. On the other hand, a water-based electrolyte has also been proposed as a cost-effective energy storage system, which was successfully commercialized.[18,569] In this section, we discuss SIB electrolytes, including salts, solvents, and additives. In addition, we briefly summarized the currently employed binders as well as their effects on the electrochemical performances based on various electrodes and/or sodium ion full cells.

4.1. Electrolytes

A general list of properties needed for SIB electrolytes complies with those usually compiled for LIB oriented electrolytes: (1) chemically stable, (2) electrochemically stable, (3) thermally

3590 | Chem. Soc. Rev., 2017, 46, 3529–3614

This journal is © The Royal Society of Chemistry 2017

stable, (4) ionically conductive and electronically insulating and (5) low toxicity with low production cost.[570,571] These features intrinsically depend on the nature of the salts and the solvents as well as the possible use of additives. For suitable electrolytes, we should consider the major parameter of solvents and salts, which can mainly affect the cell performances. The salt should exhibit: (1) solubility in the solvent, (2) stability *vs.* reduction as well as oxidation, and (3) chemical stability with the cell component.[568] The solvent should: (1) be polar with a high dielectric constant, (2) exhibit low viscosity in order to improve the ionic mobility, (3) remain inert to the charged surfaces of the cathode and the anode during cell operation, and (4) have a wide liquid range (*i.e.* a low melting point and a high boiling point).[568] Over the past few decades, based on such basic properties, the scientific community has made tremendous efforts in finding the best combination of suitable electrolytes; however, not yet currently available for the direct use for practical SIBs. While being of only academic interest, carbonate ester-based electrolyte solution containing sodium salts is considered to be one of the most appropriate electrolyte media for SIB applications. In early reports, in the 1980s, the properties of sodium ion cells are tested using NaI, $NaPF_6$, and $NaClO_4$ salts in organic solvents as the electrolyte.[572,573] Then, either $NaClO_4$ or $NaPF_6$ is used as the electrolyte salts in carbonate-ester binary or ternary mixtures, which have become the main stream electrolyte composition used for Na^+ chemistry.[571]

Although the sodium perchlorates have some concern of safety and are notoriously difficult to dry, in terms of only academic interest, the commonly used salt is $NaClO_4$ due to a combination of historical and cost reasons.[28,570,573] Delmas *et al.* demonstrated the electrochemical properties of a P2-type Na_xCoO_2 electrode in $NaClO_4$ in a propylene carbonate solvent.[573] In 2000s, D. A. Stevens and J. R. Dahn *et al.* investigated the reversible insertion of sodium into hard-carbon host structures at room temperature in 1 M $NaClO_4$ in EC : DEC (30 : 70, v/v) as an electrolyte.[247] Alcantara *et al.* reported the dependency of sodium salts on the electrochemical properties of carbonaceous materials using $NaPF_6$ and $NaClO_4$ salts in EC : DMC 1 : 1 mixture solvents.[575] They suggested that using a sodium $NaClO_4$ based electrolyte for a carbonaceous electrode demonstrated a higher capacity with high Coulombic efficiency. They also reported the dependency of electrolyte solvents on the electrochemical properties of carbonaceous materials using an EC : DMC, DME, and EC : THF solvent containing 1 M $NaClO_4$ salt (Fig. 42a). The THF-solvent and EC : THF mixture have shown to improve the electrochemical performance as compared to only carbonate-based solvents. Komaba *et al.* investigated electrochemical performance of hard carbon anodes in Na cells with various electrolyte solvents of EC, PC, BC, EC : DMC (50 : 50, v/v), EC : EMC (50 : 50, v/v), EC : DEC (50 : 50, v/v), and PC : VC (98 : 2, v/v) containing 1 M $NaClO_4$ salt in beaker-type cells.[27] The results show that 1 M $NaClO_4$ in PC, EC and EC:DEC solution demonstrated better electrochemical performances than the other
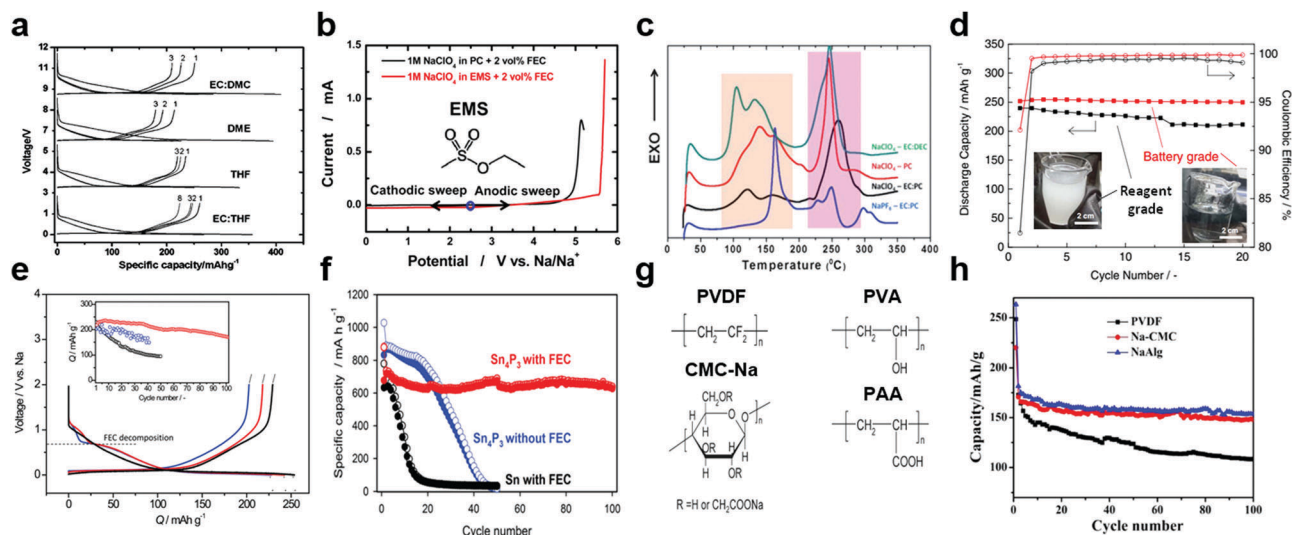
Fig. 42 (a) Voltage/capacity plots corresponding to the first discharge/charge cycles of carbon aerogel microspheres in sodium cells, 1 M $NaClO_4$ dissolved in EC:DMC, DME, THF, and EC:THF as electrolytes. (Reproduced with permission from ref. 575 Copyright 2005 The Electrochemical Society.) (b) Linear sweep voltammetry of a sodium cell using two electrolytes, namely, 1 M $NaClO_4$ in PC + 2 vol% FEC and 1 M $NaClO_4$ in EMS + 2 vol% FEC. (Reproduced with permission from ref. 51, Copyright 2014 American Chemical Society.) (c) DSC heating curves of fully sodiated hard carbon in various electrolyte formulations. (Reproduced with permission from ref. 28, Copyright 2012 The Royal Society of Chemistry.) (d) Comparison of capacity retention of hard carbon electrodes between reagent grade and battery grade $NaPF_6$ PC solution. Photographs of the electrolyte solution use are inserted. (Reproduced with permission from ref. 18, Copyright 2015 The Electrochemical Society.) (e) Initial reduction/oxidation curves for hard-carbon electrodes in 1 M $NaClO_4$ PC solution without and with FEC. Inset shows variation in reversible oxidative capacities for the hard-carbon during successive cycle test. (Reproduced with permission from ref. 577, Copyright 2011 American Chemical Society.) (f) Cycle performance of Sn_4P_3 and Sn electrodes obtained with or without an FEC additive. (Reproduced from ref. 460 with permission, Copyright 2014 Wiley-VCH Verlag GmbH & Co. KGaA.) (g) Structure of polymer binder: PVDF, PVA, CMC-NA, PAA. (Reproduced with permission from ref. 610, Copyright 2011 American Chemical Society.) (a) Cyclic performance of $Na_{0.11}Li_{3.89}Ti_5O_{12}$ electrodes with different binders. (Reproduced with permission from ref. 616, Copyright 2016 The Electrochemical Society.)

mixture solutions. Interestingly, VC is commonly accepted as a suitable additive to modify the interface *via* thin film forming of the electrodes; however, the addition of VC in a PC solvent was not found to play the same role in hard carbon electrodes. Appropriate additives for SIBs are specifically discussed in the additive part. On the other hand, anodic stability without electrolyte decomposition at high voltage is also a crucial issue for achieving practical SIBs without gas evolution and battery swelling.[568] Recently, Oh *et al.* proposed an ethyl methanesulfonate-based (EMS) electrolyte containing the NaClO$_4$ salt (Fig. 42b). A high anodic stability (up to 5.6 V *versus* Na/Na$^+$) and ionic conductivity (6.0 × 10^{-3} S cm^{-1}) can be achieved by replacing the PC with EMS.[51]

On the other hand, in order to realize practical SIBs, many researchers have explored alternative Na salts with high battery performances as well as good battery safety. Ponrouch *et al.* systematically investigated the most appropriate electrolyte formulation so as to minimize the interface reactions and enhance both cell performances and safety aspects.[28] They evaluated the basic properties of the electrolyte solution such as viscosity, ionic conductivity, and thermal and electrochemical stability in diverse solvent mixtures and Na-based salts having either F-based or perchlorate anions. Especially, safety issues, in which they evaluated the thermal stability using fully reduced hard carbon powders in the selected electrolytes *via* DSC measurements: (i) NaClO$_4$ in PC, (ii) NaClO$_4$ in EC:PC, (iii) NaClO$_4$ in EC:DEC and (iv) NaPF$_6$ in EC:PC. Among them, NaPF$_6$ in the EC:PC electrolyte exhibited the high thermal stability with a first exothermic peak onset temperature of 156.2 °C and a low heat generation of 717.2 J g^{-1} (Fig. 42c). The appearance of an exothermic peak at a high temperature of NaPF$_6$ in the EC:PC electrolyte can be ascribed to how a significantly more thermally stable SEI layer is formed on a hard carbon surface after cycling compared to those of the other electrolytes. On the other hand, Komaba *et al.* observed the stable cycling performances in hard carbon electrodes with the NaPF$_6$-based electrolyte solution in comparison to those of the NaClO$_4$-based electrolyte.[27] Bhide *et al.* carried out a comparative study of the physico-chemical properties of non-aqueous liquid electrolytes based on NaPF$_6$, NaClO$_4$ and NaCF$_3$SO$_3$ salts in the binary mixture of ethylene carbonate (EC) and dimethyl carbonate (DMC).[576] Bhide *et al.* also observed that the NaPF$_6$-based electrolyte demonstrated a higher ionic conductivity as a function of composition and temperature. Additionally, in view of practical Na-ion battery systems, the electrolytes are electrochemically tested with Na$_{0.7}$CoO$_2$ as a cathode. The results showed that the electrolyte NaPF$_6$–EC:DMC is favorable for the formation of a stable surface film and the reversibility of the Na$_{0.7}$CoO$_2$ cathode material. Ponrouch *et al.* also achieved a high rate capability for the Na$_3$V$_2$(PO$_4$)$_2$F$_3$ cathode and the hard carbon/Na$_3$V$_2$(PO$_4$)$_2$F$_3$ full cell in 1 M NaPF$_6$ in the EC:PC:DMC (45:45:10, v/v) electrolyte.[574] However, when using the NaPF$_6$ containing electrolyte for the electrode materials, negative effects also occurred, such as low ionic conductivity of the SEI formation associated with the presence of NaF. In addition, Bhide *et al.* proved the

presence of NaF in NaPF$_6$ using X-ray diffraction and the observation of the insoluble fraction in NaPF$_6$/EC:DMC solution by the naked eye when exceeding concentrations of 0.4 M.[576] Recently, Kubota *et al.* discuss the influence of the NaPF$_6$ salts with different purities on the solubility of the organic solvents and the electrochemical properties.[18] When they tried to dissolve the reagent grade NaPF$_6$, 1 M NaPF$_6$ was not completely dissolved in PC. However, by selecting the battery grade NaPF$_6$, 1 M NaPF$_6$ in the PC solution was revealed to be colorless and transparent because of the complete dissolution of 1 M NaPF$_6$. As anticipated from the electrolyte coloration, the hard carbon anode exhibited better electrochemical performances in the battery grade NaPF$_6$ containing electrolyte solution (Fig. 42d). The above results convinced that the choice of a well-balanced mixture solvent and high purity Na-salt is very important for identifying suitable electrolyte solutions.[567,568,570]

Recently, for improving the Na storage performances, ether-based electrolytes also have been reported for SIBs.[259,261,262,413,429,453,578–581] Especially in graphite anodes, it is found that by using ether-based electrolytes rather than conventionally used ester-based electrolytes, the co-insertion of solvent and sodium ions can be successfully achieved. Kim *et al.* and Zhu *et al.* systematically studied the application and the mechanism of graphite as an anode material for SIBs in some ether-based electrolytes.[259,262] Some research groups enabled transition-metal disulfides to achieve high-rate capability and long-term cyclability by optimizing the electrolytes and voltage windows in ether-based electrolytes. With regard to transition-metal chalcogenides, ether-based electrolytes exhibited a higher solvent-salt stability and a lower reaction energy barrier than those of carbonate-based electrolytes.[407,413,429,578]

4.2. Additives

Another major component, often needed to create a functional electrolyte is the choice of additives. Generally, additives are used in functional electrolyte formulations for stable SEI formation and to enhance its electrochemical stability, and are also required for battery safety issues such as reducing flammability and preventing overcharging processes.[99,569,577] Komaba *et al.* examined and compared the electrochemical performance of Na cells with several additives in 1 M NaClO$_4$ in PC solution, including fluoroethylene carbonate (FEC), trans-difluoroethylene carbonate (DFEC), ethylene sulfite (ES), and vinylene carbonate (VC), which are well-known to be efficient electrolyte additives for Li-ion batteries.[577] The results demonstrated that FEC is the only efficient electrolyte additive for both the cathode and anode. According to Komaba *et al.*'s reports, an appropriate amount of FEC additive (2 volume%) is helpful for forming high quality passivation films on the electrode surface, as well as for suppressing the side reactions between the Na metal and propylene carbonate solution containing Na salts (Fig. 42e). Meanwhile, Ponrouch *et al.* observed a decrease in specific capacity and Coulombic efficiency of the hard carbon electrode when FEC was used in the EC:PC solution containing 1 M NaClO$_4$ salt.[249] Unlike the PC only based electrolyte, the EC:PC mixture based electrolyte promoted efficient SEI layer

formation on the hard carbon electrode surface without the need of FEC additives. Recently, Dahbi *et al.* reported the electrochemical sodium insertion for hard carbon in a cyclic alkylene carbonate based (PC, PC/EC) solution containing a $NaClO_4$ or $NaPF_6$ salt with or without a fluoroethylene carbonate (FEC) additive to study electrolyte dependency for sodium-ion batteries.[588] According to their report, by adding a FEC additive in both $NaPF_6$ and $NaClO_4$ based electrolytes, the hard carbon electrode exhibited an additional voltage plateau at approximately 0.7 V *vs.* Na/Na^+ during the first reduction due to decomposition of FEC and delivered a higher reversible capacity than without a FEC additive electrolyte. Namely, the irreversible reaction during the initial cycle in both $NaPF_6$ and $NaClO_4$ based electrolytes was effectively suppressed by the FEC additive, which enhanced the reversibility of hard carbon anodes. The passivation layer would be further stabilized and become a thinner surface layer in the presence of FEC because the fluorine compounds dissolved in the electrolyte would efficiently induce the formation of an electronically insulating, ionically conducting, and insoluble surface layer to effectively passivate the electrode surface.

On the other hand, the significant influence of the electrolyte additive is clearly observed in alloying and/or conversion reaction based anodes.[384,460,539,561,564] Such electrode materials accompany dramatic volume changes, which has led to severe electrode pulverization upon the sodiation–desodiation process. Therefore, a stable passivation film on an electrode surface is required for effectively preventing such drawback. The formation of stable SEI films can stabilize the electrode and improve the migration kinetics of Na by using FEC additives. The main components of FEC-containing electrolytes were proposed as important compounds in effectively protecting surface films. The final SEI composition can be affected by a multitude of different factors, such as the order of the bond breaking events, the relative stability of resulting radical ions, and the thermodynamic feasibility of different decomposition reactions.[582] When FEC free electrolytes were used in Na cells, the XPS results suggest that the SEI in SIBs has a higher percentage of inorganic salts, alkyl carbonates, and C=O rich compounds, which are unstable upon electrochemical cycling.[352,486] Recently, Dahbi *et al.* reported the possible mechanism for FEC reduction reactions in Na cells.[522] In addition, Kumar *et al.* proposed the reaction pathways for the reduction induced decomposition of FEC–Na^+ in one electron reduction states.[583] When FEC is added in a Na cell, it is believed that FEC reduces first, then polymerizes through the opening of a five-membered ring, and forms very thin and stable protective films which may contain NaF, Na polycarbonate and polyenes (oxygen-free polymer).[584–587] As a result, previous reports have indicated that FEC addition in organic electrolyte solutions leads to a significant improvement of the cyclability. Kim *et al.* and Li *et al.* examined and compared electrochemical performances of tin–phosphide electrodes with/without FEC additives[460–462] (Fig. 42f). More recently, Dahbi *et al.* investigated the electrode/electrolyte interface and reported the positive effect of VC additives in black phosphorous electrodes.[522] VC added electrolytes

especially improve the reversible capacity and achieve a longer cycle life for black P electrodes with $NaPF_6$ in EC/DEC. The outermost surface layer of the SEI in the VC additive is composed of both inorganic and organic compounds. According to their report, the organic compounds that contain fragments (m/z = 55 ($C_5H_7^+$), 57 ($C_4H_9^+$), 67 ($C_5H_7^+$), 69 ($C_5H_9^+$), 71 ($C_5H_{11}^+$), and 83 ($C_6H_{11}^+$) in TOF-SIMS result) play an important role as components of SEI layers in the electrode, which results in the improvement of electrochemical performance and suppression of SEI dissolution. On the other hand, VC did not form efficient surface layer films on hard-carbon electrodes with $NaClO_4$ in PC.[577]

As mentioned above, a solid electrolyte interphase (SEI) is one of the crucial determinants of battery life. The final SEI composition can be affected by a multitude of different factors, such as the order of the bond breaking events, the relative stability of resulting radical ions, and the thermodynamic feasibility of different decomposition reactions.[582] Previous studies suggested that prolonged decomposition of electrolytes forming a thick and unstable solid–electrolyte interphase continues to be a major drawback in designing sodium-ion batteries. Recently, Kumar *et al.* investigated the fundamental mechanisms of solvent decomposition involved in SEI formation in SIBs using the density functional theory (DFT) method.[583] According to their calculations, in EC based electrolytes, the high reduction potential and a low barrier for the ring opening of EC is the main cause for the continuous growth of a SEI in SIBs. They also studied the effect of additive molecules on the decomposition pathways of the EC. On the other hand, Dahbi *et al.* reported the formation mechanism and the main component of surface films on the phosphorus and hard carbon electrode with different electrolyte solutions.[522,588] In the $NaPF_6$ based electrolyte, they proposed the decomposition mechanism of $NaPF_6$ in the electrolyte in the following four step. (1) $NaPF_6 \leftrightarrow NaF + PF_5$, (2) $PF_5 + nNa^+ + ne^- \rightarrow Na_xPF_y + NaF$, (3) $NaPF_6 + H_2O \rightarrow NaF + POF_3 + 2HF$ and (4) $POF_3 + nNa^+ + ne^- \rightarrow Na_xPOF_y + NaF$. In other words, $NaPF_6$ is reduced to a gaseous product, phosphorus pentafluoride (PF_5), according to step 1. F^- ions are also released and react with Na^+ ions in the electrolyte to form NaF on the electrode surface. They also suggested the possible mechanism for additive (FEC and VC) reduction reactions in Na cells. When FEC is added in a Na cell, it is believed that FEC reduces first, then polymerizes through the opening of a five-membered ring, and forms very thin and stable protective films which may contain NaF, Na polycarbonate and polyenes (oxygen-free polymers). In contrast, VC-based electrolytes are also reduced, resulting in the formation of oxygen-containing species. The electrochemical reduction of VC forms $CHCHCO_2^-$ radical anions, which could be stabilized by Na^+ cations in Na cells. They speculate that such organic compounds that contain fragments play an important role as components of the SEI in the electrode. Such results clearly show that the additive molecules protect solvent molecules from reductive decomposition but also they can promote alternate pathways for decomposition, leading to qualitatively different and potentially stable SEI products.[584–587]

4.3. Ionic liquids, polymer electrolytes, all-solid electrolytes

The study of ionic liquids (ILs) and polymer electrolytes containing a fraction of sodium salts is still at a very early stage.[99,568] Ionic liquids generally have a negligibly low volatility, non-flammability, and high thermal and electrochemical stability. The use of an ionic liquid electrolyte solution has been introduced by several research groups.[589–592] However, unsolved drawbacks such as high viscosities at room temperature and expensive production cost still remain for practical utilization as an electrolyte in SIBs. Polymer electrolytes are mainly considered as solvents because of their thermal, and chemical stabilities, as well as their flexibility for cell manufacturing.[568] In addition, all-solid-state batteries with inorganic solid electrolytes and electrodes are promising power sources for a wide range of applications because of their safety, long-cycle lives and versatile geometries.[18,99,568,593–597] By West et al. a Na/NaClO$_4$-PEO/V$_2$O$_5$ cell was proposed in 1985 to avoid the use of a Na metal anode.[593] Later, Ma et al. reported on a SIB cell built using Na$_{0.7}$CoO$_2$ as the cathode, Na$_{15}$Pb$_4$ as the anode and NaTf(PEO)$_8$ as the solid polymer electrolyte.[72] A phosphate-based all-solid-state symmetrical cell, Na$_3$V$_2$(PO$_4$)/Na$_3$Zr$_2$Si$_2$PO$_{12}$/Na$_3$V$_2$(PO$_4$), has been successfully fabricated, but the reported electrode performances are for under 80 °C conditions.[596] Recently, Hayashi et al. realized an all-solid-state rechargeable sodium cell based on a Na-Sn/Na$_3$PS$_4$ glass-ceramic/TiS$_2$ cell configuration at room temperature. Although the capacity was limited to approximately 40% of the theoretical capacity of TiS$_2$, the all-solid-state cell has the potential to realize good charge–discharge reversibility at ambient and moderate temperatures.[597]

In summary, the main electrolyte for practical use in SIBs is as follows. First, NaPF$_6$ has been largely used as electrolyte salts in carbonate-ester binary or ternary mixtures, which have become the main electrolyte composition used for SIBs. Second, propylene carbonate (PC) is a key component in both binary and ternary solvent mixtures, which has intrinsic advantages derived from its high dielectric constant and wide operating electrochemical and temperature windows.[568] Third, the use of FEC as an additive plays the important role of stable passivation film formation on the electrode surface, which effectively prevents electrode destruction as a result of the sodiation–desodiation process.[577] Finally, the choice of high purity solvents and Na-salt is necessary for identifying a suitable electrolyte solution.[18,28,568,574]

4.4. Binders

Another important key component to improving the electrode performance is the choice of a binder used for powdery active materials. Especially, in anode materials, Na storage performances are dramatically affected by selecting the appropriate binders. Thus, investigation of desirable binders is also necessary to stabilize the electrode surface and suppress electrode distortion during the sodiation–desodiation process. Commonly, most electrodes of commercial and/or scientific studies are made using poly(vinylidene fluoride) (PVDF) as a binder to form an electrode layer from a powdery electrode material on a metal current collector due to its good chemical and electrochemical stabilities.[99] However, some problems remain in terms of making electrode slurries, such as the relatively high production cost and the necessary use of a volatile and toxic organic solvent (N-methyl pyrrolidone).[99,598,599,610] Recently, in both LIBs and SIBs, alternative water-soluble binders have been introduced such as sodium carboxymethyl cellulose (Na-CMC), poly(acrylic acid) (PAA) and sodium alginate (Na-Alg)[600–612] (Fig. 42g). Generally, such binders were introduced for alloying reaction materials undergoing a large volume change during lithiation–delithiation or sodiation–desodiation to enhance cycle performance due to the thermally cross-linked three-dimensional interconnection of those binders. A Na-CMC binder is an environmentally friendly and inexpensive material that is derived from cellulose as natural polymers. During the electrochemical reaction process, the Na-CMC binder could play an important role in improving the solid electrolyte interface (SEI) passive layer on the electrode surface, which reduces the irreversible capacity and somehow leads to a better cycle life.[601–603] Na-Alg is a high-modulus natural polysaccharide extracted from brown algae, which yields a remarkably stable battery anode.[604–606] In particular, Na-Alg is much more polar than the Na-CMC polymer chains, which can ensure a better interfacial interaction between the polymer binder and particles, as well as stronger adhesion between the electrode layer and the Cu substrate. Comparing the chemical character between PVDF and PAA, it is a general assumption that the carboxylic groups of the PAA binder play an important role in achieving better uniformity and stronger binding ability in the composite electrode; this is due to their amorphous and cross-linking nature via the hydrogen bonds between carboxylic groups.[608–611,613] A PAA binder allows for the formation of a stable deformable SEI layer on the elastic binder-coated electrode surface, in which the elasticity of the polymer matrix may prevent cracking in the SEI when the volume changes.[609,610] The polymeric cross-linkage network can regulate the mechanical/chemical stress that results from large volume expansion in the composite electrode.[517,610] In addition, the decomposition reaction of an electrolyte was reduced compared to the PVDF binder due to the stable SEI layer formation via a PAA binder.[458,613,614] In 2014, Dahbi et al. compared and examined the binder and electrolyte additive effects in a hard carbon electrode using Na-CMC and PVDF binders.[601] Decomposition of the electrolyte on hard-carbon during the initial cycle was sufficiently suppressed by the CMC binder. Moreover, Dahbi et al. noted that uniform coverage with CMC was proposed to be advantageous in stabilizing the electrochemical performance, leading to excellent capacity retention with a higher efficiency compared to the PVDF binder.[601,615] To overcome the capacity fading resulting from volume expansion of insertion materials, Sun et al. used the Na-CMC binder in their Li$_4$Ti$_5$O$_{12}$ electrode.[337] Recently, Zhao et al. introduced the Na-doped Li$_4$Ti$_5$O$_{12}$ electrode using the Na-CMC and Na-alginate binder instead of the PVDF binder. These binders exhibited a slightly higher Coulombic efficiency than that of the PVDF binder. After 100 cycles, the Na-CMC and Na-alginate binders exhibited an excellent cyclability compared to that of the PVDF binder[616] (Fig. 42h). When applied to alloy

and conversion reaction anode materials in SIBs, their electro-chemical performance is dramatically changed depending on binders. Kim *et al.* achieved excellent cycling performances of red phosphorous carbon composite anodes by using the PAA binder. Upon the sodiation–desodiation process, the PAA binder effectively suppresses a large volume change of phosphorous electrodes compared to that of the PVDF binder.[511]

5. Sodium-ion full cells

Along with the development of LIBs, SIB technologies have been rapidly developing. The gravimetric energy density of SIBs as full cells operable at room temperature has become competitive in the state-of-the-art LIBs with graphite and layered oxides.[99] However, current research concentrated mostly on sodium-ion half cells (employing Na metal). Therefore, development of practical sodium ion full cells (without Na metal) remains critical challenges. Recently, in order to realize the practical SIBs, many research groups focus on developing rational full cell design. Furthermore, battery companies such as Aquion Energy (USA), FARADION (UK) and Sumitomo Electric Industries Ltd (Japan) are constantly striving to develop full cell designs, thus resulting in the remarkable improvement of practical SIBs.

Historically, sodium-ion full cell studies were conducted earlier than the commercialization of LIBs.[71,617–619] In 1988, sodium-ion full cells were proposed based on sodium-lead alloy composite anodes and the P2-type Na_xCoO_2 cathode, which

demonstrated excellent cyclability for over 300 cycles.[71] Later, a full cell with a P2-type $Na_{0.6}CoO_2$ cathode and a petroleum coke anode was also proposed with the solid polymer electrolyte $P(EO)_8NaCF_3SO_3$, at a high operation temperature of 100 °C[251] (Fig. 43a). However, these full cell systems did not attract much attention compared to LIBs due to their average discharge potential being lower than 3 V. On the other hand, the performances of sodium-ion full cells have dramatically improved since hard carbon anodes were introduced by Dahn *et al.*[247] As mentioned in the anode section in Section 3.1, hard carbon anodes usually demonstrated a reasonable capacity of 300 mA h g^{-1} with a low operating potential (nearly ~0 V), which is beneficial for increasing the average discharge potential and energy density of fabricated full cells with the appropriate cathode. In the case of cathode materials, various types of phosphate- and pyrophosphate-based poly-anion materials, which exhibit high operating potentials, are employed for high energy density sodium ion full cells.[237] In 2003, Barker *et al.* reported the preliminary performance data of sodium-ion full cells based on hard carbon/$NaVPO_4F$ chemistry[181] (Fig. 43b). The average discharge voltage for this cell was demonstrated to be around 3.7 V, which is comparable with commercially available lithium-ion cells based on $LiCoO_2$ or $LiMn_2O_4$ cathode materials. However, this full cell consisting of hard carbon/$NaVPO_4F$ exhibited a relatively low discharge capacity of 82 mA h g^{-1}. Therefore, to increase both the operating potential and discharge capacity, various full cell configurations have been investigated.[27,181,206,574,620–629]
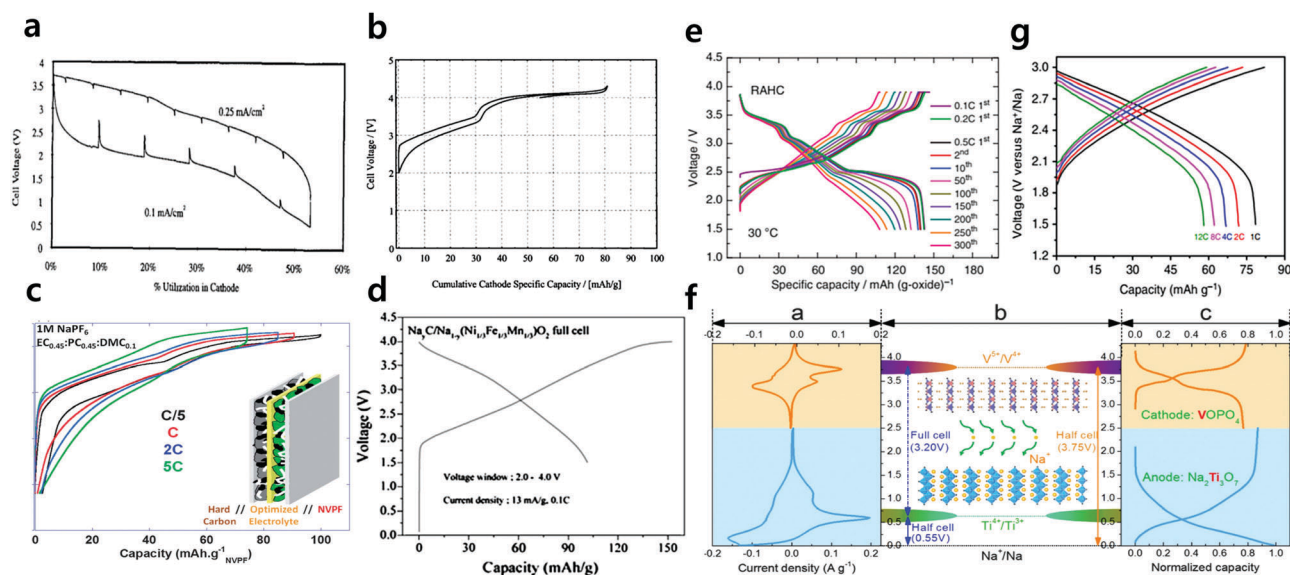
Fig. 43 (a) First cycle of an $Na_{0.6}CoO_2$/$P(EO)_8NaCF_3SO_3$/(ground) petroleum coke cell. (Reproduced with permission from ref. 251, Copyright 1993 The Electrochemical Society.) (b) EVS voltage profile for a typical hard carbon//$NaVPO_4F$ full cell cycled between 2.00 and 4.30 V in 1 M solution of $NaClO_4$ in EC/DMC (2 : 1 weight). (Reproduced with permission from ref. 181, Copyright 2003 The Electrochemical Society.) (c) Voltage *versus* capacity profiles for NVPF//HC full Na-ion cells cycled in 1 M $NaPF_6$ in $EC_{0.45}$:$PC_{0.45}$:$DMC_{0.1}$. (Reproduced with permission from ref. 574, Copyright 2013 The Royal Society of Chemistry.) (d) First cycle of a full Na-ion cell Na_yC/$Na_{1-y}(Ni_{1/3}Fe_{1/3}Mn_{1/3})O_2$. (Reprinted from ref. 50, Copyright 2012, with permission from Elsevier.) (e) Long-term cycle test of C/RAHC full cells in the voltage range of 1.5–3.9 V. (Reproduced by permission from ref. 87, Nature Publishing Group, Copyright 2015.) (f) Schematic of $Na_2Ti_3O_7$//$VOPO_4$ full cells with electrochemical characterization. (Reproduced with permission from ref. 625, Copyright 2016 The Royal Society of Chemistry.) (g) Discharge profiles of the $Na_{0.6}[Cr_{0.6}Ti_{0.4}]O_2$/$Na_{0.6}[Cr_{0.6}Ti_{0.4}]O_2$ sodium-ion full cell at various rates. (Reproduced by permission from ref. 626, Nature Publishing Group, Copyright 2015.)

This journal is © The Royal Society of Chemistry 2017

Chem. Soc. Rev., 2017, **46**, 3529–3614 | **3595**

Applying the $Na_3V_2(PO_4)_2F_3$ cathode and hard carbon anode for fabricating sodium-ion full cells, this full cell exhibited a high capacity of 110 mA h g^{-1} with an operation voltage of 3.65 V, as well as excellent capacity retention upon cycling with a satisfactory Coulombic efficiency ($>$98.5%) and very good power performance in the EC : PC : DMC (45 : 45 : 10, v/v) electrolyte solution[574] (Fig. 43c). Later, Nose et al. assembled a new type of Na-ion full cell by combining $Na_4Co_3(PO_4)_2P_2O_7$ as a cathode and hard carbon as an anode; this battery demonstrated a 4.0 V-class high operating voltage with long-term operation.[206] Layered structured cathodes such as P2-type and O3-type materials are also considered for sodium ion full cells with hard carbon anodes. Previous work has shown that P2-type cathode materials (Na_xMO_2; $x \leq 0.7$, M = transition metal) result in high rechargeable capacities.[46] However, a lower initial sodium content in the crystal structure of P2-type layered cathode led to an abnormal Coulombic efficiency above $\sim$100% in the 1st cycle.[100] Therefore, the intrinsic properties hinder practical full cell fabrication. Meanwhile, the practical benefits of O3-type (Na_xMO_2; $x \approx 1.0$, M = transition metal) cathodes are that they are able to fabricate sodium-ion full cells similar to commercial LIBs. Komaba et al. fabricated the full cell combined with a hard carbon anode and O3-tpye $Na[Ni_{1/2}Mn_{1/2}]O_2$ cathode, which demonstrated acceptable battery performance with approximately 3 V for the operating voltage.[27] Later, Kim et al. proposed O3-type layered $Na[Ni_{1/3}Fe_{1/3}Mn_{1/3}]O_2$ cathode materials and fabricated a high capacity full cell with hard carbon, which exhibited a high discharge capacity of 100 mA h g^{-1} and stable cycle retention after 150 cycles with a high operating potential above 3 V[50] (Fig. 43d). On the other hand, the sodium ion-full cells used in some works utilize a hard carbon anode that was presodiated in order to reduce the irreversible capacity during the first cycle. Moreover, such a presodiated system needs a different electrode balancing to prevent sodium plating.[624] This technique is not intended for commercial applications, but rather for scientific queries, to test the long-term electrochemical performance of such materials using full cells; this is because metallic sodium deposition on the Na metal anode does not warrant a long-term cycling test.[87] Hwang et al. fabricated sodium ion full cells with a compositional graded O3-type $Na[Ni_{0.60}Co_{0.05}Mn_{0.35}]O_2$ cathode and presodiated hard carbon anodes, which demonstrated a reversible discharge capacity of 257 mA h g^{-1} ($Na_{0.68}C_6$) with non-irreversible capacity (Fig. 43e). This full cell exhibited an excellent rate capability of 132.6 mA h g^{-1} at 1.5 A g^{-1} and stable cycle retentions at various temperatures (-20, 0, 30 and 55 °C). Especially, it demonstrated a superior cycle retention of $\sim$80% under extensive cycling conditions for over 300 cycles with an average operation voltage of 2.84 V on discharge at 30 °C. More recently, Keller et al. proposed sodium-ion full cells based on a presodiated hard carbon anode and a mixed layered oxide cathode of P2/P3/O2-$Na_{0.76}[Mn_{0.5}Ni_{0.3}Fe_{0.1}Mg_{0.1}]O_2$.[624] Presodiation of hard carbon was carried out until 135 mA h g^{-1} to prevent excess sodium in the full cell. The developed sodium-ion full cells demonstrated high specific energies (200–240 W h per kg of cathode and anode active materials),

high average discharge voltages (3.3 V), high energy efficiencies and an extraordinary long-term cycling stability of 80% capacity retention after 700 cycles.

However, such full cells based on hard carbon anodes suffer from an inferior rate capability, and the voltage plateau related to most capacities is too close to the sodium plating voltage, causing a safety concern. Li et al. designed a full sodium-ion battery based on nanostructured $Na_2Ti_3O_7$ and $VOPO_4$ materials as the anodes and cathodes[625] (Fig. 43f). In order to reduce the polarization and irreversibility effect of the electrode materials in the first discharge process (both for the anode and cathode sides), pre-desodiated $Na_2Ti_3O_7$ and pre-sodiated $VOPO_4$ were prepared in advance. This full cell shows outstanding rate capability and excellent cycling stability in the wide temperature range of -20 to 55 °C. Recently, sodium-ion full cells were proposed using the same materials as both cathodes and anodes, namely symmetric full cells.[626–629] The greatest advantage of using the same materials for both cathodes and anodes is that they significantly decrease the material's processing cost. Wang et al. proposed the P2-$Na_{0.6}[Cr_{0.6}Ti_{0.4}]O_2$ cation-disordered electrode for high-rate symmetric rechargeable SIBs[626] (Fig. 43g). This symmetric full cell exhibited an average operating voltage plateau at $\sim$2.53 V, as well as an extraordinary rate capability of 75% retention at 12C-rate and superior cycling performance. The $Na_3V_2(PO_4)_3$ materials also exhibit both cathode and anode potentials (3.4 V with a V^{4+}/V^{3+} redox reaction and 1.6 V with a V^{3+}/V^{2+} redox reaction), so a novel symmetric full cell system could be designed by employing $Na_3V_2(PO_4)_3$ as a bipolar electrode material.[628]

Such present results regarding sodium-ion full cells based on several platforms of cathodes and nonmetallic anodes have brought forth great advances in practical issues. Nevertheless, to obtain practical SIBs with high safety, outstanding rate capability, and cycling stability, further investigation of rationally designed full cells, including capacity balancing between the cathode and the anode, the voltage range, and stable electrolyte solution, is still necessary. Further studies of functional additives and binders to effectively control the solid electrolyte interface formation of cathodes and anodes are essential parameters for high safety SIBs. In addition, the total production cost of active materials of the electrode and the cost of battery components should be considered. In summary, a strategy for battery design in realizing practical SIBs is needed to find a good balance between an increase in battery performance with high safety and a decrease in the total cost of the batteries.

6. Summary

Even though SIBs were studied around the same time as LIBs, they were also abandoned at one point, particularly after the commercialization of LIBs by Sony in the early 1990s. However, the growth of technology and the exigency for large-scale applications such as ESSs have opened the door for SIBs to be utilized again. Lithium is not uniformly scattered on the Earth's crust, and given the demand that it is continually

3596 | Chem. Soc. Rev., 2017, 46, 3529–3614

This journal is © The Royal Society of Chemistry 2017

increasing, its reserves (specifically in lithium-constrained areas) will be exhausted. This will lead to an escalating price for lithium, and thereby the use of LIBs for ESS applications will not be cost-effective. With the recognition that SIBs have recently received, the hurdles for making them as applicable as LIBs cannot be taken lightly.

Electrodes with open frameworks are more desirable in sodium systems, as the larger-sized Na^+ (in comparison to Li^+) can be introduced into the framework. However, given how the immense structural changes that occur when introducing Na^+ cannot be avoided, disruption of structure's durability while trying to maintain its original state is bound to happen.[630] Moreover, sodiated transition metal materials are particularly hygroscopic, even upon brief exposure to air. Thus, the preparation of sodiated cathode materials and batteries requires meticulous handling and moisture-free conditions. The hydration of materials will deteriorate the electrochemical performance of the electrode due to the formation of intrinsically insulating NaOH. One recent study on cathode materials for SIBs has focused on this hygroscopic problem. Specifically, the Sumitomo Chemical Co., Ltd research group has successfully synthesized O3-type Ca-doped $NaFe_{0.4}Ni_{0.3}Mn_{0.3}O_2$, and they managed to suppress its tendency to absorb moisture through Ca doping. Although it is reasonable to suspect that the kinetics of Na^+ ion diffusion might be a problem due to the larger ionic size relative to that of Li^+, Ceder *et al.* reported that Na^+ extraction/re-insertion from/into Na-containing materials is experimentally and computationally faster compared to Li systems due to the low Lewis acidity of Na^+. By contrast, the insertion of Na^+ into non Na-containing compounds with a smaller bottleneck size may be slower compared to the insertion of Li^+. Furthermore, β-Al_2O_3; the fast Na^+ ionic conductor, was discovered almost 50 years ago, which is even earlier than Li^+.

Studies on cathode materials are considerably broad, including oxides, polyanions, NASICON (Na Super Ionic Conductor) types and organic compounds. Through studies on the O3-type sodium-containing layered transition metal oxides $Na_{1-x}FeO_2$, it has been found that this material is electrochemically active based on Fe^{3+}/Fe^{4+} redox couples, which is in contrast to O3-type lithium containing the same layered transition metal oxides in a Li system. Moreover, the irreversible capacity that results from the migration of iron ions in $Na_{1-x}FeO_2$ can be suppressed with the help of Co or Mn occupation in transition metal sites as a substitute to Fe.[39,47,50] However, the problem of insufficient cycle stability has yet to be solved. In the case of polyanion compounds, they exhibit better thermal stabilities compared to those of oxides, owing to the presence of the P–O covalent bonds in the crystal structure. They have an operating voltage comparable to that of the Li system. In addition, as opposed to the earlier mentioned information regarding the kinetic diffusion of Na^+ ions, a few studies on $NaFePO_4$ have reported that the migration energy of Na^+ ions is 0.05 eV higher than that of Li^+, which is actually a slower kinetic diffusion than reported here.[173] Hong *et al.*[631] and Goodenough *et al.*[632] initially proposed NASICON type compounds for use in Na^+ ion solid electrolytes due to the high Na^+ ionic conductivity

associated with their three-dimensional open framework. However, these compounds can be used as electrode materials with the incorporation of transition metals into their structure. $Na_3V_2(PO_4)_3$, for example, showed improved capacity at both higher and lower voltage regions after the modification of its surface with carbons derived from sugar. Their earlier work showed unsatisfactory results when tested as cathodes in a full symmetrical cell. Prussian blue and its analogues have also attracted attention due to their high energy, power density and electrochemical properties. However, unlike polyanions, their poor thermal stabilities remain a hindrance. Types of cathode materials, their redox couple, capacity, and operation voltage are summarized in Table 1.

Given that the electrochemical insertion of Na^+ into graphite, which is a commonly used anode material in LIBs, has not been considered suitable for Na-ion batteries, an alternative system for large-scale energy storage is needed because of the thermodynamic instability of binary Na-intercalated GICs.[258,259] Therefore, the search for appropriate anodes with proper Na voltage storage, large reversible capacity and high structural stability is necessary in order for SIBs to be successfully developed. Sodium metal is not recommended for use in an anodes due to its high reactivity and formation of dendrite. Many non-graphitic materials such as carbon black, pitch-based carbon-fibers have been demonstrated to insert Na^+. Hard carbons, *i.e.*, non-graphitic but graphene containing, carbonaceous materials, are considered as the "the first-generation" anode of choice for SIBs.[22,23,241] The low BET surface area of hard carbon appears to be a pivotal factor in achieving good reversible cycling of SIBs. However, the low operational potential of carbonaceous anodes raises severe safety issues for practical applications. Hence, transition metal oxide compounds, especially titanium-based oxides, have been widely studied.[300] The most common form of titanium oxide compounds, titanium dioxide (TiO_2), has been tested in Na systems by downsizing the size to the nanometer-scale. It was found that the pseudo-capacitance mechanism was responsible for the charge storage. The pseudocapacitive effect on typical insertion electrodes is believed to be a potential solution to overcoming the capacity limitation for Na insertion anodes. Conversion reactions of metal oxides can also be useful for anodes in SIBs.[243] These conversion reactions, which depend on the transition metals, occasionally combined with the insertion–extraction or alloy-dealloying reactions. The reaction concept was first introduced with spinel $NiCo_2O_4$, which delivered a reversible capacity of ~ 200 mA h g^{-1} after the initial discharge of ~ 600 mA h g^{-1}. Previous research has shown that the conversion reaction that forms sodium oxide is the primary reaction because spinel $NiCo_2O_4$ cannot accommodate for the large size of Na^+ into its vacant sites.[365] Various metal sulfides such as cobalt sulfides (CoS, CoS_2), molybdenum sulfides (Mo_2S, MoS_2), iron sulfides (FeS, FeS_2), and tin sulfides (SnS, SnS_2) have been extensively investigated as high capacity anode materials for NIBs. The weaker M–S bond in metal sulfides compared to the corresponding M–O bond in metal oxides is kinetically favorable for conversion reactions with Na ions.[410] Hence, the smaller volume changes and better

Table 1 Summary of cathode materials for sodium-ion batteries

Cathode materials for sodium-ion batteries

Structure	Compositions	Redox couples	Voltages (V)	Theoretical capacity (mA h g^{-1})	Experimental capacity (mA h g^{-1})	Ref.
Two-dimensional layer transition metal oxide $Na_{1-x}FeO_2$	$NaFeO_2$	$Fe^{3+/4+}$	1.3–4	241	125	49
	$Na[Fe_{0.5}Mn_{0.5}]O_2$	$Fe^{3+/4+}$ $Mn^{3+/4+}$	1.5–4.2	242	100–110	46
	$Na[Fe_{0.5}Co_{0.5}]O_2$	$Fe^{3+/4+}$ $Co^{3+/4+}$	2.5–4.0	240	160	47
	$Na[Fe_{0.3}Ni_{0.7}]O_2$	$Fe^{3+/4+}$ $Ni^{3+/4+}$	2.0–3.6	237	135	39
	$Na[Ni_{1/3}Fe_{1/3}Mn_{1/3}]O_2$	$Ni^{2+/4+}$ $Fe^{3+/4+}$ Co^{4+}	2–4	239	120	50
	$Na[Ni_{0.25}Fe_{0.5}Co_{0.25}]O_2$	$Ni^{2+/4+}$ $Fe^{3+/4+}$ Co^{4+}	2.1–3.9	239	140	51
	$Na[Ni_{0.25}Fe_{0.5}Mn_{0.25}]O_2$	$Ni^{2+/4+}$ $Fe^{3+/4+}$	2.1–3.9	240	140	52
	$Na[Li_{0.05}(Ni_{0.25}Fe_{0.5}Mn_{0.25})_{0.95}]O_2$	$Ni^{2+/4+}$ $Fe^{3+/4+}$	1.7–4.4	246	180	52
$Na_{1-x}[Fe_{1-y}Mn_y]O_2$	$Na_{2/3}[Fe_{0.5}Mn_{0.5}]O_2$	$Fe^{3+/4+}$ $Mn^{3+/4+}$	1.5–4.3	260	190	54
	$Na_{0.62}[Fe_{0.5}Mn_{0.5}]O_2$	$Fe^{3+/4+}$ $Mn^{3+/4+}$	1.5–4.3	263	185	55
	$Na_{0.7}[Fe_{0.5}Co_{0.5}]O_2$	$Fe^{3+/4+}$ $Co^{3+/4+}$	2.5–4.0	256	170	47
$Na_{1-x}CoO_2$	$NaCoO_2$	$Co^{3+/4+}$	2.0–4.0	239	170	33
	$Na_{0.55}CoO_2$	$Co^{3+/4+}$	2.7–3.5	263	140	62
	$Na_{2/3}[Co_{2/3}Mn_{1/3}]O_2$	$Co^{2+/3+}$ $Mn^{3+/4+}$	1.5–4.3	258	180	73 and 74
	$Na_{5/8}Ca_{1/24}CoO_2$	$Co^{3+/4+}$	2.0–4.0	255	124	79
$Na_{1-x}NiO_2$	$NaNiO_2$	$Ni^{3+/4+}$	2.0–4.5	235	145	81
			1.25–3.75	235	121	81
	$Na[Ni_{0.5}Mn_{0.5}]O_2$	$Ni^{2+/4+}$	2.0–4.5	239	185	83
			2.2–3.8	239	125	83
			2.0–4.0	239	124	84
	$NaFe_{0.2}Ni_{0.4}Mn_{0.4}O_2$	$Fe^{3+/4+}$ $Ni^{3+/4+}$	2.0–4.0	240	130	84
	$Na[Ni_{0.5}Ti_{0.5}]O_2$	$Ni^{2+/4+}$	1.5–4.7	247	121	88
Na_xMnO_2	$NaMnO_2$	$Mn^{3+/4+}$	2–3.8	243	197	90
	$Na_{0.7}MnO_2$	$Mn^{3+/4+}$	2–3.8	260	150	98
		$Mn^{3+/4+}$	1.5–4.4	260	216	97
		$Mn^{3+/4+}$	1.5–4.4	260	198	97
	$Na_{2/3}[Ni_{1/3}Mn_{2/3}]O_2$	$Ni^{2+/4+}$	2.0–4.5	258	162	101, 107 and 113
	$Na_{2/3}[Ni_{1/3-x}Mg_xMn_{2/3}]O_2$	$Ni^{2+/4+}$	2.0–4.5	Around 258	120–145	107
	$Na_{2/3}[Ni_{1/3-x}Al_xMn_{2/3}]O_2$	$Ni^{2+/4+}$	2.0–4.5	Around 258	147	113
	$Na_{2/3}[Ni_{1/3-x}Fe_xMn_{2/3}]O_2$	$Fe^{3+/4+}$ $Ni^{2+/4+}$	2.0–4.5	Around 258	145	113
	$Na_{0.7}[Mn_{0.65}Ni_{0.15}Fe_{0.2}]O_2$	$Fe^{3+/4+}$ $Ni^{2+/4+}$	1.5–4.3	258	208	117
	$Na_{2/3}[Ni_{1/3-x}Co_xMn_{2/3}]O_2$	$Ni^{2+/4+}$	2.0–4.5	Around 258	144	113
	$Na_{2/3}[Ni_{1/3-x}Zn_xMn_{2/3}]O_2$	$Ni^{2+/4+}$	2.2–4.3	Around 258	140	111 and 112
	$Na_{0.7}[Mn_{0.6}Ni_{0.3}Co_{0.1}]O_2$	$Ni^{2+/4+}$	1.5–4.3	256	185	114
	$Na_{2/3}[Ni_{1/3}Mn_{1/6}Ti_{1/6}]O_2$	$Ni^{2+/4+}$	2.5–4.5	319	127	118 and 119
	$Na_{2/3}[Mg_{0.28}Mn_{0.72}]O_2$	$Mn^{3+/4+}$	1.5–4.4	286	220	120
	$Na_{5/6}[Li_{1/4}Mn_{3/4}]O_2$	$Mn^{3+/4+}$	1.5–4.4	267	180	121
	$Na_{0.85}[Li_{0.17}Ni_{0.21}Mn_{0.64}]O_2$	$Ni^{2+/4+}$ $Mn^{3+/4+}$	1.5–4.4	266	200	7
$Na_{1-x}TiO_2$	$NaTiO_2$	$Ti^{3+/4+}$	2.0–3.5	260	75	124 and 125
$Na_{1-x}CrO_2$	$NaCrO_2$	$Cr^{3+/4+}$	2–3.6	250	110	126
$Na_{1-x}VO_2$	$NaVO_2$	$V^{4+/3+}$	1.2–2.4	253	120	134
	$Na_{0.7}VO_2$	$V^{4+/3+}$	1.2–2.6	270	105	136
Na_2RuO_3	Na_2RuO_3	$Ru^{4+/5+}$	1.5–4.0	137	147	137

Table 1 (continued)

Cathode materials for sodium-ion batteries

Structure		Compositions	Redox couples	Voltages (V)	Theoretical capacity (mA h g^{-1})	Experimental capacity (mA h g^{-1})	Ref.
Two-or three-dimensional layer transition metal oxide and fluorides	Manganese oxide	α-MnO$_2$ [hollandite]	Mn$^{3+/4+}$	1.0–4.3	308	280	146 and 147
		β-MnO$_2$[hollandite]	Mn$^{3+/4+}$	1.0–4.3	308	300	146
	Vanadium oxide	α-V$_2$O$_5$	V$^{5+/4+}$	1.5–3.8	294	250	151
		VO$_2$(B)	V$^{4+/3+}$	1.0–3.8	323	189	153
	Metal fluorides	FeF$_3$	Fe$^{3+/2+}$	1.5–4.0	712	150	153–156 and 178
		NaFeF$_3$	Fe$^{3+/2+}$	1.5–4.0	198	128	178
		NaNiF$_3$	Ni$^{3+/2+}$	1.5–4.0	193	Below 40	155
		NaMnF$_3$	Mn$^{3+/2+}$	1.5–4.0	198	Below 40	155
Three-dimensional polyanion compounds	Phosphates and fluorophosphates	Amorphous NaFePO$_4$	Fe$^{3+/2+}$	Around 2.4	154	150	156
		Olivine NaFePO$_4$	Fe$^{3+/2+}$	Around 2.8	154	120	163–173
		Na$_2$FePO$_4$F	Fe$^{3+/2+}$	2.0–3.8	124	100	178
		Na$_2$[Fe$_{0.5}$Mn$_{0.5}$]PO$_4$F	Mn$^{2+/3+}$ Fe$^{2+/3+}$	2.0–4.5	124	110	180
		NaV$_{0.96}$Cr$_{0.04}$PO$_4$F	V$^{5+/3+}$	3.0–4.5	142	80	184 and 185
		Na$_3$V$_2$(PO$_4$)$_2$F	V$^{4+/5+}$	3.0–4.2	156	87	186
		Na$_{1.5}$VPO$_{4.8}$F$_{0.7}$	V$^{3.8+/5+}$	2.0–4.5	134	130	187
		Na$_3$V$_2$(PO$_4$)$_3$F$_3$	V$^{3+/4+}$	2.0–4.2	128.2	120	188–190
	Pyrophosphates	(MoO2)$_2$P$_2$O$_7$	Mo^{6+}	1.0–3.5	250	190	192
		Na$_2$FeP$_2$O$_7$	Fe$^{2+/3+}$	2.0–3.8	97	88	196
		Na$_{3.32}$Fe$_{2.34}$(P$_2$O$_7$)$_2$ [Na$_{1.66}$Fe$_{1.17}$P$_2$O$_7$]	Fe$^{2+/3+}$	1.7–4.0	117.6	90	201
		β-Na$_2$MnP$_2$O$_7$	Mn$^{3+/2+}$	2.0–4.45	97.5	80	202
		Na$_2$(VO)P$_2$O$_7$	V$^{5+/4+}$	2.0–4.2	93.4	80	203
	Mixed phosphates	Na$_4$Co$_3$(PO$_4$)$_2$P$_2$O$_7$	Co$^{2+/3+}$	3.0–4.7	170	95	206
		Na$_4$Co$_{2.4}$Mn$_{0.3}$Ni$_{0.3}$(PO$_4$)$_2$P$_2$O$_7$	Co$^{2+/3+}$ Mn$^{3+/4+}$ Ni$^{2+/3+}$	3.0–4.8	170	80	207
		Na$_7$V$_4$(P$_2$O$_7$)PO$_4$	V$^{3+/4+}$	2.0–4.2	92.8	90	208
	NASICON type phosphates	Na$_3$V$_2$(PO$_4$)$_3$	V$^{4+/3+}$	2.7–3.8	117.6	93	209
	Sulfates, fluorosulfates, and carbonophosphates	Na$_3$MnPO$_4$CO$_3$	Mn$^{2+/3+}$ Mn$^{3+/4+}$	2.0–4.5	250	125	221
	Cyanides and organic compounds	KMnFe[CN]$_6$	Mn^{3+} Fe$^{3+/2+}$	2.0–4.0	81	70	228
		KFeFe[CN]$_6$	Fe$^{3+/2+}$	2.0–4.0	81	90	228
		KCoFe[CN]$_6$	Co^{3+} Fe$^{3+/2+}$	2.0–4.0	81	55	228
		KNiFe[CN]$_6$	Ni^{2+} Fe$^{3+/2+}$	2.0–4.0	80	50	228
		KCuFe[CN]$_6$	Cu^{2+} Fe$^{3+/2+}$	2.0–4.0	79	55	228
		KZnFe[CN]$_6$	Zn^{2+} Fe$^{3+/2+}$	2.0–4.0	79	32	228
		Na$_{1.4}$MnFe[CN]$_6$	Mn$^{3+/2+}$ Fe$^{3+/2+}$	2.0–4.2	82	131	229
		Na$_{1.72}$MnFe[CN]$_6$	Mn$^{3+/2+}$ Fe$^{3+/2+}$	2.0–4.2	81	120	229
		Na$_4$Fe[CN]$_6$	Fe$^{3+/2+}$	2.0–3.8	89	87	231
		Na$_4$C$_8$H$_2$O$_6$		1.6–2.8	187	180	236
		Na$_2$C$_6$O$_6$		1.5–2.9	237	180	237
		Aniline–nitroaniline copolymer		2.0–4.0		180	238

reversibility of Na$_2$S compared to that of Na$_2$O during the sodiation–desodiation process result in better mechanical stabilities and higher initial Coulombic efficiency, respectively.

Apart from electrode materials, suitable electrolytes, additives and binders are equally important for the development of NIBs. With appropriate electrolyte formulation, the interface reaction can be minimized and both cell performances and safety aspects can be strengthened. As reported by Bhide *et al.*, NaPF$_6$ in EC:DMC is favorable for the formation of a stable surface film,

as well as the reversibility of the Na$_{0.7}$CoO$_2$ cathode.[576] NaPF$_6$-based electrolyte solution demonstrated higher ionic conductivity, while in a report by Komaba *et al.*, NaPF$_6$-based electrolytes with hard carbon electrodes exhibited more stable cycling performance than that of hard carbon electrodes with NaClO$_4$-based electrolytes.[27] According to studies reported by Palacin's group, they have discovered that NaPF$_6$ in the EC:PC:DMC solvent mixture is the best electrolyte for the hard carbon anode.[574] On the other hand, Ponrouch *et al.* reported

This journal is © The Royal Society of Chemistry 2017

Chem. Soc. Rev., 2017, **46**, 3529–3614 | 3599

that NaPF$_6$ in EC:PC exhibited a low generation of heat and a high thermal stability, which can be attributed to the more thermally stable SEI layer that is formed on the HC after cycling.[28] As organic liquid electrolytes are less safe than the other electrolytes, using an aqueous electrolyte is a good approach to prevent safety hazards, and additionally they are of a relatively low cost. Developing aqueous Na-ion batteries is meaningful and practical because of the huge abundance of Na resources (NaCl, Na$_2$SO$_4$, NaNO$_3$, etc.). Using poly(vinylidene fluoride) (PVDF) as a binder is very common due to its good chemical and electrochemical stabilities. However, with the use of a volatile and toxic organic solvent (N-methyl pyrrolidone) and relatively high production cost when using PVDF to make the slurry, water-soluble binders such as sodium carboxymethyl cellulose (Na-CMC), poly(acrylic acid) (PAA) and sodium alginate (NaAlg) have been introduced. Na-CMC, an environmentally friendly and inexpensive material, could play an important role in improving the solid electrolyte interface (SEI) passive layer, which reduces the irreversible capacity and somehow leads to a better cycle life. Na-Alg, which is more polarized than CMC, can ensure better interfacial interaction between the polymer binder and the particles, as well as create stronger adhesion between the electrode layer and the Cu substrate. Use of the PAA binder allows for the formation of a stable SEI layer on the elastic binder-coated electrode surface, in which the elasticity of a polymer matrix may prevent cracking at the SEI upon volume changes.

Na-ion based electrochemical systems are alternatives to Li-ion systems. The study of electrode materials, carbon additives, binders, electrolyte salts, solvents, and current collectors is important and must be established in order to realize the practicality of SIBs in large-scale applications such as ESS. We believe that improving the understanding and more findings of materials can accelerate the development of SIBs which are compatible to commercial level LIBs.

7. Perspectives

LIBs have realized their adoption from portable devices to vehicle applications because of their high operation voltage and energy density, so that battery performances including price and safety are very important concern in technological evolution of electronic devices in future. In addition, demands on batteries for zero-emission EVs and energy storage are expected to increase exponentially from the year of 2020, and the secondary battery market will expand almost twice of the current level, 112 billion US dollars.[633] Albeit the expandability of LIBs, the geological issue, in which lithium resources are localized in mainly South America, is thought of as a serious situation to be resolved. Use of cobalt or other rare metals as electrode materials is another concern on the price of batteries for future mass production for the purpose of mounting LIBs to EVs and energy storage applications. Indeed, the battery pack price should reach 20–30% of the current value to spread LIBs for those applications from 2020. This is controversial for the use of present high capacity lithiated Ni-rich cathode materials because each metal price except manganese is expected to

further increase as more of the present cathode materials are consumed in future. Depletion of these resources, particularly cobalt, should be considered at the same time.

Academic and industrial societies are recently raising the alarm about this situation and speaking up about the necessity of alternative rechargeable batteries that can substantially substitute present LIBs. Indeed, sodium-ion batteries (SIBs) were developed together with LIBs in 1980s; however, the inferior battery performance of SIBs relative to LIBs was the main reason for the fade of SIBs, which led to the birth of commercialized LIBs by Sony in 1990s. However, the recent upsurge of EVs and energy storage using LIBs as power sources could cause a shortage of LIBs so a great deal of attention has been paid again to development of SIBs, in which sodium is inexpensive and evenly distributed. Since 2010 with the slogan of beyond lithium, research trends in SIBs have been intensively focused on electrode materials rather than battery systems in order to distinguish the feasibility of commercialization. There are some merits of SIBs versus LIBs as follows; (i) possibility of high performance electrode materials because of the abundance of sodium transition metal compounds relative to lithium compounds, (ii) fast diffusion of sodium ions in the solid phase, which indicates high rate performance of Na cells, (iii) lowering of the manufacturing cost due to the use of Al foil instead of Cu current collectors for anodes and the transfer of the production line of LIBs to SIBs, which does not need new production facility, (iv) superior safety properties of the cathode even at a highly charged state, and (v) less risk for sodium supply. By contrast, there are some demerits of SIBs; (i) low operation approximately 0.3 V versus Li, (ii) a large ionic radius of Na$^+$ (1.02 Å) relative to Li$^+$ (0.76 Å), which induces a simultaneous structure change during Na$^+$ insertion and extraction that may cause gradual capacity fade, and (iii) high reactivity of Na metal which necessitates basic solution for formation of metallic sodium deposition onto anodes that can seriously threaten safety of Na cells.

As mentioned in Fig. 1 and Table 1 development of cathode materials has been progressing towards layer and polyanion structure materials. In particular, know-hows accumulated by the development of LIBs are leading to significant progress in layered structure materials. O3 type layer compounds are very fascinating because they have the same crystal structure as commercial LiCoO$_2$ and Ni-rich derivatives of LIBs, but their capacities are usually limited below 130 mA h g^{-1} due to simultaneous structural changes induced from the presence of large Na$^+$ ions in the crystal structure.[83,634] Different from the O3 type materials, P2 type cathode materials are of interest due to their high capacity approaching approximately 200 mA h g^{-1}.[46] Despite the high capacities, the serious flaw of the P2 materials is the lack of extractable sodium content in the compounds, namely, Na$_{0.7}$MO$_2$ (M: transition metals), of which the first discharge capacity is similar to that of O3 type compounds. Nonetheless, many works have been directed toward stabilization of cycling performances. Appropriate sacrificing agents can show oxidative decomposition at the first charge, which can be used to solve the irreversible capacity at the first cycle. This enables the resulting Coulombic efficiency approaching

3600 | Chem. Soc. Rev., 2017, 46, 3529–3614

This journal is © The Royal Society of Chemistry 2017

close to 100%. Provided that the abnormal behavior is resolved commercialization of high capacity SIBs can be readily advanced, because many kinds of dopants are known to be effective to retain the capacity for long term cycling. For this purpose, pioneering works were conducted using Na_3N[60,635,636] and Na_3P[637] as the sacrificing agents to minimize the abnormally high Coulombic efficiency of over 130% at the first cycle and to compensate the sodium deficiency. Although such works could improve the first irreversible capacity of P2-type layer cathodes, the resulting Coulombic efficiency at the first cycle is still not sufficient to fabricate the practical SIBs in comparison with O3-type layer cathodes. Therefore, to compete with LIBs, academic community should revisit O3-type layer cathode materials such as Co-free $Na[Ni_{0.5}Mn_{0.5}]O_2$[83] and carbon-coated $NaCrO_2$[131] which show high Coulombic efficiency at initial cycle and excellent cyclability. The know-hows accumulated from LIBs were further used to synthesize O3-type full concentration gradient (FCG) cathode materials that demonstrate high capacity and good cycling performances.[87,160,566] Full cells adopting hard carbon anodes confirmed cycling stability of the materials for a long time. Spoke-like assembly of nanorods greatly improved the strength of the particles, and this enabled unprecedentedly good cycling stability and rate performances. Although the chemistries are very interesting for P2 type layer cathodes for investigation of the structural change during Na^+ insertion and extraction, elaboration is required in order to stabilize the Coulombic efficiency at the first cycle. Polyanion materials are attractive because of high operation voltage and cycling stability, whereas low capacities below 100 mA h g^{-1} and more seriously moisture uptake in air are the critical issues to be resolved for those compounds. These suggest suitability of O3 type cathode materials in practical uses for future EVs and energy storage applications.

Anode materials are activated by insertion, conversion, and alloying reactions as summarized in Fig. 1. Due to the low operation voltage and extraordinary cycling stability, hard carbon proposed by Dahn et al.[22] in 2000 is regarded as the better candidate than any other electrode material for anode materials. Since the first LIBs adopted hard carbon as the anode materials, hard carbon can be the first commercial anode materials even in SIBs as well. Most of all, most urgent is the sodium metal deposition onto the surface of hard carbon at low voltage, in which safety issues should be considered because of the high reactivity of sodium metal. In addition, capacity below 300 mA h g^{-1}, which is lower than graphite anodes for LIBs, is not advantageous to improve the energy density of SIBs. Thus, conversion and alloying reaction based materials are intensively being studied to find alternative anode materials that deliver high capacity and do not have sodium metal deposition on discharge. It is evident that these conversion and alloying materials have superiority in capacity, while volume expansion of electrodes in the sodiate state arising from the large ionic size of Na^+ is the intrinsic problem for these electrodes. Low Coulombic efficiency at the first cycle is another critical issue to be studied further. Provided that the above-mentioned issues are cleared, phosphorous materials that deliver over 2000 mA h g^{-1} are expected to be some of the candidate materials for anodes to improve energy density of SIBs. So far, various anode materials are under investigation, it is believed that

hard carbon is thought to be the best candidate in practical applications due to its low operation voltage, cycling stability, and high Coulombic efficiency at the first cycle. Reviewing many kinds of cathode and anode materials in the present review, in summary, there is no doubt about the practical use of the O3 type cathode and hard carbon anode assembly for successful full cell configuration.

At present, leading companies are promoting several prototypes of SIBs for commercialization. Sumitomo Chemical Co. Ltd demonstrated a pouch type full cell using the O3-type $NaNi_{0.3}Fe_{0.4}Mn_{0.3}O_2$ cathode in 2013.[638] Recently, CNRS and RS2E have launched the first commercial cylindrical 18 650 SIBs, which guaranty 2000 cycles with an energy density of 90 W h kg^{-1}.[639] In 2015, FRADION developed prototype SIBs and successfully mounted SIBs into E-bikes.[640] Sharp Laboratory also promotes SIBs that adopt O3 type or Prussian white cathodes, hard carbon anodes, and conventional carbonate-based electrolytes for high energy density SIBs.[641,642] Recent a report by Choi et al. and Doron et al.[643] proposed the importance of minimization of energy consumption ($ W h^{-1}) rather than lowering of material costs to successful spread of SIBs towards energy storage applications. Also, SIBs are faced with intrinsic low energy density relative to LIBs, and this further lowers volumetric energy density in the limited space in battery pack. One option proposed is to improve the tap density of cathode materials. Our recent work on the radially aligned hierarchical columnar (RAHC) structure[87] and spoke-like nanorod assembly (SNA) in a spherical secondary particle[566] can be a good example to have high capacity and, more importantly, to maximize the electrode density achieved from its unique feature of intrinsic robustness under high compression pressure in the electrode pressing process. To date, specific energy density of SIBs was only estimated based on the weight of active materials by calculation with the assumption of 300 mA h g^{-1} for hard carbon as a negative electrode material for full cells. Such an estimated specific energy density of SIBs with some of the cathode materials reaches and/or exceeds 300 W h kg^{-1}.[18,643] Unfortunately, in consideration of not only the active materials but all components that compose SIBs, the actual value of energy density in the first commercial cylindrical 18 650 SIBs is dramatically lowered below 100 W h kg^{-1}. Therefore, it is very important to keep in our mind how we can improve the energy density of a SIB system when developing high capacity cathode and anode materials and stable electrolytes including additives that operate in a high voltage region, in particular, to maximize the energy density. Furthermore, more systematic studies on surface modification of active materials to minimize the side reactions with electrolytes, binders, current collectors, and the other components should be intensively progressed so as to advance the SIBs in practical use towards energy storage applications.

Conflict of interest

The authors declare that there is no conflict of interest for publishing this review in *Chemical Society Reviews*.

This journal is © The Royal Society of Chemistry 2017

Chem. Soc. Rev., 2017, 46, 3529–3614 | 3601

Acknowledgements

References

1 B. Dunn, H. Kamath and J.-M. Tarascon, *Science*, 2011, **334**, 928–935.

2 H. Pan, Y.-S. Hu and L. Chen, *Energy Environ. Sci.*, 2013, **6**, 2338–2360.

3 Y. Nishi, *J. Power Sources*, 2001, **100**, 101–106.

4 J.-M. Tarascon, *Nat. Chem.*, 2010, **2**, 510.

5 C.-X. Zhu and H. Li, *Energy Environ. Sci.*, 2011, **4**, 2614–2624.

6 E. de la Llave, V. Borgel, K. J. Park, J.-Y. Hwang, Y.-K. Sun, P. Hartmann, F. F. Chesneau and D. Aurbach, *ACS Appl. Mater. Interfaces*, 2016, **8**, 1867–1875.

7 M. D. Slater, D. Kim, E. Lee and C. S. Johnson, *Adv. Funct. Mater.*, 2013, **23**, 947–958.

8 T. B. Reddy and D. Linden, *Linden's Handbook of Batteries*, McGraw-Hill, 2010.

9 P. Adelhelm, P. Hartmann, C. L. Bender, M. Busche, C. Eufinger and J. Janek, *J. Nanotechnol.*, 2015, **6**, 1016–1055.

10 K. Mizushima, P. C. Jones, P. J. Wiseman and J. B. Goodenough, *Mater. Res. Bull.*, 1980, **15**, 783–789.

11 A. S. Nagelberg and W. L. Worrell, *J. Solid State Chem.*, 1979, **29**, 345–354.

12 J. P. Parant, R. Olazcuag, M. Devalett, C. Fouassie and P. Hagenmul, *J. Solid State Chem.*, 1971, **3**, 1–5.

13 C. Delmas, C. Fouassier and P. Hagenmuller, *Physica B+C*, 1980, **99**, 81–85.

14 J. J. Braconnier, C. Delmas, C. Fouassier and P. Hagenmuller, *Mater. Res. Bull.*, 1980, **15**, 1797–1804.

15 M. S. Whittingham, *Prog. Solid State Chem.*, 1978, **12**, 41–99.

16 L. W. Shacklette, J. E. Toth and R. L. Elsenbaumer, *Conjugated polymer as substrate for the plating of alkali metal in a nonaqueous secondary battery*, Allied Corp., USA, 1985.

17 T. Shishikura and M. Takeuchi, *Secondary batteries*, ShowaDenko K. K. Hitachi, Ltd, Japan, 1987.

18 K. Kubota and S. Komaba, *J. Electrochem. Soc.*, 2015, **162**, A2538–A2550.

19 D. P. Divincenzo and E. J. Mele, *Phys. Rev. B: Condens. Matter Mater. Phys.*, 1985, **32**, 2538–2553.

20 R. Alcántara, J. M. Jiménez-Mateos, P. Lavela and J. L. Tirado, *Electrochem. Commun.*, 2001, **3**, 639–642.

21 P. Thomas, J. Ghanbaja and D. Billaud, *Electrochim. Acta*, 1999, **45**, 423–430.

22 D. A. Stevens and J. R. Dahn, *J. Electrochem. Soc.*, 2000, **147**, 4428–4431.

23 D. A. Stevens and J. R. Dahn, *J. Electrochem. Soc.*, 2001, **148**, A803–A811.

24 L. Joncourt, M. Mermoux, P. H. Touzain, L. Bonnetain, D. Dumas and B. Allard, *J. Phys. Chem. Solids*, 1996, **57**, 877–882.

25 X. Xia and J. R. Dahn, *J. Electrochem. Soc.*, 2012, **159**, A515–A519.

26 V. Palomares, P. Serras, I. Villaluenga, K. B. Hueso, J. Carretero-Gonzalez and T. Rojo, *Energy Environ. Sci.*, 2012, **5**, 5884–5901.

27 S. Komaba, W. Murata, T. Ishikawa, N. Yabuuchi, T. Ozeki, T. Nakayama, A. Ogata, K. Gotoh and K. Fujiwara, *Adv. Funct. Mater.*, 2011, **21**, 3859–3867.

28 A. Ponrouch, E. Marchante, M. Courty, J. M. Tarascon and M. R. Palacin, *Energy Environ. Sci.*, 2012, **5**, 8572–8583.

29 X. Wu, Y. Cao, X. Ai, J. Qian and H. Yang, *Electrochem. Commun.*, 2013, **31**, 145–148.

30 J. Y. Luo, W. J. Cui, P. He and Y. Y. Xia, *Nat. Chem.*, 2010, **2**, 760–765.

31 Y. Wang, J. Yi and Y. Xia, *Adv. Energy Mater.*, 2012, **2**, 830–840.

32 E. Monyoncho and R. Bissessur, *Mater. Res. Bull.*, 2013, **48**, 2678–2688.

33 C. Delmas, J.-J. Braconnier, C. Fouassier and P. Hagenmuller, *Solid State Ionics*, 1981, **3/4**, 165–169.

34 R. Famery, P. Bassoul and F. Queyroux, *J. Solid State Chem.*, 1985, **57**, 178–190.

35 R. Famery, P. Bassoul and F. Queyroux, *J. Solid State Chem.*, 1986, **61**, 293–300.

36 S. Kikkawa, H. Ohkura and M. Koizumi, *Mater. Chem. Phys.*, 1987, **18**, 375–380.

37 B. Fuchs and S. Kemmler-Sack, *Solid State Ionics*, 1994, **68**, 279–285.

38 T. Shirane, R. Kanno, Y. Kawamoto, Y. Takeda, M. Takano, T. Kamiyama and F. Izumi, *Solid State Ionics*, 1995, **79**, 279–285.

39 Y. Takeda, K. Nakahara, M. Nishijima, N. Imanishi, O. Yamamoto and M. Takano, *Mater. Res. Bull.*, 1994, **29**, 659–666.

40 V. L. McLaren, A. R. West, M. Tabuchi, A. Nakashima, H. Takahara, H. Kobayashi, H. Sakaebe, H. Kageyama, A. Hirano and Y. Takeda, *J. Electrochem. Soc.*, 2004, **151**, A672–A681.

41 T. Matsumura, N. Sonoyama and R. Kanno, *Solid State Ionics*, 2003, **161**, 31–39.

42 S. Miyazaki, S. Kikkawa and M. Koizumi, *Synth. Met.*, 1983, **6**, 211–217.

43 S. Kikkawa, S. Miyazaki and M. Koizumi, *J. Power Sources*, 1984, **14**, 231–234.

44 N. Yabuuchi, H. Yoshida and S. Komaba, *Electrochemistry*, 2012, **80**, 716–719.

45 J. Zhao, L. Zhao, N. Dimov, S. Okada and T. Nishida, *J. Electrochem. Soc.*, 2013, **160**, A3077–A3081.

46 N. Yabuuchi, M. Kajiyama, J. Iwatate, H. Mishikawa, S. Hitomi, R. Okuyama, R. Usui, Y. Yamada and S. Komaba, *Nat. Mater.*, 2012, **11**, 512–517.

3602 | *Chem. Soc. Rev.*, 2017, **46**, 3529–3614

This journal is © The Royal Society of Chemistry 2017

47 H. Yoshida, N. Yabuuchi and S. Komaba, *Electrochem. Commun.*, 2013, **34**, 60–63.

48 X. Wang, G. Liu, T. Iwao, M. Okubo and A. Yamada, *J. Phys. Chem. C*, 2014, **118**, 2970.

49 Y. Nanba, T. Iwao, B. M. D. Boisse, W. Zhao, E. Hosono, D. Asakura, H. Niwa, H. Kiuchi, J. Miyawaki, Y. Harada, M. Okubo and A. Yamada, *Chem. Mater.*, 2016, **28**, 1058–1065.

50 D. Kim, E. Lee, M. Slater, W. Lu, S. Rood and C. S. Johnson, *Electrochem. Commun.*, 2012, **18**, 66–69.

51 S.-M. Oh, S.-T. Myung, C. S. Yoon, J. Lu, J. Hassoun, B. Scrosati, K. Amine and Y.-K. Sun, *Nano Lett.*, 2014, **14**, 1620–1626.

52 S.-M. Oh, S.-T. Myung, J.-Y. Hwang, B. Scrosati, K. Amine and Y.-K. Sun, *Chem. Mater.*, 2014, **26**, 6165–6171.

53 S. Komaba, T. Nakayama, A. Ogata, T. Shimizu, C. Takei, S. Takada, A. Hokura and I. Nakai, *ECS Trans.*, 2009, **16**, 43–55.

54 G. Singh, J. Miguel Lopez del Amo, M. Calceran, S. Perez-Villar and T. Rojo, *J. Mater. Chem. A*, 2015, **3**, 6954–6961.

55 B. Mortemard de Boisse, D. Carlier, M. Guignard, L. Bourgeois and C. Delmas, *Inorg. Chem.*, 2014, **53**, 11197–11205.

56 E. Talaie, V. Duffort, H. L. Smith, B. Fultz and L. F. Nazar, *Energy Environ. Sci.*, 2015, **8**, 2512–2523.

57 J. S. Thorne, R. A. Dunlap and M. N. Obrovac, *J. Electrochem. Soc.*, 2013, **160**, A361–A367.

58 Y. H. Jung, A. S. Christiansen, R. E. Johnsen, P. Norby and D. K. Kim, *Adv. Funct. Mater.*, 2015, **25**, 3227–3237.

59 B. Mortemard de Boisse, D. Carlier, M. Guignard and C. Delmas, *J. Electrochem. Soc.*, 2013, **160**, A569–A574.

60 G. Singh, B. Acebedo, M. C. Cabanas, D. Shanmukarag, M. Armand and T. Rojo, *Electrochem. Commun.*, 2013, **37**, 61–63.

61 V. Duffort, E. Talaie, R. Black and L. F. Nazar, *Chem. Mater.*, 2015, **27**, 2515–2524.

62 R. Berthelot, D. Carlier and C. Delmas, *Nat. Mater.*, 2011, **10**, 74–80.

63 K. Takeda, H. Sakurai, E. Takayama-Muromachi, F. Izumi, R. A. Dilanian and T. Sasaki, *Nature*, 2003, **422**, 53–55.

64 Q. Huang, M. L. Foo, J. W. Lynn, H. W. Zandbergen, G. Lawes, Y. Wang, B. H. Toby, A. P. Ramirez, N. P. Ong and R. J. Cava, *J. Phys.: Condens. Matter*, 2004, **16**, 5803–5814.

65 M. Lee, L. Viciu, L. Li, Y. Wang, M. L. Foo, S. Watauchi, R. A. Pascal Jr., R. J. Cava and P. Ong, *Nat. Mater.*, 2006, **5**, 537–540.

66 M. Roger, D. J. P. Morris, D. A. Tennant, M. J. Gutmann, J. P. Goff, J.-U. Hoffmann, R. Feyerherm, E. Dudzik, D. Prabhakaran, A. T. Boothroyd, N. Shannon, B. Lake and P. P. Deen, *Nature*, 2007, **445**, 631–634.

67 Y. Hinuma, Y. S. Meng and G. Ceder, *Phys. Rev. B: Condens. Matter Mater. Phys.*, 2008, **77**, 224111.

68 T. A. Platova, I. R. Mukhamedshin, H. Alloul, A. V. Dooglav and G. Collin, *Phys. Rev. B: Condens. Matter Mater. Phys.*, 2009, **80**, 224106.

69 J. Molenda, C. Delmas, P. Dordor and A. Stoklosa, *Solid State Ionics*, 1984, **12**, 473–477.

70 F. C. Chou, E. T. Abel, J. H. Cho and Y. S. Lee, *J. Phys. Chem. Solids*, 2005, **66**, 155–160.

71 L. W. Shacklette, T. R. Jow and L. Townsend, *J. Electrochem. Soc.*, 1988, **135**, 2669–2674.

72 Y. Ma, M. M. Doeff, J. Steven, J. De and C. Lutgard, *J. Electrochem. Soc.*, 1993, **140**, 2726–2733.

73 F. Tournadre, L. Croguennec, I. Saadoune, D. Carlier, Y. Shao-Horn, P. Willmann and C. Delmas, *J. Solid State Chem.*, 2004, **177**, 2790–2802.

74 F. Tournadre, L. Croguennec, P. Willmann and C. Delmas, *J. Solid State Chem.*, 2004, **177**, 2803–2809.

75 J.-H. Cheng, C.-J. Pan, J.-F. Lee, J.-M. Chen, M. Guignard, C. Delmas, D. Carlier and B.-J. Hwang, *Chem. Mater.*, 2014, **26**, 1219–1225.

76 D. Carlier, J. H. Cheng, R. Berthelot, M. Guignard, M. Yoncheva, R. Stoyanova, B. J. Hwang and C. Delmas, *Dalton Trans.*, 2011, **40**, 9306–9312.

77 P. Yang, C. Zhang, M. Li, X. Yang, C. Wang, X. Bie, Y. Wei, G. Chen and F. Du, *ChemPhysChem*, 2015, **16**, 3408–3412.

78 X. Chen, X. Zhou, M. Hu, J. Liang, D. Wu, J. Wei and Z. Zhou, *J. Mater. Chem. A*, 2015, **3**, 20708–20714.

79 M. Matsui, F. Mizukoshi and N. Imanishi, *J. Power Sources*, 2015, **280**, 205–209.

80 X. Xia and J. R. Dahn, *J. Electrochem. Soc.*, 2012, **159**, A647–A650.

81 P. Vassilaras, X. Ma, X. Li and G. Ceder, *J. Electrochem. Soc.*, 2013, **160**, A207–A211.

82 M. H. Han, E. Gonzalo, G. Singh and T. Rojo, *Energy Environ. Sci.*, 2015, **8**, 81–102.

83 S. Komaba, N. Yabuuchi, T. Nakayama, A. Ogata, T. Ishikawa and I. Nakai, *Inorg. Chem.*, 2012, **51**, 6211–6220.

84 D. D. Yuan, Y. X. Wang, Y. L. Cao, X. P. Ai and H. X. Yang, *ACS Appl. Mater. Interfaces*, 2015, **7**, 8585–8591.

85 J.-Y. Hwang, S.-T. Myung, D. Aurbach and Y.-K. Sun, *J. Power Sources*, 2016, **324**, 106–112.

86 H.-J. Oh, K.-J. Noh, B.-R. Kim, W. Kang, S.-C. Jung and S.-J. Kim, *Jpn. J. Appl. Phys.*, 2013, **52**, 1AC15 1-4.

87 J.-Y. Hwang, S.-M. Oh, S.-T. Myung, K. Y. Chung, I. Belharouak and Y.-K. Sun, *Nat. Commun.*, 2014, **6**, 6856.

88 H. Yu, S. Guo, Y. Zhu, M. Ishida and H. Zhou, *Chem. Commun.*, 2014, **50**, 457–459.

89 J. P. Parant, R. Olazcuaga, M. Devalette, C. Fouassier and P. Hagenmuller, *J. Solid State Chem.*, 1971, **3**, 1–11.

90 X. Ma, H. Chen and G. Ceder, *J. Electrochem. Soc.*, 2011, **158**, A1307–A1312.

91 A. Mendiboure, C. Delmas and P. Hagenmuller, *J. Solid State Chem.*, 1985, **57**, 323–331.

92 X. Li, X. Ma, D. Su, L. Liu, R. Shisnell, S. P. Ong, H. Chen, A. Toumar, J.-C. Idrobo, Y. Lei, J. Bai, F. Wang, J. W. Lynn, Y. S. Lee and G. Ceder, *Nat. Mater.*, 2014, **13**, 586–592.

93 O. I. Velikokhantnyi, C.-C. Chang and P. N. Kumta, *J. Electrochem. Soc.*, 2003, **150**, A1262–A1266.

94 R. Hoppe, G. Brachtel and M. Jansen, *Z. Anorg. Allg. Chem.*, 1975, **417**, 1.

This journal is © The Royal Society of Chemistry 2017

Chem. Soc. Rev., 2017, **46**, 3529–3614 | 3603

95 R. Stoyanova, D. Carlier, M. Sendova-Vassileva, M. Yoncheva, E. Zhecheva, D. Nihtianova and C. Delmas, *J. Solid State Chem.*, 2010, **183**, 1372–1379.

96 M. Yoncheva, R. Stoyanova, E. Zhecheva, E. Kuzmanova, M. Sendova-Vassileva, D. Nihtianova, D. Carlier, M. Guignard and C. Delmas, *J. Mater. Chem.*, 2012, **22**, 23418–23427.

97 S. Kumakura, Y. Tahara, K. Kubota, K. Chihara and S. Komaba, *Angew. Chem., Int. Ed.*, 2016, **55**, 1–5.

98 A. Caballero, L. Hernan, J. Morales, L. Sanchez, J. Santos Pena and M. A. G. Aranda, *J. Mater. Chem.*, 2012, **12**, 1142–1147.

99 N. Yabuuchi, K. Kubota, M. Dahbi and S. Komaba, *Chem. Rev.*, 2014, **114**, 11636–11682.

100 N. Yabuuchi and S. Komaba, *Sci. Technol. Adv. Mater.*, 2014, **15**, 043501.

101 Z. Lu and J. R. Dahn, *J. Electrochem. Soc.*, 2001, **148**, A1225–A1229.

102 K. Hemalatha, M. Jayakumar, P. Bera and A. S. Prakash, *J. Mater. Chem. A*, 2015, **3**, 20908–20912.

103 D. H. Lee, J. Xu and Y. S. Meng, *Phys. Chem. Chem. Phys.*, 2013, **15**, 3304–3312.

104 A. Van der Ven and G. Ceder, *Electrochem. Solid-State Lett.*, 2000, **2**, 301–304.

105 J. Xu, D. H. Lee, R. J. Clement, X. Yu, M. Leskes, A. J. Pell, G. Pintacuda, X.-Q. Yang, C. P. Grey and Y. S. Meng, *Chem. Mater.*, 2014, **26**, 1260–1269.

106 P.-F. Wang, Y. Yu, Y.-X. Yin, Y.-S. Wang, L.-J. Wan, L. Gu and Y.-G. Guo, *Angew. Chem., Int. Ed.*, 2016, **128**, 7571–7575.

107 G. Singh, N. Tapia-Ruiz, J. Miguel Lopez del Amo, U. Maitra, J. W. Somerville, A. R. Armstrong, J. Martinez de Ilarduya, T. Rojo and P. G. Bruce, *Chem. Mater.*, 2016, **28**, 5087–5094.

108 D. Buchholz, C. Vaalma, L. G. Chagas and S. Passerini, *J. Power Sources*, 2015, **282**, 581–585.

109 J. Billuad, G. Singh, A. R. Armstrong, E. Gonzalo, V. Roddatis, M. Armand, T. Rojo and P. G. Bruce, *Energy Environ. Sci.*, 2014, **7**, 1387–1391.

110 R. J. Clement, J. Billuad, A. R. Armstrong, G. Singh, T. Rojo, P. G. Bruce and C. P. Grey, *Energy Environ. Sci.*, 2016, **9**, 3240–3251.

111 X. Wu, G.-L. Xu, G. Zhong, Z. Going, M. J. McDonald, S. Zheng, R. Fu, Z. Chen, K. Amine and Y. Yang, *ACS Appl. Mater. Interfaces*, 2016, **8**, 22227–22237.

112 X. Wu, J. Guo, D. Wang, G. Zhong, M. J. McDonald and Y. Yang, *J. Power Sources*, 2015, **281**, 18–26.

113 W. Zhao, H. Kirie, A. Tanaka, M. Unno, S. Yamamoto and H. Noguchi, *Mater. Lett.*, 2014, **135**, 131–134.

114 J. Yoshida, E. Guerin, M. Arnault, C. Constantin, B. Mortemard de Boisse, D. Calier, M. Guignard and C. Delmas, *J. Electrochem. Soc.*, 2014, **161**, A1987–A1991.

115 R. Kataoka, T. Mukai, A. Yoshizawa, K. Inoue, T. Kiyobayashi and T. Sakai, *J. Electrochem. Soc.*, 2015, **162**, A553–A558.

116 Z.-Y. Li, J. Zhang, R. Gao, H. Zhang, Z. Hu and X. Liu, *ACS Appl. Mater. Interfaces*, 2016, **8**, 15439–15448.

117 D. Yuan, X. Hu, J. Qian, F. Pei, F. Wu, R. Mao, X. Ai, H. Yang and Y. Cao, *Electrochim. Acta*, 2014, **116**, 300–305.

118 H. Yoshida, N. Yabuuchi, K. Kubota, I. Ikeuchi, A. Garsuch, M. Schulz-Dobric and S. Komaba, *Chem. Commun.*, 2014, **50**, 3677–3680.

119 W. Zao, A. Tanaka, K. Momosaki, S. Yamamoto, F. Zhang, Q. Guo and H. Noguchi, *Electrochim. Acta*, 2015, **170**, 171–181.

120 N. Yabuuchi, R. Hara, K. Kubota, J. Paulsen, S. Kumakura and S. Komaba, *J. Mater. Chem. A*, 2014, **2**, 16851–16855.

121 N. Yabuuchi, R. Hara, M. Kajiyama, K. Kubota, T. Ishigaki, A. Hoshikawa and S. Komaba, *Adv. Energy Mater.*, 2014, **4**, 1301453.

122 N. Yabuuchi, K. Yoshii, S.-T. Myung, I. Nakai and S. Komaba, *J. Am. Chem. Soc.*, 2011, **133**, 4404–4419.

123 Y. Liu, X. Fang, A. Zhang, C. Shen, Q. Lium, H. A. Enaya and C. Zhou, *Nano Energy*, 2016, **27**, 27–34.

124 P. Hagenmuller, A. Le Cerf and M. Onillon, *C. R. Acad. Sci.*, 1962, 255–928.

125 A. Maazaz, C. Delmas and P. Hagenmuller, *J. Inclusion Phenom.*, 1983, **1**, 45–51.

126 J. J. Broconnier, C. Delmas and P. Hagenmuller, *Mater. Res. Bull.*, 1982, **17**, 993–1000.

127 S. Miyazaki, S. Kikkawa and M. Koizumi, *Rev. Chim. Miner.*, 2981, **19**, 301.

128 S. Komaba, C. Takei, T. Nakayama, A. Ogata and N. Yabuuchi, *Electrochem. Commun.*, 2010, **12**, 355–358.

129 X. Xia and J. R. Dahn, *Electrochem. Solid-State Lett.*, 2012, **15**, A1–A4.

130 J. J. Ding, Y. Zhou, Q. Sun and Z. Fu, *Electrochem. Commun.*, 2012, **22**, 85–88.

131 C.-Y. Yu, J.-S. Park, H.-G. Jung, K.-Y. Chung, D. Aurbach, Y.-K. Sun and S.-T. Myung, *Energy Environ. Sci.*, 2015, **8**, 2019–2026.

132 C.-Y. Chen, K. Matsumoto, T. Nohira, R. Hagiwara, A. Fukunaga, S. Sakai, K. Nitta and S. Ninazawa, *J. Power Sources*, 2013, **237**, 52–57.

133 M. Onoda, *J. Phys.: Condens. Matter*, 2008, **20**, 145205.

134 T. McQueen, P. Stephenes, Q. Huang, T. E. Klimczuk, F. Ronning and R. Cava, *Phys. Rev. Lett.*, 2008, **101**, 166402.

135 D. Hamani, M. Ati, J. M. Tarascon and P. Rozier, *Electrochem. Commun.*, 2011, **13**, 938–941.

136 M. Guignard, C. Didier, J. Darriet, P. Bordet, E. Elkaim and C. Delmas, *Nat. Mater.*, 2013, **12**, 74–80.

137 M. Tamaru, X. Wang, M. Okubo and A. Yamada, *Electrochem. Commun.*, 2013, **33**, 23–26.

138 S. Guo, Y. Sun, J. Yi, K. Zhu, P. Liu, Y. Zhu, G. Zhu, M. Chen, M. Ishida and H. Zhou, *NPG Asia Mater.*, 2016, **8**, e266.

139 M. M. Doeff, M. Y. Peng, Y. Ma and L. C. De Jonghe, *J. Electrochem. Soc.*, 1994, **141**, L145–L147.

140 M. M. Doeff, T. J. Richardson and L. Kepley, *J. Electrochem. Soc.*, 1996, **143**, 2507–2516.

141 F. Sauvage, L. Faffont, J. M. Tarascon and E. Baudrin, *Inorg. Chem.*, 2007, **46**, 3289–3294.

142 Y. Cao, L. Xiao, W. Wang, D. Choi, Z. Nie, J. Yu, L. V. Saraf, Z. Yang and J. Liu, *Adv. Mater.*, 2011, **23**, 3155–3160.

143 H. Kim, D. J. Kim, D.-H. Seo, M. S. Yeom, K. Kang, D. K. Kim and Y. Jung, *Chem. Mater.*, 2012, **24**, 1205–1211.

3604 | *Chem. Soc. Rev.*, 2017, **46**, 3529–3614

This journal is © The Royal Society of Chemistry 2017

144 J. F. Whitacre, A. Tevar and S. Sharma, *Electrochem. Commun.*, 2010, **12**, 463–466.

145 Z. Li, D. Young, K. Xiang, W. C. Carter and Y.-M. Chiang, *Adv. Energy Mater.*, 2013, **3**, 290–294.

146 D. Su, H.-J. Ahn and G. Wang, *J. Mater. Chem. A*, 2013, **1**, 4845–4850.

147 D. A. Tompsett and M. S. Islam, *Chem. Mater.*, 2013, **25**, 2515–2526.

148 F. Jiao and P. G. Bruce, *Adv. Mater.*, 2007, **19**, 657–660.

149 J. M. Tarascon, D. Guyomard, B. Wilkens, W. R. McKinnon and P. Barboux, *Solid State Ionics*, 1992, **57**, 113–120.

150 N. Yabuuchi, M. Yano, S. Kuze and S. Komaba, *Electrochim. Acta*, 2012, **82**, 296–301.

151 K. West, B. Zachau-Christiansen, T. Jacobsen and S. Skaarup, *Solid State Ionics*, 1988, **28–30**, 1129–1131.

152 S. Tepavcevic, H. Xiong, V. R. Stamenkovic, X. Zuo, M. Balasubramanian, V. B. Prakapenka, C. S. Johnson and T. Rajh, *ACS Nano*, 2012, **6**, 530–538.

153 N. B. Mahadi, J.-S. Park, J.-H. Park, K. Y. Chung, S. Y. Yi, Y.-K. Sun and S.-T. Myung, *J. Power Sources*, 2016, **326**, 522–532.

154 H. Arai, S. Okada, Y. Sakurai and J.-I. Yamaki, *J. Power Sources*, 1997, **68**, 716–719.

155 I. D. Gocheva, M. Nishijima, T. Doi, S. Okada, J.-I. Yamaki and T. Nishida, *J. Power Sources*, 2009, **187**, 247–252.

156 M. Nishijima, I. D. Gocheva, S. Okada, T. Doi, J.-I. Yamaki and T. Nishida, *J. Power Sources*, 2009, **190**, 558–562.

157 Y. Yamada, T. Doi, I. Tanaka, S. Okada and J.-I. Yamaki, *J. Power Sources*, 2011, **196**, 4837–4841.

158 S.-T. Myung, A. Ogata, K.-S. Lee, S. Komaba, Y.-K. Sun and H. Yashiro, *J. Electrochem. Soc.*, 2008, **155**, A374–A383.

159 S.-T. Myung, K.-S. Lee, C. S. Yoon, Y.-K. Sun, K. Amine and H. Yashiro, *J. Phys. Chem. C*, 2010, **114**, 4710–4718.

160 Y.-K. Sun, Z. Chen, H.-J. Noh, D.-J. Lee, H.-G. Jung, Y. Ren, S. Wang, C. S. Yoon, S.-T. Myung and K. Amine, *Nat. Mater.*, 2012, **11**, 942–947.

161 C.-H. Jo, D.-H. Cho, J.-W. Lee, H. Yashiro and S.-T. Myung, *J. Power Sources*, 2016, **282**, 511–519.

162 J. H. Jo, C.-H. Jo, H. Yashiro and S.-T. Myung, *J. Power Sources*, 2016, **313**, 1–8.

163 M. Avdeev, Z. Mohamed, C. D. Ling, J. Lu, M. Tamaru and A. Yamada, *Inorg. Chem.*, 2013, **52**, 8685–8693.

164 P. Moreau, D. Guyomard, J. Gaubicher and F. Boucher, *Chem. Mater.*, 2010, **22**, 4126–4128.

165 C. Li, X. Miao, W. Chu, P. Wu and D. G. Tong, *J. Mater. Chem. A*, 2015, **3**, 8265–8271.

166 A. Whiteside, C. A. Fisher, S. C. Park and M. S. Islam, *Phys. Chem. Chem. Phys.*, 2014, **16**, 21788–21794.

167 K. Zaghib, J. Trottier, P. Hovington, F. Brochu, A. Guerfi, A. Mauger and C. M. Julien, *J. Power Sources*, 2011, **196**, 9612–9617.

168 K. T. Lee, T. N. Ramesh, F. Nan, G. Botton and L. F. Nazar, *Chem. Mater.*, 2011, **23**, 3593–3600.

169 S.-M. Oh, S.-T. Myung, J. Hassoun, B. Scrosati and Y.-K. Sun, *Electrochem. Commun.*, 2012, **22**, 149–152.

170 M. Casas-Cabanas, V. V. Roddatis, D. Saurel, P. Kubiak, J. Carretero-Gonzalez, V. Palomares, Pl. Serras and T. Rojo, *J. Mater. Chem.*, 2012, **22**, 17421–17423.

171 W. Tang, X. Song, Y. Du, C. Peng, M. Lin, S. Xi, B. Tian, J. Zheng, Y. Wu, F. Pan and K. P. Loh, *J. Mater. Chem. A*, 2016, **4**, 4822–4892.

172 M. Nakayama, S. Yamada, R. Jalem and T. Kasuga, *Solid State Ionics*, 2016, **286**, 40–44.

173 G. Ali, J.-H. Lee, D. Susanto, S.-W. Choi, B. W. Cho, K.-W. Nam and K. Y. Chung, *ACS Appl. Mater. Interfaces*, 2016, **8**, 15422–15429.

174 J. N. Reimer and J. R. Dahn, *J. Electrochem. Soc.*, 1992, **139**, 2091–2097.

175 Y. Zhu, Y. Xu, Y. Liu, C. Luo and C. Wang, *Nanoscale*, 2013, **5**, 780–787.

176 B. L. Ellis, W. R. M. Makahnouk, Y. Makimura, K. Toghill and L. F. Nazar, *Nat. Mater.*, 2007, **6**, 749–753.

177 N. Rechan, J.-N. Chotard, L. Dupont, K. Djellab, M. Armand and J.-M. Tarascon, *J. Electrochem. Soc.*, 2009, **156**, A993–A999.

178 Y. Kawabe, N. Yabuuchi, M. Kajiyama, N. Fukuhara, T. Inamasu, R. Okuyama, I. Nakai and S. Komaba, *Electrochem. Commun.*, 2011, **13**, 1225–1228.

179 R. Triphthi, S. M. Wood, M. S. Islam and L. F. Nazar, *Energy Environ. Sci.*, 2013, **6**, 2257–2264.

180 Y. Kawabe, N. Yabuuchi, M. Kajiyama, N. Fujuhara, T. Inamasu, R. Okuyama, I. Nakai and S. Komaba, *Electrochemistry*, 2011, **80**, 80–84.

181 J. Barker, M. Y. Saidi and J. L. Swoyer, *Electrochem. Solid-State Lett.*, 2003, **6**, Al–A4.

182 J.-M. Le Meins, M.-P. Crosnier-Lopez, A. Hemon-Ribaud and G. Courbion, *J. Solid State Chem.*, 1999, **148**, 260–277.

183 J. Zhao, J. He, X. Ding, J. Zhou, Y. Ma, S. Wu and R. Huang, *J. Power Sources*, 2010, **198**, 6854–6859.

184 H. Zhuo, X. Yang, A. Tang, Z. Liu, S. Gamboa and P. J. Sebastian, *J. Power Sources*, 2006, **160**, 698–703.

185 Z.-M. Liu, X.-Y. Wang, Y. Wang, A. P. Tang, S.-Y. Yang and L.-F. He, *Trans. Nonferrous Met. Soc. China*, 2008, **18**, 346–350.

186 F. Sauvage, E. Quarez, J.-M. Tarascon and E. Baudrin, *Solid State Sci.*, 2006, **8**, 1215–1221.

187 Y.-U. Park, D.-H. Seo, H.-S. Kwon, B. Kim, J. Kim, H. Kim, I. Kim, H.-I. Yoo and K. Kang, *J. Am. Chem. Soc.*, 2013, **135**, 13870–13878.

188 R. A. Shakoor, D.-H. Seo, H. Kim, Y.-U. Park, J. Kim, S.-W. Kim, H. Gwon, S. Lee and K. Kang, *J. Mater. Chem.*, 2012, **22**, 20535–20541.

189 P. Serras, V. Palomares, A. Goni, I. Gil de Muro, P. Kubiak, L. Lezama and T. Rojo, *J. Mater. Chem.*, 2012, **22**, 22301–22308.

190 K. Chihara, A. Kitajou, I. D. Gocheva, S. Okada and J.-I. Yamaki, *J. Power Sources*, 2013, **227**, 80–85.

191 M. Bianchini, N. Brisset, F. Fauth, F. Weill, E. Elkaim, E. Uard, C. Masquelier and L. Croguennec, *Chem. Mater.*, 2014, **26**, 4238–4247.

192 Y. Uebou, S. Okada and J.-I. Yamaki, *J. Power Sources*, 2003, **115**, 119–124.

193 L. Adam, N. Guesdon and B. Raveau, *J. Solid State Chem.*, 2008, **181**, 3110–3115.

This journal is © The Royal Society of Chemistry 2017

Chem. Soc. Rev., 2017, **46**, 3529–3614 | 3605

194 S. Nishimura, M. Nakamura, R. Natsui and A. Yamada, *J. Am. Chem. Soc.*, 2010, **132**, 13596–13597.

195 H. Zhou, S. Upreti, N. A. Chernova, G. Hautier, G. Ceder and M. S. Whittingham, *Chem. Mater.*, 2011, **23**, 293–300.

196 T. Honma, T. Togashi, N. Ito and T. Komatsu, *J. Ceram. Soc. Jpn.*, 2012, **120**, 344–346.

197 P. Barpanda, T. Ye, S. Nishimura, S.-C. Chung, Y. Yamada, M. Okubo, H. Zhou and A. Yamada, *Electrochem. Commun.*, 2012, **24**, 116–119.

198 H. Kim, R. A. Shakoor, C. Park, S. Y. Lim, J.-S. Kim, Y. N. Jo, W. Cho, K. Miyasaka, R. Kahraman, Y. Jung and J. W. Choi, *Adv. Funct. Mater.*, 2013, **23**, 1147–1155.

199 J. M. Clark, P. Barpanda, A. Yamada and M. S. Islam, *J. Mater. Chem. A*, 2014, **2**, 11807–11812.

200 C.-Y. Chen, K. Matsumoto, T. Nohira and R. Hagiwara, *J. Power Sources*, 2014, **246**, 783–787.

201 K. H. Ha, S. H. Woo, D. Mok, N.-S. Choi, N.-S. Choi, Y. Park, S. M. Oh, Y. Kim, J. Lee, L. F. Nazar and K. T. Lee, *Adv. Energy Mater.*, 2013, **3**, 770–776.

202 P. Barpanda, T. Ye, M. Avdeev, S.-C. Chung and A. Yamada, *J. Mater. Chem. A*, 2013, **1**, 4194–4197.

203 P. Barpanda, G. Liu, M. Avdeev and A. Yamada, *ChemElectroChem*, 2014, **1**, 1488–1491.

204 F. Sanz, C. Parada, J. M. Rojo and C. Ruiz-Valero, *Chem. Mater.*, 2001, **13**, 1334–1340.

205 H. Kim, I. Park, D.-H. Seo, S. Lee, S.-W. Kim, W. J. Kwon, Y.-U. Park, C. S. Kim, S. Jeon and K. Kang, *J. Am. Chem. Soc.*, 2012, **134**, 10369–10372.

206 M. Nose, H. Nakayama, K. Nobuhara, H. Yamaguchi, S. Nakanishi and H. Iba, *J. Power Sources*, 2013, **234**, 175–179.

207 M. Nose, S. Shiotani, H. Nakayama, K. Nobuhara, S. Nakanishi and H. Iba, *Electrochem. Commun.*, 2013, **34**, 266–269.

208 S. Y. Lim, H. Kim, J. Chung, J. H. Lee, B. G. Kim, J.-J. Choi, K. Y. Chung, W. Cho, S.-J. Kim, W. A. Goddard III, Y. Jung and J.-W. Choi, *Proc. Natl. Aacd. Sci. U. S. A.*, 2014, **111**, 599–604.

209 Z. Jian, L. Zhao, H. Pan, Y.-S. Hu, H. Li, W. Chen and L. Chen, *Electrochem. Commun.*, 2012, **14**, 86–89.

210 J. Gopalakrishnan and K. K. Rangan, *Chem. Mater.*, 1992, **4**, 745–747.

211 C. Masquelier, in *Lithium Batteries Science and Technology*, ed. G.-A. Nazri and G. Pistoia, Kluwer Academic, Boston, 2004, ch. 15, p. 445.

212 L. S. Plashnitsa, E. Kobayashi, Y. Noguchi, S. Okada and J.-I. Yamaki, *J. Electrochem. Soc.*, 2010, **157**, A536–A543.

213 Z. Jian, W. Han, X. Lu, H. Yang, Y.-S. Hu, J. Zhou, Z. Zhou, J. Li, W. Chen, D. Chen and L. Chen, *Adv. Energy Mater.*, 2013, **3**, 156–160.

214 K. Saravanan, C. W. Mason, A. Rudola, K. H. Wong and P. Balaya, *Adv. Energy Mater.*, 2013, **3**, 444–450.

215 Z. Jian, C. Yuan, W. Han, X. Lu, L. Gu, X. Xi, Y.-S. Hu, H. Li, W. Chen, D. Chen, Y. Ikuhara and L. Chen, *Adv. Funct. Mater.*, 2014, **24**, 4265–4272.

216 N. Recham, J. N. Chotard, L. Dupont, C. Delacourt, W. Walker, M. Armand and J.-M. Tarascon, *Nat. Mater.*, 2010, **9**, 68–74.

217 P. Barpanda, J.-N. Chotard, N. Rcham, C. Delacourt, M. Ati, L. Dupont, M. Armand and J.-M. Tarascon, *Inorg. Chem.*, 2010, **49**, 7401–7413.

218 R. Tripathi, G. R. Gardiner, M. S. Islam and L. F. Nazar, *Chem. Mater.*, 2011, **23**, 2278–2284.

219 P. Barpanda, G. Oyama, S. Nishimura, S.-C. Chung and A. Yamada, *Nat. Commun.*, 2014, **5**, 4358.

220 H. Chen, G. Hautier and G. Ceder, *J. Am. Chem. Soc.*, 2012, **134**, 19619–19627.

221 H. Chen, Q. Hao, O. Zivkovic, G. Hautier, L.-S. Du, Y. Tang, Y.-Y. Hu, X. Ma, C. P. Grey and G. Ceder, *Chem. Mater.*, 2013, **25**, 2777–2786.

222 G. Hautier, A. Jain, H. L. Chen, C. Moore, S. P. Ong and G. Ceder, *J. Mater. Chem.*, 2001, **21**, 17147–17153.

223 A. Eftekhari, *J. Power Sources*, 2004, **126**, 221–228.

224 N. Imanishi, T. Morikawa, J. Kondo, Y. Takeda, O. Yamamoto, N. Kinugasa and T. Yamagishi, *J. Power Sources*, 1999, **79**, 215–219.

225 C. D. Wessells, M. T. McDowell, S. V. Peddada, M. Pasta, R. A. Huggins and Y. Cui, *ACS Nano*, 2012, **6**, 1688–1694.

226 C. D. Wessells, S. V. Peddada, M. T. McDowell, R. A. Huggins and Y. Cui, *J. Electrochem. Soc.*, 2012, **159**, A98–A103.

227 C. D. Wessells, R. A. Huggins and Y. Cui, *Nat. Commun.*, 2011, **2**, 550.

228 Y. H. Lu, L. Wang, J. G. Cheng and J. B. Goodenough, *Chem. Commun.*, 2012, **48**, 6544–6546.

229 L. Wang, Y. Lu, J. Liu, M. Xu, J. Cheng, D. Zhang and J. B. Goodenough, *Angew. Chem., Int. Ed.*, 2013, **52**, 1964–1967.

230 X. Wu, W. Deng, J. Qian, Y. Cao, X. Ai and H. Yang, *J. Mater. Chem. A*, 2013, **1**, 10130–10134.

231 J. Qian, M. Zhou, Y. Cao, Z. Ai and H. Yang, *Adv. Energy Mater.*, 2012, **2**, 410–414.

232 Z. P. Song and H. S. Zhou, *Energy Environ. Sci.*, 2013, **6**, 2280–2301.

233 Y. L. Liang, Z. L. Tao and J. Chen, *Adv. Energy Mater.*, 2012, **2**, 742–769.

234 H. Nishide and K. Oyaizu, *Science*, 2008, **319**, 737–738.

235 H. Y. Chen, M. Armand, G. Demailly, F. Dolhem, P. Poizot and J. M. Tarascon, *ChemSusChem*, 2008, **1**, 348–355.

236 S. Wang, L. Wang, Z. Zhu, Z. Hu, Q. Zhao and J. Chen, *Angew. Chem., Int. Ed.*, 2014, **53**, 5892–5896.

237 K. Chihara, N. Chujo, A. Kitajou and S. Okada, *Electrochim. Acta*, 2013, **110**, 240–246.

238 R. Zhao, L. Zhu, Y. Cao, X. Ai and H. X. Yang, *Electrochem. Commun.*, 2012, **21**, 36–38.

239 X. Xiang, K. Zhang and J. Chen, *Adv. Mater.*, 2015, **27**, 5343–5364.

240 Y. Kim, K. H. Ha, S. M. Oh and K. T. Lee, *Chemistry*, 2014, **20**, 11980–11992.

241 M.-S. Balogun, Y. Luo, W. Qiu, P. Liu and Y. Tong, *Carbon*, 2016, **98**, 162–178.

242 Y. Mei, Y. Huang and X. Hu, *J. Mater. Chem. A*, 2016, **4**, 12001–12013.

243 F. Klein, B. Jache, A. Bhide and P. Adelhelm, *Phys. Chem. Chem. Phys.*, 2013, **15**, 15876–15887.

3606 | *Chem. Soc. Rev.*, 2017, **46**, 3529–3614

This journal is © The Royal Society of Chemistry 2017

244 V. L. Chevrier and G. Ceder, *J. Electrochem. Soc.*, 2011, **158**, A1011–A1014.

245 M. Mortazavi, Q. Ye, N. Birbilis and N. V. Medhekar, *J. Power Sources*, 2015, **285**, 29–36.

246 S. P. Ong, V. L. Chevrier, G. Hautier, A. Jain, C. Moore, S. Kim, X. Ma and G. Ceder, *Energy Environ. Sci.*, 2011, **4**, 3680–3688.

247 D. A. Stevens and J. R. Dahn, *J. Electrochem. Soc.*, 2000, **147**, 1271–1273.

248 P.-C. Tsai, S.-C. Chung, S.-K. Lin and A. Yamada, *J. Mater. Chem. A*, 2015, **3**, 9763–9768.

249 E. Irisarri, A. Ponrouch and M. R. Palacin, *J. Electrochem. Soc.*, 2015, **162**, A2476–A2482.

250 C. Bommier, T. W. Surta, M. Dolgos and X. Ji, *Nano Lett.*, 2015, **15**, 5888–5892.

251 M. M. Doeff, Y. P. Ma, S. J. Visco and L. C. Dejonghe, *J. Electrochem. Soc.*, 1993, **140**, L169–L170.

252 D. Aurbach, M. D. Levi, E. Levi, H. Teller, B. Markovsky and G. Salitra, *J. Electrochem. Soc.*, 1988, **145**, 3024–3034.

253 Y. F. Reynier, R. Yazami and B. Fultz, *J. Electrochem. Soc.*, 2004, **151**, A422–A426.

254 P. Ge and M. Fouletier, *Solid State Ionics*, 1988, 1172–1175.

255 R. Raccichini, A. Varzi, S. Passerini and B. Scrosati, *Nat. Mater.*, 2015, **14**, 271–279.

256 Z. Wang, S. M. Selbach and T. Grande, *RSC Adv.*, 2014, **4**, 3973–3983.

257 K. Nobuhara, H. Nakayama, M. Nose, S. Nakanishi and H. Iba, *J. Power Sources*, 2013, **243**, 585–587.

258 B. Jache and P. Adelhelm, *Angew. Chem., Int. Ed.*, 2014, **53**, 10169–10173.

259 Z. Zhu, F. Cheng, Z. Hu and J. Chen, *J. Power Sources*, 2015, **293**, 626–634.

260 B. Jache, J. O. Binder, T. Abe and P. Adelgelm, *Phys. Chem. Chem. Phys.*, 2016, **18**, 14299–14316.

261 H. Kim, J. Hong, G. Yoon, H. Kim, K.-Y. Park, M.-S. Park, W.-S. Yoon and K. Kang, *Energy Environ. Sci.*, 2015, **8**, 2963–2969.

262 H. Kim, J. Hong, Y.-U. Park, J. Kim, I. Hwang and K. Kang, *Adv. Funct. Mater.*, 2015, **25**, 534–541.

263 Y. Wen, K. He, Y. Zhu, F. Han, Y. Xu, I. Matsuda, Y. Ishii, J. Cumings and C. Wang, *Nat. Commun.*, 2014, **5**, 4033.

264 Y.-J. Kang, S. C. Jung, J. W. Choi and Y.-K. Han, *Chem. Mater.*, 2015, **27**, 5402–5406.

265 K. Gotoh, T. Ishikawa, S. Shimadzu, N. Yabuuchi, S. Komaba, K. Takeda, A. Goto, K. Deguchi, S. Ohki, K. Hashi, T. Shimizu and H. Ishida, *J. Power Sources*, 2013, **225**, 137–140.

266 S. Wenzel, T. Hara, J. Janek and P. Adelhelm, *Energy Environ. Sci.*, 2011, **4**, 3342–3345.

267 C. Berger, Z. Song, X. Li, X. Wu, N. Brown, C. Naud, D. Mayou, T. Li, J. Hass, A. N. Marchenkov, E. H. Conrad, P. N. First and W. A. de Heer, *Science*, 2006, **312**, 1191–1195.

268 J. Liu and X. W. Liu, *Adv. Mater.*, 2012, **24**, 4097–4111.

269 J. Zhu, D. Yang, Z. Yin, Q. Yan and H. Zhang, *Small*, 2014, **10**, 3480–3498.

270 J. Zhu, R. Duanm, S. Zhang, N. Jiang, Y. Zhang and J. Zhu, *SpringerPlus*, 2014, **3**, 585.

271 G. Kucinskis, G. Bajars and J. Kleperis, *J. Power Sources*, 2013, **240**, 66–79.

272 S. Wu, R. Xu, M. Lu, R. Ge, J. Iocozzia, C. Han, B. Jiang and Z. Lin, *Adv. Energy Mater.*, 2015, **5**, 1500400.

273 X.-F. Luo, C.-H. Yang, Y.-Y. Peng, N.-W. Pu, M.-D. Ger, C.-T. Hsieh and J.-K. Chang, *J. Mater. Chem. A*, 2015, **3**, 10320–10326.

274 Y.-X. Wang, S.-L. Chou, H.-K. Liu and S.-X. Dou, *Carbon*, 2013, **57**, 202–208.

275 J. Ding, H. Wang, Z. Li, A. Kohandehghan, K. Cui, Z. Xu, B. Zahiri, X. Tan, E. M. Lotfabad, B. C. Olsen and D. Mitlin, *ACS Nano*, 2013, **7**, 11004–11015.

276 D. Datta, J. Li and V. B. Shenoy, *ACS Appl. Mater. Interfaces*, 2014, **6**, 1788–1795.

277 J. P. Paraknowitsch and A. Thomas, *Energy Environ. Sci.*, 2013, **6**, 2839–2855.

278 H. Song, N. Li, H. Cui and C. Wang, *Nano Energy*, 2014, **4**, 81–87.

279 Z. Wang, L. Qie, L. Yuan, W. Zhang, X. Hu and Y. Huang, *Carbon*, 2013, **55**, 328–334.

280 J. Xu, M. Wang, N. P. Wickramaratne, M. Jaroniec, S. Dou and L. Dai, *Adv. Mater.*, 2015, **27**, 2042–2048.

281 B. Ruan, J. Wang, D. Shi, Y. Xu, S. Chou, H. Liu and J. Wang, *J. Mater. Chem. A*, 2015, **3**, 19011–19017.

282 S. Wang, L. Xia, L. Yu, L. Zhang, H. Wang and X. W. D. Lou, *Adv. Energy Mater.*, 2016, **6**, 1502217.

283 H. G. Wang, Z. Wu, F. L. Meng, D. L. Ma, X. L. Huang, L. M. Wang and X. B. Zhang, *ChemSusChem*, 2013, **6**, 56–60.

284 C. Ling and F. Mizuno, *Phys. Chem. Chem. Phys.*, 2014, **16**, 10419–10424.

285 L. Fu, K. Tang, K. Song, P. A. van Aken, Y. Yu and J. Maier, *Nanoscale*, 2014, **6**, 1384–1389.

286 F. Yang, Z. Zhang, K. Du, X. Zhao, W. Chen, Y. Lai and J. Li, *Carbon*, 2015, **91**, 88–95.

287 G. Ma, K. Huang, Q. Zhuang and Z. Ju, *Mater. Lett.*, 2016, **174**, 221–225.

288 W. Li, M. Zhou, H. Li, K. Wang, S. Cheng and K. Jiang, *Energy Environ. Sci.*, 2015, **8**, 2916–2921.

289 L. Qie, W. Chen, X. Xiong, C. Hu, F. Zou, P. Hu and Y. Huang, *Adv. Sci.*, 2015, **2**, 1500195.

290 J. Ye, J. Zang, Z. Tian, M. Zheng and Q. Dong, *J. Mater. Chem. A*, 2016, **4**, 13223–13227.

291 Y. Li, Z. Wang, L. Li, S. Peng, L. Zhang, M. Srinivasan and S. Ramakrishna, *Carbon*, 2016, **99**, 556–563.

292 F. Shen, W. Luo, J. Dai, Y. Yao, M. Zhu, E. Hitz, Y. Tang, Y. Chen, V. L. Sprenkle, X. Li and L. Hu, *Adv. Energy Mater.*, 2016, **6**, 1600377.

293 E. M. Lotfabad, J. Ding, K. Cui, A. Kohandehghan, W. P. Kalisvaart, M. Hazelton and D. Mitlin, *ACS Nano*, 2014, **8**, 7115–7129.

294 H. Li, F. Shen, W. Luo, J. Dai, X. Han, Y. Chen, Y. Yao, H. Zhu, K. Fu, E. Hitz and L. Hu, *ACS Appl. Mater. Interfaces*, 2016, **8**, 2204–2210.

295 L. Wu, D. Buchholz, C. Vaalma, G. A. Giffin and S. Passerini, *ChemElectroChem*, 2015, **3**, 292–298.

296 T. Yang, T. Qian, M. Wang, X. Shen, N. Xu, Z. Sun and C. Yan, *Adv. Mater.*, 2016, **28**, 539–545.

This journal is © The Royal Society of Chemistry 2017

Chem. Soc. Rev., 2017, **46**, 3529–3614 | 3607

297 K.-L. Hong, L. Qie, R. Zeng, Z.-Q. Yi, W. Zhang, D. Wang, W. Yin, C. Wu, Q.-J. Fan, W.-X. Zhang and Y.-H. Huang, *J. Mater. Chem. A*, 2014, **2**, 12733–12738.

298 H. Zheng, J. Li, X. Song, G. Liu and V. S. Battaglia, *Electrochim. Acta*, 2012, **71**, 258–265.

299 V. Aravindan, Y.-S. Lee, R. Yazami and S. Madhavi, *Mater. Today*, 2015, **18**, 345–351.

300 S. Guo, J. Yi, Y. Sun and H. Zhou, *Energy Environ. Sci.*, 2016, **9**, 2978–3006.

301 F. Legrain, O. Malyi and S. Manzhos, *J. Power Sources*, 2015, **278**, 197–202.

302 D. Su, S. Dou and G. Wang, *Chem. Mater.*, 2015, **27**, 6022–6029.

303 S. Lunell, A. Stashans, L. Ojamae, H. Lindstrom and A. Hagfeldt, *J. Am. Chem. Soc.*, 1997, **119**, 7374–7380.

304 H. Xiong, M. D. Slater, M. Balasubramanian, C. S. Johnson and T. Rajh, *J. Phys. Chem. Lett.*, 2011, **2**, 2560–2565.

305 M. Stromme Mattsson, M. Veszelei, G. A. Niklasson, C.-G. Granqvist, A. Stashan and S. Lunell, in *Cation Diffusion in Electrochromic Fluorinated Ti Dioxide. In Electrochromic Materials and Their Applications III*, ed. K. C. Ho, C. B. Greenberg and D. M. MacArthur, The Electrochemical Society, Pennington, NJ, 1997.

306 Y. Xu, E. M. Lotfabad, H. Wang, B. Farbod, Z. Xu, A. Kohandehghan and D. Mitlin, *Chem. Commun.*, 2013, **49**, 8973–8975.

307 L. Wu, D. Buchholz, D. Bresser, L. Gomes Chagas and S. Passerini, *J. Power Sources*, 2014, **251**, 379–385.

308 J. R. González, R. Alcántara, F. Nacimiento, G. F. Ortiz and J. L. Tirado, *CrystEngComm*, 2014, **16**, 4602–4609.

309 K. T. Kim, G. Ali, K. Y. Chung, C. S. Yoon, H. Yashiro, Y.-K. Sun, J. Lu, K. Amine and S. T. Myung, *Nano Lett.*, 2014, **14**, 416–422.

310 L. Wu, D. Bresser, D. Buchholz, G. A. Giffin, C. R. Castro, A. Ochel and S. Passerini, *Adv. Energy Mater.*, 2015, **5**, 1401142.

311 Y. Yeo, J. W. Jung, K. Park and I. D. Kim, *Sci. Rep.*, 2015, **5**, 13862.

312 J.-Y. Hwang, S.-T. Myung, J.-H. Lee, A. Abouimrane, I. Belharouak and Y.-K. Sun, *Nano Energy*, 2015, **16**, 218–226.

313 B. Wang, F. Zhao, G. Du, S. Porter, Y. Liu, P. Zhang, Z. Cheng, H. K. Liu and Z. Huang, *ACS Appl. Mater. Interfaces*, 2016, **8**, 16009–16015.

314 Y. Xu, M. Zhou, L. Wen, C. Wang, H. Zhao, Y. Mi, L. Liang, Q. Fu, M. Wu and Y. Lei, *Chem. Mater.*, 2015, **27**, 4274–4280.

315 N. O. Gopal, H.-H. Lo and S.-C. Ke, *J. Am. Chem. Soc.*, 2008, **130**, 2760–2761.

316 Y. Yang, X. Ji, M. Jing, H. Hou, Y. Zhu, L. Fang, X. Yang, Q. Chen and C. E. Banks, *J. Mater. Chem. A*, 2015, **3**, 5648–5655.

317 S. K. Das, B. Jache, H. Lahon, C. L. Bender, J. Janek and P. Adelhelm, *Chem. Commun.*, 2016, **52**, 1428–1431.

318 S.-M. Oh, J.-Y. Hwang, C. S. Yoon, J. Lu, K. Amine, I. Belharouak and Y.-K. Sun, *ACS Appl. Mater. Interfaces*, 2014, **6**, 11295–11301.

319 X. Yang, C. Wang, Y. Yang, Y. Zhang, X. Jia, J. Chen and X. Ji, *J. Mater. Chem. A*, 2015, **3**, 8800–8807.

320 Z. Hong, K. Zhou, Z. Huang and M. Wei, *Sci. Rep.*, 2015, **5**, 11960.

321 Y. Ge, H. Jiang, J. Zhu, Y. Lu, C. Chen, Y. Hu, Y. Qiu and X. Zhang, *Electrochim. Acta*, 2015, **157**, 142–148.

322 M. N. Tahir, B. Oschmann, D. Buchholz, X. Dou, I. Lieberwirth, M. Panthofer, W. Tremel, R. Zentel and S. Passerini, *Adv. Energy Mater.*, 2016, **6**, 1501489.

323 J. Ni, S. Fu, C. Wu, J. Maier, Y. Yu and L. Li, *Adv. Mater.*, 2016, **28**, 2259–2265.

324 Z. Hong, J. Hong, C. Xie, Z. Huang and M. Wei, *Electrochim. Acta*, 2016, **202**, 203–208.

325 Z. Hong, K. Zhou, J. Zhang, Z. Huang and M. Wei, *J. Mater. Chem. A*, 2015, **3**, 17412–17416.

326 H. Usui, S. Yoshioka, K. Wasada, M. Shimizu and H. Sakaguchi, *ACS Appl. Mater. Interfaces*, 2015, **7**, 6567–6573.

327 Y. Zhang, X. Pu, Y. Yang, Y. Zhu, H. Hou, M. Jing, X. Yang, J. Chen and X. Ji, *Phys. Chem. Chem. Phys.*, 2015, **17**, 15764–15770.

328 Y. Zhang, C. W. Foster, C. E. Banks, L. Shao, H. Hou, G. Zou, J. Chen, Z. Huang and X. Ji, *Adv. Mater.*, 2016, **28**, 9391–9399.

329 J. P. Huang, D. D. Yuan, H. Z. Zhang, Y. L. Cao, G. R. Li, H. X. Yang and X. P. Gao, *RSC Adv.*, 2013, **3**, 12593–12597.

330 J. Lee, J. K. Lee, K. Y. Chung, H.-G. Jung, H. Kim, J. Mun and W. Choi, *Electrochim. Acta*, 2016, **200**, 21–28.

331 C. Chen, Y. Wen, X. Hu, X. Ji, M. Yan, L. Mai, P. Hu, B. Shan and Y. Huang, *Nat. Commun.*, 2015, **6**, 6929.

332 L. Wu, D. Bresser, D. Buchholz and S. Passerini, *J. Electrochem. Soc.*, 2015, **162**, A3052–A3058.

333 M. Søndergaard, K. J. Dalgaard, E. D. Bøjesen, K. Wonsyld, S. Dahl and B. B. Iversen, *J. Mater. Chem. A*, 2015, **3**, 18667–18674.

334 T. Umebayashi, T. Yamaki, H. Itoh and K. Asai, *Appl. Phys. Lett.*, 2002, **81**, 454–456.

335 H.-G. Jung, S.-T. Myung, C. S. Yoon, S.-B. Son, K. H. Oh, K. Amine, B. Scrosati and Y.-K. Sun, *Energy Environ. Sci.*, 2011, **4**, 1345–1351.

336 L. Zhao, H.-L. Pan, Y.-S. Hu, H. Li and L.-Q. Chen, *Chin. Phys. B*, 2012, **21**, 028201.

337 Y. Sun, L. Zhao, H. Pan, X. Lu, L. Gu, Y. S. Hu, H. Li, M. Armand, Y. Ikuhara, L. Chen and X. Huang, *Nat. Commun.*, 2013, **4**, 1870.

338 M. Kitta, K. Kuratani, M. Tabuchi, R. Kataoka, T. Kiyobayashi and M. Kohyama, *Electrochemistry*, 2015, **83**, 989–992.

339 K.-T. Kim, C.-Y. Yu, C. S. Yoon, S.-J. Kim, Y.-K. Sun and S.-T. Myung, *Nano Energy*, 2015, **12**, 725–734.

340 X. Yu, H. Pan, W. Wan, C. Ma, J. Bai, Q. Meng, S. N. Ehrlich, Y. S. Hu and X. Q. Yang, *Nano Lett.*, 2013, **13**, 4721–4727.

341 G. Hasegawa, K. Kanamori, T. Kiyomura, H. Kurata, K. Nakanishi and T. Abe, *Adv. Energy Mater.*, 2015, **5**, 1400730.

342 P. Yu, C. Li and X. Guo, *J. Phys. Chem. C*, 2014, **118**, 10616–10624.

343 C. Chen, H. Xu, T. Zhou, Z. Guo, L. Chen, M. Yan, L. Mai, P. Hu, S. Cheng, Y. Huang and J. Xie, *Adv. Energy Mater.*, 2016, **6**, 1600322.

344 Q. Zhou, L. Liu, J. Tan, Z. Yan, Z. Huang and X. Wang, *J. Power Sources*, 2015, **283**, 243–250.

345 L. Y. Yang, H. Z. Li, J. Liu, S. S. Tang, Y. K. Lu, S. T. Li, J. Min, N. Yan and M. Lei, *J. Mater. Chem. A*, 2015, **3**, 24446–24452.

346 X. Feng, H. Zou, H. Xiang, X. Guo, T. Zhou, Y. Wu, W. Xu, P. Yan, C. Wang, J. G. Zhang and Y. Yu, *ACS Appl. Mater. Interfaces*, 2016, **8**, 16718–16726.

347 P. Senguttuvan, G. Rousse, V. Seznec, J.-M. Tarascon and M. R. Palacín, *Chem. Mater.*, 2011, **23**, 4109–4111.

348 J. Xu, C. Ma, M. Balasubramanian and Y. S. Meng, *Chem. Commun.*, 2014, **50**, 12564–12567.

349 A. Rudola, K. Saravanan, C. W. Mason and P. Balaya, *J. Mater. Chem. A*, 2013, **1**, 2653–2662.

350 A. Rudola, N. Sharma and P. Balaya, *Electrochem. Commun.*, 2015, **61**, 10–13.

351 H. Pan, X. Lu, X. Yu, Y.-S. Hu, H. Li, X.-Q. Yang and L. Chen, *Adv. Energy Mater.*, 2013, **3**, 1186–1194.

352 M. A. Muñoz-Márquez, M. Zarrabeitia, E. Castillo-Martinez, A. Eguia-Barrio, T. Rojo and M. Casas-Cabanas, *ACS Appl. Mater. Interfaces*, 2015, **7**, 7801–7808.

353 W. Zou, J. Li, Q. Deng, J. Xue, X. Dai, A. Zhou and J. Li, *Solid State Ionics*, 2014, **262**, 192–196.

354 N. D. Trinh, O. Crosnier, S. B. Schougaard and T. Broussre, *ECS Trans.*, 2011, **35**, 91–98.

355 A. Rudola, K. Saravanan, S. Devaraj, H. Gong and P. Balaya, *Chem. Commun.*, 2013, **49**, 7451–7453.

356 K. Shen and M. Wagemaker, *Inorg. Chem.*, 2014, **53**, 8250–8256.

357 M. Shirpour, J. Cabana and M. Doeff, *Energy Environ. Sci.*, 2013, **6**, 2538–2547.

358 S. H. Woo, Y. Park, W. Y. Choi, N.-S. Choi, S. Nam, B. Park and K. T. Lee, *J. Electrochem. Soc.*, 2012, **159**, A2016–2023.

359 P. J. P. Naeyaert, M. Avdeev, N. Sharma, H. B. Yahia and C. D. Ling, *Chem. Mater.*, 2014, **26**, 7067–7072.

360 A. Maazaz, C. Delmas and P. Hagenmuller, *J. Inclusion Phenom. Macrocyclic Chem.*, 1983, **1**, 45–51.

361 D. Wu, X. Li, B. Xu, N. Twu, L. Liu and G. Ceder, *Energy Environ. Sci.*, 2015, **8**, 195–202.

362 Y. Wang, X. Yu, S. Xu, J. Bai, R. Xiao, Y. S. Hu, H. Li, X. Q. Yang, L. Chen and X. Huang, *Nat. Commun.*, 2013, **4**, 2365.

363 A. D. Wadsley and W. G. Mumme, *Acta Crystallogr.*, 1968, **24**, 392–396.

364 H. Li, H. Fei, X. Liu, J. Yang and M. Wei, *Chem. Commun.*, 2015, **51**, 9298–9300.

365 R. Alcantara, M. Jaraba, P. Lavela and J. L. Tirado, *Chem. Mater.*, 2002, **14**, 2847–2848.

366 S. Komaba, T. Mikumo, N. Yabuuchi, A. Ogata, H. Yoshida and Y. Yamada, *J. Electrochem. Soc.*, 2010, **157**, A60–A65.

367 S. Hariharan, K. Saravanan, V. Ramar and P. Balaya, *Phys. Chem. Chem. Phys.*, 2013, **15**, 2945–2953.

368 D. Y. Park and S. T. Myung, *ACS Appl. Mater. Interfaces*, 2014, **6**, 11749–11757.

369 S. Liu, Y. Wang, Y. Dong, Z. Zhao, Z. Wang and J. Qiu, *ChemElectroChem*, 2016, **3**, 38–44.

370 B. Koo, S. Chattopadhyay, T. Shibata, V. B. Prakapenka, C. S. Johnson, T. Rajh and E. V. Shevchenko, *Chem. Mater.*, 2013, **25**, 245–252.

371 P. R. Kumar, Y. H. Jung, K. K. Bharathi, C. H. Lim and D. K. Kim, *Electrochim. Acta*, 2014, **146**, 503–510.

372 J. Ming, H. Ming, W. Yang, W.-J. Kwak, J.-B. Park, J. Zheng and Y.-K. Sun, *RSC Adv.*, 2015, **5**, 8793–8800.

373 Z. Jian, B. Zhao, P. Liu, F. Li, M. Zheng, M. Chen, Y. Shi and H. Zhou, *Chem. Commun.*, 2014, **50**, 1215–1217.

374 B. Huang, K. Tai, M. Zhang, Y. Xiao and S. J. Dillon, *Electrochim. Acta*, 2014, **118**, 143–149.

375 X. Liu, T. Chen, H. Chu, L. Niu, Z. Sun, L. Pan and C. Q. Sun, *Electrochim. Acta*, 2015, **166**, 12–16.

376 M. Valvo, F. Lindgren, U. Lafont, F. Björefors and K. Edström, *J. Power Sources*, 2014, **245**, 967–978.

377 B. Philippe, M. Valvo, F. Lindgren, H. Rensmo and K. Edström, *Chem. Mater.*, 2014, **26**, 5028–5041.

378 M. M. Rahman, A. M. Glushenkov, T. Ramireddy and Y. Chen, *Chem. Commun.*, 2014, **50**, 5057–5060.

379 M. M. Rahman, I. Sultana, Z. Chen, M. Srikanth, L. H. Li, X. J. Dai and Y. Chen, *Nanoscale*, 2015, **7**, 13088–13095.

380 Q. Deng, L. Wang and J. Li, *J. Mater. Sci.*, 2015, **50**, 4142–4148.

381 Z. Jian, P. Liu, F. Li, M. Chen and H. Zhou, *J. Mater. Chem. A*, 2014, **2**, 13805–13809.

382 K. C. Klavetter, S. Garcia, N. Dahal, J. L. Snider, J. Pedro de Souza, T. H. Cell, M. A. Cassara, A. Heller, S. M. Humphrey and C. B. Mullins, *J. Mater. Chem. A*, 2014, **2**, 14209–14221.

383 M. Gu, A. Kushima, Y. Shao, J. G. Zhang, J. Liu, N. D. Browning, J. Li and C. Wang, *Nano Lett.*, 2013, **13**, 5203–5211.

384 Y.-X. Wang, Y.-G. Lim, M.-S. Park, S.-L. Chou, J. H. Kim, H.-K. Liu, S.-X. Dou and Y.-J. Kim, *J. Mater. Chem. A*, 2014, **2**, 529–534.

385 M. Dirican, Y. Lu, Y. Ge, O. Yildiz and X. Zhang, *ACS Appl. Mater. Interfaces*, 2015, **7**, 18387–18396.

386 Y. C. Lu, C. Ma, J. Alvarado, T. Kidera, N. Dimov, Y. S. Meng and S. Okada, *J. Power Sources*, 2015, **284**, 287–295.

387 D. Su, X. Xie and G. Wang, *Chemistry*, 2014, **20**, 3192–3197.

388 X. Xie, S. Chen, B. Sun, C. Wang and G. Wang, *ChemSusChem*, 2015, **8**, 2948–2955.

389 R. S. Kalubarme, J. Y. Lee and C. J. Park, *ACS Appl. Mater. Interfaces*, 2015, **7**, 17226–17237.

390 X. Xie, D. Su, J. Zhang, S. Chen, A. K. Mondal and G. Wang, *Nanoscale*, 2015, **7**, 3164–3172.

391 L. Wang, K. Zhang, Z. Hu, W. Duan, F. Cheng and J. Chen, *Nano Res.*, 2013, **7**, 199–208.

392 S. Yuan, X. L. Huang, D. L. Ma, H. G. Wang, F. Z. Meng and X. B. Zhang, *Adv. Mater.*, 2014, **26**, 2273–2279.

393 X. Zhang, W. Qin, D. Li, D. Yan, B. Hu, Z. Sun and L. Pan, *Chem. Commun.*, 2015, **51**, 16413–16416.

394 H. Liu, F. Cao, H. Zheng, H. Sheng, L. Li, S. Wu, C. Liu and J. Wang, *Chem. Commun.*, 2015, **51**, 10443–10446.

395 Y. Lu, N. Zhang, Q. Zhao, J. Liang and J. Chen, *Nanoscale*, 2015, **7**, 2770–2776.

396 Z. Zhang, J. Feng, L. Ci, Y. Tian and S. Xiong, *Mater. Technol.*, 2016, **31**, 497–500.

This journal is © The Royal Society of Chemistry 2017

Chem. Soc. Rev., 2017, **46**, 3529–3614 | 3609

397 L.-L. Feng, G.-D. Li, Y. Liu, Y. Wu, H. Chen, Y. Wang, Y.-C. Zou, D. Wang and X. Zou, *ACS Appl. Mater. Interfaces*, 2015, **7**, 980–988.

398 Y. Jiang, M. Hu, D. Zhang, T. Yuan, W. Sun, B. Xu and M. Yan, *Nano Energy*, 2014, **5**, 60–66.

399 F. Zou, Y. M. Chen, K. Liu, Z. Yu, W. Liang, S. M. Bhaway, M. Gao and Y. Zhu, *ACS Nano*, 2016, **10**, 377–386.

400 L. L. Feng, G. D. Li, Y. Liu, Y. Wu, H. Chen, Y. Wang, Y. C. Zou, D. Wang and X. Zou, *ACS Appl. Mater. Interfaces*, 2015, **7**, 980–988.

401 Q. Wang, L. Jiao, H. Du, W. Peng, Y. Han, D. Song, Y. Si, Y. Wang and H. Yuan, *J. Chem. Mater.*, 2011, **21**, 327–329.

402 D. He, D. Wu, J. Gao, X. Wu, X. Zeng and W. Ding, *J. Power Sources*, 2015, **294**, 643–649.

403 S.-J. Bao, C. M. Li, C.-X. Guo and Y. Qiao, *J. Power Sources*, 2008, **180**, 676–681.

404 Q. Wang, L. Jiao, H. Du, W. Peng, Y. Han, D. Song, Y. Si, Y. Wang and H. Yuan, *J. Mater. Chem.*, 2011, **21**, 327–329.

405 J. Liu, C. Wu, D. Xiao, P. Kopold, L. Gu, P. A. van Aken, J. Maier and Y. Yu, *Small*, 2016, **12**, 2354–2364.

406 D. Yin, G. Huang, F. Zhang, Y. Qin, Z. Na, Y. Wu and L. Wang, *Chemistry*, 2016, **22**, 1467–1474.

407 Z. Shadike, M. H. Cao, F. Ding, L. Sang and Z. W. Fu, *Chem. Commun.*, 2015, **51**, 10486–10489.

408 Q. Zhou, L. Liu, G. Guo, Z. Yan, J. Tan, Z. Huang, X. Chen and X. Wang, *RSC Adv.*, 2015, **5**, 71644–71651.

409 S. Peng, X. Han, L. Li, Z. Zhu, F. Cheng, M. Srinivansan, S. Adams and S. Ramakrishna, *Small*, 2016, **12**, 1359–1368.

410 Q. Zhou, L. Liu, Z. Huang, L. Yi, X. Wang and G. Cao, *J. Mater. Chem. A*, 2016, **4**, 5505–5516.

411 J. Park, J.-S. Kim, J.-W. Park, T.-H. Nam, K.-W. Kim, J.-H. Ahn, G. Wang and H.-J. Ahn, *Electrochim. Acta*, 2013, **92**, 427–432.

412 L. David, R. Bhandavt and G. Singh, *ACS Nano*, 2014, **8**, 1759–1770.

413 Z. Hu, L. Wang, K. Zhang, J. Wang, F. Cheng, Z. Tao and J. Chen, *Angew. Chem., Int. Ed.*, 2014, **53**, 12794–12798.

414 Y. X. Wang, K. H. Seng, S. L. Chou, J. Z. Wang, Z. Guo, D. Wexler, H. K. Liu and S. X. Dou, *Chem. Commun.*, 2014, **50**, 10730–10733.

415 W. H. Ryu, J. W. Jung, K. Park, S. J. Kim and I. D. Kim, *Nanoscale*, 2014, **6**, 10975–10981.

416 Y. X. Wang, S. L. Chou, D. Wexler, H. K. Liu and S. X. Dou, *Chemistry*, 2014, **20**, 9607–9612.

417 S. Zhang, X. Yu, H. Yu, Y. Chen, P. Gao, C. Li and C. Zhu, *ACS Appl. Mater. Interfaces*, 2014, **6**, 21880–21885.

418 D. Su, S. Dou and G. Wang, *Adv. Energy Mater.*, 2015, **5**, 1401205.

419 X. Xie, Z. Ao, D. Su, J. Zhang and G. Wang, *Adv. Funct. Mater.*, 2015, **25**, 1393–1403.

420 S. Kalluri, K. H. Seng, Z. Guo, A. Du, K. Konstantinov, H. K. Liu and S. X. Dou, *Sci. Rep.*, 2015, **5**, 11989.

421 S. H. Choi, Y. N. Ko, J.-K. Lee and Y. C. Kang, *Adv. Funct. Mater.*, 2015, **25**, 1780–1788.

422 Y. Lu, Q. Zhao, N. Zhang, K. Lei, F. Li and J. Chen, *Adv. Funct. Mater.*, 2016, **26**, 911–918.

423 T. B. Kim, W. H. Jung, H. S. Ryu, K. W. Kim, J. H. Ahn, K. K. Cho, G. B. Cho, T. H. Nam, I. S. Ahn and H. J. Ahn, *J. Alloys Compd.*, 2008, **449**, 304–307.

424 T. B. Kim, J. W. Choi, H. S. Ryu, G. B. Cho, K. W. Kim, J. H. Ahn, K. K. Cho and H. J. Ahn, *J. Power Sources*, 2007, **174**, 1275–1278.

425 A. Kitajou, J. Yamaguchi, S. Hara and S. Okada, *J. Power Sources*, 2014, **247**, 391–395.

426 A. Douglas, R. Carter, L. Oakes, K. Share, A. P. Cohn and C. L. Pint, *ACS Nano*, 2015, **9**, 11156–11165.

427 Y. Zhu, L. Suo, T. Gao, X. Fan, F. Han and C. Wang, *Electrochem. Commun.*, 2015, **54**, 18–22.

428 S. Y. Lee and Y. C. Kang, *Chemistry*, 2016, **22**, 2769–2774.

429 Z. Hu, Z. Zhu, F. Cheng, K. Zhang, J. Wang, C. Chen and J. Chen, *Energy Environ. Sci.*, 2015, **8**, 1309–1316.

430 M. Walter, T. Zund and M. V. Kovalenko, *Nanoscale*, 2015, **7**, 9158–9163.

431 X. Wei, W. Li, J. A. Shi, L. Gu and Y. Yu, *ACS Appl. Mater. Interfaces*, 2015, **7**, 27804–27809.

432 Y. X. Wang, J. Yang, S. L. Chou, H. K. Liu, W. X. Zhang, D. Zhao and S. X. Dou, *Nat. Commun.*, 2015, **6**, 8689.

433 L. Wu, H. Lu, L. Xiao, J. Qian, X. Ai, H. Yang and Y. Cao, *J. Mater. Chem. A*, 2014, **2**, 16424–16428.

434 L. Wu, H. Lu, L. Xiao, X. Ai, H. Yang and Y. Cao, *J. Power Sources*, 2015, **293**, 784–789.

435 Y. C. Lu, C. Ma, J. Alvarado, N. Dimov, Y. S. Meng and S. Okada, *J. Mater. Chem. A*, 2015, **3**, 16971–16977.

436 C. Zhu, P. Kopold, W. Li, P. A. van Aken, J. Maier and Y. Yu, *Adv. Sci.*, 2015, **2**, 1500200.

437 L. Wu, X. Hu, J. Qian, F. Pei, F. Wu, R. Mao, X. Ai, H. Yang and Y. Cao, *J. Mater. Chem. A*, 2013, **1**, 7181.

438 X. Xie, D. Su, S. Chen, J. Zhang, S. Dou and G. Wang, *Chem. – Asian J.*, 2014, **9**, 1611–1617.

439 B. Qu, C. Ma, G. Ji, C. Xu, J. Xu, Y. S. Meng, T. Wang and J. Y. Lee, *Adv. Mater.*, 2014, **26**, 3854–3859.

440 Y. Zhang, P. Zhu, L. Huang, J. Xie, S. Zhang, G. Cao and X. Zhao, *Adv. Funct. Mater.*, 2015, **25**, 481–489.

441 J. Wnag, C. Luo, J. Mao, Y. Zhu, X. Fan, T. Gao, A. C. Mignerey and C. Wang, *ACS Appl. Mater. Interfaces*, 2015, **7**, 11476–11481.

442 Y. Liu, H. Kang, L. Jiao, C. Chen, K. Cao, Y. Wang and H. Yuan, *Nanoscale*, 2015, **7**, 1325–1332.

443 P. V. Prikhodchenko, D. Y. W. Yu, S. K. Batabyal, V. Uvarov, J. Gun, S. Sladkevich, A. A. Mikhaylov, A. G. Medvedev and O. Lev, *J. Mater. Chem. A*, 2014, **2**, 8431–8437.

444 J. Wang, C. Luo, J. Mao, Y. Zhu, X. Fan, T. Gao, A. C. Mignerey and C. Wang, *ACS Appl. Mater. Interfaces*, 2015, **7**, 11476–11481.

445 Q. Pan, J. Xie, T. Zhu, G. Cao, X. Zhao and S. Zhang, *Inorg. Chem.*, 2014, **53**, 3511–3518.

446 J.-S. Kim, D.-Y. Kim, G.-B. Cho, T.-H. Nam, K.-W. Kim, H.-S. Ryu, J.-H. Ahn and H.-J. Ahn, *J. Power Sources*, 2009, **189**, 864–868.

447 X. Xu, S. Ji, M. Gu and J. Liu, *ACS Appl. Mater. Interfaces*, 2015, **7**, 20957–20964.

448 Q. Pan, J. Xie, T. Zhu, G. Cao, X. Zhao and S. Zhang, *Inorg. Chem.*, 2014, **53**, 3511–3518.

3610 | *Chem. Soc. Rev.*, 2017, **46**, 3529–3614

This journal is © The Royal Society of Chemistry 2017

449 T. Wang, P. Hu, C. Zhang, H. Du, Z. Zhang, X. Wang, S. Chen, J. Xiong and G. Cui, *ACS Appl. Mater. Interfaces*, 2016, **8**, 7811–7817.

450 H.-S. Ryu, J.-E. Kim, J.-S. Park, J.-W. Park, K.-W. Kim, J.-H. Ahn, T.-H. Nam, G. Wang and H.-J. Ahn, *J. Electrochem. Soc.*, 2013, **160**, A338–A343.

451 D. Su, S. Dou and G. Wang, *Chem. Commun.*, 2014, **50**, 4192–4195.

452 Y. Liu, N. Zhang, H. Kang, M. Shang, L. Jiao and J. Chen, *Chemistry*, 2015, **21**, 11878–11884.

453 D. Su, K. Kretschmer and G. Wang, *Adv. Energy Mater.*, 2016, **6**, 1501785.

454 W. Qin, D. Li, X. Zhang, D. Yan, B. Hu and L. Pan, *Electrochim. Acta*, 2016, **191**, 435–443.

455 J. Fullenwarth, A. Darwiche, A. Soares, B. Donnadieu and L. Monconduit, *J. Mater. Chem. A*, 2014, **2**, 2050–2059.

456 S. O. Kim and A. Manthiram, *Chem. Commun.*, 2016, **52**, 4337–4340.

457 M. Fan, Y. Chen, Y. Xie, T. Yang, X. Shen, N. Xu, H. Yu and C. Yan, *Adv. Funct. Mater.*, 2016, **26**, 5019–5027.

458 W. J. Li, S. L. Chou, J. Z. Wang, H. K. Liu and S. X. Dou, *Chem. Commun.*, 2015, **51**, 3682–3685.

459 J. Qian, Y. Xiong, Y. Cao, X. Ai and H. Yang, *Nano Lett.*, 2014, **14**, 1865–1869.

460 Y. Kim, Y. Kim, A. Choi, S. Woo, D. Mok, N. S. Choi, Y. S. Jung, J. H. Ryu, S. M. Oh and K. T. Lee, *Adv. Mater.*, 2014, **26**, 4139–4144.

461 W. Li, S. L. Chou, J. Z. Wang, J. H. Kim, H. K. Liu and S. X. Dou, *Adv. Mater.*, 2014, **26**, 4037–4042.

462 X. Fan, J. Mao, Y. Zhu, C. Luo, L. Suo, T. Gao, F. Han, S.-C. Liou and C. Wang, *Adv. Energy Mater.*, 2015, **5**, 1500174.

463 J. Liu, P. Kopold, C. Wu, P. A. van Aken, J. Maier and Y. Yu, *Energy. Environ. Sci.*, 2015, **8**, 3531–3538.

464 W.-J. Li, Q.-R. Yang, S.-L. Chou, J.-Z. Wang and H.-K. Liu, *J. Power Sources*, 2015, **294**, 627–632.

465 J. Mao, X. Fan, C. Luo and C. Wang, *ACS Appl. Mater. Interfaces*, 2016, **8**, 7147–7155.

466 W. Zhang, M. Dahbi, S. Amagasa, Y. Yamada and S. Komaba, *Electrochem. Commun.*, 2016, **69**, 11–14.

467 F. Luo, B. Liu, J. Zheng, G. Chum, K. Zhong, H. Li, X. Huang and L. Chen, *J. Electrochem. Soc.*, 2015, **16**, A2509–A2528.

468 J. H. Lee, C. S. Yoon, J.-Y. Hwang, S.-J. Kim, F. Maglia, P. Lamp, S.-T. Myung and Y.-K. Sun, *Energy Environ. Sci.*, 2016, **9**, 2152–2158.

469 H. Morito, T. Yamada, T. Ikeda and H. Yamane, *J. Alloys Compd.*, 2009, **480**, 723–726.

470 S. C. Jung, D. S. Jung, J. W. Choi and Y. K. Han, *J. Phys. Chem. Lett.*, 2014, **5**, 1283–1288.

471 O. I. Malyi, T. L. Tan and S. Manzhos, *Appl. Phys. Express*, 2013, **6**, 027301.

472 O. Malyi, V. V. Kulish, T. L. TA464:C464an and S. Manzhos, *Nano Energy*, 2013, **2**, 1149–1157.

473 F. Legrain, O. I. Malyi and S. Manzhos, *Comput. Mater. Sci.*, 2014, **94**, 214–217.

474 V. V. Kulish, O. I. Malyi, M. F. Ng, Z. Chen, S. Manzhos and P. Wu, *Phys. Chem. Chem. Phys.*, 2014, **16**, 4260–4267.

475 Y. Xu, E. Swaans, S. Basak, H. W. Zandbergen, D. M. Borsa and F. M. Mulder, *Adv. Energy Mater.*, 2016, **6**, 1501436.

476 L. Zhang, X. Hu, C. Chen, H. Guo, X. Liu, G. Xu, H. Zhong, S. Chung, P. Wu, J. Meng, Y. Huang, S. Dou and H. Liu, *Adv. Mater.*, 2017, **29**, 1604708.

477 J. Sangster and A. D. Pelton, *J. Phase Equilib.*, 1997, **18**, 295.

478 C. Yue, C. Yu, S. Sun, X. He, B. Chen, W. Lin, B. Xu, M. Zheng, S. Wu, J. Li, J. Kang and L. Lin, *Adv. Funct. Mater.*, 2015, **25**, 1386–1392.

479 P. R. Abel, Y.-M. Lin, T. de Souza, C.-Y. Chou, A. Gupta, J. B. Goodenough, G. S. Hwang, A. Heller and C. B. Mullins, *J. Phys. Chem. C*, 2013, **117**, 18885–18890.

480 L. Baggetto, J. K. Keum, J. F. Browning and G. M. Veith, *Electrochem. Commun.*, 2013, **34**, 41–44.

481 A. Kohandehghan, K. Cui, M. Kupsta, J. Ding, E. Memarzadeh Lotfabad, W. P. Kalisvaart and D. Mitlin, *Nano Lett.*, 2014, **14**, 5873–5882.

482 S. Komaba, Y. Matsuura, T. Ishikawa, N. Yabuuchi, W. Murata and S. Kuze, *Electrochem. Commun.*, 2012, **21**, 65–68.

483 L. D. Ellis, T. D. Hatchard and M. N. Obrovac, *J. Electrochem. Soc.*, 2012, **159**, A1801–A1805.

484 J. W. Wang, X. H. Liu, S. X. Mao and J. Y. Huang, *Nano Lett.*, 2012, **12**, 5897–5902.

485 J. Wang, C. Eng, Y. C. Chen-Wiegart and J. Wang, *Nat. Commun.*, 2015, **6**, 7496.

486 L. Baggetto, P. Ganesh, R. P. Meisner, R. R. Unocic, J.-C. Jumas, C. A. Bridges and G. M. Veith, *J. Power Sources*, 2013, **234**, 48–59.

487 Y. Xu, Y. Zhu, Y. Liu and C. Wang, *Adv. Energy Mater.*, 2013, **3**, 128–133.

488 H. Zhu, Z. Jia, Y. Chen, N. Weadock, J. Wan, O. Vaaland, X. Han, T. Li and L. Hu, *Nano Lett.*, 2013, **13**, 3093–3100.

489 D. Bresser, F. Mueller, D. Buchholz, E. Paillard and S. Passerini, *Electrochim. Acta*, 2014, **128**, 163–171.

490 X. Xie, K. Kretschmer, J. Zhang, B. Sun, D. Su and G. Wang, *Nano Energy*, 2015, **13**, 208–217.

491 Y. Liu, N. Zhang, L. Jiao and J. Chen, *Adv. Mater.*, 2015, **27**, 6702–6707.

492 Y. Liu, N. Zhang, L. Jiao, Z. Tao and J. Chen, *Adv. Funct. Mater.*, 2015, **25**, 214–220.

493 B. Luo, T. Qiu, D. Ye, L. Wang and L. Zhi, *Nano Energy*, 2016, **22**, 232–240.

494 Z. Li, J. Ding and D. Mitlin, *Acc. Chem. Res.*, 2015, **48**, 1657–1665.

495 C. Kim, K.-Y. Lee, I. Kim, J. Park, G. Cho, K.-W. Kim, J.-H. Ahn and H.-J. Ahn, *J. Power Sources*, 2016, **317**, 153–158.

496 J. Sangster and A. D. Pelton, *J. Phase Equilib.*, 1993, **14**, 291.

497 J. Qian, Y. Chen, L. Wu, Y. Cao, X. Ai and H. Yang, *Chem. Commun.*, 2012, **48**, 7070–7072.

498 A. Darwiche, C. Marino, M. T. Sougrati, B. Fraisse, L. Stievano and L. Monconduit, *J. Am. Chem. Soc.*, 2012, **134**, 20805–20811.

499 L. Xiao, Y. Cao, J. Xiao, W. Wang, L. Kovarik, Z. Nie and J. Liu, *Chem. Commun.*, 2012, **48**, 3321–3323.

500 Y. Zhu, X. Han, Y. Xu, Y. Liu, S. Zheng, K. Xu, L. Hu and C. Wang, *ACS Nano*, 2013, **7**, 6378–6386.

This journal is © The Royal Society of Chemistry 2017

Chem. Soc. Rev., 2017, **46**, 3529–3614 | 3611

501 X. Zhou, Z. Dai, J. Bao and Y.-G. Guo, *J. Mater. Chem. A*, 2013, **1**, 13727–13731.

502 H. Hou, M. Jing, Y. Yang, Y. Zhang, W. Song, X. Yang, J. Chen, Q. Chen and X. Ji, *J. Power Sources*, 2015, **284**, 227–235.

503 M. He, K. Kravchyk, M. Walter and M. V. Kovalenko, *Nano Lett.*, 2014, **14**, 1255–1262.

504 L. Wu, X. Hu, J. Qian, F. Pei, F. Wu, R. Mao, X. Ai, H. Yang and Y. Cao, *Energy Environ. Sci.*, 2014, **7**, 323–328.

505 H. Hou, Y. Yang, Y. Zhu, M. Jing, C. Pan, L. Fang, W. Song, X. Yang and X. Ji, *Electrochim. Acta*, 2014, **146**, 328–334.

506 C. Nithya and S. Gopukumar, *J. Mater. Chem. A*, 2014, **2**, 10516–10525.

507 X. Zhou, Y. Zhong, M. Yang, M. Hu, J. Wei and Z. Zhou, *Chem. Commun.*, 2014, **50**, 12888–12891.

508 L. Hu, X. Zhu, Y. Du, Y. Li, X. Zhou and J. Bao, *Chem. Mater.*, 2015, **27**, 8138–8145.

509 N. Zhang, Y. Liu and Y. Lu, *Nano Res.*, 2015, **8**(10), 3384–3393.

510 J. M. Sangster, *J. Phase Equilib. Diffus.*, 2009, **31**, 62–67.

511 Y. Kim, Y. Park, A. Choi, N. S. Choi, J. Kim, J. Lee, J. H. Ryu, S. M. Oh and K. T. Lee, *Adv. Mater.*, 2013, **25**, 3045–3049.

512 J. Sun, H. W. Lee, M. Pasta, H. Yuan, G. Zheng, Y. Sun, Y. Li and Y. Cui, *Nat. Nanotechnol.*, 2015, **10**, 980–985.

513 J. Song, Z. Yu, M. L. Gordin, S. Hu, R. Yi, D. Tang, T. Walter, M. Regula, D. Choi, X. Li, A. Manivannan and D. Wang, *Nano Lett.*, 2014, **14**, 6329–6335.

514 J. Qian, X. Wu, Y. Cao, X. Ai and H. Yang, *Angew. Chem., Int. Ed.*, 2013, **52**, 4633–4636.

515 W. J. Li, S. L. Chou, J. Z. Wang, H. K. Liu and S. X. Dou, *Nano Lett.*, 2013, **13**, 5480–5484.

516 T. Ramireddy, T. Xing, M. M. Rahman, Y. Chen, Q. Dutercq, D. Gunzelmann and A. M. Glushenkov, *J. Mater. Chem. A*, 2015, **3**, 5572–5584.

517 J. Song, Z. Yu, M. L. Gordin, X. Li, H. Peng and D. Wang, *ACS Nano*, 2015, **9**, 11933–11941.

518 J. Sun, G. Zheng, H. W. Lee, N. Liu, H. Wang, H. Yao, W. Yang and Y. Cui, *Nano Lett.*, 2014, **14**, 4573–4580.

519 C. Zhang, X. Wang, Q. Liang, X. Liu, Q. Weng, J. Liu, Y. Yang, Z. Dai, K. Ding, Y. Bando, J. Tang and D. Golberg, *Nano Lett.*, 2016, **16**, 2054–2060.

520 A. Morita, *Appl. Phys.*, 1986, **39**, 227–242.

521 K. P. S. S. Hembram, H. Jung, B. C. Yeo, S. J. Pai, S. Kim, K.-R. Lee and S. S. Han, *J. Phys. Chem. C*, 2015, **119**, 15041–15046.

522 M. Dahbi, N. Yabuuchi, M. Fukunishi, K. Kubota, K. Chihara, K. Tokiwa, X. Yu, H. Ushiyama, K. Yamashita, J.-Y. Son, Y.-T. Cui, H. Oji and S. Komaba, *Chem. Mater.*, 2016, **28**, 1625–1635.

523 L. Kou, C. Chen and S. C. Smith, *J. Phys. Chem. Lett.*, 2015, **6**, 2794–2805.

524 G. L. Xu, Z. Chen, G. M. Zhong, Y. Liu, Y. Yang, T. Ma, Y. Ren, X. Zuo, X. H. Wu, X. Zhang and K. Amine, *Nano Lett.*, 2016, **16**, 3955–3965.

525 N. Nitta and G. Yushin, *Part. Part. Syst. Charact.*, 2014, **31**, 317–336.

526 C.-M. Park, S. Yoon, S.-I. Lee and H.-J. Sohn, *J. Power Sources*, 2009, **186**, 206–210.

527 L. D. Ellis, B. N. Wilkes, T. D. Hatachard and M. N. Obrovac, *J. Electrochem. Soc.*, 2014, **161**, A416–A421.

528 F. Yang, F. Yu, Z. Zhang, K. Zhang, Y. Lai and J. Li, *Chemistry*, 2016, **22**, 2333–2338.

529 J. Sottmann, M. Herrmann, P. Vajeeston, Y. Hu, A. Ruud, C. Drathen, H. Emerich, H. Fjellvåg and D. S. Wragg, *Chem. Mater.*, 2016, **28**, 2750–2756.

530 D. Su, S. Dou and G. Wang, *Nano Energy*, 2015, **12**, 88–95.

531 S. Liu, J. Feng, X. Bian, J. Liu and H. Xu, *J. Mater. Chem. A*, 2016, **4**, 10098–10104.

532 J. Liu, Y. Wen, P. A. van Aken, J. Maier and Y. Yu, *Nano Lett.*, 2014, **14**, 6387–6392.

533 L. Baggetto, K. J. Carroll, H.-Y. Hah, C. E. Johnson, D. R. Mullins, R. R. Unocic, J. A. Johnson, Y. S. Meng and G. M. Veith, *J. Phys. Chem. C*, 2014, **118**, 7856–7864.

534 L. Baggetto, H. Y. Hah, C. E. Johnson, C. A. Bridges, J. A. Johnson and G. M. Veith, *Phys. Chem. Chem. Phys.*, 2014, **16**, 9538–9545.

535 Y. M. Lin, P. R. Abel, A. Gupta, J. B. Goodenough, A. Heller and C. B. Mullins, *ACS Appl. Mater. Interfaces*, 2013, **5**, 8273–8277.

536 E. D. Jackson, S. Green and A. L. Prieto, *ACS Appl. Mater. Interfaces*, 2015, **7**, 7447–7450.

537 L. Baggetto, E. Allcorn, R. R. Unocic, A. Manthiram and G. M. Veith, *J. Mater. Chem. A*, 2013, **1**, 11163–11169.

538 I. T. Kim, S.-O. Kim and A. Manthiram, *J. Power Sources*, 2014, **269**, 848–854.

539 L. Ji, M. Gu, Y. Shao, X. Li, M. H. Engelhard, B. W. Arey, W. Wang, Z. Nie, J. Xiao, C. Wang, J. G. Zhang and J. Liu, *Adv. Mater.*, 2014, **26**, 2901–2908.

540 L. Ji, W. Zhou, V. Chabot, A. Yu and X. Xiao, *ACS Appl. Mater. Interfaces*, 2015, **7**, 24895–24901.

541 Y. Zhao and A. Manthiram, *Chem. Mater.*, 2015, **27**, 3096–3101.

542 J. Hassoun, S. Panero, P. Simon, P. L. Taberna and B. Scrosati, *Adv. Mater.*, 2007, **19**, 1632–1635.

543 B. Häupler, A. Wild and U. S. Schubert, *Adv. Energy Mater.*, 2015, **5**, 1402034.

544 L. Zhao, J. Zhao, Y.-S. Hu, H. Li, Z. Zhou, M. Armand and L. Chen, *Adv. Energy Mater.*, 2012, **2**, 962–965.

545 Y. Park, D. S. Shin, S. H. Woo, N. S. Choi, K. H. Shin, S. M. Oh, K. T. Lee and S. Y. Hong, *Adv. Mater.*, 2012, **24**, 3562–3567.

546 Q. Zhao, J. Wang, Y. Lu, Y. Li, G. Liang and J. Chen, *Angew. Chem., Int. Ed.*, 2014, **55**(38), 12528–12532.

547 A. Abouimrane, W. Weng, H. Eltayeb, Y. Cui, J. Niklas, O. Poluektov and K. Amine, *Energy Environ. Sci.*, 2012, **5**, 9632–9638.

548 X. Wu, S. Jin, Z. Zhang, L. Jiang, L. Mu, Y.-S. Hu, H. Li, X. Chen, M. Armand, L. Chen and X. Huang, *Sci. Adv.*, 2015, **1**, e1500330.

549 W. Deng, X. Liang, X. Wu, J. Qian, Y. Cao, X. Ai, J. Feng and H. Yang, *Sci. Rep.*, 2013, **3**, 2671.

550 W. Deng, J. Qian, Y. Cao, X. Ai and H. Yang, *Small*, 2016, **12**, 583–587.

551 Y. Wang, K. Kretschmer, J. Zhang, A. K. Mondal, X. Guo and G. Wang, *RSC Adv.*, 2016, **6**, 57098–57102.

3612 | *Chem. Soc. Rev.*, 2017, **46**, 3529–3614

This journal is © The Royal Society of Chemistry 2017

552 C. Wang, Y. Xu, Y. Fang, M. Zhou, L. Liang, S. Singh, H. Zhao, A. Schober and Y. Lei, *J. Am. Chem. Soc.*, 2015, **137**, 3124–3130.

553 A. Choi, Y. K. Kim, T. K. Kim, M.-S. Kwon, K. T. Lee and H. R. Moon, *J. Mater. Chem. A*, 2014, **2**, 14986–14993.

554 R. R. Zhao, Y. L. Cao, X. P. Ai and H. X. Yang, *J. Electroanal. Chem.*, 2013, **688**, 93–97.

555 H.-G. Wang, S. Yuan, Z. Si and X.-b. Zhang, *Energy Environ. Sci.*, 2015, **8**, 3160–3165.

556 S. Renault, V. A. Mihali, K. Edström and D. Brandell, *Electrochem. Commun.*, 2014, **45**, 52–55.

557 L. Chen, W. Li, Y. Wang, C. Wang and Y. Xia, *RSC Adv.*, 2014, **4**, 25369.

558 Z. Li, J. Zhou, R. Xu, S. Liu, Y. Wang, P. Li, W. Wu and M. Wu, *Chem. Eng. J.*, 2016, **287**, 516–522.

559 C. Luo, Y. Zhu, Y. Xu, Y. Liu, T. Gao, J. Wang and C. Wang, *J. Power Sources*, 2014, **250**, 372–378.

560 H. Zhu, J. Yin, X. Zhao, C. Wang and X. Yang, *Chem. Commun.*, 2015, **51**, 14708–14711.

561 H. Wang, P. Hu, J. Yang, G. Gong, L. Guo and X. Chen, *Adv. Mater.*, 2015, **27**, 2348–2354.

562 C. Luo, J. Wang, X. Fan, Y. Zhu, F. Han, L. Suo and C. Wang, *Nano Energy*, 2015, **13**, 537–545.

563 Z. Zhu, H. Li, J. Liang, Z. Tao and J. Chen, *Chem. Commun.*, 2015, **51**, 1446–1448.

564 E. Castillo-Martinez, J. Carretero-Gonzalez and M. Armand, *Angew. Chem., Int. Ed.*, 2014, **53**, 5341–5345.

565 M. López-Herraiz, E. Castillo-Martínez, J. Carretero-González, J. Carrasco, T. Rojo and M. Armand, *Energy Environ. Sci.*, 2015, **8**, 3233–3241.

566 J.-Y. Hwang, S.-T. Myung, C. S. Yoon, S.-S. Kim, D. Aurbach and Y.-K. Sun, *Adv. Funct. Mater.*, 2016, **26**, 8083–8093.

567 K. Vignarooban, R. Kushagra, A. Elango, P. Badami, B. E. Mellander, X. Xu, T. G. Tucker, C. Nam and A. M. Kannan, *Int. J. Hydrogen Energy*, 2016, **41**, 2829–2846.

568 A. Ponrouch, D. Monti, A. Boschin, B. Steen, P. Johansson and M. R. Palacín, *J. Mater. Chem. A*, 2015, **3**, 22–42.

569 H. Kim, J. Hong, K. Y. Park, H. Kim, S. W. Kim and K. Kang, *Chem. Rev.*, 2014, **114**, 11788–11827.

570 D. Aurbach, Y. Talyosef, B. Markovsky, E. Markevich, E. Zinigrad, L. Asraf, J. S. Gnanaraj and H.-J. Kim, *Electrochim. Acta*, 2004, **50**, 247–254.

571 K. Xu, *Chem. Rev.*, 2014, **114**, 11503–11618.

572 G. H. Newman and L. P. Klelmann, *J. Electrochem. Soc.*, 1980, **127**, 2097–2099.

573 J.-J. Braconnierm, C. Delmas, C. Fouassier and P. Hagenmuller, *Mater. Res. Bull.*, 1980, **15**, 1797–1804.

574 A. Ponrouch, R. Dedryvère, D. Monti, A. E. Demet, J. M. Ateba Mba, L. Croguennec, C. Masquelier, P. Johansson and M. R. Palacín, *Energy Environ. Sci.*, 2013, **6**, 2361–2369.

575 R. Alcántara, P. Lavela, G. F. Ortiz and J. L. Tirado, *Electrochem. Solid-State Lett.*, 2005, **8**, A222–A225.

576 A. Bhide, J. Hofmann, A. K. Durr, J. Janek and P. Adelhelm, *Phys. Chem. Chem. Phys.*, 2014, **16**, 1987–1998.

577 S. Komaba, T. Ishikawa, N. Yabuuchi, W. Murata, A. Ito and Y. Ohsawa, *ACS Appl. Mater. Interfaces*, 2011, **3**, 4165–4168.

578 T. Kajita and T. Itoh, *Phys. Chem. Chem. Phys.*, 2017, **19**, 1003–1009.

579 K. Zhang, M. Park, L. Zhou, G.-H. Lee, J. Shin, Z. Hu, S.-L. Chou, J. Chen and Y.-M. Kang, *Angew. Chem., Int. Ed.*, 2016, **55**, 12822–12826.

580 K. Zhang, M. Park, L. Zhou, G.-H. Lee, W. Li and Y.-M. Kang, *Adv. Funct. Mater.*, 2016, **26**, 6728–6735.

581 K. Zhang, Z. Hu, X. Liu, Z. Tao and J. Chen, *Adv. Mater.*, 2015, **27**, 3305–3309.

582 I. A. Shkrob, Y. Zhu, T. W. Marin and D. Abraham, *J. Phys. Chem. C*, 2013, **117**, 19255–19269.

583 H. Kumar, E. Detsi, D. P. Abraham and V. B. Shenoy, *Chem. Mater.*, 2016, **28**, 8930–8941.

584 V. Etacheri, O. Haik, Y. Goffer, G. A. Roberts, I. C. Stefan, R. Fasching and D. Aurbach, *Langmuir*, 2011, **28**, 965–976.

585 X. Chen, X. Li, D. Mei, J. Feng, M. Y. Hu, J. Hu, M. Engelhard, J. Zheng, W. Xu, J. Xiao, J. Liu and J.-G. Zhang, *ChemSusChem*, 2014, **7**, 549–554.

586 L. Ji, M. Gu, Y. Shao, X. Li, M. H. Engelhard, B. W. Arey, W. Wang, Z. Nie, J. Xiao, C. Wang, J.-G. Zhang and J. Liu, *Adv. Mater.*, 2014, **26**, 2901–2908.

587 E. Markevich, K. Fridman, R. Sharabi, R. Elazari, G. Salitra, H. E. Gottlieb, G. Gershinsky, A. Garsuch, G. Semrau, M. A. Schmidt and D. Aurbach, *J. Electrochem. Soc.*, 2013, **160**, A1824–A1833.

588 M. Dahbi, T. Nakano, N. Yabuuchhi, S. Fujimura, K. Chihara, K. Kobota, J.-Y. Son, Y.-T. Cui, H. Oji and S. Komaba, *ChemElectroChem*, 2016, **3**, 1856–1867.

589 M. Egashira, T. Tanaka, N. Yoshimoto and M. Morita, *Electrochemistry*, 2012, **80**, 755–758.

590 A. Fukunaga, T. Nohira, Y. Kozawa, R. Hagiwara, S. Sakai, K. Nitta and S. Inazawa, *J. Power Sources*, 2012, **209**, 52–56.

591 D. Monti, E. Jónsson, M. R. Palacín and P. Johansson, *J. Power Sources*, 2014, **245**, 630–636.

592 S. A. Mohd Noor, P. C. Howlett, D. R. MacFarlane and M. Forsyth, *Electrochim. Acta*, 2013, **114**, 766–771.

593 K. West, B. Zachau-Christiansen, T. Jacobsen and S. Atlung, *J. Electrochem. Soc.*, 1985, **132**, 3061–3062.

594 H. Gao, B. Guo, J. Song, K. Park and J. B. Goodenough, *Adv. Energy Mater.*, 2015, **5**, 1402235.

595 Y. L. Ni'mah, M.-Y. Cheng, J. H. Cheng, J. Rick and B.-J. Hwang, *J. Power Sources*, 2015, **278**, 375–381.

596 Y. Noguchi, E. Kobayashi, L. S. Plashnitsa, S. Okada and J.-I. Yamaki, *Electrochim. Acta*, 2013, **101**, 59–65.

597 A. Hayashi, K. Noi, A. Sakuda and M. Tatsumisago, *Nat. Commun.*, 2012, **3**, 856.

598 S. F. Lux, F. Schappacher, A. Balducci, S. Passerini and M. Winter, *J. Electrochem. Soc.*, 2010, **157**, A320–A325.

599 Z. P. Cai, Y. Liang, W. S. Li, L. D. Xing and Y. H. Liao, *J. Power Sources*, 2009, **189**, 547–551.

600 J. Ming, H. Ming, W. J. Kwak, C. Shin, J. Zheng and Y.-K. Sun, *Chem. Commun.*, 2014, **50**, 13307–13310.

601 M. Dahbi, T. Nakano, N. Yabuuchi, T. Ishikawa, K. Kubota, M. Fukunishi, S. Shibahara, J.-Y. Son, Y.-T. Cui, H. Oji and S. Komaba, *Electrochem. Commun.*, 2014, **44**, 66–69.

This journal is © The Royal Society of Chemistry 2017

Chem. Soc. Rev., 2017, **46**, 3529–3614 | 3613

602 L. Qiu, Z. Shao, W. Wang, F. Wang, D. Wang, Z. Zhou, P. Xiang and C. Xu, *RSC Adv.*, 2014, **4**, 2485–24862.

603 B. Koo, H. Kim, Y. Cho, K. T. Lee, N. S. Choi and J. Cho, *Angew. Chem., Int. Ed.*, 2012, **51**, 8762–8767.

604 I. Kovalenko, B. Zdyrko, A. Magasinski, B. Hertzberg, Z. Milicev, R. Burtovyy, I. Luzinov and G. Yushin, *Science*, 2011, **334**, 75–79.

605 X. Zhao, S. A. Vail, Y. Lu, J. Song, W. Pan, D. R. Evans and J. J. Lee, *ACS Appl. Mater. Interfaces*, 2016, **8**, 13871–13878.

606 Y. Li, Y.-S. Hu, M.-M. Titirici, L. Chen and X. Huang, *Adv. Energy Mater.*, 2016, **6**, 1600659.

607 K. Ui, S. Kikuchi, F. Mikami, Y. Kadoma and N. Kumagai, *J. Power Sources*, 2007, **173**, 518–521.

608 V. Palomares, M. Casas-Cabanas, E. Castillo-Martínez, M. H. Han and T. Rojo, *Energy Environ. Sci.*, 2013, **6**, 2312–2337.

609 A. Magasinski, B. Zdyrko, I. Kovalenko, B. Hertzberg, R. Burtovyy, C. F. Huebner, T. F. Fuller, I. Luzinov and G. Yushin, *ACS Appl. Mater. Interfaces*, 2010, **2**, 3004–3010.

610 S. Komaba, K. Shimomura, N. Yabuuchi, T. Ozeki, H. Yui and K. Konno, *J. Phys. Chem. C*, 2011, **115**, 13487–13495.

611 S. L. Chou, Y. Pan, J. Z. Wang, H. K. Liu and S. X. Dou, *Phys. Chem. Chem. Phys.*, 2014, **16**, 20347–20359.

612 Q. Fan, W. Zhang, J. Duan, K. Hong, L. Xue and Y. Huang, *Electrochim. Acta*, 2015, **174**, 970–977.

613 D. Ma, Z. Cao and A. Hu, *Nano-Micro Lett.*, 2014, **6**, 347–358.

614 D. Mazouzi, Z. Karkar, C. Reale Hernandez, P. Jimenez Manero, D. Guyomard, L. Roué and B. Lestriez, *J. Power Sources*, 2015, **280**, 533–549.

615 W. Zhang, M. Dahbi and S. Komaba, *Curr. Opin. Chem. Eng.*, 2016, **13**, 36–44.

616 F. Zhao, P. Xue, H. Ge, L. Li and B. Wang, *J. Electrochem. Soc.*, 2016, **163**, A690–A695.

617 L. W. Shacklette, J. E. Toth and R. L. Elsenbaumer, *Conjugated polymer as substrate for the plating of alkali metal in a nonaqueous secondary battery*, Allied Corp., USA, 1985.

618 T. Shishikura and M. Takeuchi, *Secondary batteries*, Showa Denko K. K. Hitachi, Ltd, Japan, 1987.

619 K. Kubota, N. Yabuuchi, H. Yoshida and M. Dahbi, *MRS Bull.*, 2014, **39**, 416–422.

620 R. Dugas, B. Zhang, P. Rozier and J. M. Tarascon, *J. Electrochem. Soc.*, 2016, **163**, A867–A874.

621 Y. Li, S. Xu, X. Wu, J. Yu, Y. Wang, Y.-S. Hu, H. Li, L. Chen and X. Huang, *J. Mater. Chem. A*, 2015, **3**, 71–77.

622 S. Xu, Y. Wang, L. Ben, Y. Lyu, N. Song, Z. Yang, Y. Li, L. Mu, H.-T. Yang, L. Gu, Y.-S. Hu, H. Li, Z.-H. Cheng, L. Chen and X. Huang, *Adv. Energy Mater.*, 2015, 1501156.

623 H. Wang, Y. Xiao, C. Sun, C. Lai and X. Ai, *RSC Adv.*, 2015, **5**, 106519–106522.

624 M. Keller, C. Vaalma, D. Buchholz and S. Passerini, *ChemElectroChem*, 2016, **3**, 1124–1132.

625 H. Li, L. Peng, Y. Zhu, D. Chen, X. Zhang and G. Yu, *Energy Environ. Sci.*, 2016, **9**, 3399–3405.

626 Y. Wang, R. Xiao, Y. S. Hu, M. Avdeev and L. Chen, *Nat. Commun.*, 2015, **6**, 6954.

627 S. Guo, H. Yu, P. Liu, Y. Ren, T. Zhang, M. Chen, M. Ishida and H. Zhou, *Energy Environ. Sci.*, 2015, **8**, 1237–1244.

628 Y. Zhang, H. Zhao and Y. Du, *J. Mater. Chem. A*, 2016, **4**, 7155–7159.

629 H. Gao and J. B. Goodenough, *Angew. Chem., Int. Ed.*, 2016, **55**, 12768–12772.

630 J.-Y. Hwang, C. S. Yoon, I. Belharouak and Y.-K. Sun, *J. Mater. Chem. A*, 2016, **4**, 17952–17959.

631 H. Y.-P. Hong, *Mater. Res. Bull.*, 1976, **11**, 173–182.

632 J. B. Goodenough, H. Y.-P. Hong and J. A. Kafalas, *Mater. Res. Bull.*, 1976, **11**, 203–220.

633 http://www.businesswire.com/news/home/20160129005028/en/Global-Rechargeable-Battery-Market-Reach-Close-USD.

634 M. Sathiya, K. Hemalatha, K. Ramesha, J.-M. Tarascon and A. S. Prakash, *Chem. Mater.*, 2012, **24**, 1846–1853.

635 G. Singh, B. Acebedo, M. C. Cabanas, D. Shanmukaraj, M. Armand and T. Rojo, *Electrochem. Commun.*, 2013, **37**, 61–63.

636 J. M. D. Ilarduya, L. Otaegui, J. M. L. D. Amo, M. Armand and G. Singh, *J. Power Sources*, 2017, **337**, 197–203.

637 B. Zhang, R. Dugas, G. Rousse, P. Rozier, A. M. Abakumov and J.-M. Tarascon, *Nat. Commun.*, 2016, **7**, 10308.

638 Development of a Sodium Ion Secondary Battery, Sumitomo Chemical Co. Ltd, https://www.sumitomo-chem.cO.jp/english/rd/report/theses/docs/2013E_3.pdf.

639 A battery Revolution in Motion, CNRS News, https://news.cnrs.fr/articles/a-battery-revolution-in-motion.

640 Faradion Electric Bike: Prototype Powered By Sodium-Ion Batteries, http://www.greencarreports.com/news/1098434_faradion-electric-bike-prototype-powered-by-sodium-ion-batteries.

641 L. Wangm, J. Song, R. Qiao, L. A. Wray, M. A. Hossain, Y.-D. Chuang, W. Yang, Y. Lu, D. Evans, J.-J. Lee, S. Vail, X. Zhao, M. Nishijima, S. Kakimoto and J. B. Goodenough, *J. Am. Chem. Soc.*, 2015, **137**, 2548–2554.

642 Noble High Energy Density Sodium Layered Oxide Cathode Materials: from Material to cells, https://ecs.confex.com/ecs/230/webprogram/Paper88422.html.

643 J. W. Choi and D. Aurbach, *Nat. Rev. Mater.*, 2016, **1**, 16013.